Thermomechanical Properties of Polymers at High Rates of Strain

A thesis submitted to the Department of Engineering Science of Oxford University in partial fulfilment of the requirements for the degree of Doctor of Philosophy

by

Albin S. Trojanowski

Exeter College

Oxford

Trinity Term 1997

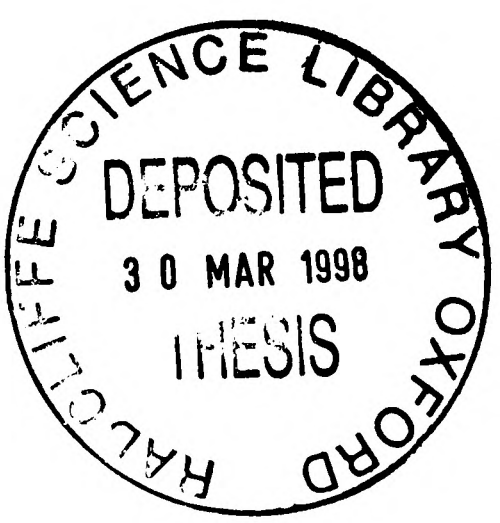

Abstract

Albin S. Trojanowski D.Phil.

Exeter College Trinity Term 1997

Thermomechanical Properties of Polymers at High Rates of Strain

The objective of this project was to develop a suitable testing technique which will allow the measurement of the bulk surface temperature of a specimen during high strain-rate compression testing. A fast response infra-red radiometer was developed which has the capability of measuring bulk surface temperature changes with an estimated accuracy of ±2 °C and with a response time of 1.4μs. The radiometer is capable of measuring temperature changes above 20 °C, when the signal-to-noise ratio becomes greater than 1.

The properties of polymeric materials are extremely temperature sensitive, particularly when the glass transition temperature is approached. Models such as Eyring predict the yield of a polymer at constant temperature; the yield stress being unaffected by temperature rises. Temperature as well as mechanical data will allow models to be revised to include strain and dynamic temperature terms to predict the flow under adiabatic conditions. Strain-rates of *ca.* $2500s^{-1}$ were achieved when testing specimens and this rate was obtained using a split Hopkinson pressure bar. A substantial number of preliminary tests were conducted in order to obtain a suitable specimen size which was then used in the temperature measurement process. Quasistatic, intermediate and high strain-rate tests were performed; the last utilised the radiometer for temperature measurement. An Eyring plot was constructed from which fundamental values for activation volumes and enthalpies were obtained. Full descriptions of the testing techniques used have been included and a brief photoelastic analysis has been carried out on a partially deformed specimen which shows molecular alignment.

Acknowledgements

I would like to thank my supervisors, Professor Carlos Ruiz and Dr. John Harding, for their great help throughout the project.

The project was funded by the Defence Evaluation and Research Agency. The help and encouragement of Marcus Simmons was greatly appreciated.

I am grateful to Mr. Peter Rockett for his help with designing the radiometer. Thanks also to Mr. Neil Warland for manufacturing test specimens; Mr. Phil Webb for strain gauging loading bars; and Mr. Richard Duffin for his help with high speed photography.

I would also like to thank members of the Solid Mechanics group for useful comments and discussions.

Preface

This thesis is an account of the work which was carried out by the author at the Department of Engineering Science at the University of Oxford, under the joint supervision of Prof. Carlos Ruiz and Dr. John Harding.

No part of this thesis has been submitted for a degree at any other university. The research described here is original, although the work of others has been drawn upon freely with due acknowledgements in the text.

Contents

Nomenclature

A_0 initial cross-sectional area

A_b cross sectional area of loading bars

A_d area of detector

A_s specimen cross-sectional area

A_α material constant for α-relaxation process

A'_α combined material constant for α-relaxation process

A_β material constant for β-relaxation process

A'_β combined material constant for β-relaxation process

c elastic wave velocity

C_α material constant for α-relaxation process

C_β material constant for β-relaxation process

C_1 Planck radiation constant

C_2 Planck radiation constant

D^* specific detectivity

E modulus

or photon incidence on detector

E_a apparent modulus

E_m modulus of spring (Maxwell)

$\dot{E}_{th}$ rate of thermal energy evolution

E_v modulus of spring (Voigt)

f frequency

f_c cut-off frequency

f_σ material fringe constant

F force

G shear modulus

k Boltzmann constant

K constant

K_1 constant

K_2 constant

l_g gauge length

L_λ Planck spectral luminosity

N fringe order

p pressure

P_1 force at input end of specimen

P_2 force at output end of specimen

P_{av} average force

Q activation energy

Q_α activation energy for α-relaxation

Q_β activation energy for β-relaxation

R responsivity

S-N signal to noise ratio

t time

or specimen thickness

T temperature

or transmissibility

T_1 static temperature T_1

T_2 static temperature T_2

$\dot{T}$ rate of temperature rise

T_{c1} temperature calculated using pre-test calibration polynomial

T_{c2} temperature calculated using post-test calibration polynomial

T_t true temperature (emissivity corrected)

T_g glass transition temperature

u_1 displacement of input end of specimen

u_2 displacement of output end of specimen

V activation volume (Eyring volume)

V_r radiometer output

$\dot{W}$ work rate per unit volume

x_{dt} displacement measured by the displacement transducer

α angle

β proportion of work converted to heat

$\dot{\gamma}$ macroscopic shear strain-rate

$\dot{\gamma}_0$ macroscopic quasistatic shear strain-rate

Δ relative phase shift

ΔE difference between two energy states

ΔH activation enthalpy

ε strain

or emissivity

ε_{av} average specimen strain

ε_i incident pulse

ε_r reflected pulse

ε_t transmitted pulse

ε_{true} true strain

$\dot{\varepsilon}$ macroscopic plastic strain-rate

$\dot{\varepsilon}_0$ macroscopic quasistatic strain-rate

$\dot{\varepsilon}_{av}$ average strain-rate

$\dot{\varepsilon}_y$ macroscopic plastic strain-rate to produce yielding

Δf system bandwidth

ΔG Gibbs' free energy

η_m damping coefficient (Maxwell)

η_v damping coefficient (Voigt)

θ relative orientation of the applied shear stress

ρ density

ΔS entropy

σ stress

σ_1 principal stress in direction 1

σ_2 principal stress in direction 2

σ_{av} average stress

σ_h hydrostatic stress

σ_y yield stress

τ shear stress

or detectable rise time

τ_c critical shear stress

τ_a fraction of the applied stress borne by thermally activated processes

φ loss modulus

ω angular frequency

Ω solid angle

$\Omega(p)$ pressure activation volume

To my Parents

Chapter 1

Introduction

1.1 General Types of Polymer

Polymers are becoming widely used in many important emerging technologies of the twentieth century. Raw materials for synthetic polymers are petroleum, coal and natural gas, which are sources of ethylene, methane, alkenes and aromatics. Polymers are used in a vast range of everyday applications, in clothing, housing materials, appliance housings, automotive, aerospace, military applications, and also in communications.

Polymers have advantages over other types of materials, such as metals and ceramics, because of their low processing costs, low weight and properties such as transparency and toughness, thus forming a unique combination.

There are three major polymer classes: thermoplastics, thermosets and rubbers (or elastomers). Polymers that are typical of each of these classes are listed in Table 1.1. *Thermoplastics* are among the most common polymers and these materials are commonly termed 'plastics'. Linear or branched thermoplastics can be reversibly melted or can be dissolved in a suitable solvent. Thermoplastic polymers are those that when heated, flow in the

manner of a highly viscous liquid, and do so reversibly time and time again on subsequently being heated and cooled.

Plastics - Thermoplastics	Polyethylene (PE) Polyamide (NYLON) Polycarbonate (PC) Acrylic (PMMA) Polypropylene (PP)
Plastics - Thermosets:	Epoxy (EP) Phenolic (PF) Unsaturated Polyester (UP)
Elastomers:	Natural Rubber (NR) Polybutadiene (BR) Ethylene-propylene Styrene-butadiene (SBR)

Table 1.1 Different Classes of Polymers

In *thermosets* there is a three dimensional network structure, a single highly connected molecule, which exhibits rigidity and immobility. Thermosets are heated to form rigid structures but once set, they do not melt upon prolonged heating nor do they dissolve in solvents. Thermosets generally have only short chains between cross-links and exhibit glassy brittle behaviour. This class of polymer is used as a high performance adhesive, eg. epoxy. Thermosets are heated to an appropriate temperature for a short time, so that they flow as a viscous liquid. A slow chemical cross-linking reaction then causes the liquid to solidify to form an infusible mass.

Polymers with long flexible chains between cross-links are known as *rubbers* or *elastomers* which, like the thermosets, cannot be melted. Elastomers are characterised by a three dimensional cross-linked network which has the well known property of being stretchable and springing back to the original form.

Amorphous polymers (meaning that the material has no long-range order in its lattice),

such as epoxy resins (the second grouping), do not crystallise even when cooled from the melt extremely slowly. The main effect of cooling the melt is to decrease the violence of the thermal agitation of the molecular segments. In the melt, segments of the molecules change place by thermally activated jumps, at a rate of over 10^6 s^{-1}. If cooling is continued, a temperature is reached at which the rate of segmental movement is extremely sluggish, and then on further cooling, finally stops altogether. The polymeric specimen then consists of long molecules tangled in a liquid-like manner, which is called the *glassy state*. As the polymeric glass is heated through a relatively narrow temperature range, known as T_g, in which segments of molecules commence to change position by discrete jumps, many of its properties, mechanical, electrical, optical and thermal, undergo a drastic change described below.

Cross linked polymers can respond to stresses in three different ways, depending on the temperature, which influences the mobility of chain segments. Below T_g, the glass transition temperature) they behave like glasses. That is, their extension is due mainly to bending of valency angles and to bond extension. In this temperature range the modulus of the resin is high; the extension is instantaneous and fully recovers on the removal of the stress.

Secondly, at a sufficiently high temperature thermal energy allows segmental rearrangements, involving bond rotation, to take place practically instantaneously. Above this temperature the resin behaves like a rubber. Its modulus is low, usually several orders of magnitude lower than it was in the glassy region. The extension is again instantaneous and fully recoverable. Because of the chemical bonds linking each segment, cross linked polymers cannot flow as linear polymers do at high temperature.

The third way of response relates to the transition between the glassy and the rubbery behaviour. In this region the moving segments have to force their way against a viscous drag.

The extension is therefore time dependant, and the strain lags behind the stress. Deformation in the glassy and in the rubbery states is mainly elastic, where the energy of deformation is stored. In the transition region part of the energy is dissipated, because of the viscous element, during the deformation. As a result of stress the polymer segments move into a new equilibrium position and this motion is called the *relaxation phenomenon*. The most important relaxation occurs when the polymer changes from a glass to a rubber, which is called the glass-rubber relaxation (also α-relaxation).

The term 'epoxy resin' is commonly applied to a broad range of materials, both pre-polymers (which contain reactive epoxy groups) and cured polymers (which are still called epoxy resins although all the reactive groups have reacted during the polymerisation process).

1.2 Epoxies

Historically, the first products which would now be called epoxy resins were synthesised as early as 1891 (Dearborn *et al*, 1953, & Lee *et al*, 1967) although their commercialisation did not come until much later when the resin forming reaction was found to produce a material suitable for dental restoration. The use of these epoxy resins as a potential replacement for 'Vulcanite' as a denture base material was attractive because of the former's ability to undergo an addition cure at relatively low moulding pressures without the evolution of low molecular weight species.

The consumption of epoxy resins has increased steadily over the last fifty years, showing an average annual increase of 5%. The predicted epoxy consumption for 1996 was 660,000 tonnes, with the USA and combined European countries the largest users, at approximately 220,000 tonnes, followed by Japan with 160,000 tonnes shown schematically

in Figure 1.1 (Lavabre, 1994).

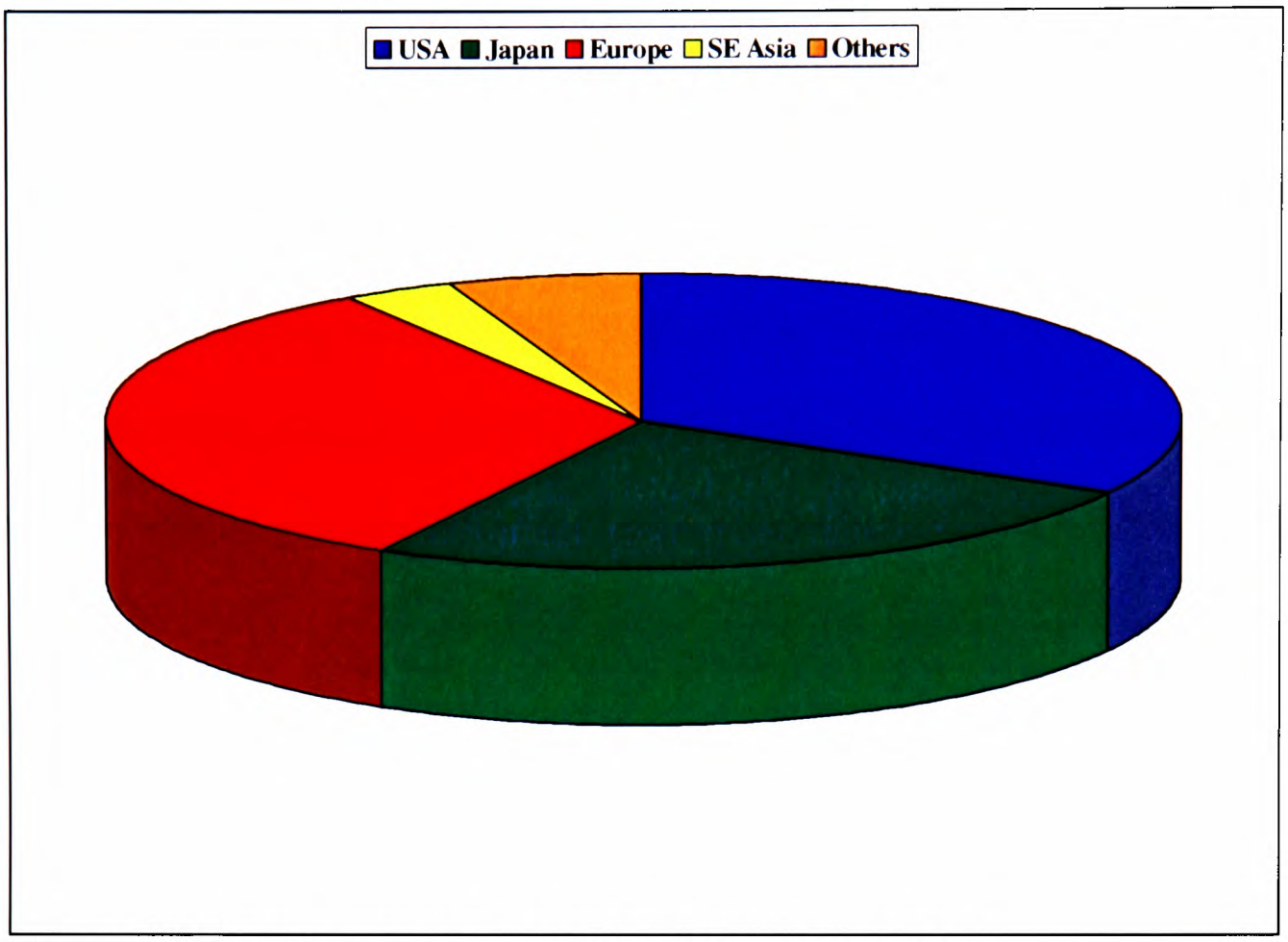

Figure 1.1 The Current World Market for Epoxy Resins

Many applications in defence and aerospace encounter deformation of materials at high rates of strain. It is often useful for design engineers to be able to predict the behaviour of structures under impact loading using computer simulations. Material models can be created, involving one or more equations defining the relationship between stress, strain, strain-rate and temperature. Finite element analysis can be performed in order to fit a model to test data, which can then be subsequently used to predict the material behaviour. In order to create accurate material models, all four quantities must be measured precisely. The stress, strain and strain-rate are generally easily measurable quantities. The measurement of the fourth quantity, temperature, can be complex, depending on the testing conditions, such as strain-rate. As the strain-rate increases the ease of measuring temperature decreases.

1.3 Aim of the Investigation and Structure of the Thesis

The aim of this investigation is to characterise the properties of an epoxy resin at high rates of strain by means of compression tests combined with temperature measurement.

Chapter 2 presents a literature review which comments on existing constitutive models and the effects observed by previous workers on various polymeric materials. This is followed by two chapters which detail the testing techniques developed for this investigation - Chapter 3 is concerned with the split-Hopkinson pressure bar technique and demonstrates its reliability. Programs written specifically for analysing data obtained from Hopkinson bar experiments are compared, and so are high speed photographs for tests. Chapter 4 describes an improved method of measuring bulk surface temperature changes of a specimen during high rate testing. Several methods of calibration were examined - two variations of a copper block arrangement and also a free air calibration using a hot air gun. Also, the method of interpreting data obtained from the radiometer during a high strain-rate test is detailed. Chapter 5 presents results from the testing programme, and discussions and conclusions are contained in Chapters 6 & 7 respectively.

1.4 References

Dearborn, E.C., Fuoss, R.M., Mackenzie, A.K. & Shepherd, R.G., Ind.Eng.Chem, 45, p.2715, 1953.

Lavabre, S., Rev.G.Caout.Plast. No.731, p.48-51, 1994.

Lee, H. & Neville, K., "Handbook of Epoxy Resins", Sections1-2 to 1-4, McGraw-Hill, New York, 1967.

Chapter 2

Literature Review

2.1 Introduction

There are many occasions when understanding the properties of materials undergoing impact is essential in engineering design. Many complex processes occur in such cases; the material is subjected to rapid acceleration, it is strained very rapidly, there are large shock pressures and the temperature often rises by several hundreds of degrees. Although many high strain-rate studies have been performed on metals, comparatively few papers have been published on the rapid deformation properties of polymers and this is a hindrance to their use in applications where they may be subject to impact.

Geometrical effects (such as inertia or friction) are not part of a material's description, so everything is done to minimise them, or to measure them so that their effects can be calculated. However there are certain parameters which present a few difficulties.

Conventional tests are performed in uniaxial tension or compression at a nominally constant temperature and the results are interpreted under the assumption that the whole specimen is in a state of uniform stress and temperature. Referring to the compression test, the

state of stress depends on the aspect ratio of the specimen, the difference between the radial expansion of the specimen and test bars and the coefficient of friction at the contact surfaces.

Temperature can also be a major problem. It is impossible to conduct a rapid deformation experiment without changing the temperature of the material during the test. So what temperature should be quoted? It is normal to quote the ambient temperature or starting temperature, for although temperature rises can be measured, it is a difficult measurement, and is not often done.

Polymers can be described as viscoelastic since their behaviour is intermediate between that of an elastic solid and a viscous liquid. In general, their behaviour is very dependent on the testing conditions, particularly the temperature and the rate of application of the load. At low temperatures (or high strain-rates) a polymer behaves like a glass with a high Young's modulus and limited plastic flow before rupture. Conversely, at high temperatures (or low strain-rates) the polymer behaves like a rubber. The glass transition temperature, T_g, is the temperature at which large-scale molecular motion becomes possible and the glassy polymer 'unfreezes' into a more rubber like mode. The glass transition temperature is normally observed as a discontinuous change in modulus. As previously mentioned, molecular chain movement in cross-linked polymers is limited, but there is still a decrease in modulus of several orders of magnitude at T_g.

2.2 Phenomenological Models

A phenomenological description of the mechanical behaviour is provided by rheological models, which are based on elementary springs and dashpots (Derby *et al* 1992 & McCrum *et al* 1988). Using a combination of these elements as in the Voigt-Maxwell models, Figure 2.1(a), it is possible to estimate the effect of strain-rate and the energy lost through non-

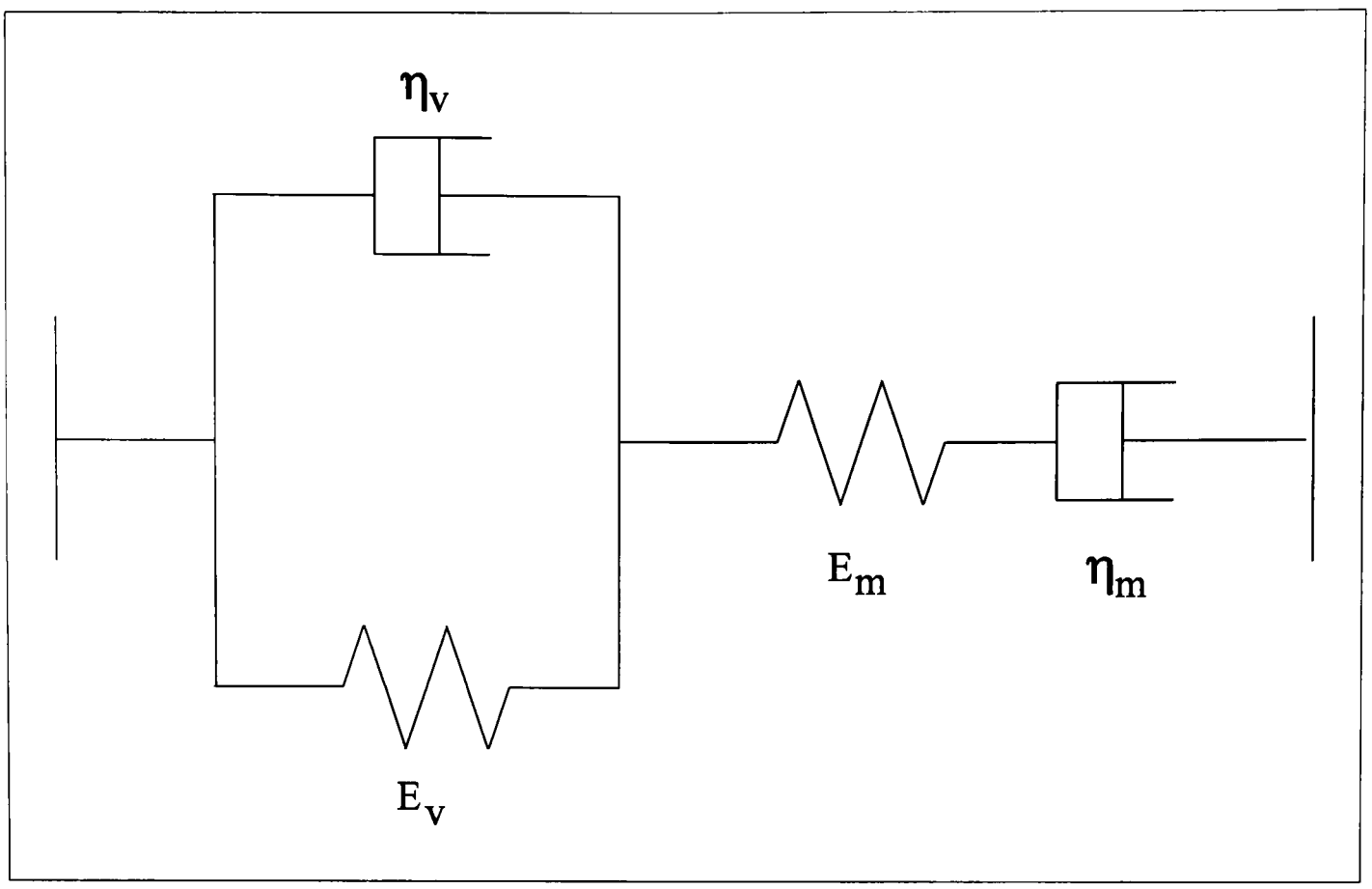

Figure 2.1(a) Combined Maxwell-Voigt Models

linear deformation. This approach, however, relies on the measurement of the elastic and anelastic properties of the material under uniaxial loading and isothermal conditions. It does not pretend to explain the fundamental processes determining the material behaviour.

Figure 2.1(b) shows the variation of the apparent Young's modulus, defined by Equation 2.1,

$$E_a = \frac{E_m E_v}{E_m + E_v} \sqrt{\frac{\left(\frac{\eta_v \omega}{E_v}\right)^2}{1 + \left(\frac{\eta_v \omega}{E_m + E_v}\right)^2}} \qquad \textbf{(2.1)}$$

in which E_m and E_v are the moduli of the springs, η_m and η_v are the damping coefficients, and ω is the loading angular frequency (rad/s). Taking $\sigma_0 = E_a \epsilon_0$, if $\sigma = \sigma_0 \sin\omega t$, ϵ follows a simple harmonic motion with an out-of-phase ϕ w.r.t. σ, given by Equation 2.2 and seen in Figure

2.1(c).

$$\tan\phi = \frac{\eta_v E_m \omega}{(E_m + E_v)E_v + \eta_v^2 \omega^2} \qquad \textbf{(2.2)}$$

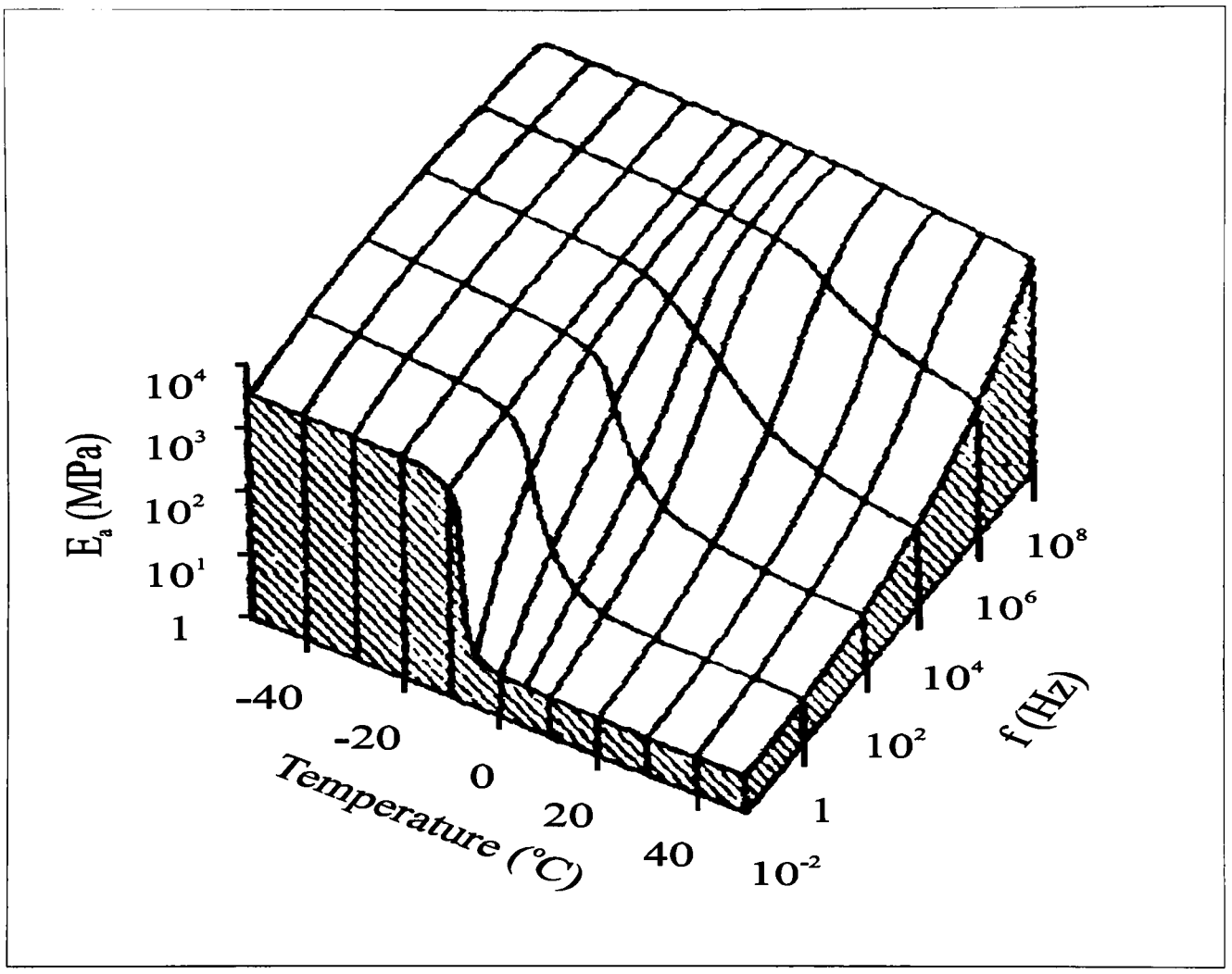

Figure 2.1(b) Variation of Modulus with Temperature and Loading Frequency

It can be seen from Figure 2.1(b) that E_a is a function of frequency (f). Now, as the frequency, f, increases, E_a increases because the 'damper' becomes stiffer, ie. as the strain-rate increases the modulus increases. Temperature is an important factor in this model, since at low temperatures there is no creep and no viscosity.

Thus purely elastic behaviour is exhibited which is frequency independent. As the temperature approaches T_g, viscosity appears. In Figure 2.1(c), $\tan\phi$ is approximately zero at low temperature, meaning that the material shows elastic behaviour and no damping is present

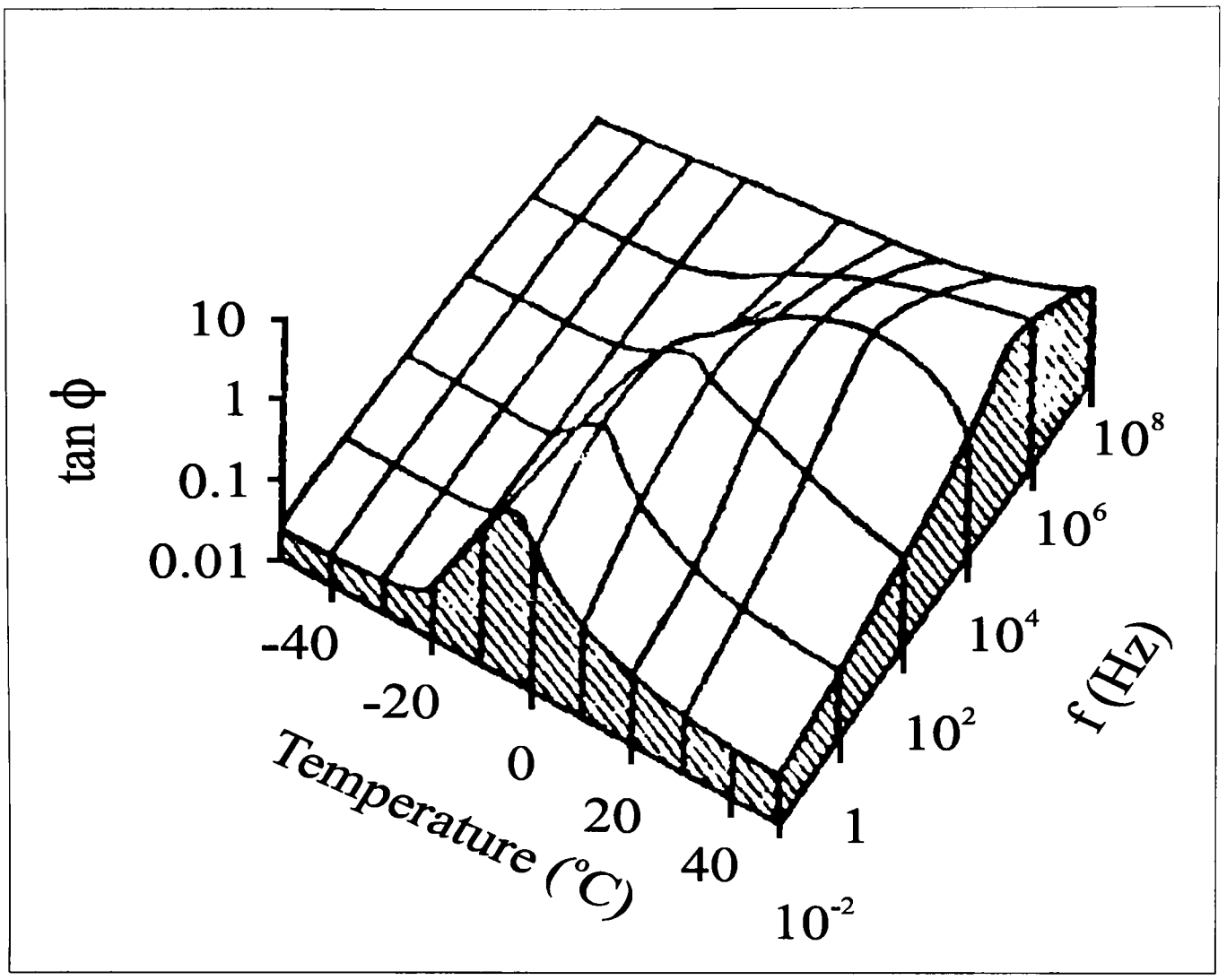

Figure 2.1(c) Variation of Loss Modulus with Temperature and Loading Frequency

(i.e. the stress and strain are in phase). However, tanϕ increases as temperature increases and this causes a retardation, meaning that the strain is now beginning to lag behind the stress. Although the simple dashpot-spring model does not explain the observed fall of E_a at around -10°C which is accompanied by a maximum in tanϕ, it is known that the large losses shown at T_g are a consequence of molecular movements commencing and energy being dissipated through intramolecular chain friction.

2.3 Constitutive Equations

Constitutive equations are an attempt to relate the observed behaviour to the physical processes thought to control this behaviour. In essence, they recognise that the process of deformation is thermally activated, like creep in the case of metals.

Escaig *et al*, 1978 suggested a thermodynamical approach to describe the thermal activation. This analysis is based on the concept of molecular flaws and the resulting deformation is stress and temperature controlled through the appearance and then growth of such flaws, associated with activation energies and volumes. The macroscopic plastic strain-rate can be written in the form:

$$\dot{\varepsilon} = \dot{\varepsilon}_0 \exp -\frac{\Delta H(\sigma,T)}{kT} \qquad \textbf{(2.3)}$$

where:

$$\Delta H = \Delta H_0 - \tau_a V \qquad \textbf{(2.4)}$$

where H is the activation enthalpy, τ_a is the fraction of the applied stress borne by thermally activated processes, k is the Boltzmann constant, V is the activation volume (also known as the "Eyring volume") so that, for a given stress at constant strain-rate:

$$\Delta H = kT \ln \dot{\varepsilon}_0 / \dot{\varepsilon} = \alpha T \qquad \textbf{(2.5)}$$

which shows that provided only one mechanism controls the deformation (providing $\dot{\varepsilon}_0$ is a constant), the activation enthalpy is proportional to the temperature. It is assumed that plastic deformation develops from germination sites when their volume reaches a critical size V_c.

The rate process theory assumes that the basic fracture events are controlled by thermally activated breakages of primary and secondary bonds, and that the accumulation of these events lead to crack formation. Many workers have applied the early formulation by Eyring, developed originally for viscous liquids, to the study of yield in polymers. For a liquid each molecule may be considered as part of a pseudo-lattice of nearest neighbours. For viscous flow (or shear) to take place, a molecule must move to an adjacent site and in doing so it must

overcome a potential barrier set by its neighbours. In the case of a polymer the model considers molecular segments vibrating over an energy barrier (of height ΔH_0). The effect of an applied stress is to reduce the height of the barrier for a jump in the forward direction and increase it for a jump in the reverse direction. It is assumed that the net jump rate in the forward direction is proportional to the strain-rate. The macroscopic shear strain-rate is then given by Equation 2.6.

$$\dot{\gamma} = \dot{\gamma}_0 \exp\left(\frac{-\Delta H_0}{kT}\right) \sinh\left(\frac{V\tau}{2kT}\right) \qquad \textbf{(2.6)}$$

where ΔH_0 is the enthalpy (or activation energy) of the process, $\dot{\gamma}_0$ is a constant with the dimensions of strain jump rate, and V is the activation volume. The quantity $V\tau$ is the work done on a mobile segment during a jump of the applied shear stress, τ. Since this equation describes a viscous process occurring at constant stress, it can be applied to yielding at constant stress. The flow stress is given (from Equation 2.6 above) by Equation 2.7.

$$\tau = \frac{2kT}{V} \sinh^{-1}\left[\frac{\dot{\gamma}}{\dot{\gamma}_0} \exp\frac{\Delta H_0}{kT}\right] \qquad \textbf{(2.7)}$$

Under conditions of low strain-rate or high temperatures, this equation predicts that the flow stress will be proportional to the applied shear strain-rate, since $\sinh^{-1} x \approx x$ for small x. This means that the jumps in the forward and reverse directions are roughly the same.

For flow under high strain-rates or lower temperatures the flow stress is proportional to the logarithm of the applied shear strain-rate since $\sinh^{-1} x \approx \log x$ for large x. The number of jumps in the reverse direction can then be neglected at high strain-rates in comparison to those in the forward direction.

Since yielding is pressure sensitive, an approach consists in taking one of the established criteria for metals and modifying it by introducing a term in the hydrostatic

pressure. The Eyring model, including a pressure term, leads to Equation 2.8 for the high strain-rate regime:

$$\dot{\gamma} = \dot{\gamma}_0 \exp\left[-\left(\frac{\Delta H - p\Omega(p)}{kT}\right)\right]\exp\left(\frac{\tau V}{kT}\right) \qquad \textbf{(2.8)}$$

where Ω(p) is a function called the "pressure activation volume" and ΔH represents the barrier height, T is the absolute temperature, V is the activation volume, $\dot{\gamma}$ is the effective shear strain-rate.

The equation predicts that for constant temperature the yield stress is a linear function of ln$\dot{\varepsilon}$. Better modelling can be realised by the fact that there is normally more than one activated rate process present with all species of flow units moving at the same rate, the stress being additive. The many constants associated with the equations can then be fitted to the test results. Actually, the number of processes operating in parallel for each specific polymer is deterministic and it can be read from the apparent curvature changes in the stress/strain-rate curves of test results.

A more detailed description of the mechanical behaviour of amorphous polymers over a wide range of temperatures and strain-rates requires the consideration of several mechanisms in an additive manner. This is done in the Bauwens-Eyring model (Bauwens-Crowet *et al*, 1974), in which it is considered that there are two processes involved in the deformation, labelled α and β. When the material exhibits a β relaxation within the investigated temperature range, the relation between the yield stress σ_y and the strain-rate is given by Equation 2.9.

$$\frac{\sigma_y}{T} = A_\alpha\left[\ln 2C_\alpha\dot{\varepsilon} + \frac{Q_\alpha}{kT}\right] + A_\beta \sin h^{-1}\left[C_\beta\dot{\varepsilon}\exp\frac{Q_\beta}{kT}\right] \qquad \textbf{(2.9)}$$

The parameters A_α, A_β, C_α and C_β are specific to the material. These values are determined experimentally using a torsion pendulum apparatus for measuring the shear modulus, G, and damping as functions of temperature. The decrease in the value of shear modulus occurs particularly rapidly in two temperature regions. In these temperature regions the loss modulus exhibits a peak. The first peak at the highest temperature is termed the α-relaxation and then the next lowest temperature is termed the β-relaxation. Subsequent local maxima in the loss modulus exhibited on cooling to lower temperatures are denoted as γ, δ etc. The α-relaxation is the mechanical manifestation of the glass transition temperature. Cooling from the rubbery state through the glass transition region, causes molecular movement to become sluggish. A peak in loss modulus is seen and the shear modulus increases from the rubbery value to the glassy value. In the glass, the molecules are frozen in particular conformations. The side-groups, however, are not affected by freezing of the molecular backbone - they continue to rotate. On further cooling, the ability for side-group rotation is reduced and is represented by another peak in ϕ and again a sudden increase in G. Q_α and Q_β are respectively activation energies of molecular movements related to the glass transition and the secondary transition. When thermal activation does not play a primary role, Equation.2.9 can be expressed in the simplified form of Equation 2.10.

$$\frac{\sigma_y}{T} = A'_\alpha \ln\dot{\varepsilon} + A'_\beta \exp(\dot{\varepsilon}) \qquad \textbf{(2.10)}$$

which indicates clearly the two processes involved in the deformation. At higher strain-rates, the β process takes over and the α or glassy transition temperature process ceases to be relevant.

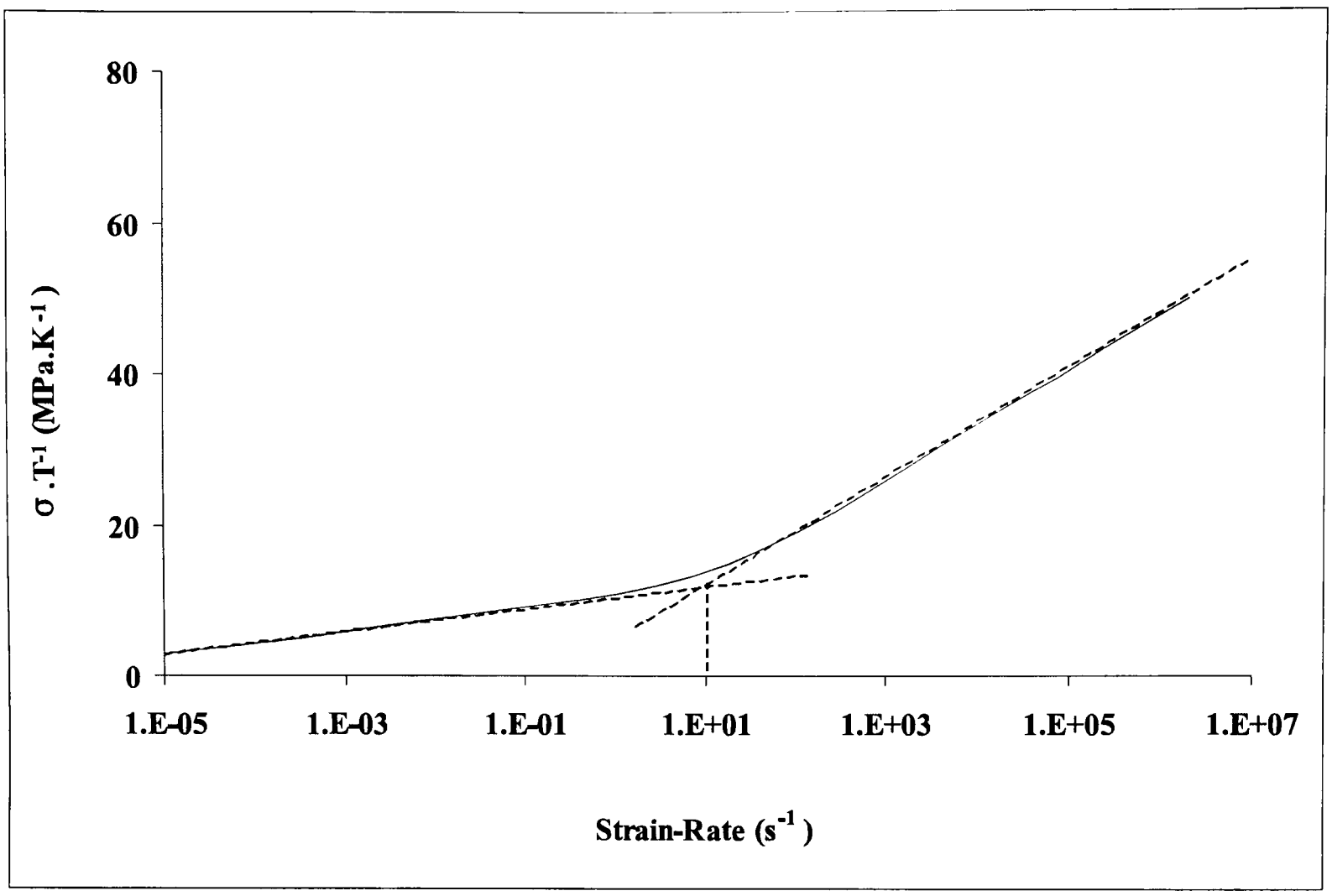

Figure 2.2 Deformation Processes for PMMA

Figure 2.2 based on experimental work by Bauwens quoted by Lataillade, illustrates this point for polymethylmethacrylate (PMMA). The critical value corresponding to the change from α to β is $\dot{\varepsilon}=10s^{-1}$.

In PMMA, thermal activation does not affect the results significantly, indeed the curve of Figure 2.2 represents a summary of isothermal test data at temperatures between -20°C and 100°C.

It is worthy of note that the thermal activation energy Q_β for the β process is found to be comparable with that from mechanical damping measurements, so it can be considered likely that the same microstructural mechanism operates in the two cases. In the case of polycarbonate (PC) in its glassy state, the evolution of its elastic limit (Bauwens-Crowet, 1974) requires only the consideration of the α process. The thermal activation energy Q_α for this process did not correlate with the activation energy for the glass transition relaxation in

dynamic damping experiments. This suggests that the yielding process at large strains is fundamentally different from the anelastic behaviour at low strains.

For higher strain-rates, such as occurring in Hopkinson bar tests, it was found (Steer *et al*, 1985) that the parameters linked in the β mechanism must vary with temperature. This idea is similar to that one obtained in Argon's model (Argon, 1973) where Q depends upon the elastic modulus. In other words, the polymer plasticity is supposed to be controlled by the thermally activated cooperative motion of several chain segments against the elastic constraint of the surrounding matrix.

2.4 Effect of Aspect Ratio and Friction

Most of the high strain-rate data for the mechanical behaviour of polymers has been obtained from compression tests using the Split Hopkinson bar described in Chapter 3. The specimen, normally a cylinder, is defined by its aspect ratio L/D (length/diameter) and is compressed between two flat ended bars. Compression tests are subjected to two major experimental errors: friction and mechanical inertia (Gorham *et al*, 1984). The shorter the gauge length, the higher the strain-rate and the faster quasistatic equilibrium is reached. It is therefore seen that a thin disc is preferable to a long cylinder for these considerations. However, friction at the ends becomes a serious problem in the case of thin disks. Failure to attend to sources of error such as friction has led workers to question previously published material (Briscoe *et al, 1984)* where an increase in the strain-rate sensitivity was reported for strain-rates higher than *ca.* $10^3 s^{-1}$ in the conventional Hopkinson bar (Chou *et al*, 1973).

In order to achieve high strain-rates in the SHPB apparatus it is necessary to reduce the gauge length of the specimen to a minimum compatible with practical considerations. Even so, inertial effects invalidate the very beginning of the test since the input and output forces will

differ by the inertia force in the specimen until such time when, through stress wave action, a state of quasistatic equilibrium prevails and both input and output forces equalise.

Friction has been taken into account (Walley *et al*, 1994) when investigating the sensitivity of the uniaxial compressive stress-strain response of seventeen different polymers at room temperature over a strain-rate range of 10^{-2} - $3x10^{4}$ s^{-1}. Hydrocarbon based lubricants were used to eliminate frictional stresses between the specimens and the anvils at all strain-rates. They found that petroleum jelly gave the best lubrication up to a strain of 40%. The advantage of studying such a large number of polymers is that specific groupings of behaviour could be identified. The diameter of the specimens was decreased at the very highest strain-rates to ensure that the contribution of radial inertial stresses to the measured yield pressure was minimal.

As is evident in the literature, the true extent of the reported increase in strain-rate sensitivity is inconsistent and depends on specimen dimensions and frictional constraints. In a recent paper (Dioh *et al*, 1993), experimental stress/strain results were presented for four polymers tested in compression at 23°C between the strain-rates of 10^{-4}-$10^{4}s^{-1}$. The high strain-rate results (10^{2}-$10^{4}s^{-1}$) were obtained in a SHPB system while the low and intermediate strain-rate tests were carried out in an Instron and a Mayes testing machine respectively. The results show that the choice of specimen thickness at high strain-rates significantly affects the measured flow stresses - thicker specimens, ie. with a higher length to diameter ratio, show a higher flow stress than those with a smaller length to diameter ratio. Some studies (Briscoe *et al*, 1984, & Walley *et al*, 1989) have suggested that by having a length to diameter ratio of 0.12 will not lead to significant frictional effects in the specimen, as long as a suitable lubricant such as petroleum jelly is applied between the specimen and the bars; otherwise an enhancement of flow stress for the wafer thin specimens will be obtained.

Figure 2.3 shows the variation of flow stress for polyester (a thermoplastic) with changing specimen dimensions. Unpublished data for epoxy, Hysol (a rubber modified epoxy containing reinforcing fibres and rubber nodules) and polyester obtained at Oxford, suggests

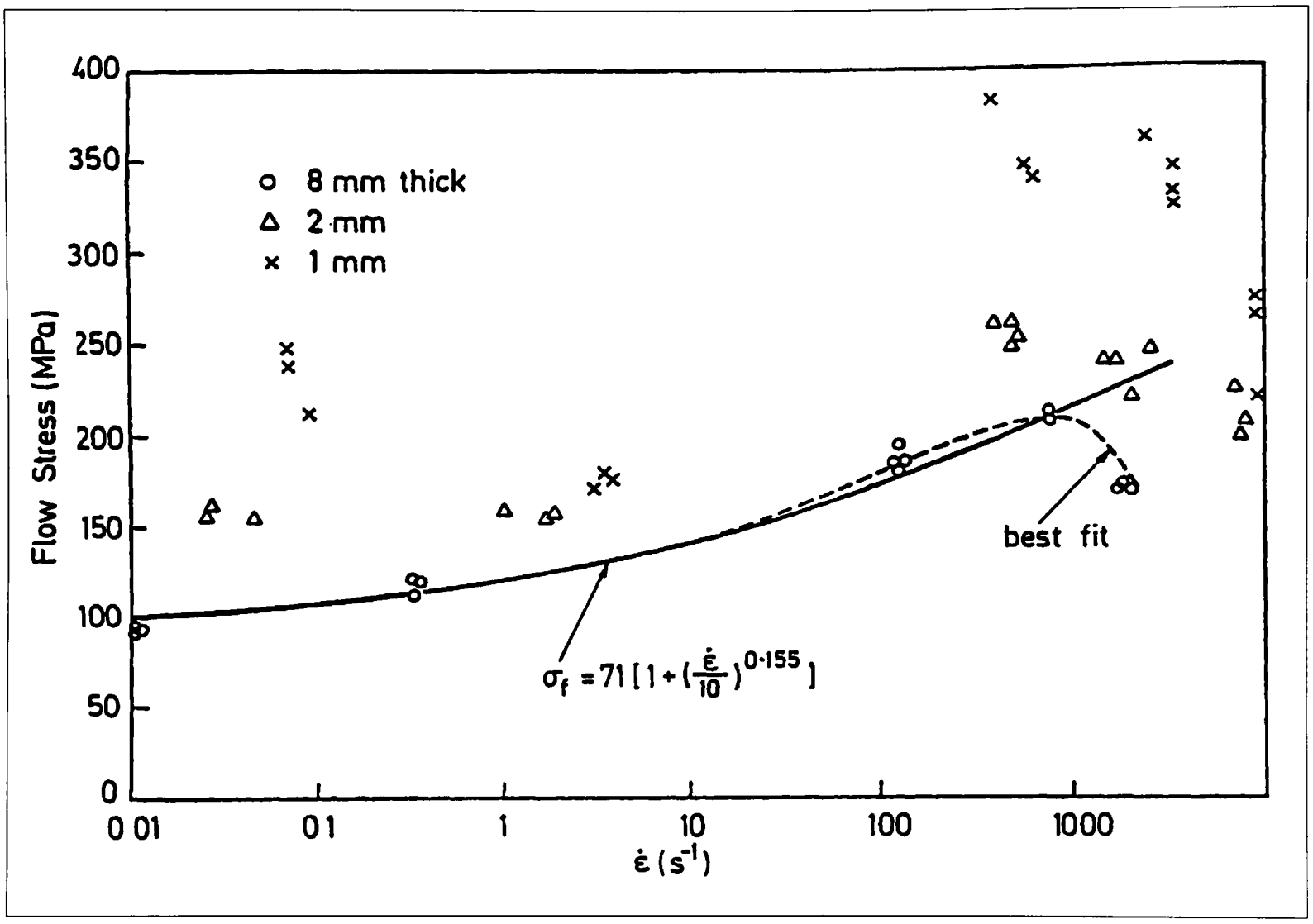

Figure 2.3 Variation of Flow Stress with Strain-Rate for Polyester at Room Temperature, Ruiz *et al*

that some thermosets show a reduction in yield strength at rates of strain in the region 10^3 - $10^4 s^{-1}$, as shown in Figures 2.3. & 2.5. This has been associated with adiabatic heating, resulting in an increase in temperature above T_g, but it may also be due to the evolution of damage or, indeed, to a feature of the actual testing conditions. In tests conducted at Oxford the specimens were lubricated. Even so, the results obtained for the very thin discs, with aspect ratios of 1/9, should be regarded as suspect, since the scatter in the data is immense, and also that the flow stress is enhanced. Unlike the data of Walley *et al* (1994), the yield point was defined at the intersection between lines tangential to the plastic and elastic parts of the curve.

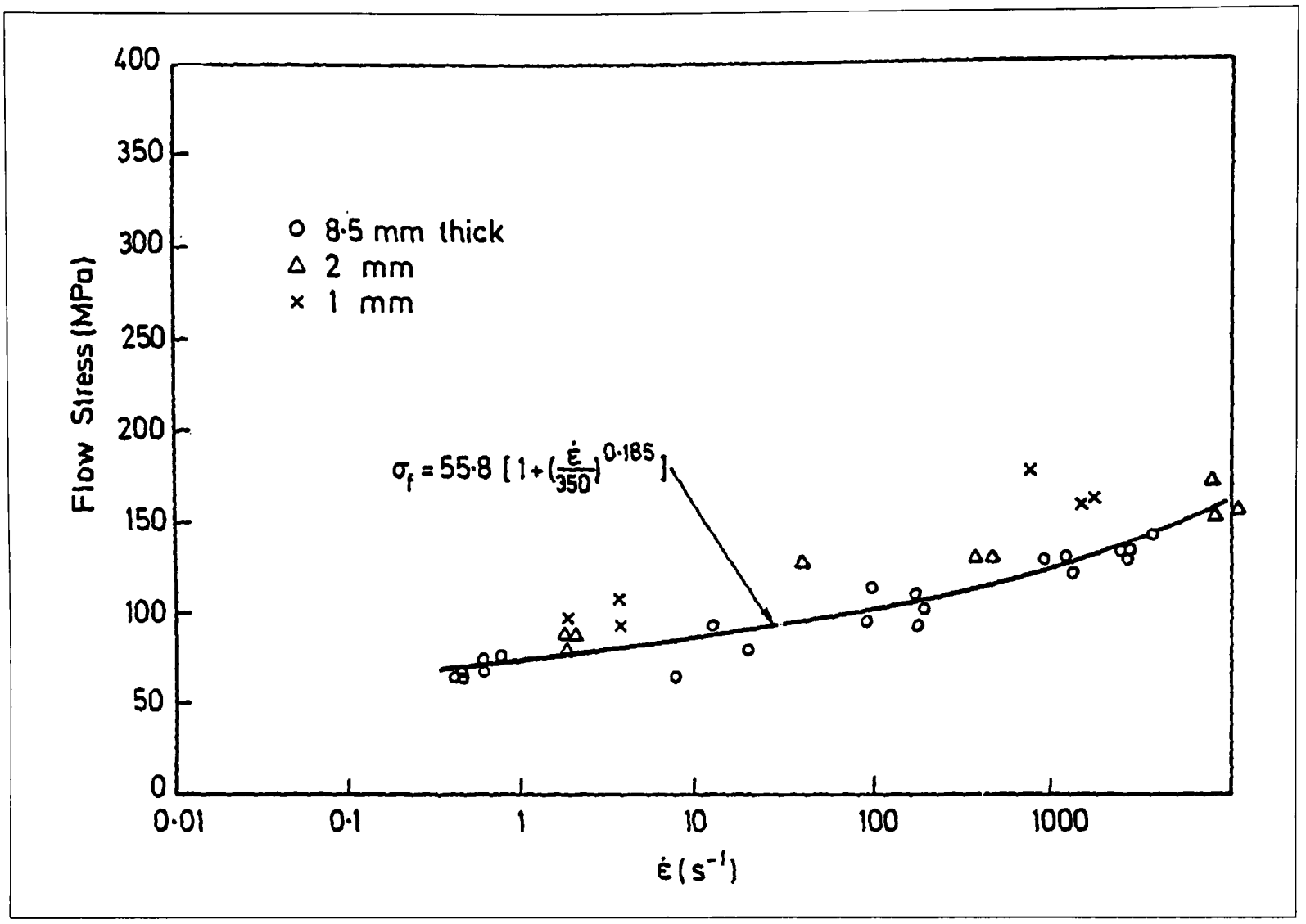

Figure 2.4 Variation of Flow Stress with Strain-Rate for HYSOL

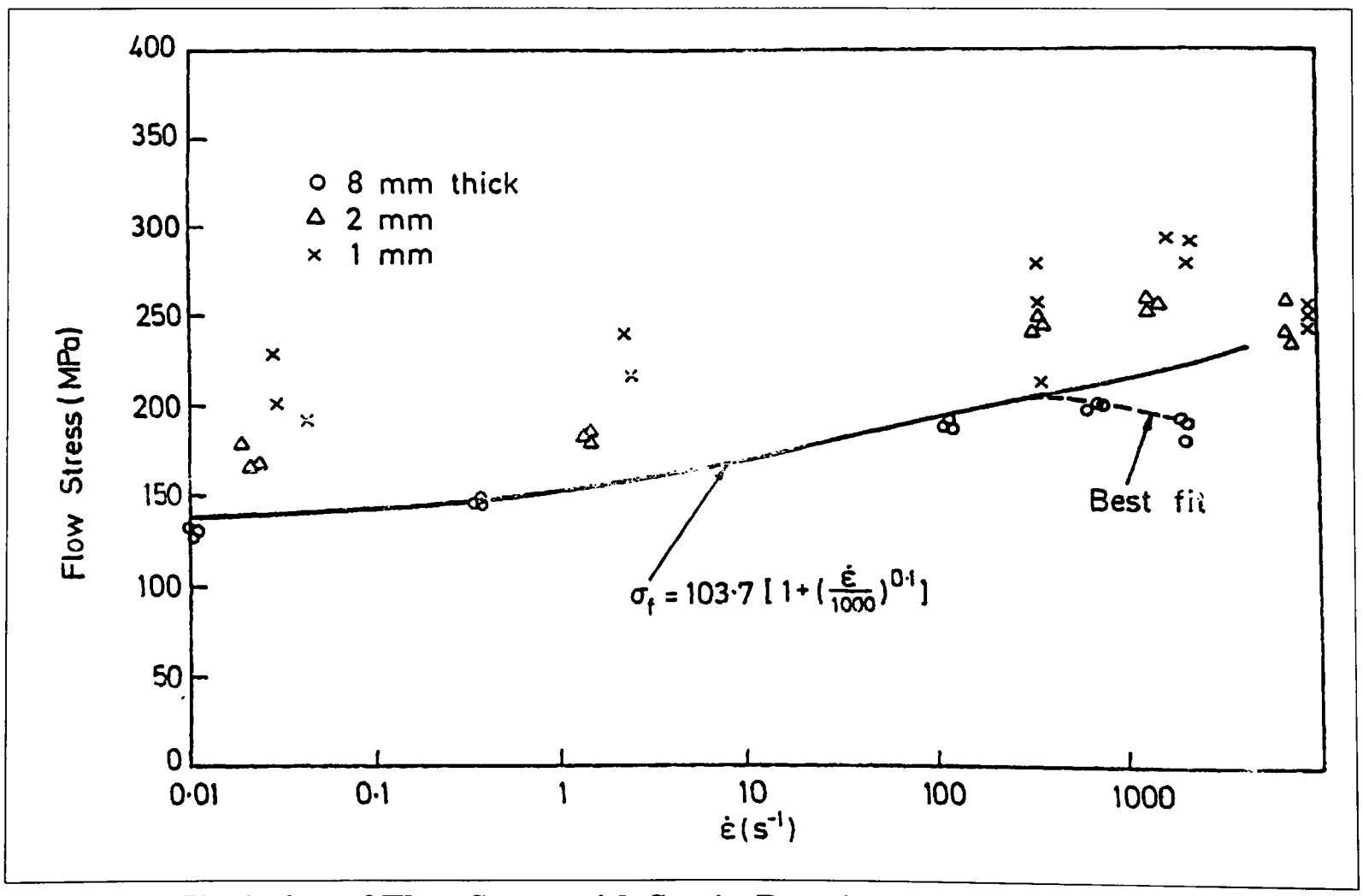

Figure 2.5 Variation of Flow Stress with Strain-Rate for MY-750

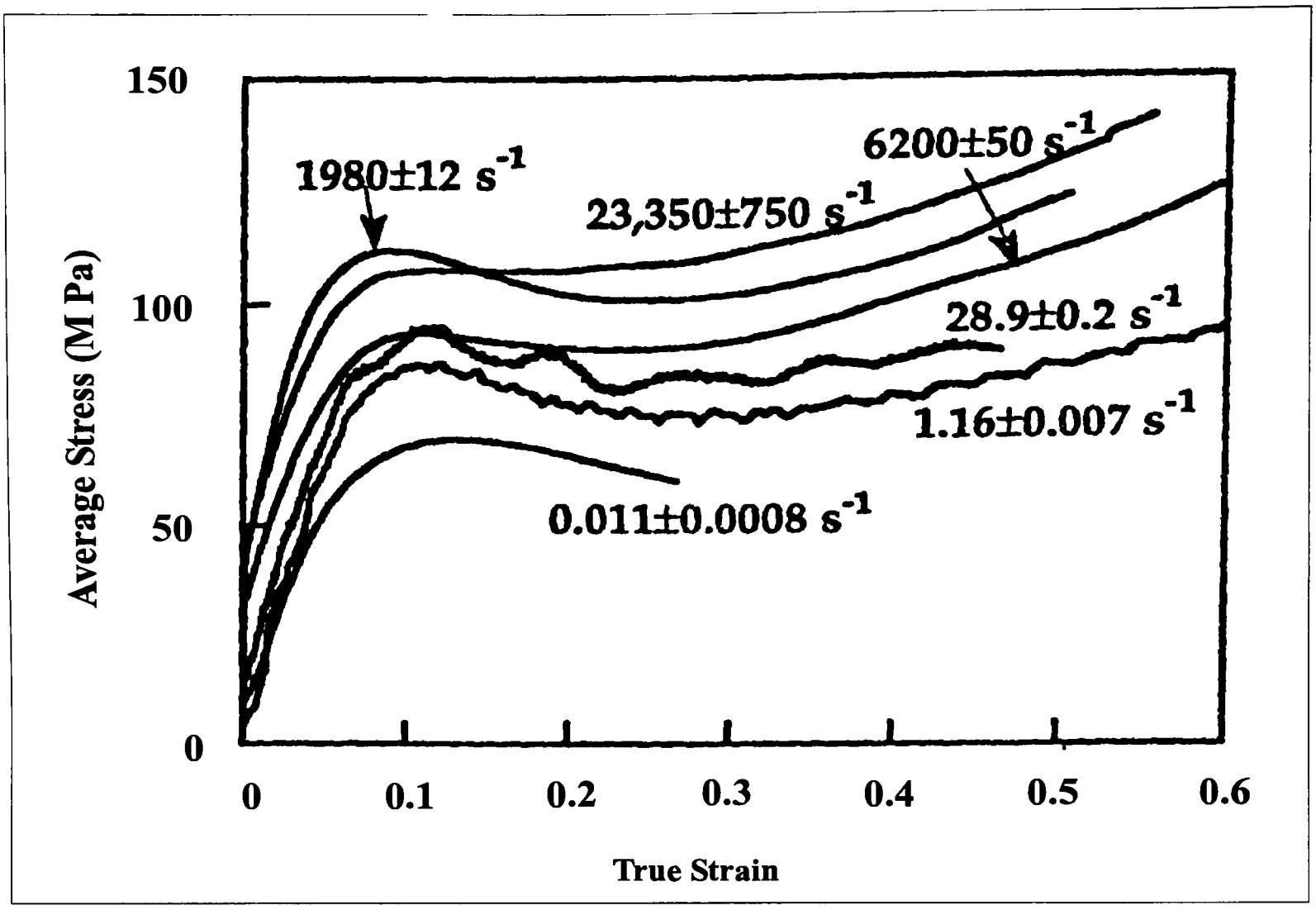

Figure 2.6 Results from Lubricated Tests (Walley *et al*, 1994)

It is interesting to see in Figure 2.6 (Walley *et al*, 1994) that the stress-strain curves do not go through the origin. Several reasons for this behaviour have been suggested . At low to medium rates a 'bedding down' process occurs where the lubricant layer adjusts to the stresses imposed upon it. At higher strain-rates an additional factor comes into play due to the dispersion of the stress pulse propagating down the bars to the gauge positions, although one would normally expect these effects to be small. The result of these experimental errors is that the compressive Young's modulus of the specimens cannot be deduced from the stress-strain curves plotted. Thus in the work of Walley *et al* (1994) they only consider the rate sensitivity of the stress after the initial maximum in the stress-strain curves. Several polymers exhibit pronounced initial maxima followed by load drops, shown schematically in Figure 2.7, at all strain-rates; these included polycarbonate (PC). Strictly speaking, the rate sensitivity should

be obtained by plotting the stress against strain-rate for material in the same microstructural state (Dorn *et al,* 1949, & Mecking *et al,* 1981). It was shown that for most polymers studied, the rate sensitivity depended only weakly on strain. Normally therefore the variation of maximum stress with strain-rate is plotted. The justification for this is that yield does not necessarily take place at the same strain for all strain-rates.

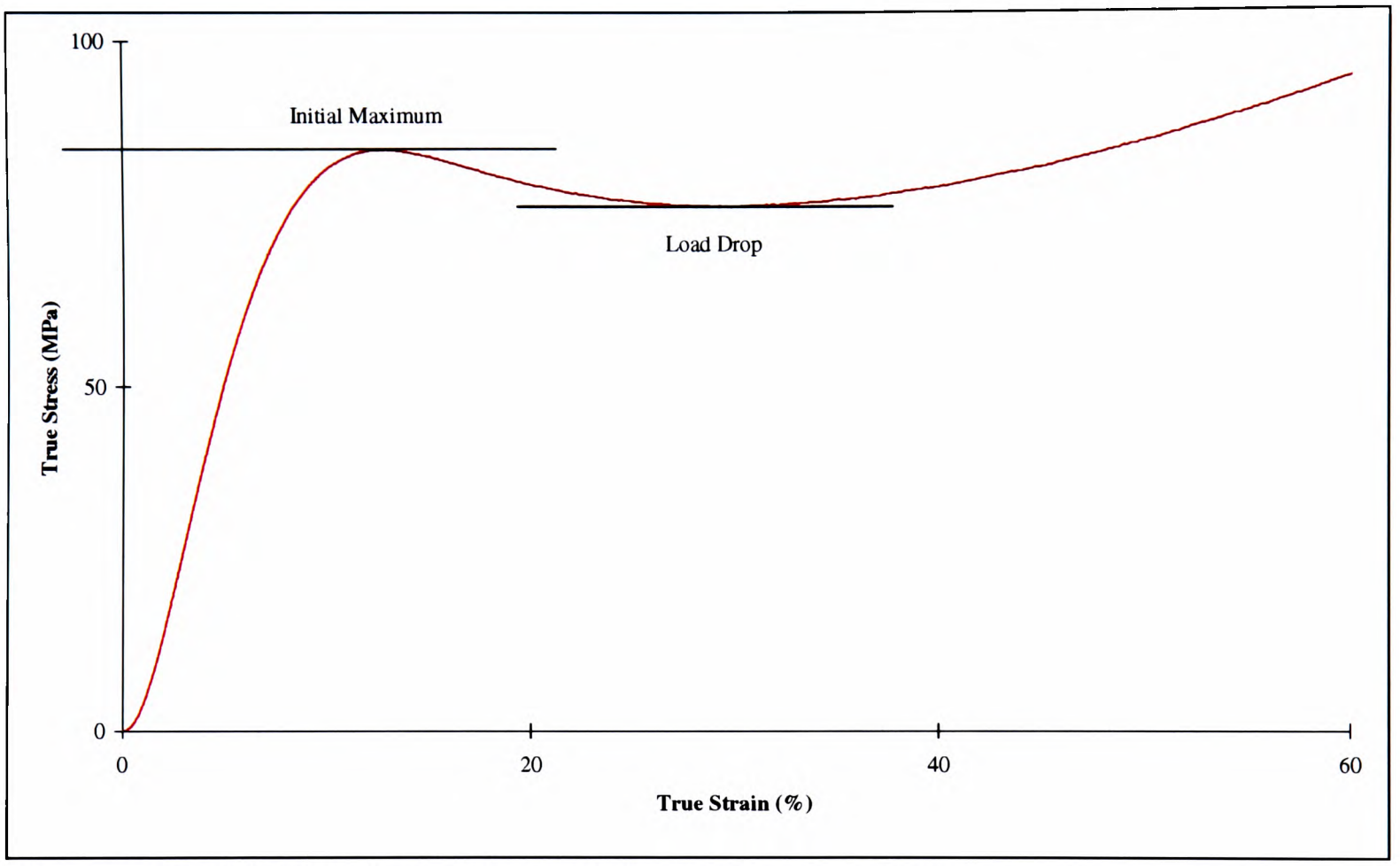

Figure 2.7 Initial Maximum Stress Followed by a Load Drop.

2.5 Effect of Hydrostatic Pressure

Many of the studies of strain-rate sensitivity and impact behaviour are concerned with fracture rather than yielding of polymers. Workers such as Birch & Williams (1969) report strain-rate sensitivity in fracture experiments on PTFE and polyethylene. Reed *et al* (1973) have studied polymers at high strain-rates with a shock tube but the behaviour was elastic deformation or brittle fracture, rather than plastic flow. There have been some studies of shock waves in polymers, for example that of Nunziato & Schuler (1973) who studied PMMA. This

approach is usually aimed at conditions of high pressure where polymers flow under very high hydrostatic pressures (often very much greater than the yield stress) rather than conventional shear yielding.

Yielding in elasto-plastic materials such as metals is taken to depend solely on the deviatoric component of the stress, and not on the hydrostatic component. This can be expressed in the form of Equation 2.11.

$$\tau_c = \frac{1}{2}\sqrt{\frac{3}{2}}\sqrt{\left(\frac{2\sigma_1-\sigma_2-\sigma_3}{3}\right)^2+\left(\frac{2\sigma_2-\sigma_1-\sigma_3}{3}\right)^2+\left(\frac{2\sigma_3-\sigma_1-\sigma_2}{3}\right)^2} \qquad \textbf{(2.11)}$$

However in polymers, hydrostatic pressure effects can be of significance and can not be ignored by using the same yield criterion as that for metals. To accommodate the extra factor of hydrostatic pressure, an extra term is introduced so,

$$\tau = \tau_c + \alpha p$$

where $p = (\sigma_1+\sigma_2+\sigma_3)/3$, τ is the shear yield stress at pressure p, τ_c is the critical shear stress and α the coefficient of increase of yield stress with hydrostatic pressure, a material property. Evidence that mechanical properties can be modified by hydrostatic pressure alone has been found. Rabinowitz *et al* (1970) also found that the pressure dependence of the amorphous polymers was greater than that of the crystalline polymers.

2.6 Effect of Temperature

The effect of increasing temperature on the yield stress is to lower it rapidly until at the glass transition temperature the yield stress tends to zero. The dependence of yield stress on temperature is quite marked. This effect has been demonstrated by numerous workers, where

the ambient temperature of the test is varied. As has been explained previously when T_g is approached the apparent modulus shows a sharp fall and losses due to viscous damping tend to a maximum. However, quantifying the effect of changing temperature within a polymeric specimen during a test at high strain-rate where adiabatic conditions prevail is still a relatively unexplored area.

At higher rates than *ca.* $1s^{-1}$, the timescale for the flow of heat away from the specimen becomes greater than the duration of the experiment, so that significant temperature rises are to be expected. This heating effect is particularly important for polymers since they show a much greater temperature dependance of mechanical properties than metals. This will tend to produce strain softening when the deformation is large, so that the stress-strain curve at a high strain-rate could fall below the curve determined for a lower strain-rate when a certain strain is exceeded, which has been observed for stainless steels (Follansbee, 1986).

As the temperature increases the strength of the secondary links in the polymer decreases. Heat treatment prior to testing, such as annealing, has in general only a small effect on the yield stress (Bowden *et al*, 1970) since the molecular structure remains the same, although this stress relieving operation can also increase the flow stress in cases where an incomplete cure of the material has taken place.

In the case of metals, where large plastic deformation precedes failure, the heat generated can be an important factor. Mason *et al* (1994) were the first to attempt to quantify the functional dependence of the plastic work rate to heat rate conversion fraction, β, on the strain and strain-rate in a range of metals. Their main conclusions were that (i) adiabatic conditions exist in the Kolsky bar for experiments on various steels and aluminiums, when experimental times are shorter than 800μs and (ii) it is possible to measure the dependence of β upon strain and strain-rate using the Kolsky bar and high speed temperature detectors,

provided the specimen deforms uniformly or nearly uniformly.

The temperature rise can be significant, leading to thermal softening and to subsequent shear localisation in many materials. The β value in Ti-6Al-4V deformed at high strain-rates is significantly dependant upon strain, and, for strains higher than 5%, β increases from 0.1 to 0.8. There is also a decrease in the maximum value of β as the strain-rate is increased. The strong variation of β with strain may suggest that it is dependant upon strain-rate as well. Such strain and strain-rate sensitivity in the mechanism of converting plastic work to heat for this material may play an important role in the determination of the width of shear localisation zones and in the determination of the maximum temperature in such zones in metals. It is not clear whether the same will apply to polymers.

The simplest method of measuring the temperature of an object is a contact method. Thermocouples and thermally sensitive films are prime examples and such devices have been used to detect rises in specimen temperature (Dawson *et al*, 1991). Such methods are inadequate for detecting rapidly changing temperature fields. Craig *et al*, 1994, reported that a K-type thermocouple had a response time of approximately 400μs. Calorimetry had also been used, but this only yields one average value after loading is completed.

Thermal imaging cameras are available as well, but the response times associated are of the order of 400μs. These employ rapidly moving optics to scan an area of the specimen with a response of 1μs, but at a frequency of about 2.5kHz, corresponding to 400μs (Noble *et al*, 1994).

Another alternative method of temperature measurement is one which utilises the thermal radiation emitted from objects which are above absolute zero. Such radiometric methods use an optical system to gather radiation and then to focus it onto a semiconductor detector. Semiconductor detectors fall into two types, *intrinsic* and *extrinsic*. Intrinsic

semiconductors are governed by characteristic energy gaps, causing a sudden drop in sensitivity below a certain energy, or at a higher wavelength. Extrinsic detectors require the use of liquid helium (5K) and so are not widely used.

Intrinsic detectors fall into two categories: photoconductive and photovoltaic detectors. Photoconductors require a small bias voltage across each element. Photons incident on the detector produce charge carriers which cause a current. Photovoltaic detectors consist of a p-n junction across which a voltage is created by incident radiation. Intrinsic detectors can operate at much higher temperatures without considerable loss in performance. Most researchers have operated these detectors at 77K using liquid nitrogen. Two variations of a photoconducting detector have been has been used; a single element detector with liquid nitrogen cooling (Trojanowski *et al*, 1998), and also thermo-electrically cooled, to about 200K, (Craig *et al*, 1994).

2.7 Interpretation of Previous Workers' Experimental Data

The interpretation of experimental data follows the thermodynamic approach based on Escaig's model, Equation2.3. A thermodynamic analysis of yield in glassy polymers was carried out (Escaig, 1982). He emphasised that the experiments measure ΔH whereas to interpret the results in terms of microscopic defect dynamics, it is ΔG, the change in Gibbs' free energy that is required. There is a large difference between the value of the activation enthalpy ΔH (which is what is often measured) and the Gibbs' free energy, ΔG (which is the one needed to characterise the deformation on a molecular scale). The difference arises from the large entropy changes associated with the deformation of polymeric materials. Thus Equation 2.3 becomes:

$$\dot{\varepsilon} = \dot{\varepsilon}_0 \exp\left[-\frac{\Delta G}{kT}\right] \tag{2.12}$$

where ΔG is the Gibbs' free energy for the process given by:

$$\Delta G = \Delta H - T\Delta S$$

There is also the problem of the size of the activation volume. The activation volume is obtained experimentally, the term $\dot{\varepsilon}_0$ is assumed to be stress independent and V can be obtained from the variation of stress with the strain-rate using Equation 2.13,

$$\dot{\varepsilon}_y = \dot{\varepsilon}_0 \exp\left[-\left(\frac{\Delta H}{kT}\right)\right] \exp\left(\frac{\sigma_s V}{2kT}\right) \tag{2.13}$$

and rearranging to (McCrum *et al*, 1988):

$$\left(\frac{\sigma_y}{T}\right) = \left(\frac{2}{V}\right)\left[\left(\frac{\Delta H}{T}\right) + 2.303.k.\log\left(\frac{\dot{\varepsilon}_y}{\dot{\varepsilon}_0}\right)\right] \tag{2.14}$$

Various methods for checking the stress dependence of the pre-exponential term ($\dot{\varepsilon}_0$) in creep experiments are given by Escaig, B, 1982, Haussey *et al*, 1980, & Lefebvre *et al*, 1985. These would be difficult to perform in high strain-rate testing. However, since the pre-exponential term does not depend exponentially on the stress, a plot of stress against $\ln\dot{\varepsilon}$ for a given strain would not be linear if the pre-exponential has, say, a strong power-law dependence on stress. Briscoe *et al*, 1985 and Fleck *et al*, 1990, found empirically that the Eyring approach outlined above is adequate to describe the high strain-rate behaviour of many polymeric materials.

Fleck and co-workers have shown that the activation flow model is quite satisfactory for engineering applications over a wide range of temperature and strain-rate up into the high strain-rate regime (*ca.* 10^3 s^{-1}) for PC and PMMA, and hence that temperature and strain-rate are reciprocal variables. They found that PC yields in accordance with the Eyring theory of viscous flow, for temperatures between the beta transition temperature $T_\beta \approx 100°C$ and the glass transition temperature $T_g=147°C$. At lower temperatures, $T<T_\beta$, backbone chain motion becomes frozen and the shear yield stress is greater than the Eyring prediction. Strain softening is an essential feature of yield of PC at all strain-rates employed. PMMA fractures before yield in the high strain-rate tests for $T<80°C$, which is close to the glass transition temperature $T_g=120°C$. It was found that the fracture stress for both materials obeys a thermal activation rate theory of Eyring type.

It was shown that the choice of specimen thickness in these tests significantly affects the measured flow stresses at high strain-rates, with the thicker specimens showing an apparent enhancement of flow stress at high rates. Comparison of the present results with published work suggests that some high strain-rate data in the literature could be erroneous due to inappropriate choice of specimen dimensions. Dioh *et al*, 1994, presented results in the form of yield stress against the logarithmic strain-rate in order to assess the strain-rate sensitivity of the material under investigation. It was only possible with PC since it was the only material tested that exhibits a yield point in compression. For the other materials, plots of flow stress at specific values of strain were produced instead.

Whereas at intermediate strain-rates there is a good agreement between the measured flow stresses for both specimen thicknesses, at high strain-rates the measured flow stresses for the thicker specimens are significantly lower for all the materials tested, possibly a feature of the material tested. Using the data for the thicker specimens at high strain-rates would lead to

the conclusion that the strain-rate sensitivity of each material increases suddenly at high strain-rates. However, even results for the thinner specimens suggest that the simple Eyring model cannot adequately describe the behaviour of PC and polyetheretherketone (PEEK) at room temperature between the strain-rates of 10^{-4} and $10^{4}s^{-1}$. The present work suggests that the simple Eyring model which has been shown to describe closely the behaviour of PC at low strain-rates, is inadequate at high strain-rates, towards which a gentle increase in strain-rate sensitivity emerges. The results presented by Dioh *et al*, 1994, show that if the specimen thickness is chosen carefully, the increase in strain-rate sensitivity of PC at high strain-rates, reported by Rietsch *et al*, 1990, does not appear. From the evidence presented, it is apparent that if results are obtained at high strain-rates are to be relied upon, then they must be shown to be independent of geometry, in particular specimen thickness.

Some results obtained by Duckett *et al*, 1970, from compression tests confirmed that the yield stress of an isotropic material depends on (i) temperature, (ii) strain-rate and (iii) hydrostatic pressure. Their experiments were carried out on specimens of fixed dimensions and all the polymers investigated showed a monotonic increase in yield stress with increasing strain-rate. The compressive yield stresses of PMMA and polyethylene teraphthalate (PET) were observed to increase with increasing strain-rate and with decreasing temperature. It was noted that in general the plots of yield stress vs $\ln\dot{\varepsilon}$ have a small but definite curvature, indicating that the theory of Eyring, in terms of a single simply activated flow process is not applicable to the data of Duckett *et al*, 1970. They also found that compressive yield stresses would be higher than tensile yield stresses. Data from their paper shows the greater sensitivity of the compressive yield stress to strain-rate than the tensile yield, i.e. compressive stresses were in general found to be more dependant on strain-rate.

They developed a phenomenological theory based on the Robertson, 1966, approach but allowing for the effects of hydrostatic pressure. As in Robertson's theory they postulated that the polymer can exist in either of two states with an energy difference ΔE between them, and that at equilibrium the fraction in each state is given by the Boltzmann distributions. Robertson suggested that the energy difference between the two states was $\Delta E - \tau V\cos(\theta)$ where $\tau V\cos\theta$ represents the work done by the shear stress τ, V is a shear volume and θ the angle between the orientation of the shear stress and the element it acts on.

Duckett *et al* suggested that a conformation change to a higher energy state implies a reduction in density due to less efficient packing. This will lead to an interaction with the hydrostatic component of stress p, so that the energy difference between the two states becomes $\Delta E - \tau V\cos\theta + p\Omega$, where $p\Omega$ represents the work done by p, the hydrostatic component of stress and Ω is a volume term. Other than this modification the theory of Robertson is followed exactly. They developed a phenomenological theory based on the Robertson approach but allowing for the effects of hydrostatic pressure.

For tensile and compression tests τ and p were assumed to be $\sigma/2$ and $\pm\sigma/3$ respectively where σ was the axial yield stress. The shear strain-rate $\dot{\gamma}$ was assumed to be half the applied axial strain-rate. Duckett *et al* could not obtain a good fit to their data using the values of the coefficients given by Robertson, so, somewhat dubiously, values were optimised to give a least squares fit keeping the shear and hydrostatic components of stress and temperature as independent variables. They claimed that yield is not a unique point on the stress-strain curve, but merely the point at which the plastic strain-rate produced by the stress just matches the machine displacement rate.

2.8 References

Argon, A.S., Phil.Mag., 28, p.839, 1973.

Bauwens-Crowet, C. & Ots J.M.,The Strain-Rate and Temperature Dependance of PC in Tension, Tensile Creep and Impact Tests, J.Mater.Sci., 9, pp.1197-1201, 1974.

Birch, M.W. & Williams J.G., Int.J.Fracture, 14, p.69, 1969.

Bowden, P.B. & Raha, S.,Phil.Mag., 22, p.463, 1970.

Briscoe, B.J. & Nosker, R.W., The Influence of Interfacial Friction on the Deformation of HDPE in a SHPB, Wear, 95, pp.241-262, 1984.

Briscoe, B.J. & Nosker, R.W., The Flow Stress of High Density Polyethylene at High Rates of Strain, Polym.Commun., 26, pp.307-308, 1985.

Chou, S.C., Robertson, K.D. & Rainey, J.H., The Effect of Strain-Rate and Heat Developed During Deformation on the Stress-Strain Curve of Plastics, Exp.Mech., 13, pp.422-432, 1973.

Craig, S.J., Gaskell, D.R., Rockett, P. & Ruiz, C., An Experimental Technique for Measuring the Temperature Rise During Impact Testing, Journal de Physique III, 4, C8 pp.41-46, 1994.

Dawson, P.C., Swallowe, G.M. & Xinwu, Z., J.Phys. III, 1, 701, 1991.

Derby, B., Hills, D. & Ruiz, C., Materials for Engineering, Longman, 1992.

Dioh, N.N., Leevers, P.S. & Williams, J.G., Thickness Effects in Split Hopkinson Bar Tests, Polymer, 34, pp.4230-4234, 1993.

Dioh, N.N., Ivankovic, A., Leevers, P.S. & Williams, J.G., The High Strain-rate Behaviour of Polymers, J.Phys IV Colloque C8, 4, 1994.

Dorn, J.E., Goldberg, A. & Tietz, T.E., The Effect of Thermal-Mechanical History on the Strain Hardening of Metals, Trans. AIME, 180, pp.205-224, 1949.

Duckett, R.A., Rabinowitz, S. & Ward, I.M., J. Mat. Sci., 5, 909, 1970.

Escaig, B. & Lefebvre, J.M., Rev. Phys. Appliquee, 13, p.285, 1978.

Escaig, B., Kinetics and Thermodynamics of Plastic Flow in Polymeric Glasses, In Plastic Deformation of Amorphous and Semi-Crystalline Materials (les editions de Physique, les Ulis, France), pp.187-225, 1982.

Fleck, N.A., Stronge, W.J. & Liu, J.H., High Strain-Rate Shear Response of PC and PMMA, Proc.R.Soc.Lond, A429, pp.459-479, 1990.

Follansbee, P.S., High Strain-Rate Deformation of FCC Metals and Alloys, In Metallurgical Applications of Shock-Wave and High Strain-Rate Phenomena, L.E.Murr, K.P.Sttaudhammer, M.A.Meyers Eds., pp.451-479, New York: Marcel Dekker, 1986.

Gorham, D.A., Pope, P.H. & Cox, O., Sources of Error in Very High Strain-Rate Compressions Tests, Inst.Phys.Conf.Ser., 70, pp.1510158, 1984.

Haussey, J., Cavrot, J.P., Escaig, D. & Lefebvre, J.M.,Thermodynamic Analysis of the Plastic Deformation of Glassy PMMA, J.Polym.Sci.: Polym.Phys.Edn., 18, pp.311-325, 1980.

Lataillade, J.L., High Rates of Strain and Mechanical Properties of Polymeric Materials.

Lefebvre, J.M. & Escaig, B., Plastic Deformation of Glassy Amorphous Polymers: Influence of Strain-Rate, J.Mater.Sci., 20, pp.438-448, 1985.

Mason, J.J., Rosakis, A.J. & Ravichandran, G., On the Strain and Strain-Rate Dependance of the Fraction of Plastic Work Converted to Heat: An Experimental Study Using High Speed Infra-red Detectors and the Kolsky Bar, Mech. Of Matls., 16, pp.135-145, 1994.

McCrum, N.G., Buckley, C.P. & Bucknall, C.B., Principles of Polymer Engineering, Oxford University Press, 1988.

Mecking, H. & Kocks, U.F., Kinetics of Flow and Strain Hardening, Acta Metall., 29, pp.1865-1875, 1981.

Noble, J.P. & Harding, J., Temperature Measurement in the Tensile Hopkinson Bar Test, Meas.Sci,Tech 5, pp.1163-1167, 1994.

Nunziato, J.W. & Schuler, K.W., J.Appl.Phys., p.4774, 1973.

Rabinowitz, S., Ward, I.M. & Parry, J.C.S., J.Mat.Sci.,5, p.29, 1970.

Reed, P.E., Nurse, P.J. & Andrews, E.H., J.Mat.Sci., 9, p.1977, 1973.

Rietsch, F. & Bouette, B., Eur.Polym.J., 26, 10, p.1071-1075, 1990.

Robertson, R.E., J.Chem.Phys., 44, p.3950, 1966.

Ruiz, C., Xia, Y.R. & Webb, P.A., Dynamic Properties of Adhesive Layers, Final Report, Oxford University Engineering Laboratory.

Steer, P., Rietsch F., Lataillade, J.L. & Marchand, A., J. Physique, Colloque C5, 46, p.415, 1985.

Trojanowski, A.S., Macdougall, D.A.S., & Harding, J., An Improved Technique for the Experimental Measurement of Surface Temperature During Hopkinson-bar Tests, Meas.Sci.Tech., 9, 1, pp.12-19, 1998.

Walley, S.M., Field, J.E., Pope, P.H. & Safford, N.A., A Study of the Rapid Deformation Behaviour of a Range of Polymers, Phil. Trans. R. Soc. Lond A, 328, 1-33, 1989.

Walley, S.M. & Field, J.E., Strain-rate Sensitivity of Polymers in Compression from Low to High Rates, DYMAT, 1, No.3, pp.211-227, 1994.

Chapter 3

Mechanical Testing Technique

3.1 Quasistatic Compression Testing

Quasistatic testing was carried out using a standard screw-driven Instron testing machine shown schematically in Figure 3.1. Tests were carried out on a specimen (diameter 9.0mm, length 5.5mm) at a loading rate of approximately $2mm.min^{-1}$, which corresponds to a strain-rate of approximately $0.006s^{-1}$. The Instron testing machine was connected to a computer which logged values of cross-head load and displacement. The stress was calculated from the recorded load using Equation 3.1.

$$\sigma = \frac{F}{A_0} \tag{3.1}$$

where F is the applied load and A_0 is the initial cross-sectional area.

The strain could not be calculated directly from the cross-head displacement, since this represented relative displacement between the fixing plate and the cross-head, not between the two ends of the specimen. Depending on the modulus of the specimen, potentially significant

elastic strains and non-linear frictional effects occur in the testing machine during the test, invalidating the cross-head measurements of displacement. A Displacement Transducer (D.T.) was attached to the Instron machine which measured the relative displacements of the platens. By using this D.T. measurement, the strain was calculated using Equation 3.2.

$$\varepsilon = \frac{x_{dt}}{l_g} \tag{3.2}$$

where x_{dt} is the displacement recorded using the D.T. and l_g is the original gauge length.

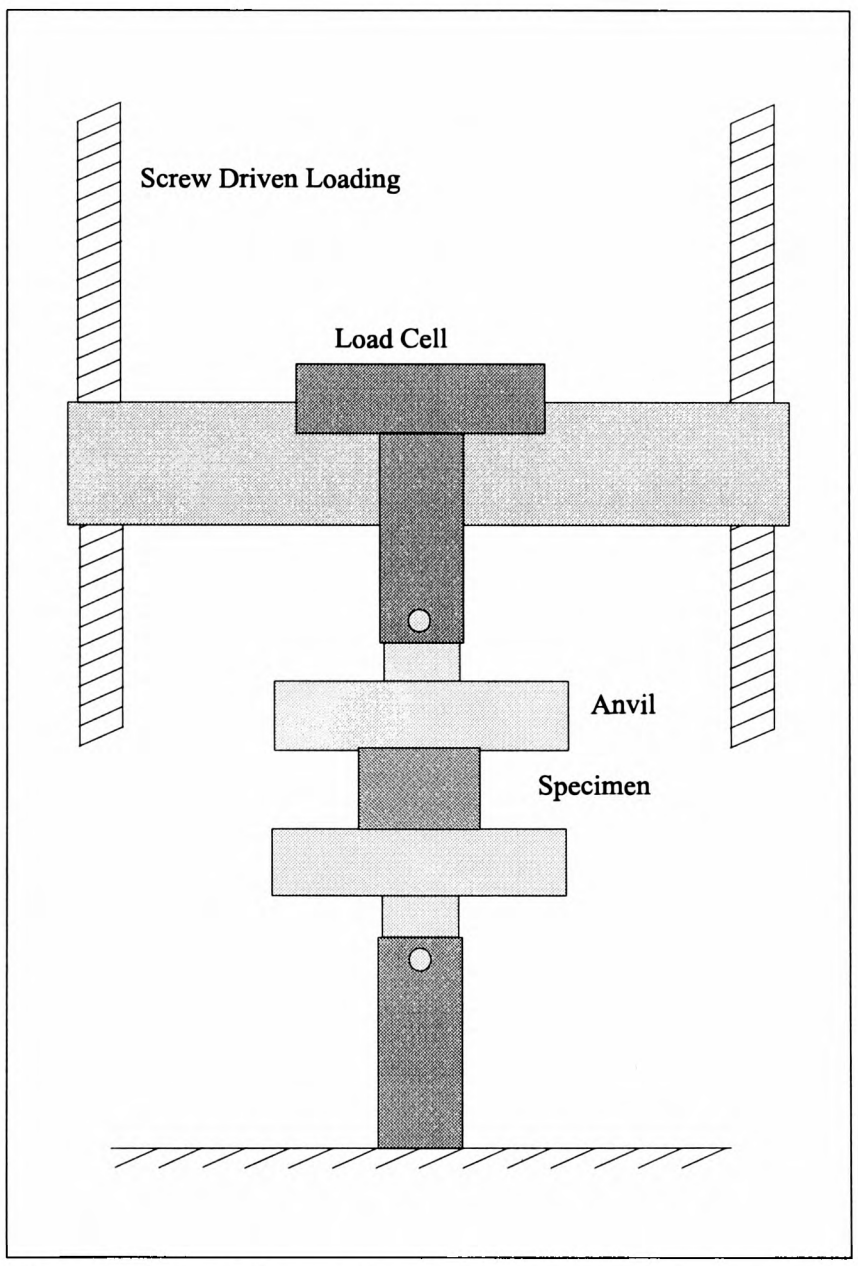

Figure 3.1 Schematic of Instron Testing Apparatus

3.2 Intermediate Rate Testing

Intermediate rates of strain in compression were achieved by employing a hydraulic machine. This machine uses a double sided hydraulic actuator filled with oil to compress a test specimen. The actuator is pressurised to approximately 200 p.s.i. on both sides. A solenoid is then used to open a valve which releases pressure on one side of the cylinder. The resulting pressure difference moves the cylinder in the desired direction - upwards in the case of compression. Upon suitable modification, tension as well as compression tests can be performed. A pair of L.V.D.T.'s monitor the displacement between the loading surfaces and a calibrated load cell measures the force exerted on the specimen. A typical loading time for such a test was approximately 4.5ms, producing a strain-rate in the region of $10^2 s^{-1}$.

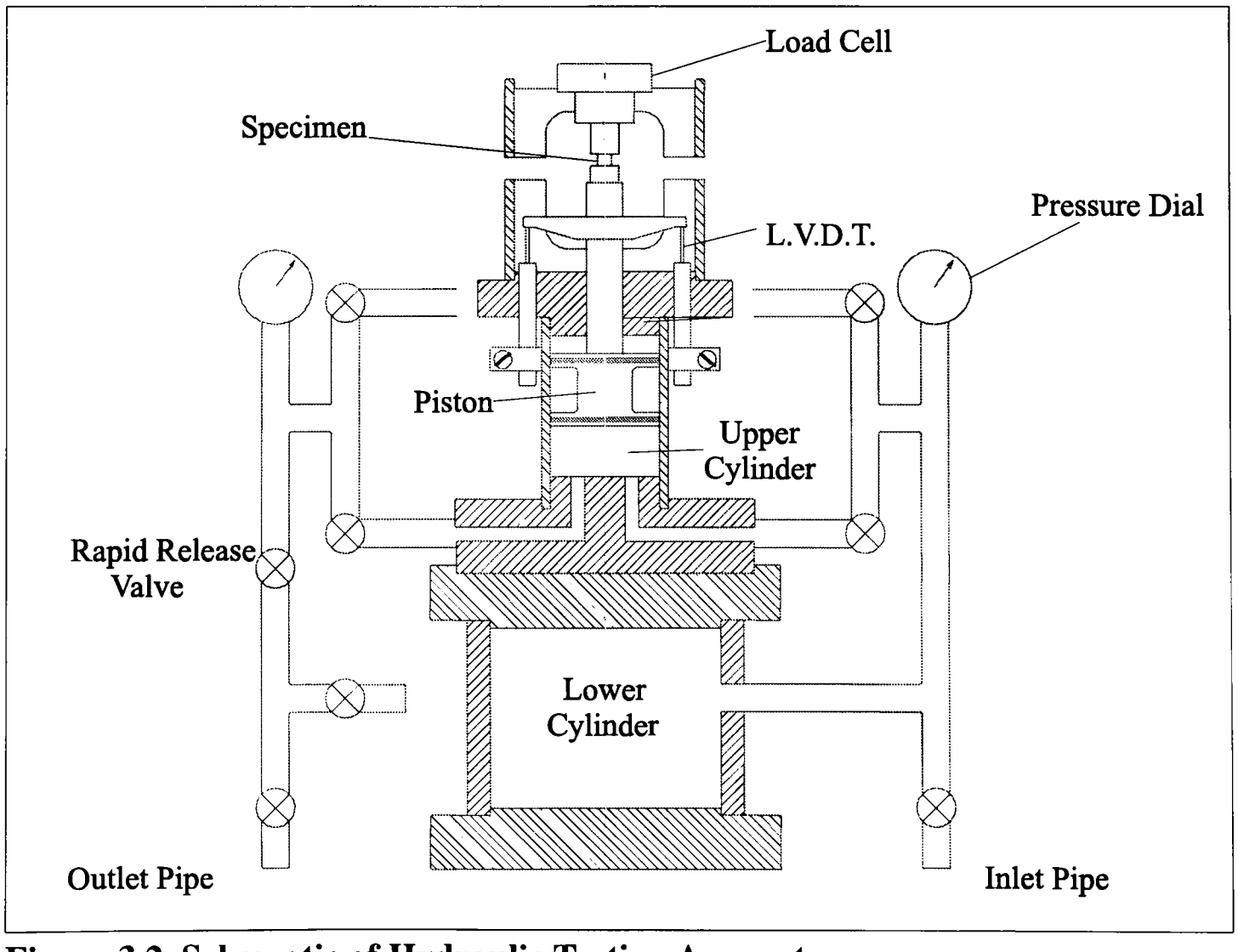

Figure 3.2 Schematic of Hydraulic Testing Apparatus

3.3 High Rate Testing Using the Split-Hopkinson Pressure Bar (SHPB)

3.3.1 Description of Apparatus and SHPB Theory

One of the simplest and most widely used testing techniques for high strain-rate testing is that developed by Kolsky (1949) and commonly called the split Hopkinson pressure bar (after pioneering work by Bertram Hopkinson (1914)), or Kolsky apparatus, which was originally used for loading a cylindrical specimen in uniaxial compression. Tensile and torsional derivatives have subsequently been produced. In each case, a specimen is sandwiched between two bars, an input and an output bar. A stress pulse is initiated at the upstream end of the input bar and travels towards the specimen at the elastic wave velocity $c=(E/\rho)^{1/2}$.

Initiation of the stress pulse is through a steel projectile, accelerated to velocities of between $10m.s^{-1}$ and $18m.s^{-1}$ with the aid of a reservoir of compressed air. Just prior to impact, the projectile passes two diodes, triggering an electronic counter-timer for impact velocity measurement. When the compressive pulse in the incident bar reaches the specimen, part of it is transmitted through the specimen and part is reflected because of mismatch in the cross-sectional area and acoustic impedance of the bar and the specimen. The basic principle of the Hopkinson bar depends only on the knowledge of the longitudinal wave speed to shift the pulse in time and the assumption of non-dispersive elastic waves in the pressure bars. A schematic diagram of the apparatus is shown in Figure 3.3.

The equations for the analysis of the split Hopkinson pressure bar in compression assume that stresses and velocities at the end of the specimen are propagated down the bars in an undispersed manner. By assuming that the wave-transit time in the short specimen is small compared to the total time of the test, many wave reflections can take place back and forth in the specimen. Analysis of a SHPB test is based on the premises that the loading bars themselves remain linear elastic, isotropic and homogeneous, that plane sections remain plane

and that the stress is uniformly distributed over the bar cross-section. The stress and strain are then assumed to be uniform along the specimen. A set of relatively simple relations can be derived for the stress, strain, and strain-rate in the specimen.

The two bars are assumed to be linear elastic. Hence, by monitoring strains in the bars with strain gauges, it is possible to ascertain the stress-time and displacement-time history at the bar/specimen interfaces. The gauge stations (two on the input bar and one on the output bar) form the arms of Wheatstone bridge circuits. The out-of-balance voltages of the bridge circuits are amplified and stored on digital transient recorders (DataLab DL912's) for later analysis.

The bar stresses at the strain gauge positions can be used to derive force and velocity histories at the specimen interfaces. Integration of the relative velocity between the specimen input and output faces gives their relative displacement. A measure of the strain and strain-rate can be derived by dividing the displacement and velocity by the specimen gauge length.

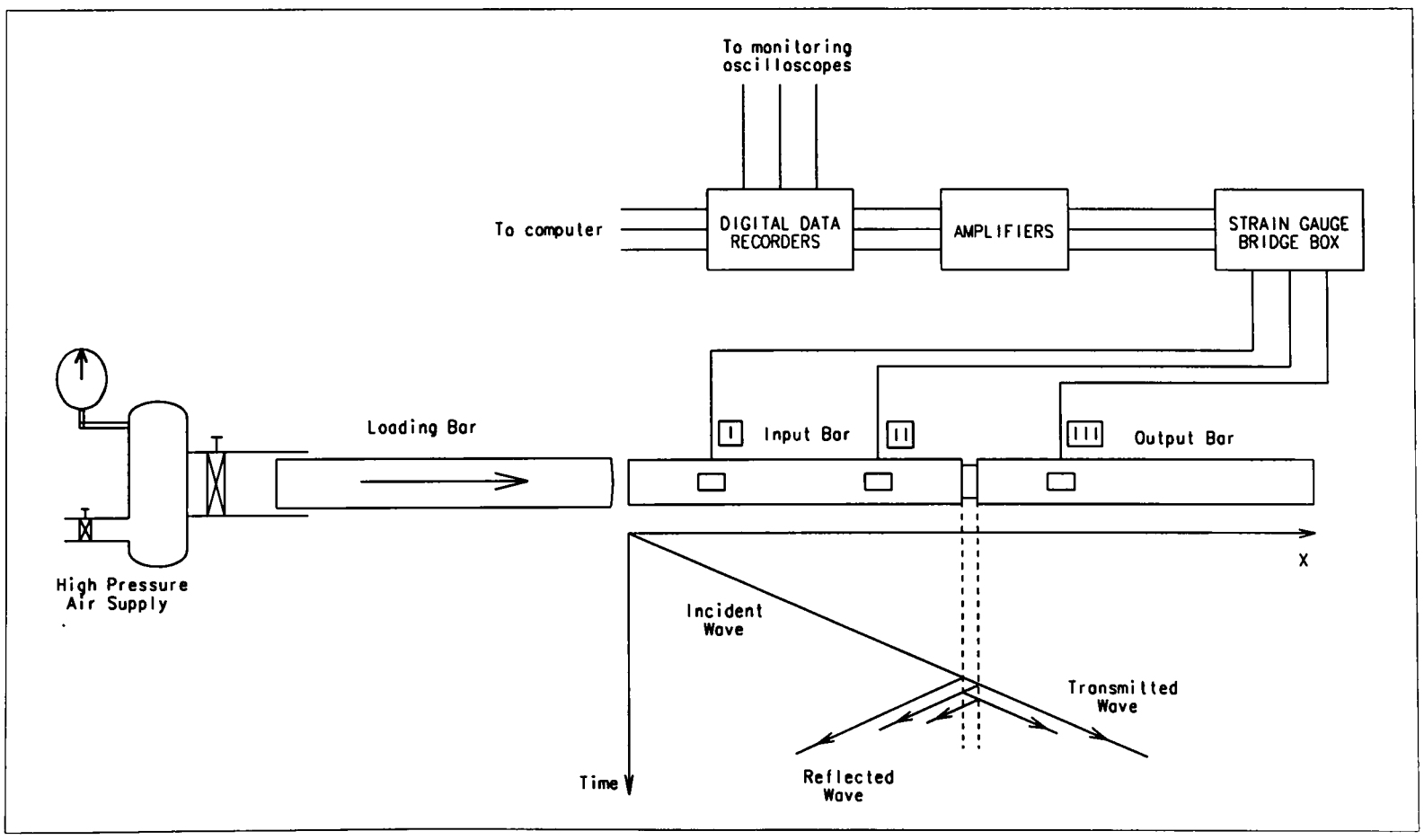

Figure 3.3 Split Hopkinson Bar Apparatus in Compression

Figure 3.4 is a schematic of the specimen and Hopkinson bars and shows the incident, reflected, and transmitted pulses, ε_i, ε_r, and ε_t. Using subscripts 1 and 2 to represent the two ends of the specimen as shown, the displacements, u, at the ends of the specimen are given by:

$$u_1 = \int_0^t c.\varepsilon_1 dt \tag{3.3}$$

$$u_2 = \int_0^t c.\varepsilon_2 dt \tag{3.4}$$

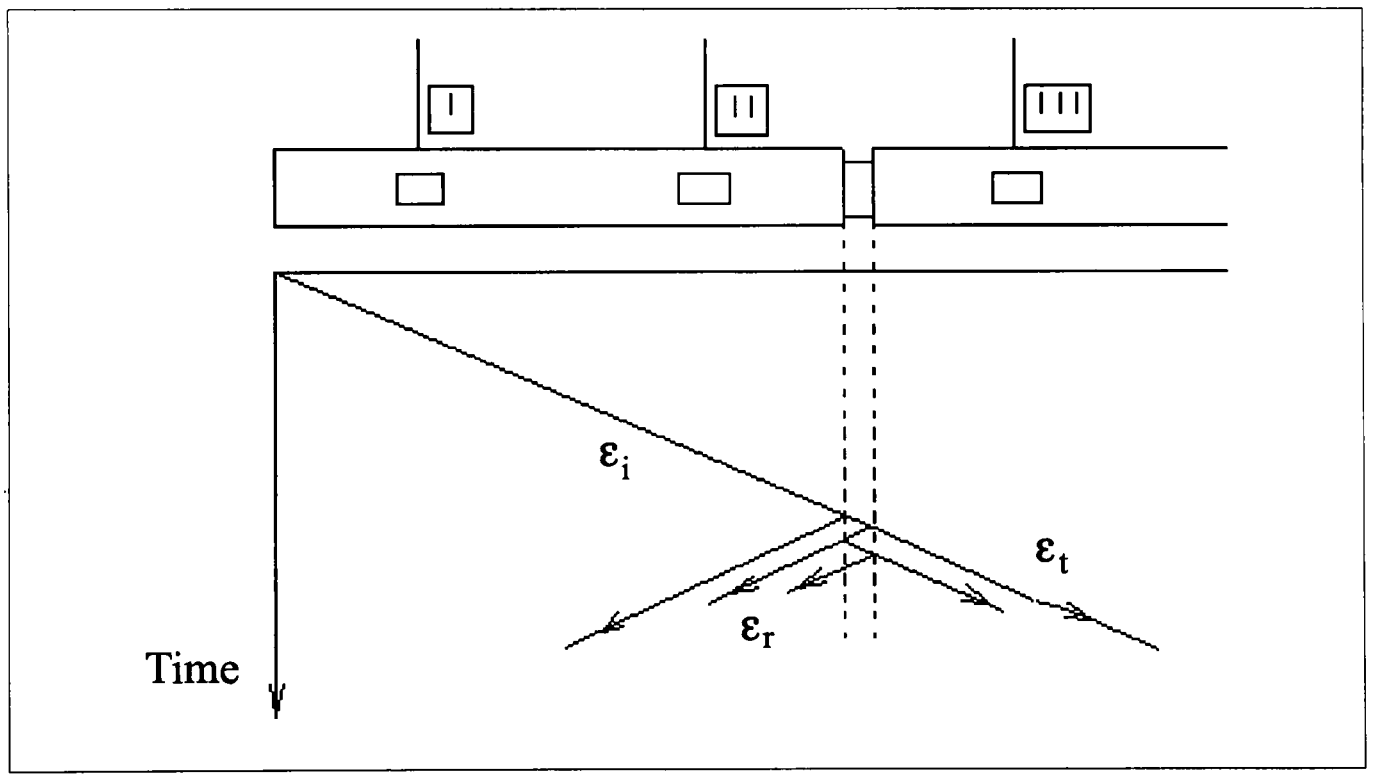

Figure 3.4 Incident, Reflected and Transmitted Pulses at Specimen/Bar Interface

where c is the elastic-wave velocity in the Hopkinson bars. The displacement of the input bar face, u_1, is due to both the incident and the reflected pulse, ε_i and ε_r, so:

$$u_1 = c\int_0^t \varepsilon_i dt + (-c)\int_0^t \varepsilon_r dt = c\int_0^t (\varepsilon_i - \varepsilon_r) dt \tag{3.5}$$

Similarly, the output bar displacement is:

$$u_2 = c\int_0^t \varepsilon_t dt \tag{3.6}$$

The average strain in the specimen, is given by:

$$\varepsilon_{av} = \frac{u_1 - u_2}{l_g} = \frac{c}{l_g}\int_0^t (\varepsilon_i - \varepsilon_r - \varepsilon_t) dt \tag{3.7}$$

where l_g is the length of the specimen. The forces at the ends of the specimen are obtained from:

$$P_1 = EA(\varepsilon_i + \varepsilon_r)$$
$$P_2 = EA\varepsilon_t \tag{3.8}$$

where E and A are the Young's modulus and the cross-sectional area of the Hopkinson bars. The average force is calculated from:

$$P_{av} = \frac{EA}{2}(\varepsilon_i + \varepsilon_r + \varepsilon_t) \tag{3.9}$$

If it is assumed that P_1=P_2, that is, that the forces are equal at both ends of the specimen, then from Equation 3.8, we obtain:

$$\varepsilon_i + \varepsilon_r = \varepsilon_t \tag{3.10}$$

For the specimen of cross-sectional area A_s, the strain, stress, and strain-rate in the

specimen become:

$$\varepsilon_{av} = -2\frac{c}{l_g}\int_0^t \varepsilon_r \, dt \tag{3.11}$$

$$\sigma_{av} = E\frac{A_b}{A_s}\varepsilon_t \tag{3.12}$$

$$\dot{\varepsilon}_{av} = -2\frac{c}{L}\varepsilon_r \tag{3.13}$$

It is important to note that the stress, strain, and strain-rate are average values, and that they are calculated from a uniaxial stress-state assumption. Also important to note that Equations 3.11 & 3.12 require accurate determination of ε_r and all the above theory assumes that ε_i and ε_r are measured independently. In the present tests, as will be described later, this was not the case and a modified approach was required.

3.3.2 Interpretation of Strain Gauge Signals

In the standard Hopkinson-bar analysis it is required to determine separately the incident and reflected waves in the input bar and the transmitted wave in the output bar. Although it is possible, if the incident loading wave is of limited duration, to separate the incident and reflected waves by siting the input bar strain gauges a sufficient distance from the specimen, this may limit the maximum strain which may be applied to the specimen. To avoid this limitation strain gauges may be sited at two different positions along the input bar. Both sets of strain gauges will record the incident wave and its subsequent modification by the reflected wave. Since, however, the reflected wave reaches the two sets of strain gauges at

different times it is possible, using simple one-dimensional longitudinal elastic wave theory, to distinguish between the incident and reflected waves. While this allows the velocity at the input end of the specimen to be determined with reasonable accuracy, if the force transmitted through the specimen is much less than that sustained by the input bar, either because the strength of the material is low or because its cross-sectional area is much less than that of the input bar, then the accuracy with which the stress on the input end of the specimen can be calculated is generally low. So, if the reflected wave is large, the input stress is difficult to measure accurately. Also, if the reflected wave is small, the specimen strain is difficult to measure accurately. Figure 3.5 shows a typical set of strain gauge signals. In the input bar, G_I precedes G_{II} by a calculated 56μs, approximately corresponding to the diagram of Figure 3.5. G_{III}, in the output bar, gives the transmitted stress wave.

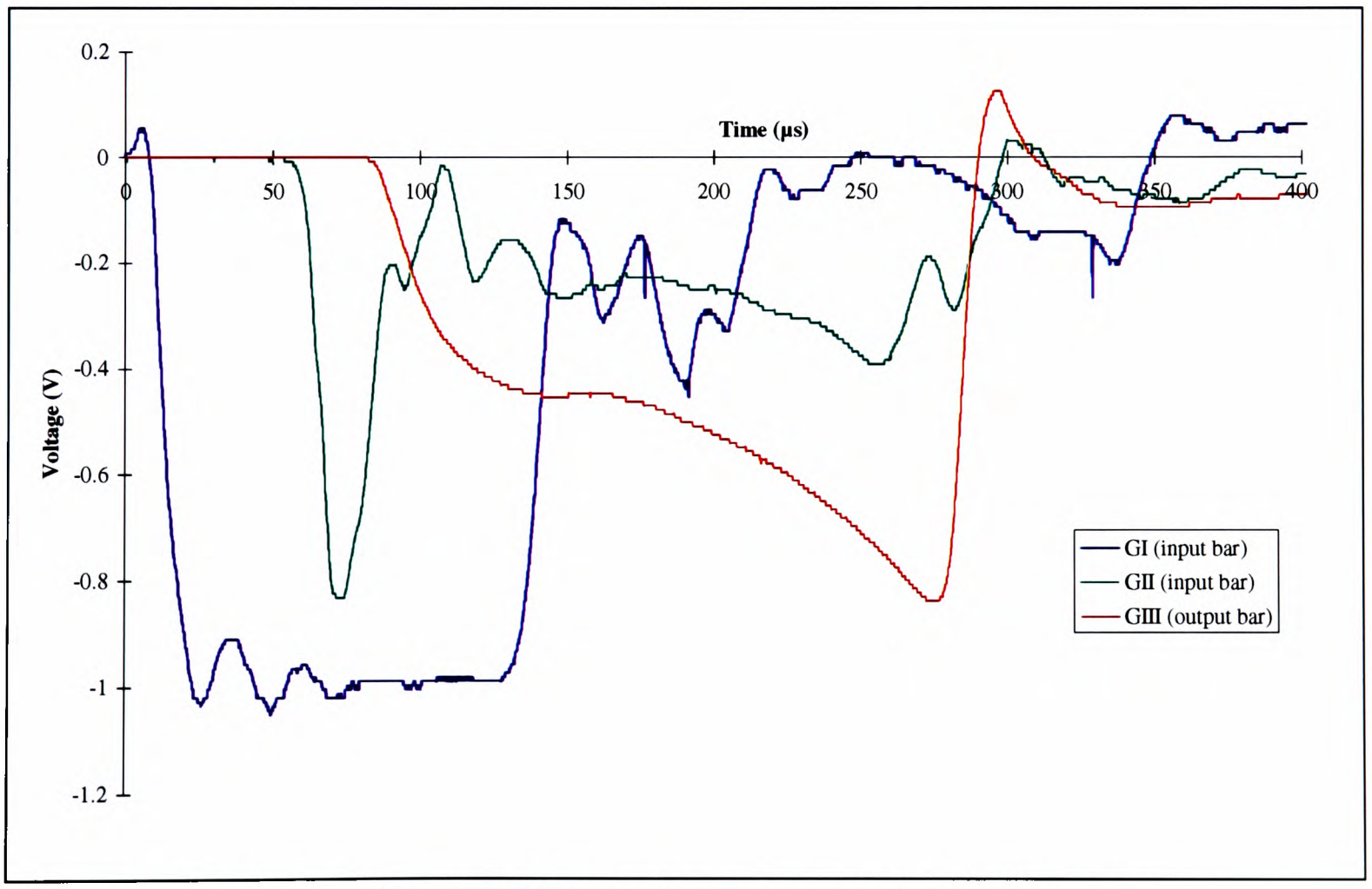

Figure 3.5 Typical Strain Gauge Signals for an Impact Compression Test

Thus the specimen stress is normally determined from the transmitted wave recorded from the output bar strain gauges. Provided the specimen is short enough for equilibrium to be attained at an early stage in the test and provided it fails before the first reflected wave from the free end of the output bar arrives back at the strain gauges, the transmitted stress wave gives a good measure of the average stress in the specimen. For materials where strains to failure are high, the effect of reflected waves on the output bar strain gauge signal may also have to be taken into account. The calculated stresses at the specimen input and output interface are shown in Figure 3.6. Analysis of a SHPB test in compression is based on the premises that the loading bars themselves remain linear elastic, isotropic and homogeneous, the plane sections remain plane and that the stress is uniformly distributed over the bar cross-section. One-dimensional theory of wave propagation in rods is covered at length by Kolsky (1949). It is on this theory that the 'methods of characteristics' for the analysis of stress waves in bars is based. The derivation is included below.

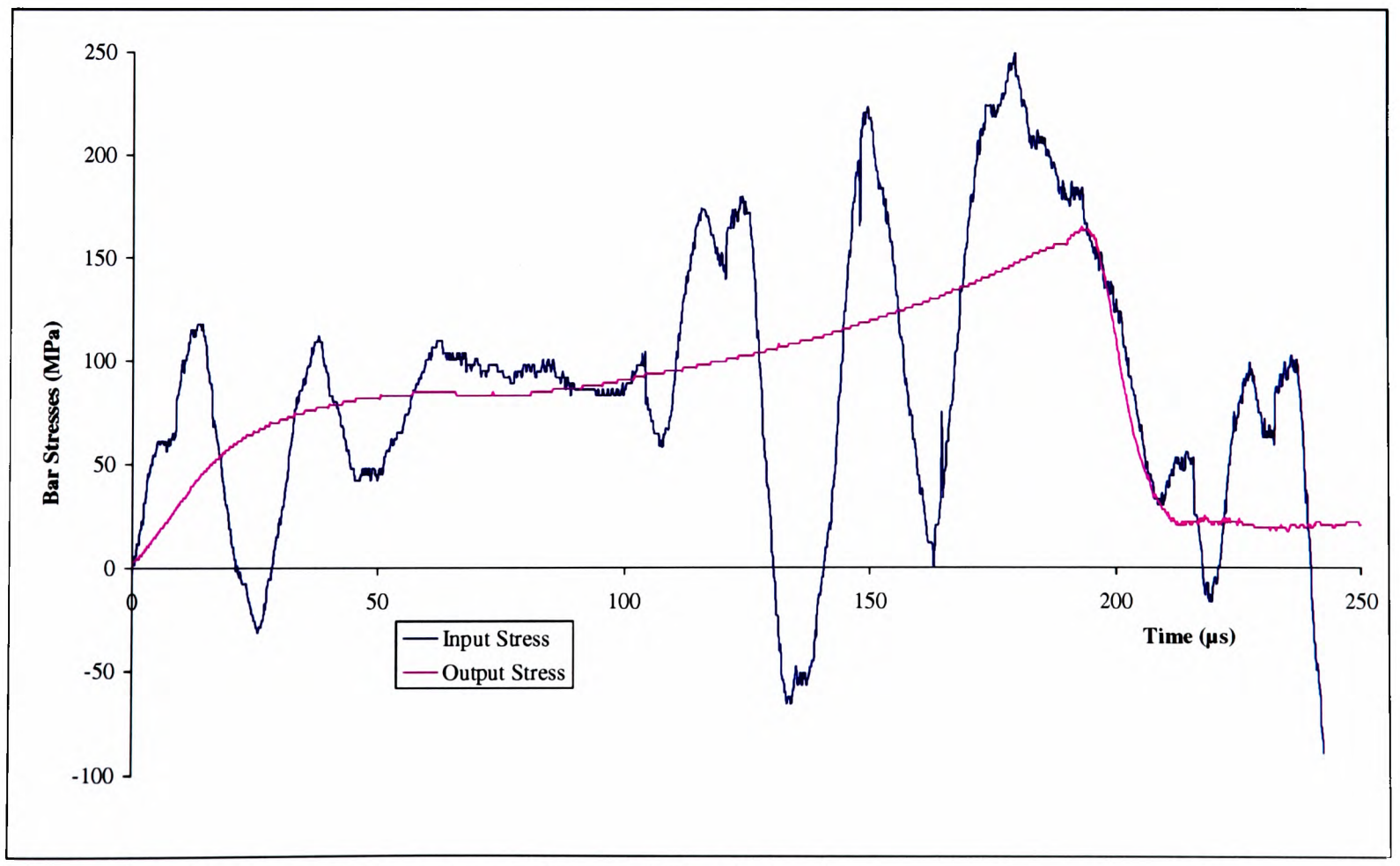

Figure 3.6 Stresses at Input and Output Bar Interfaces

3.4 Verification of Test Data

3.4.1 Manual Analysis

One method of calculating and obtaining strain data is by applying the method of characteristics and perform a 'manual analysis' of the strain gauge signals. This process involves using a spreadsheet program, such as Microsoft Excel, and applying the equations shown in Appendix A. These equations define the durations of the elastic wave in the bar and subsequent plastic wave in the specimen.

The Lagrange (x,t) diagram for wave propagation in the input bar of a standard SHPB assembly is shown in Figure 3.7. Forward travelling waves, ie. propagating in the positive x direction, are represented by characteristic lines of slope (dx/dt) = +c, where c is the velocity of longitudinal elastic waves , given by $c=(E/\rho)^{1/2}$. Backward travelling waves, propagating in the negative x direction, are represented by characteristic lines of slope (dx/dt) = -c. Since c is a constant, along forward travelling wavefronts, dx/dt=c integrates to give:

$$(x - ct) = \text{constant}, K_1$$

while along backward travelling wavefronts, dx/dt = -c integrates to give:

$$(x + ct) = \text{constant}, K_2$$

The governing equation for the propagation of elastic stress waves is:

$$\frac{\partial^2 u}{\partial x^2} = c^2 \frac{\partial^2 u}{\partial t^2} \qquad \text{where} \qquad c^2 = \frac{E}{\rho} \tag{3.14}$$

where the particle displacement u, is a continuous function of position x, and time t. This has d'Alembert's solution:

$$u = f(x - ct) + g(x + ct) \tag{3.15}$$

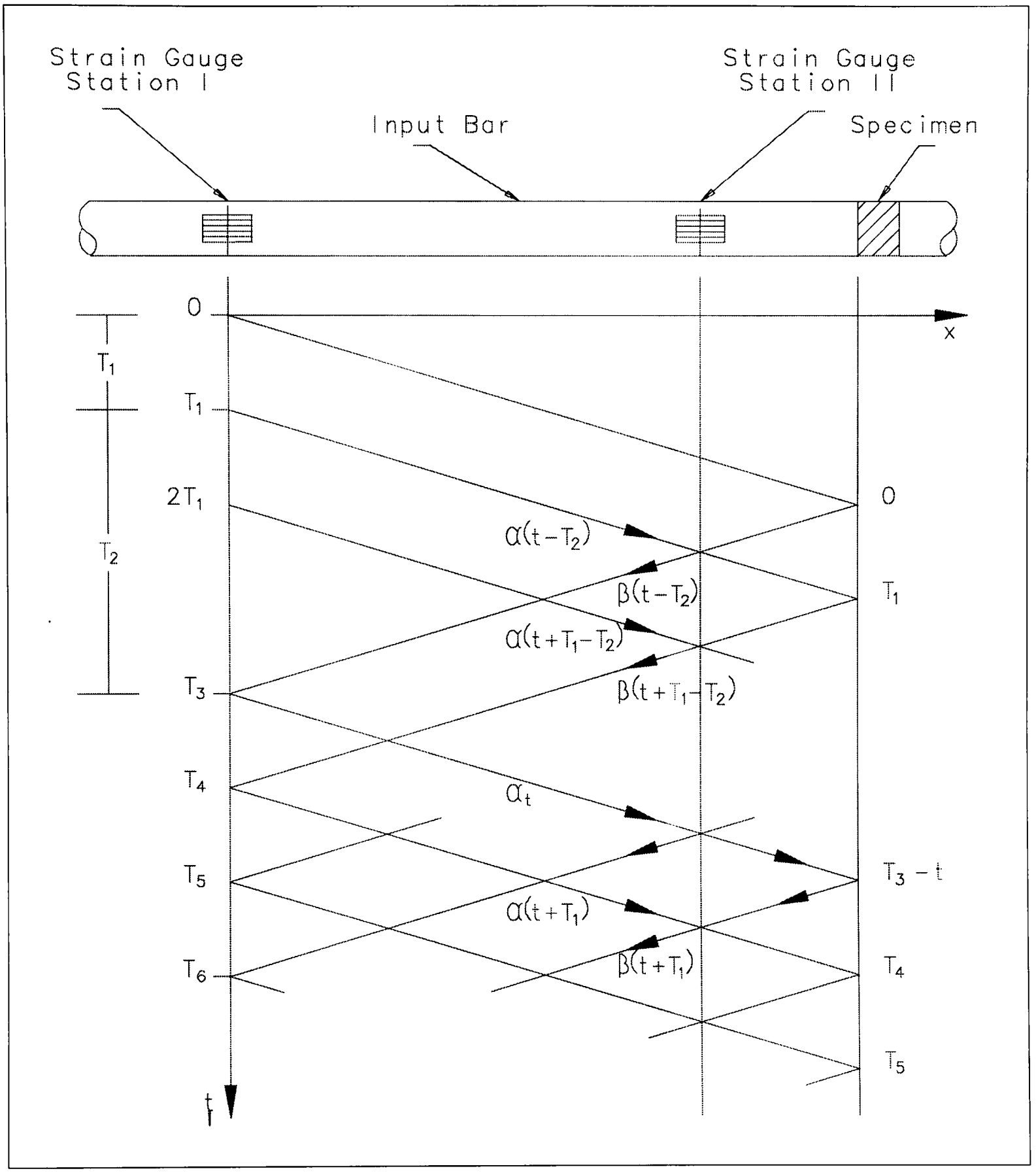

Figure 3.7 Lagrange Diagram for the Input Bar

where functions *f* and *g* are arbitrary and define the profiles of two waves travelling in opposite directions through space and time. The functions must be twice differentiable. The first term refers to a wave travelling in the direction of increasing x, ie. forwards, and the second term refers to one travelling backwards. Equation 3.15 implies that the wave propagates without

changing shape, ie. non-dispersively. Differentiating d'Alembert's solution with respect to x and t gives strain and particle velocity:

$$\varepsilon = \frac{\partial u}{\partial x} = f'(x-ct) + g'(x+ct) \quad \textbf{(3.16)}$$

$$v = \frac{\partial u}{\partial t} = -cf'(x-ct) + cg'(x+ct) \quad \textbf{(3.17)}$$

where f' and g' denote differentiation with respect to the arguments *(x-ct)* and *(x+ct)*. These arguments will be constant along lines or 'characteristics' of gradient, $dx/dt = \pm c$. But for elastic behaviour, $\sigma = E\varepsilon$, Equations 3.16 & 3.17 can be re-written as:

$$\frac{\sigma}{E} = f'(x-ct) + g'(x+ct) \quad \textbf{(3.18)}$$

$$\frac{v}{c} = -f'(x-ct) + g'(x+ct) \quad \textbf{(3.19)}$$

Combining Equations 3.18 & 3.19 gives:

$$\frac{\sigma}{E} + \frac{v}{c} = 2g'(x+ct) = const \ along \ \frac{dx}{dt} = -c \quad \textbf{(3.20)}$$

$$\frac{\sigma}{E} - \frac{v}{c} = 2f'(x-ct) = const \ along \ \frac{dx}{dt} = c \quad \textbf{(3.21)}$$

which have the units of strain. Let the values associated with the characteristics of the forward and backward travelling waves at time t and position x be defined as follows:

$$\frac{\sigma}{E} + \frac{v}{c} = \frac{2\beta}{E} \quad \textbf{(3.22)}$$

$$\frac{\sigma}{E} - \frac{v}{c} = \frac{2\alpha}{E} \quad \textbf{(3.23)}$$

where α and β are constants. Here, these two constants have units of stress. Combining Equations 3.22 & 3.23 and substituting in $c = (E/\rho)^{1/2}$ gives:

$$\sigma = \alpha + \beta \quad \textbf{(3.24)}$$

$$-\rho c v = \alpha - \beta \quad \textbf{(3.25)}$$

Finally, combining Equations 3.24 & 3.25 and substituting in $c = (E/\rho)^{1/2}$ gives:

$$\alpha = Ef'(x - ct) \quad \textbf{(3.26)}$$

$$\beta = Eg'(x + ct) \quad \textbf{(3.27)}$$

3.4.1.1 Input bar

The Lagrange diagram in Figure 3.7 has axes x and t. Characteristic lines of slope $+c$ and $-c$ are drawn to represent the paths taken by particular points on the incident and reflected waves. Note that the time T_1 marked on the figure refers to the time for an elastic wave to travel from $\mathbf{G_{II}}$ to the end of the bar (specimen end) and back again. T_2 represents the time for an elastic wave to make a return journey between gauge stations I and II.

It is required to determine the stress at the specimen end of the input bar. Taking G_{II} as a reference point, the following three equalities hold true:

$$\sigma_{I(t)} = \alpha_{(t)} + \beta_{(t-T_2)} \quad \textbf{(3.28)}$$

$$\sigma_{II(t)} = \alpha_{(t)} + \beta_{(t)} \quad \textbf{(3.29)}$$

$$\sigma_{I/P(t)} = \alpha_{(t)} + \beta_{(t+T_1)} \quad \textbf{(3.30)}$$

where $\sigma_{I(t)}$,$\sigma_{II(t)}$,$\sigma_{I/P(t)}$ are the stresses at time t at G_I , G_{II} , and the end of the input bar.

Thus, the G_{II} stress is simply the sum of the interacting characteristics at time t at a

point on the bar. Now, because the two strain gauge signals have been shifted such that initially they are (or should be) identical, the stress at G_I is the sum of the same α characteristic measured at G_{II} at time t, plus the value of the β characteristic detected at G_{II} at time t-T_2. Similarly, the specimen stress is the sum of the incident wave detected by G_{II} at time t, and the reflected wave detected after a delay of T_1. It now remains to determine the values of $\alpha(t)$ and $\beta\ (t+T_1)$.

Before the arrival of the reflected wave at G_I at time T_1+T_2, $\alpha(t)$ and $\sigma_{I(t)}$ are identical. The value of the other characteristic can be found by rewriting the equation for stress at the second gauge station:

$$\sigma_{II(t+T_1)} = \alpha_{(t+T_1)} + \beta_{(t+T_1)} \qquad \textbf{(3.31)}$$

$$or \quad \sigma_{II(t+T_1)} = \sigma_{I(t+T_1)} + \beta_{(t+T_1)} \qquad \textbf{(3.32)}$$

The solution can be obtained for times up to the arrival of the reflection at G_I , then $t + T_1 = T_1 + T_2$, ie. when $t = T_2$. From the above, the stress at the end of the input bar is seen to be given by:

$$\sigma_{I/P(t)} = \sigma_{I(t)} - \left[\sigma_I - \sigma_{II}\right]_{(t+T_1)} \quad for \quad 0 \le t \le T_2 \qquad \textbf{(3.33)}$$

Particle velocity is determined in a similar manner, but because the α and β values for the characteristics are subtracted the expression becomes:

$$-\rho c v_{I/P(t)} = \sigma_{I(t)} + \left[\sigma_I - \sigma_{II}\right]_{(t+T_1)} \quad for \quad 0 \le t \le T_2 \qquad \textbf{(3.34)}$$

For specimens that fail in times less than T_2 this analysis is sufficient. However in general, this is not the case and as further reflections arrive at the gauges successively more terms are required in order to solve for stress and velocity. Alternatively, T_2 can be raised by

increasing the separation between gauges, preferably by using a longer input bar. If T_1 is reduced too much end effects will begin to modify the signal at G_{II}.

3.4.1.2 Output Bar

Figure 3.8 depicts an α characteristic passing though G_{III} at time t. By reference to the figure, it can be seen that T_3 is the time taken for an elastic wave to travel twice the distance between the specimen and the gauge station, while T_4 is the delay between the arrival of a stress wave at the gauge and its return from the free end of the bar.

From the figure, it is also apparent that:

$$\sigma_{O/P(t)} = \alpha_{(t)} \quad for \quad 0 \le t < T_3 + T_4 \tag{3.35}$$

$$\sigma_{III(t)} = \alpha_{(t)} \quad for \quad 0 \le t < T_4 \tag{3.36}$$

Hence,

$$\sigma_{O/P(t)} = \sigma_{III(t)} \quad for \quad 0 \le t < T_4 \tag{3.37}$$

$$-\rho c v_{O/P(t)} = \sigma_{III(t)} \tag{3.38}$$

The time limits are determined by the time of arrival of the reflected wavefront at the gauge and at the specimen, ie. at T_4 and T_3+T_4 respectively. Again, failure may not occur within these times making it necessary to consider the effects of the reflected wave on the output from G_{III}.

3.4.2 HOPBAR & ELAN

Data from a number of tests was analysed by two different programs, called HOPBAR (named so because it is used for analysing data from **HOP**kinson **BAR** tests) and ELAN (Noble, 1993) (ELAN is an acronym for **E**xtended **L**agrangian **AN**alysis - a revised version of

HOPBAR which provides an improved user interface and has been adapted to provide extended analysis for tests of long duration, where several wave reflections occur in the input and output bars prior to material failure. HOPBAR and ELAN are both 'in-house' programs, capable of interpreting data from compression, tension and torsion tests on a range of materials). These programs are essentially semi-automated versions of a 'manual' analysis and calculate stress, strain and strain-rate data.

Towards the ends of some tests, a 'blip' in stress is observed before the stress falls off towards zero, see Figure 5.1 *et seq* for clarification. This was attributed to the transmitted pulse in the output bar returning from the free end and interacting with events at the specimen. The time taken for the transmitted pulse to travel to the free end and back again is approximately 200μs, which is effectively a limiting factor for the test, since the reflected compressive wave in the output bar causes unloading of the specimen. Specimens which shattered, i.e. tested to failure, namely of shorter gauge length, showed a steep reduction in stress within a short space of time (5-10μs), showing clearly that failure had occurred. This 200μs time limit is of no relevance for tests where short specimens are used, since failure occurs before the end of this time period. Either shorter specimens should be used or the apparatus modified to accommodate longer bars which would extend the duration of the test and provide additional information.

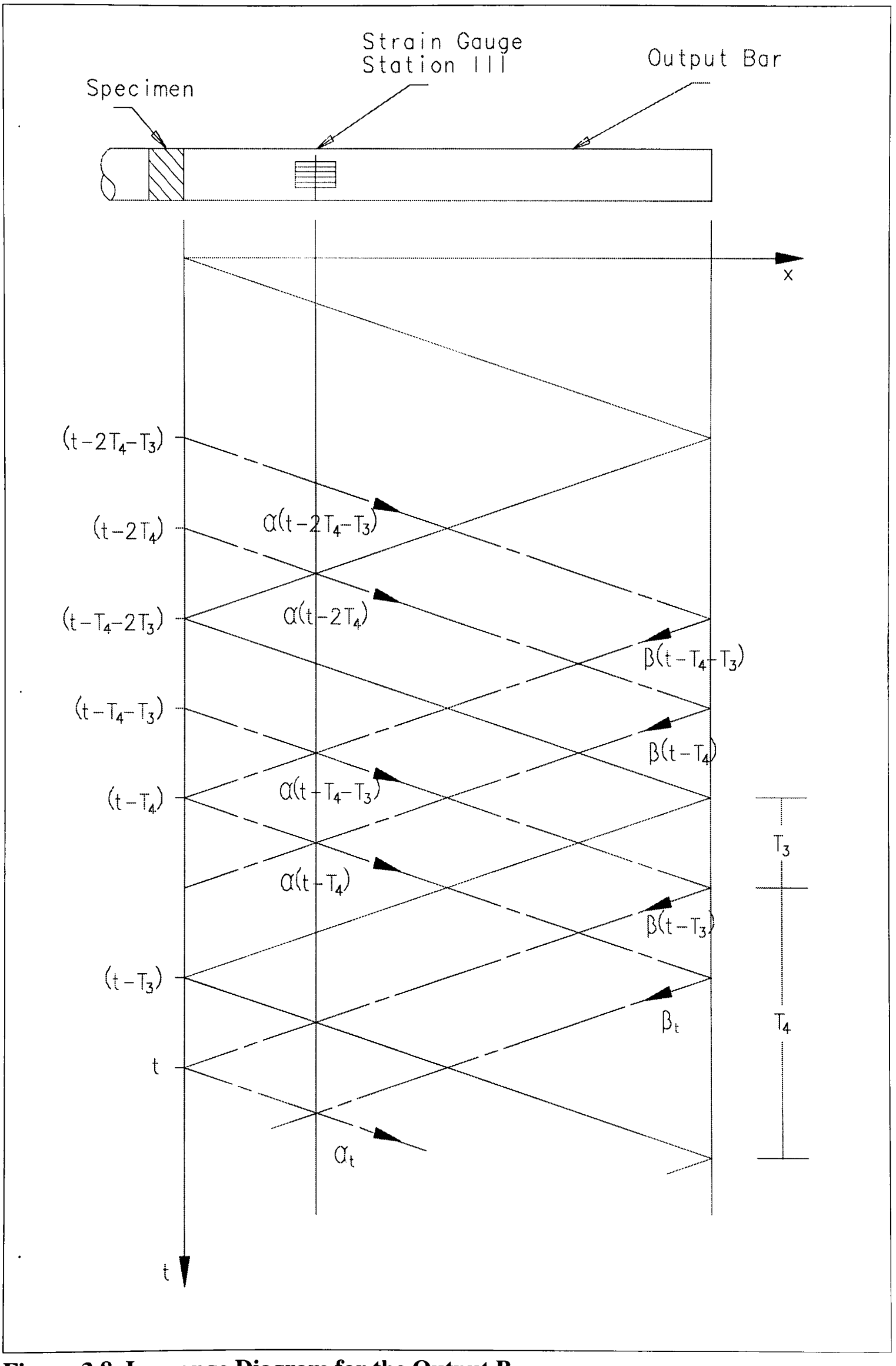

Figure 3.8 Lagrange Diagram for the Output Bar

3.4.3 Repeatability of Tests

When performing any kind of experimental work, it is essential to take as many data readings as necessary to ensure accuracy, since this reduces the effect of any systematic error. For nominally identical high strain-rate compression tests using the split Hopkinson pressure bar, it was found that the stress-strain curves had a scatter of about ±5%.

An example is shown in Figure 3.9, which clearly shows that the repeatability of these tests is very good so that only a minimum number of repeat tests, in practice three are required for any particular set of conditions.

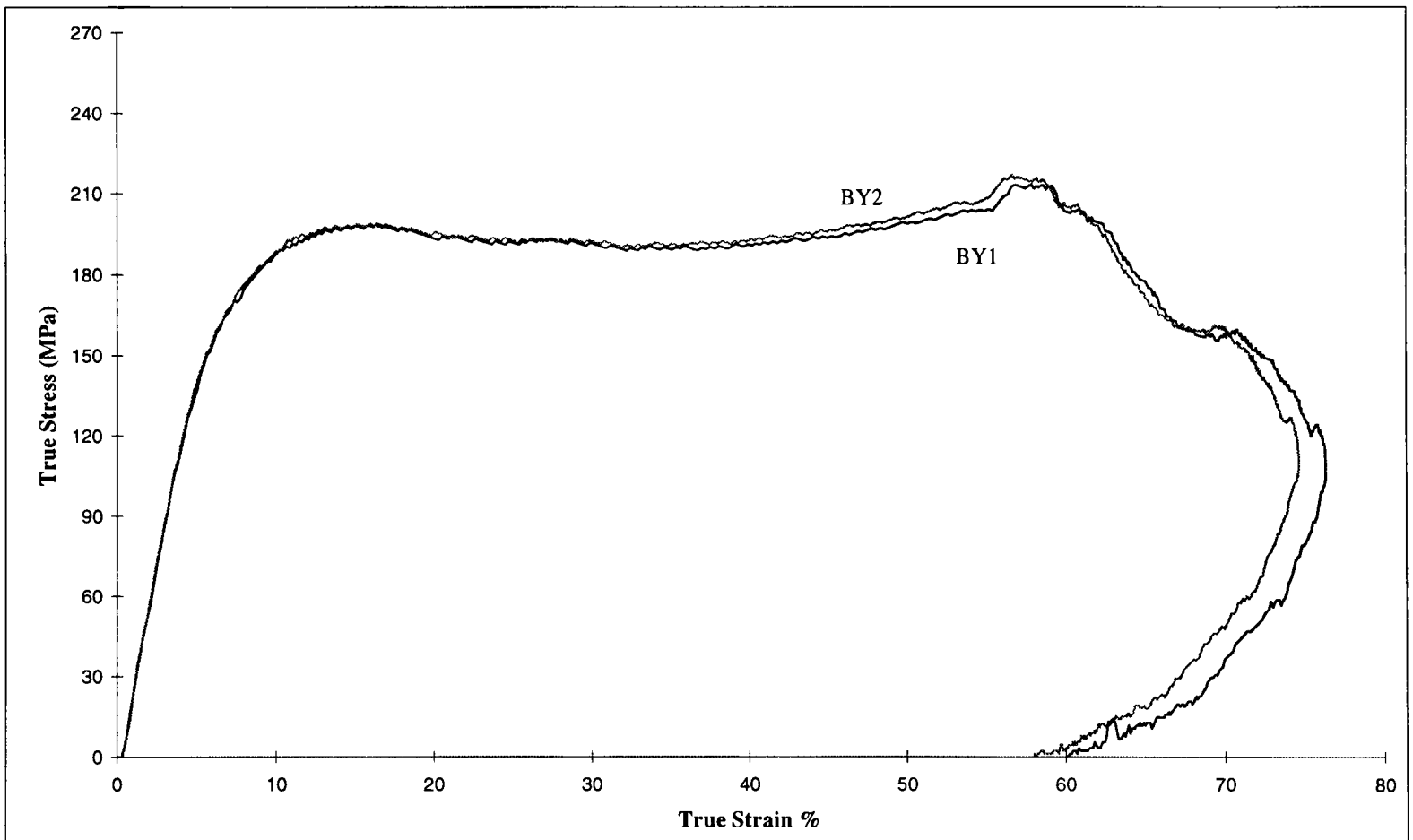

Figure 3.9 Two Nominally Identical Tests

3.4.4 Sources of Error

The variation between nominally identical tests is small and within the boundaries of experimental error, but even this small error can be attributed to several sources. Firstly, an analogue pressure indicator is used on the reservoir of compressed air. The reservoir is pressurised to a level above that which is required. The pressure falls slowly, due to small amount of leakage through the butterfly value used for release. Once the appropriate pressure is reached, the valve is opened. This relies on the operator's judgement to assess the moment when the required pressure is reached. The firing pressure and hence impact velocity are not exactly controllable. There is a small amount of scatter shown in Figure 3.10, which relates the firing pressure on the pressure gauge to the velocity of the projectile momentarily before impact, measured using a digital timer. HOPBAR or ELAN are used in the analysis of the stress waves in the input and output bars, which requires the operator to judge when the pulses are synchronised. Nevertheless it has been shown that the tests performed were repeatable.

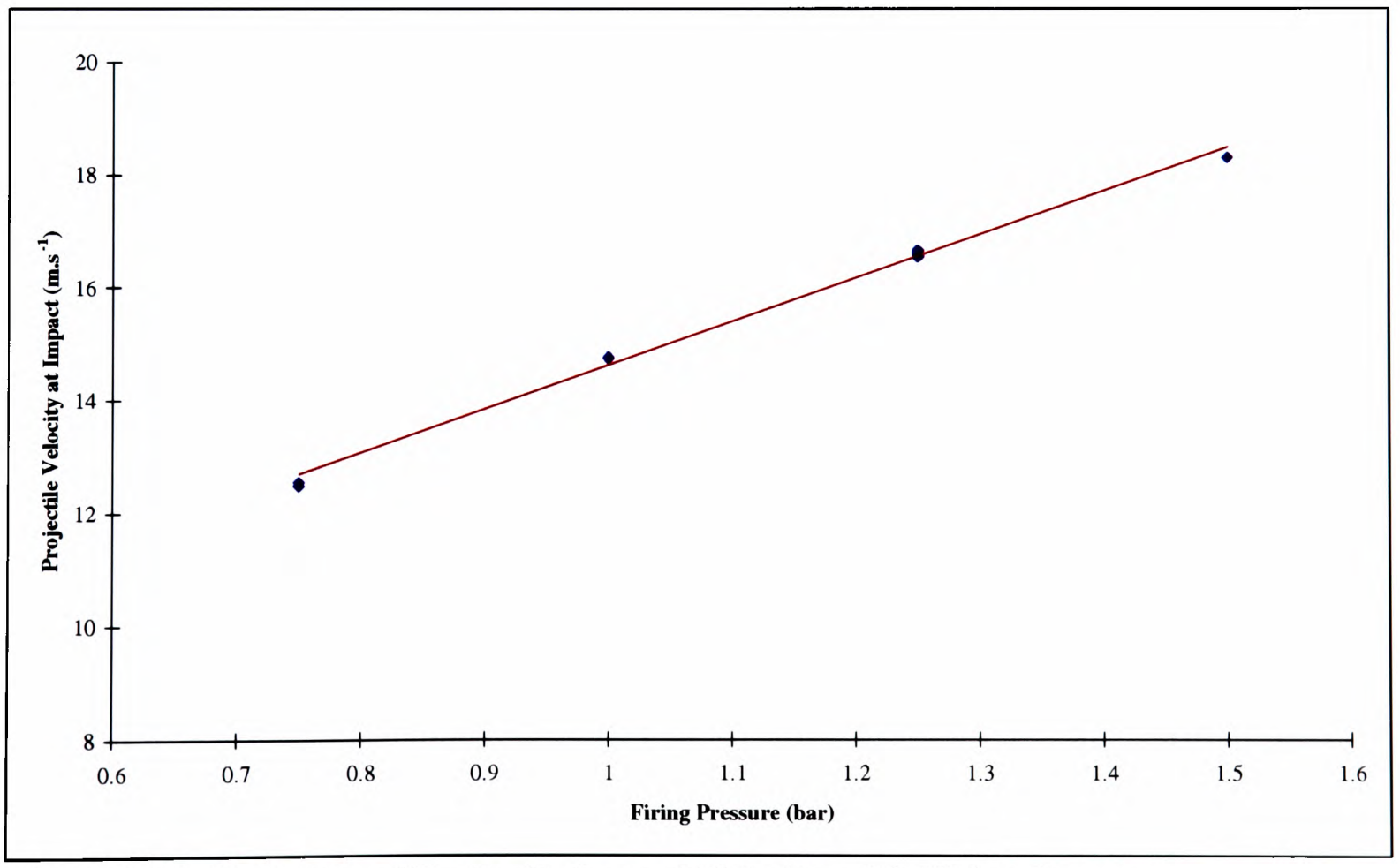

Figure 3.10 Variation of Projectile Impact Velocity with Firing Pressure

3.4.5 High Speed Photography

High speed photography was used to examine the deformation of a specimen during high strain-rate tests. Photographs were taken of compression tests which were used as a comparison against the Hopkinson Bar analysis.

The high speed photography carried out in these experiments was performed using a Cordin rotating prism camera, model 377, capable of taking up to 500 frames at speed of between 10,000 $fr.s^{-1}$ and 200,000 $fr.s^{-1}$ (this translates to a framing rate from 100μs to 5μs respectively). The experimental setup is shown schematically in Figure 3.11. This camera uses Ilford HP5 70mm wide black & white film within a rotating drum. The sequence of 500 images is produced by using a prism and a system of static and rotating mirrors to transfer the incoming light to the film. The great advantage of such a camera over, say, an imaging camera, is the resolution of image obtained and also the high framing rate, which makes it ideal for high rate testing. The relative velocity of the rotating prism and drum is indicated digitally at all times and does not vary significantly during the test.

Despite it's advantages, the Cordin camera requires several hours to set up. Testing is done in a blacked-out laboratory where the camera shutter is set permanently open and framing is obtained by illuminating the specimen by electronically controlled pulsed flash guns. The flash guns illuminate the specimen for a pre-determined period of time, controlled by a capacitor bank, which is able to provide a controlled time duration for the flash from 0.5ms up to 11ms. Before each test, the maximum recording length for the required camera speed was calculated, then a flash length was chosen which would prevent a double exposure of any of the film. The flash is triggered from a strain gauge and then a suitable delay is then introduced into the system which will ensure that the 500 frames begin just momentarily before the stress wave reaches the specimen. On completion of the test, the film must be developed before it is

known if the focussing, aperture and trigger were all set correctly. Crude focussing can be done before the test, but this is not always perfect.

3.4.5.1 Full Photographic Testing Procedure

The testing sequence using the Cordin 377 is as follows:

- cut film to length with square ends
- load cassette with Ilford HP5 70mm film in darkroom
- load cassette into camera
- with the room lights off open cassette and load film around drum
- room lights on; focus and set aperture
- evacuate camera to about 10 mTorr
- switch on camera control unit and set camera speed
- start camera motor and wait for it to get up to speed
- when almost at speed, set capacitor banks to charge for flash units
- set gun pressure and arm the transient data recorders
- switch off room lights and arm flash trigger unit
- when camera at speed and capacitors charged, ready to test
- open camera shutter, fire gun, close shutter
- switch off camera motor and capacitor banks
- when camera stopped rotating, vent to regain pressure
- retrieve film, develop and print in darkroom.

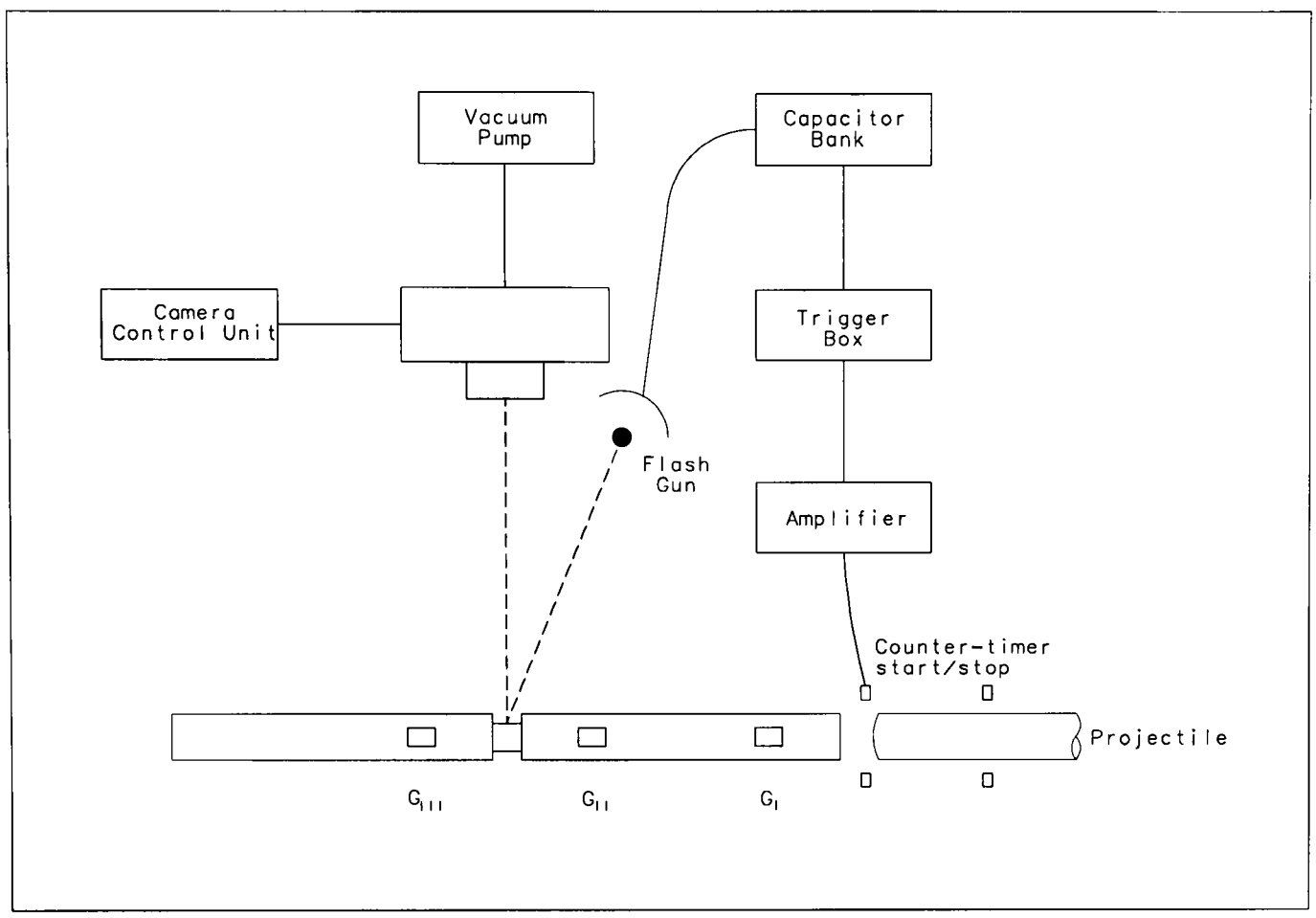

Figure 3.11 Experimental Setup for High Speed Photography

By taking measurements from prints using a travelling microscope, an accurate strain vs time graph from the sequence of photographs can be built up. One specimen size was used (Diameter 9mm, Length 5.5mm) and several successive preliminary tests were performed at strain-rates of $3000s^{-1}$. The strain-time characteristics are shown in Figure 3.12, and are compared in Figure 3.13, with the equivalent computer calculation from HOPBAR and ELAN, as explained earlier. The technique the camera uses to obtain such a high framing rate is to split the light into eight different light paths, which happen to vary fractionally in length. This means that the magnification of each of the eight sequential photographs is slightly different from the next, so a correction factor is introduced to accommodate this change. The evidence from photographs shows a good correlation with the strain calculated using HOPBAR and from the manual analysis discussed overleaf.

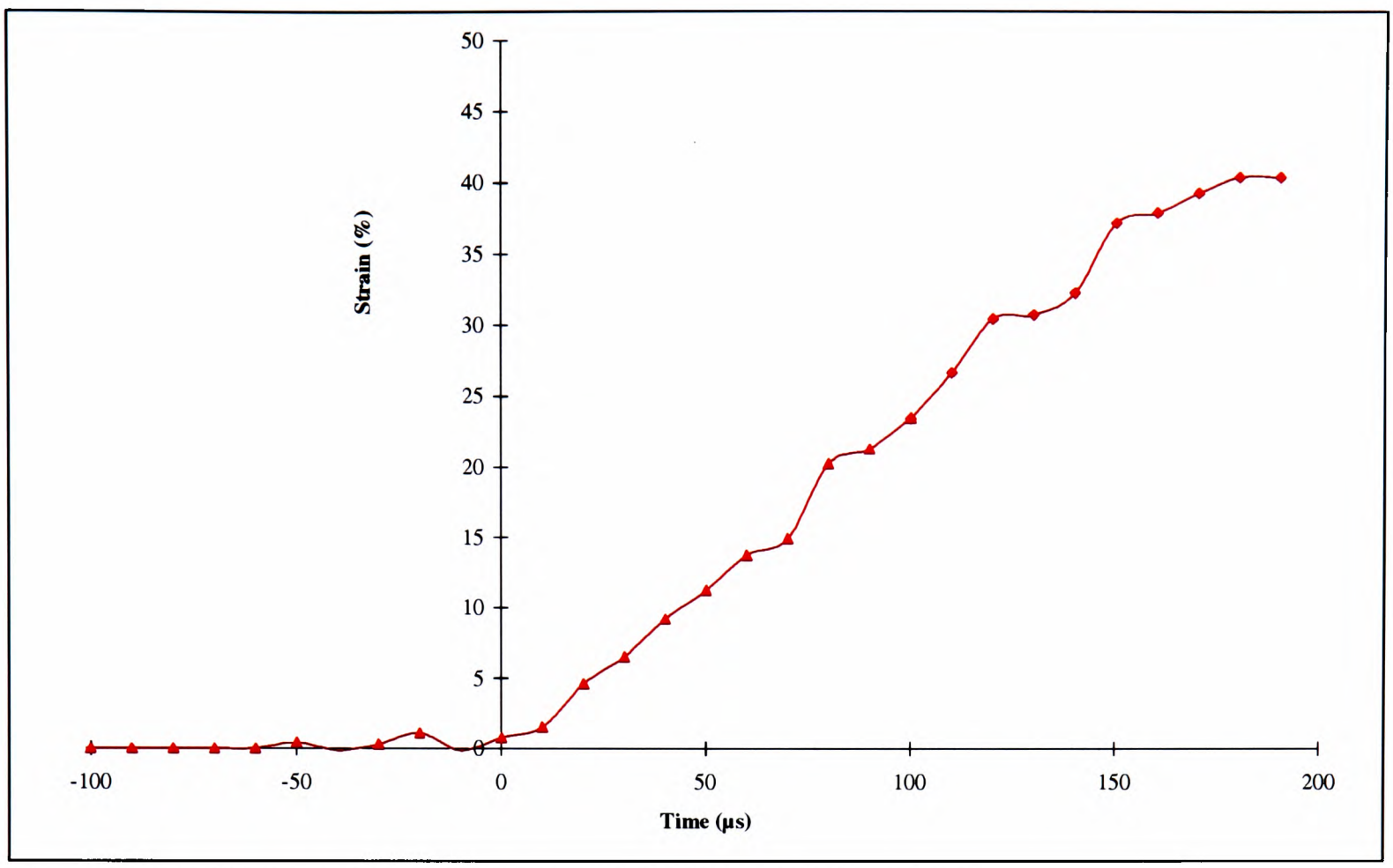

Figure 3.12 Measured Strains from High Speed Photographs

3.4.6 Comparison Between Photographic Records, HOPBAR, ELAN and Manual Analysis

The various programs and methods used for analysing SHPB test data are compared against each other in Figure 3.13 below. There is clearly an excellent agreement shown between the strains determined using both the HOPBAR and ELAN programs. The results from these two programs are also compared with strains determined from high speed photography and by manual calculation and again show a very high correlation. High strain-rate tests performed on the present testing apparatus are limited to a time of approximately 200µs. This being the time taken for the transmitted stress wave to return from the free end of the output bar and cause partial unloading of the specimen which effectively terminates the test.

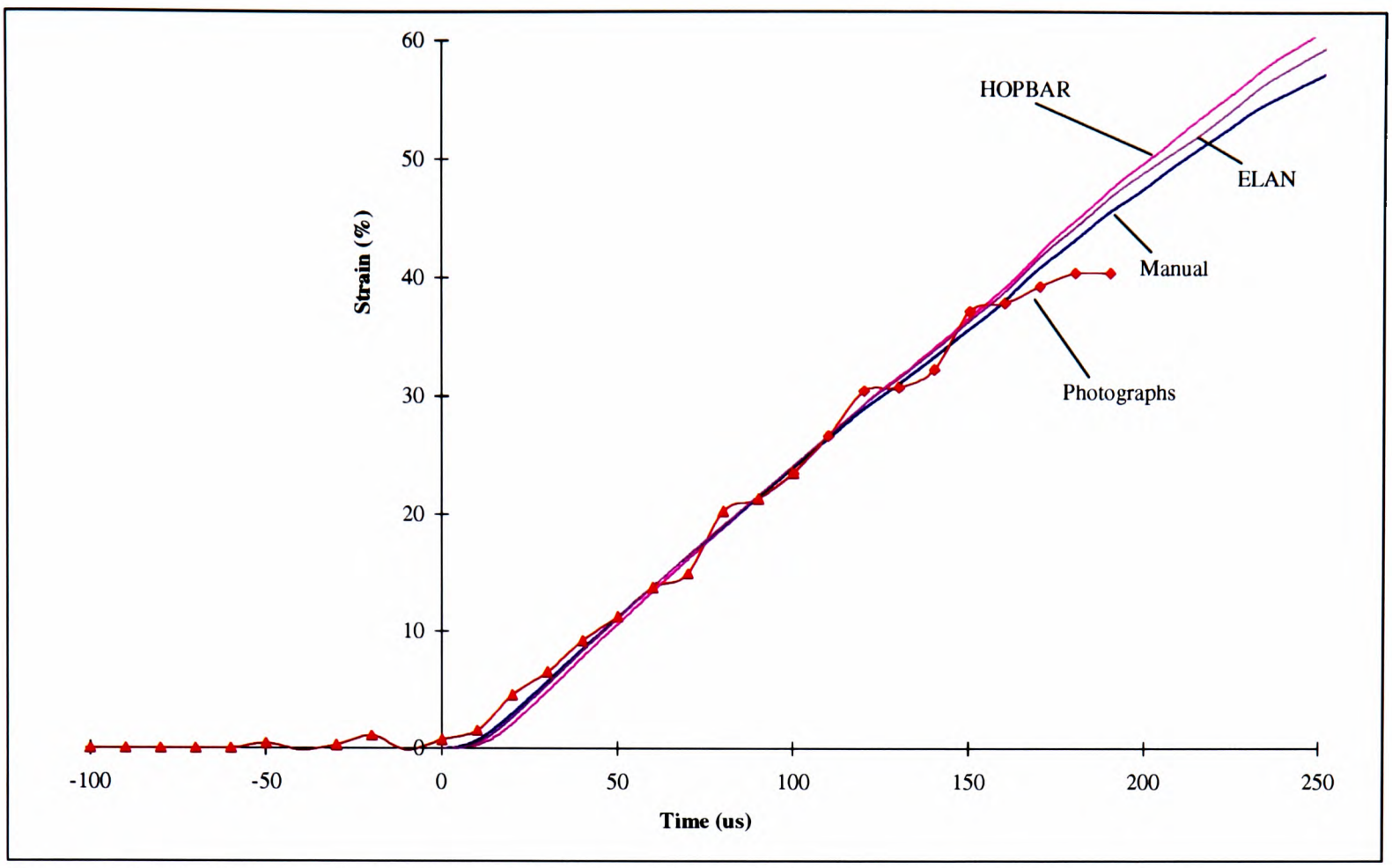

Figure 3.13 Comparison between HOPBAR, ELAN, Photographic and Manual Analysis

3.5 References

Hopkinson, B., A Method of Measuring the Pressure Produced in the Detonation of High Explosives or by the Impact of Bullets, Phil.Trans. A, 213, pp. 437-456, 1914.

Kolsky, H.,An Investigation of the Mechanical Properties of Materials at Very High Rates of Loading, Proc.Phys.Soc. B, 62, pp.676-700, 1949.

Noble, J.P, D.Phil. Thesis, University of Oxford, 1993.

Chapter 4

Radiometric Testing Technique

4.1 Introduction

During the deformation of a material under whatever loading condition, some plastic work is converted into stored strain energy and the remainder evolves as heat. At low strain-rates, the temperature changes are small and could be measured, for example by using a thermocouple, since such changes are slow and within the response time of the device. However, at higher strain-rates, changes in temperature can be large and rapid, for example, rises of several hundred degrees in a timescale of 20μs have been recorded in metals. Previous workers have proposed constitutive relations for metals which include terms for thermal effects, but have often lacked the means to carry out dynamic temperature measurement to validate these. Clearly, at high loading rates more sophisticated devices with fast response times must be used to measure the changes in temperature.

All materials above absolute zero emit thermal radiation. Radiometry is a temperature measurement technique which utilises this effect to make a measure of the surface temperature of a material. A radiometer can be split into two sections - an imaging system which gathers

and focuses radiation from the surface of the material, and a detector which reacts to the incident radiation.

A radiometric, non-contact method of surface temperature measurement has been developed at Oxford (Craig *et al*, 1994) and further developed by the author and co-workers (Trojanowski *et al*, in press) which utilises an infra-red imager and a fast response detector. Mason *et al*, 1994, have used radiometry to measure the temperature field around localised phenomena, in situations involving high temperatures. The present radiometer, however, is capable of detecting much lower temperatures, such as may be expected and are significant in the deformation of polymeric materials.

The theoretical power output from an infra-red source over the spectral band of the radiometer can be calculated by integrating the Planck distribution. Then the output of the radiometer can be given by:

$$Signal = \varepsilon.T.\Omega.R.A_d.\int_{\lambda_1}^{\lambda_2} L_\lambda \, d\lambda \qquad \textbf{(4.1)}$$

where ε is the emissivity, T is a measure of the transmissability of the imaging system (dimensionless), Ω is the solid angle, R is the responsivity of the detector (Volts/Watt), A_d is the area of the detector and L_λ is the Planck spectral luminosity at a given wavelength and temperature.

This relationship includes the surface finish (ie. the emissivity), a factor which is generally unknown and may change under test conditions. This is one of many other many uncertainties in radiometric predictions, namely the inability to quantify the transmission of filters and windows and to include reflections from nearby supporting structures.

4.2 Theory of Radiometry

The spectrum of thermal radiation emitted by an object is dependant on the nature of its surface and its temperature. For a black body emitter the spectral luminosity (power emitted per unit area per solid angle at wavelength λ and temperature T) is given by the Planck function in Equation 4 .2.

$$L(\lambda,T) = \frac{C_1}{\lambda^5.\left[\exp\left(\frac{C_2}{\lambda.T}\right) - 1\right]} \qquad \textbf{(4.2)}$$

Plots of this function have been done at a number of temperatures, shown in Figure 4.1.

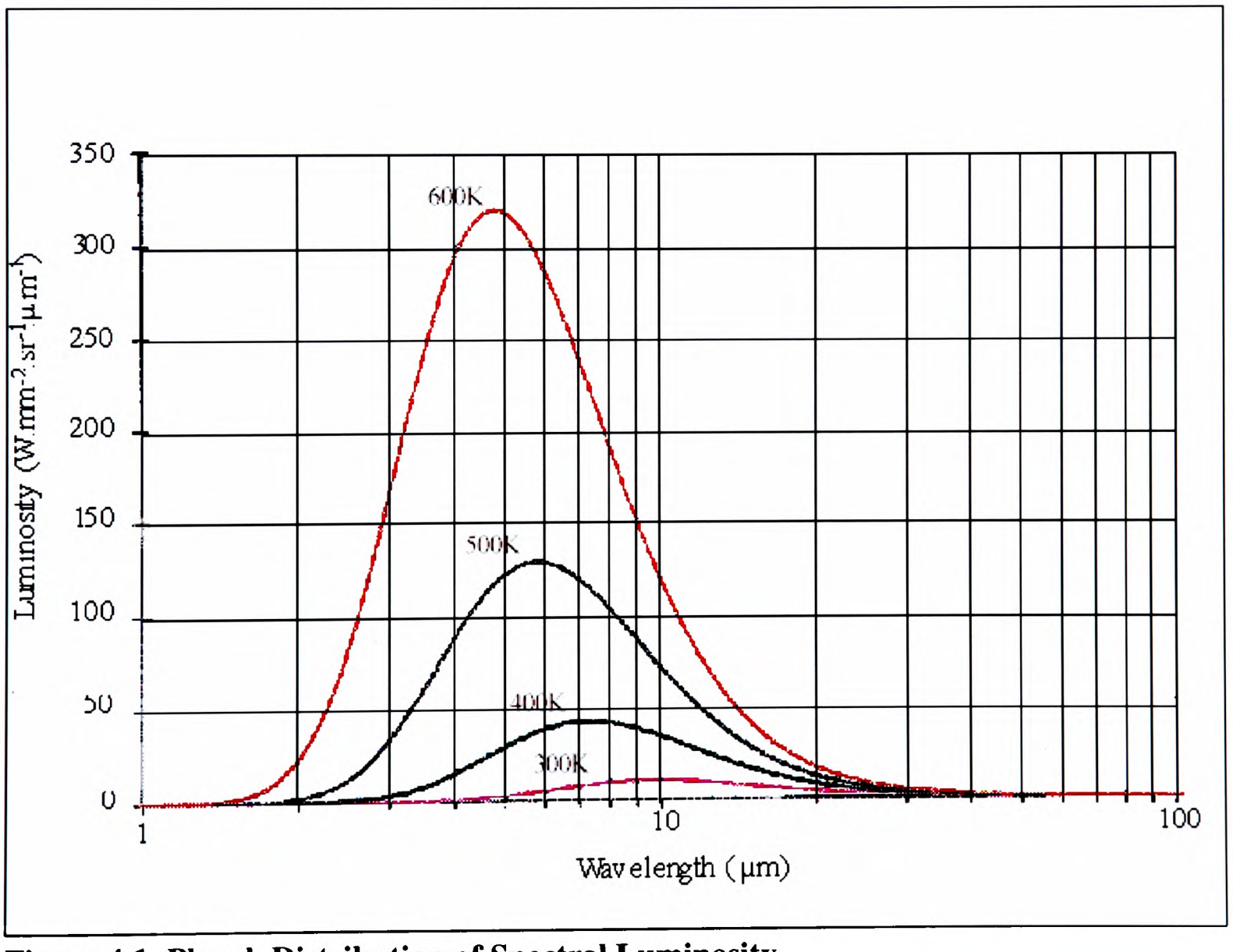

Figure 4.1 Planck Distribution of Spectral Luminosity

4.3 Development of Radiometer

A number of different design requirements and parameters were considered for the radiometer. There are many different types of detector available which are based upon differing physical principles, and in this case a fast system with broad band sensitivity was required. However, the fundamental parameter that determines the outcome of such a choice is the value of the specific detectivity, D^*, defined as:

$$D^* = \frac{S}{N} \frac{\sqrt{\Delta f}}{E\sqrt{A_d}} \qquad \textbf{(4.3)}$$

where: S/N is the signal to noise ratio

Δf is the system bandwidth (Hz)

E is the photon incidence at the detector (W/cm^2)

A_d is the detector area

The group of detectors which were considered were photon detectors, photoelectric, photoconductive and photo-electromagnetic. These have high D^* and fast response (Δt), particularly those based on either photoelectric or photoconductive effects. To suppress thermal noise, a form of refrigeration was used. The maximum temperature during testing was thought to be in the region of 100°C, which corresponds to wavelengths of thermal radiation of approximately between 4μm and 10.5μm.

A new imager was required to improve the photon throughput (power) of the system over the old design. The previous system used two parabolic mirrors with relatively low photon gathering power and was used at an angle of offset which undoubtedly introduced large aberrations. The quality of the photon gathering optics is a key factor in ensuring an adequate

infrared signal. With mirrors, the bandwidth is not a problem since the reflectivity is ~99%. In order to avoid off-axis aberrations and to simplify alignment, the system should be as closely in-line as possible. Alignment problems could be overcome by employing a Cassegrain configuration which adopts apertured mirrors. In order to minimise the collection of un-focussed emissions, the aperture/mirror area fraction was kept to <4%.

4.4 Details of Detector and Associated Electronics

Mercury-Cadmium-Telluride (HgCdTe) was selected for the detector material, due to its favourable response characteristics which make it suitable for detecting thermal emissions in the region of 5μm. This is an approximate number, since the wavelength sensitivity can be varied by altering the blend between HgTe and CdTe. The type used for the detector has dimensions of 1mm by 1mm and is sensitive to radiation in the waveband of between 2.0μm to 12.7μm, with a response time of approximately 1μs. It is cooled with liquid nitrogen to ~77K . The detector used is a photoconductive device, which requires a bias voltage of 191mV across the detector.

The frequency response for the detector and amplifier together was nominally between approximately 10Hz and 145kHz. The lower limit means that the system will be not be significantly affected by low frequency background radiation. The 145kHz upper cut-off frequency is governed by the detectable rise time of ~1.1μs, given by Equation 4.4. The response of the electronics has been modelled using a commercially available electronics modelling package, PSPICE, where it was shown that for a square wave input, the time to reach 90% of the pulse height was approximately 1.4μs, seen in Figure 4.2.

$$f_c = \frac{1}{2\pi\tau} \tag{4.4}$$

Being a photoconductive device, the detector requires a bias voltage across the element, so that charge carriers produced by incident radiation, can flow as a current. A simple two stage operational amplifier shown in Appendix B was used for this purpose. The voltage bias was set at 191mV which supplied a bias current of 1mA, since the elemental resistance was 191Ω. This bias current ensured that the detector was operating at its optimum responsivity.

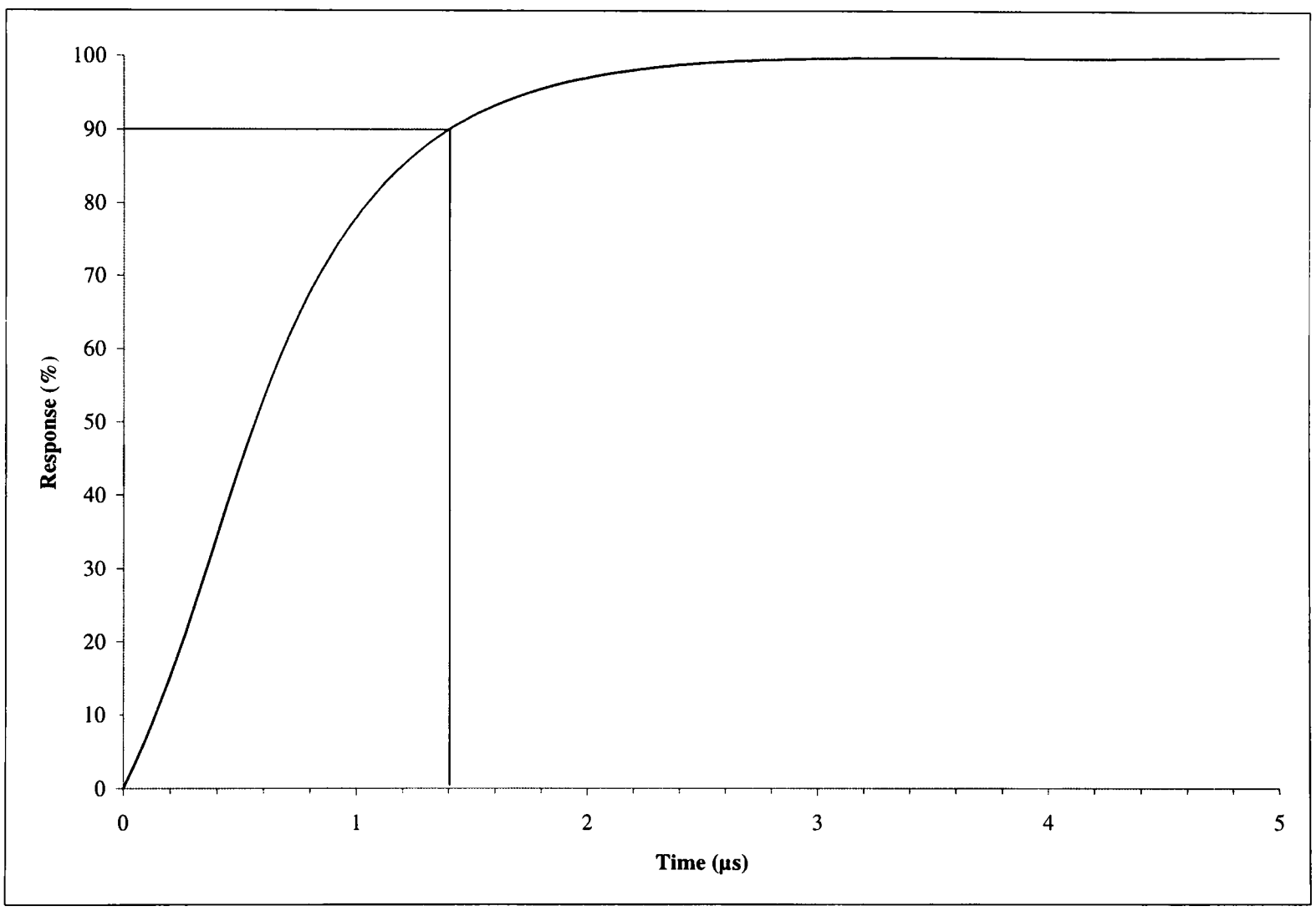

Figure 4.2 Modelled Output of Detector Electronics

Since the infrared detector was only sensitive to a.c. signals, it was necessary to chop the radiation during the calibration to generate an a.c. signal. A typical signal output is shown in Figure 4.3, which illustrates the various stages of the chopping process. The reason for the non-linear ramp was because a circular beam was being chopped. As the chopper passes

through the centre of the beam, the rate of change in the amount of radiation incident upon the detector becomes a maximum, corresponding to a maximum slope. Towards the edge of the beam, the rate is similarly reduced. When the beam was either totally obscured or totally in view, the rate of change of the incident radiation was zero. The gradient of the trace when the rate of change of incident radiation is zero, is determined by the capacitance of the system. The slope was measured to be approximately 16μV/μs. Changing the frequency of the chopper only affected the slope during phases (a) and (c). For higher frequencies the gradient was correspondingly steeper, since the time taken to completely disclose and obscure the light beam is less. The slope of phases (b) and (d) remained constant since both were independent of frequency. During testing the actual temperature being measured was changing so there was no need to chop the signal for it to become 'visible' to the radiometer.

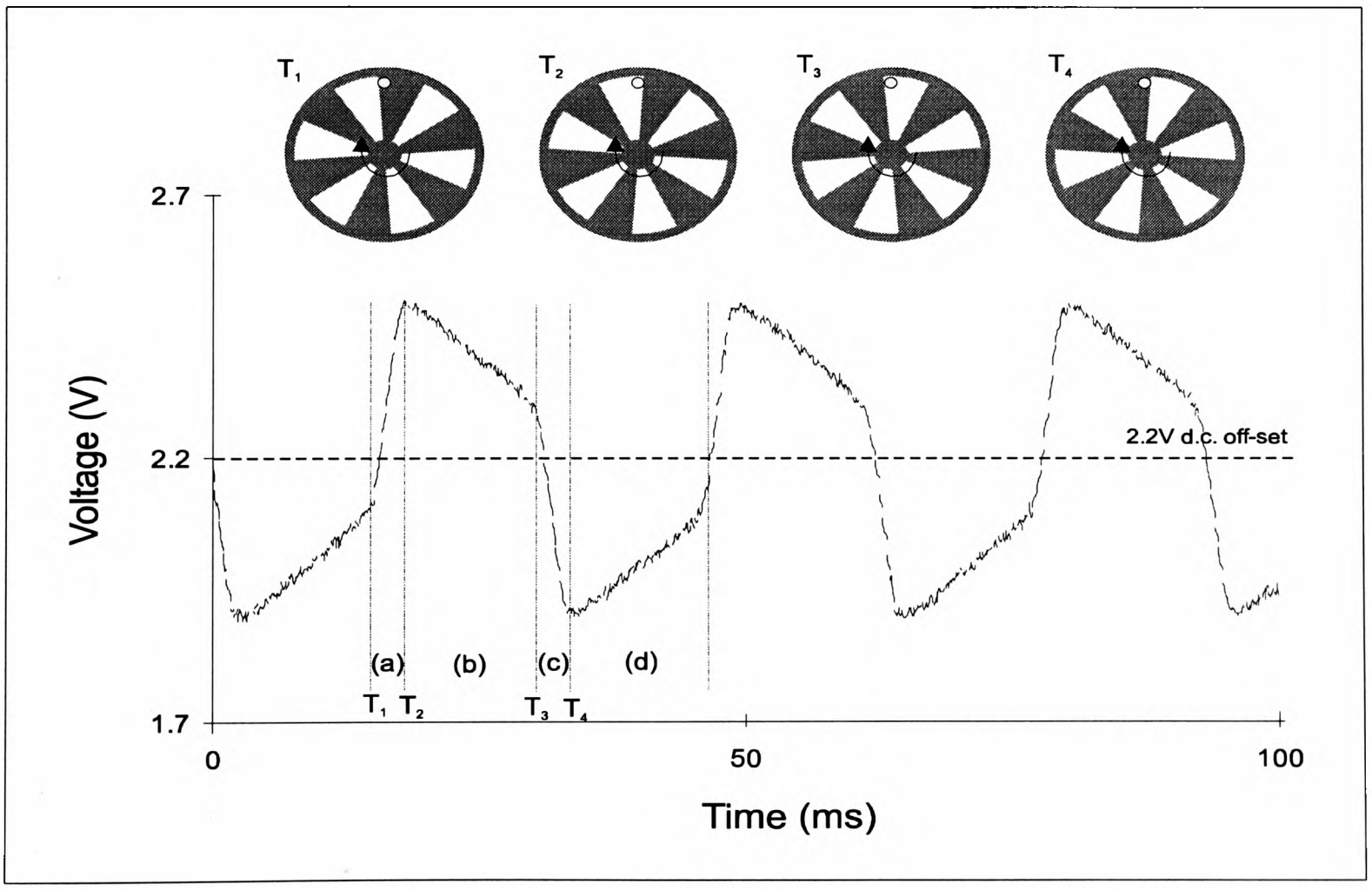

Figure 4.3 Typical Radiometer Signal During Calibration

The detecting apparatus can be affected by three types of noise: low frequency, high

frequency and thermal noise. The first two can be filtered out by using a 10Hz-145kHz bandpass. The third is dependant on the operating temperature of the detector and is the main source of noise to the detector, which can affect the performance significantly. The thermal noise, i.e. thermal collisions between neighbouring lattice atoms, is a by-product of the generation and recombination of electron hole-pairs caused by the incident radiation. The benefit of operating at a lower temperature is that the detectivity can be increased by as much as an order of magnitude, due to a reduction in the noise level, much of which is caused by the thermal agitation of the elemental atoms and which is reduced on cooling.

This design is an improvement on a radiometer previously used at Oxford (Craig *et al*, 1994). The detector used was a thermo-electrically (Peltier) cooled (~200K) single element detector, 50μm square. It has been demonstrated through experimental work that Peltier cooling is generally only satisfactory when measuring temperatures over about 70°C, when the signal to noise ratio becomes greater than 1.

The current apparatus employs a single, liquid nitrogen cooled element (~77K), 1mm square, supplied by GEC-Marconi Infrared Ltd. As previously mentioned, cooling the element by using liquid nitrogen increases the detectivity and the Signal-to-Noise ratio (S-N). To contrast the performance and suitability of the two detectors to various applications, the present Dewar detector has a S-N ratio of 1 at temperatures of around 25°C, whilst to achieve unity for the Peltier cooled detector, this threshold temperature is approximately 70°C. A lower limit of 70°C is satisfactory when studying metals where the temperature can increase to several hundred degrees. However, it was anticipated that the maximum temperature rises in polymers would be in the region of 100°C so it was felt that Peltier cooling would be unsuitable.

A detector composed of an array of twelve 50μm elements has been used at Oxford for work on metallic specimens (Macdougall,1995). This detector is again Peltier cooled, so whilst

being inferior at low temperatures, the twelve-element detector has excellent spatial resolution. The single element detector was used for measuring the bulk temperature rise at the surface of a specimen. The twelve element detector was more suited to measuring the high temperatures which exist in regions of localised plasticity such as adiabatic shear. An idealised situation would be to have a twelve element liquid nitrogen cooled detector which would enable low temperatures to be detected along with good spatial resolution.

4.5 Optics

An ideal imaging system for the radiometer will gather 100% of the emitted radiation from a region of a specimen and focus a perfect image onto the detector. In practice however, only a fraction of the emitted radiation can be gathered and some geometric aberration is inevitable. The imaging system is a vital part of the whole radiometer. If inadequately designed, it can render the radiometer useless, since geometric and chromatic aberrations, although inevitable, can be minimised with a good system. These aberrations can distort the image either by imperfect optical design, or by a variation in focal length with wavelength.

4.5.1 Off-Axis System

The imager used by Craig was composed of two gold plated parabolic mirrors in an off-axis arrangement as shown in Figure 4.4. This system was capable of gathering approximately 0.5% of the total emitted radiation and caused severe distortion (approximately ±150μm for a point source) of the image which was mainly due to the off-axis nature of the optical system.

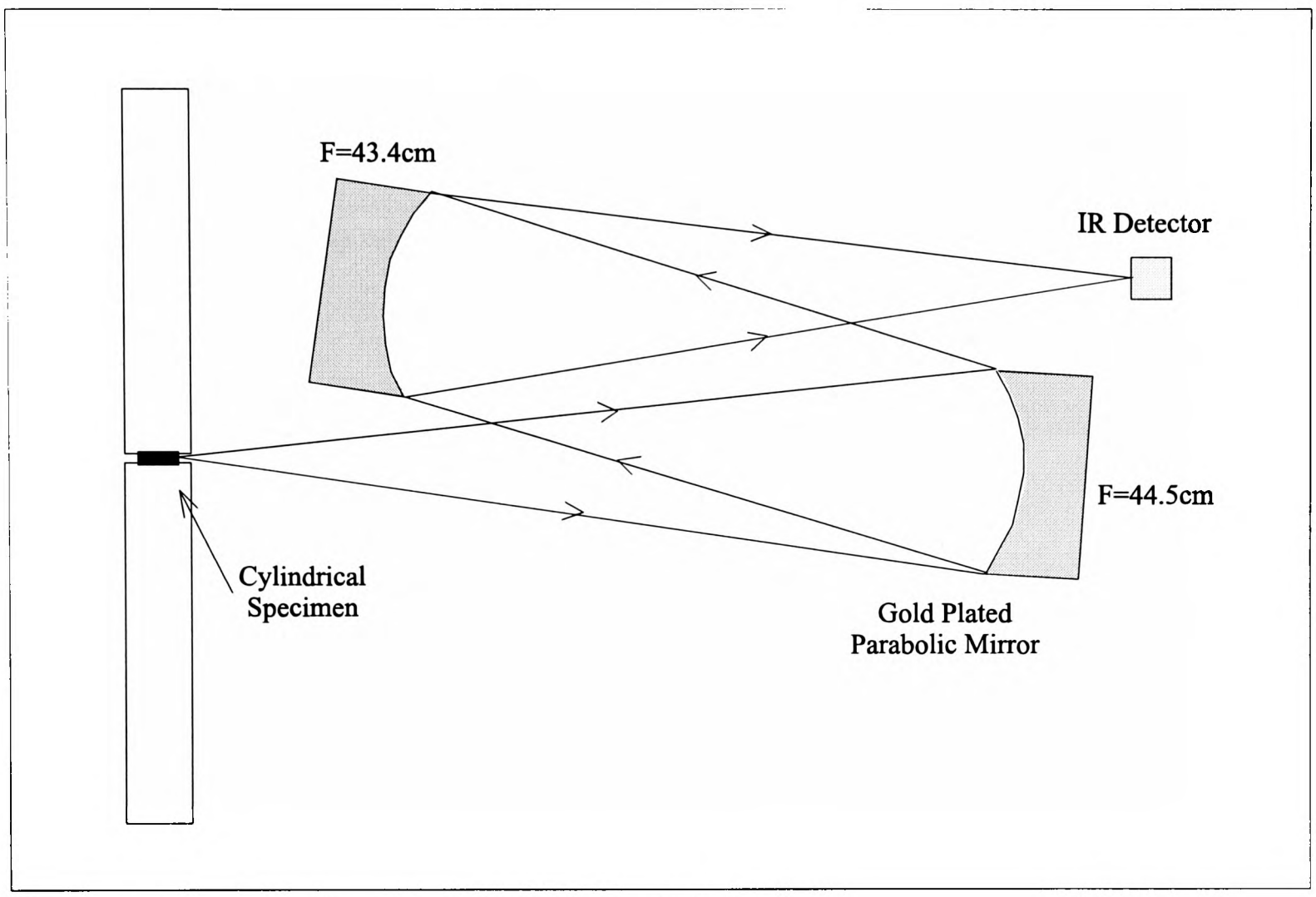

Figure 4.4 Imaging System used by Craig (1994)

4.5.2 New Improved Optics

An improved system has been developed which is based on a Cassegrain design. It consists of two annular spherical copper mirrors located on the same axis, shown in Figure 4.5a. The radiometer is shown in Figures 4.5b & 4.5c in position prior to a test. Due to reasons of cost, spherical mirrors, which cause on-axis spherical aberrations, were used rather than parabolic mirrors. To correct for these small aberrations, achromatic lens pairs are placed in the mirror apertures. The lenses, made from Potassium Chloride (KCl) and coated with Zinc Sellenide (ZnSe) are located at the centre of each mirror and were chosen for their desirable spectral transmission characteristics, 3.5μm-14μm. The new optical system offers many advantages, for example, it has a ten-fold increase in light gathering capability over the

previous off-axis system. The distortion of the image has also been reduced to approximately ±12.5μm; this varies only slightly with wavelength. The mirrors are held in an aluminium cylinder and so by making the mirrors immoveable, several degrees of freedom have been removed from the system which facilitates the setting-up process and removes significant errors in alignment.

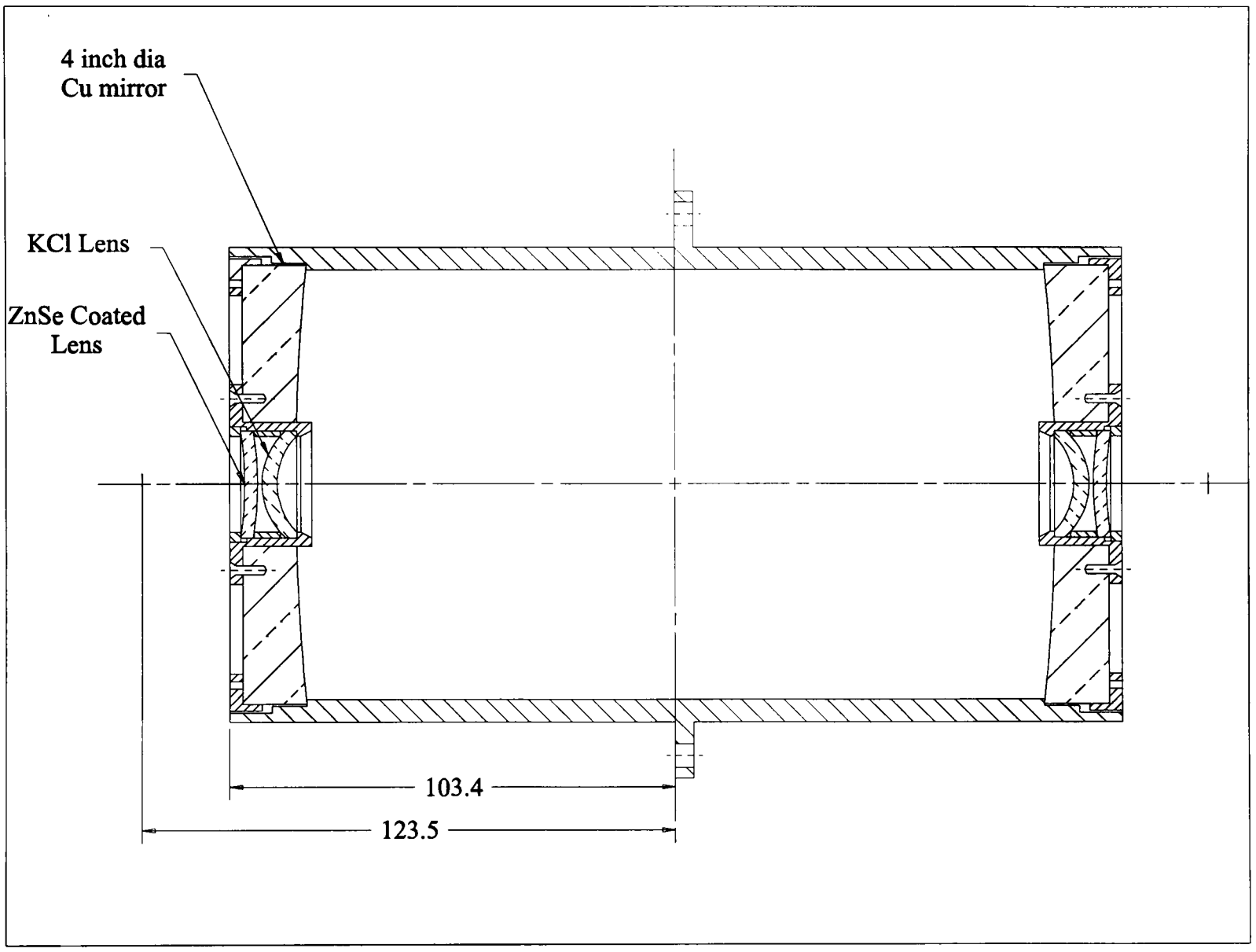

Figure 4.5a New Improved Optics

The reduction in distortion of the image is demonstrated in Figure 4.6 which compares the variation of the relative intensity with distance from the optical axis for a point source as imaged by the two optical systems, calculated by ray tracing.

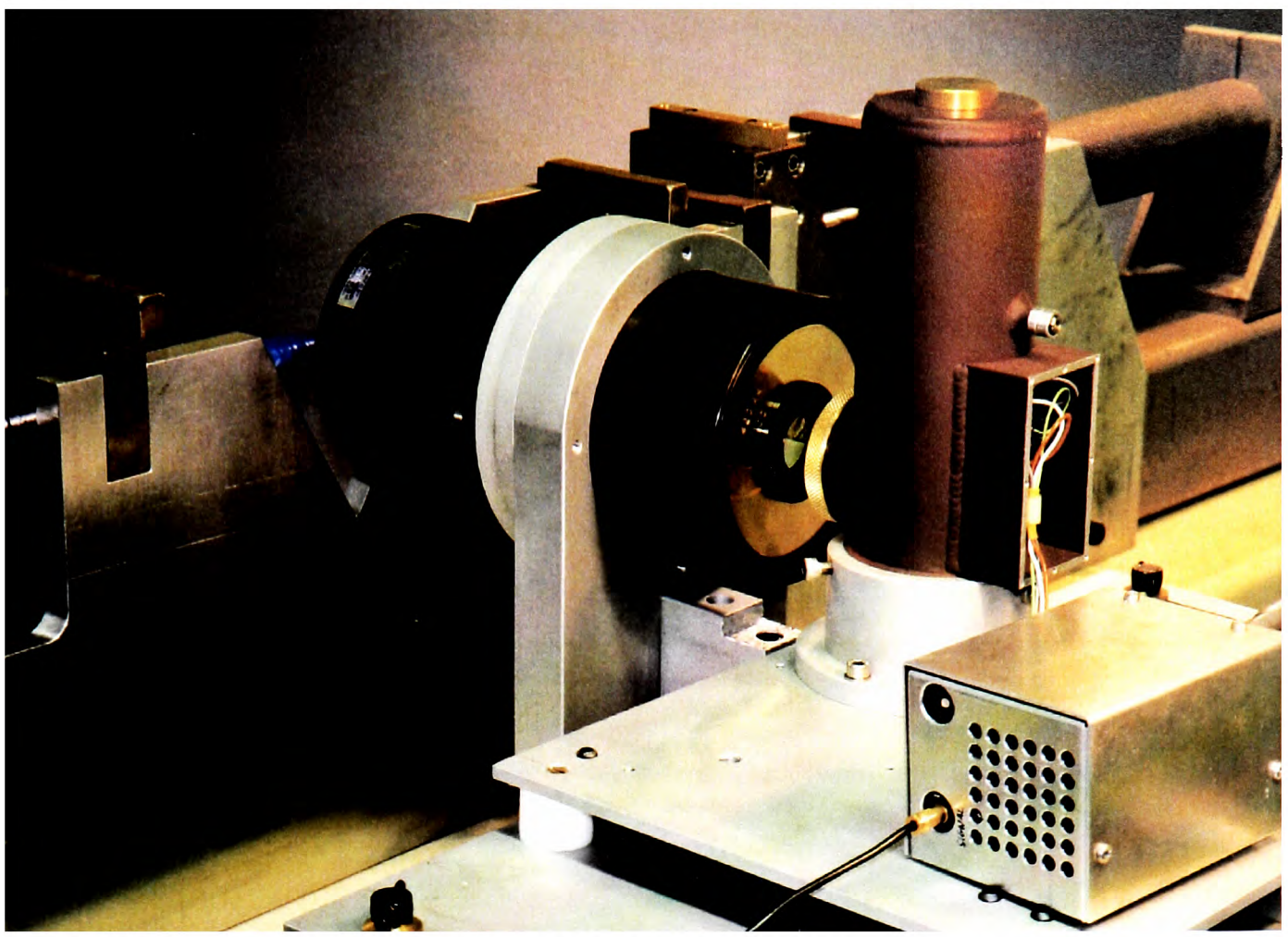

Figure 4.5b Radiometer in Position Prior to a Test

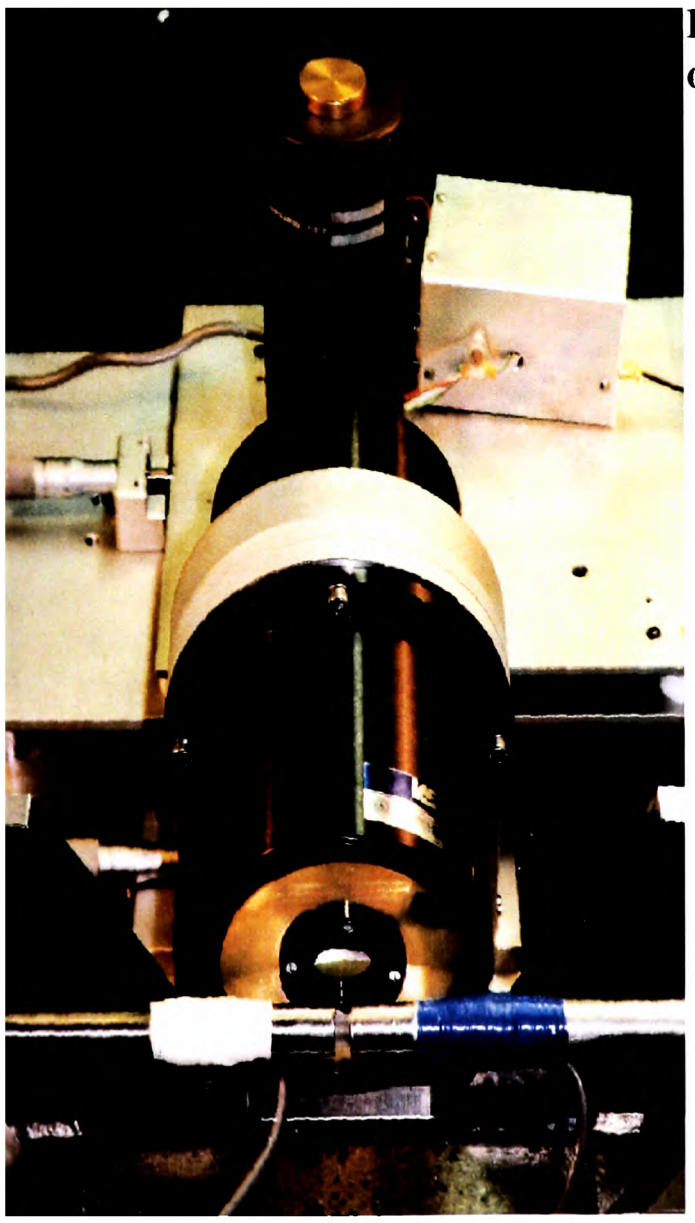

Figure 4.5c Front View of Radiometer Focussed on a Specimen Prior to a Test

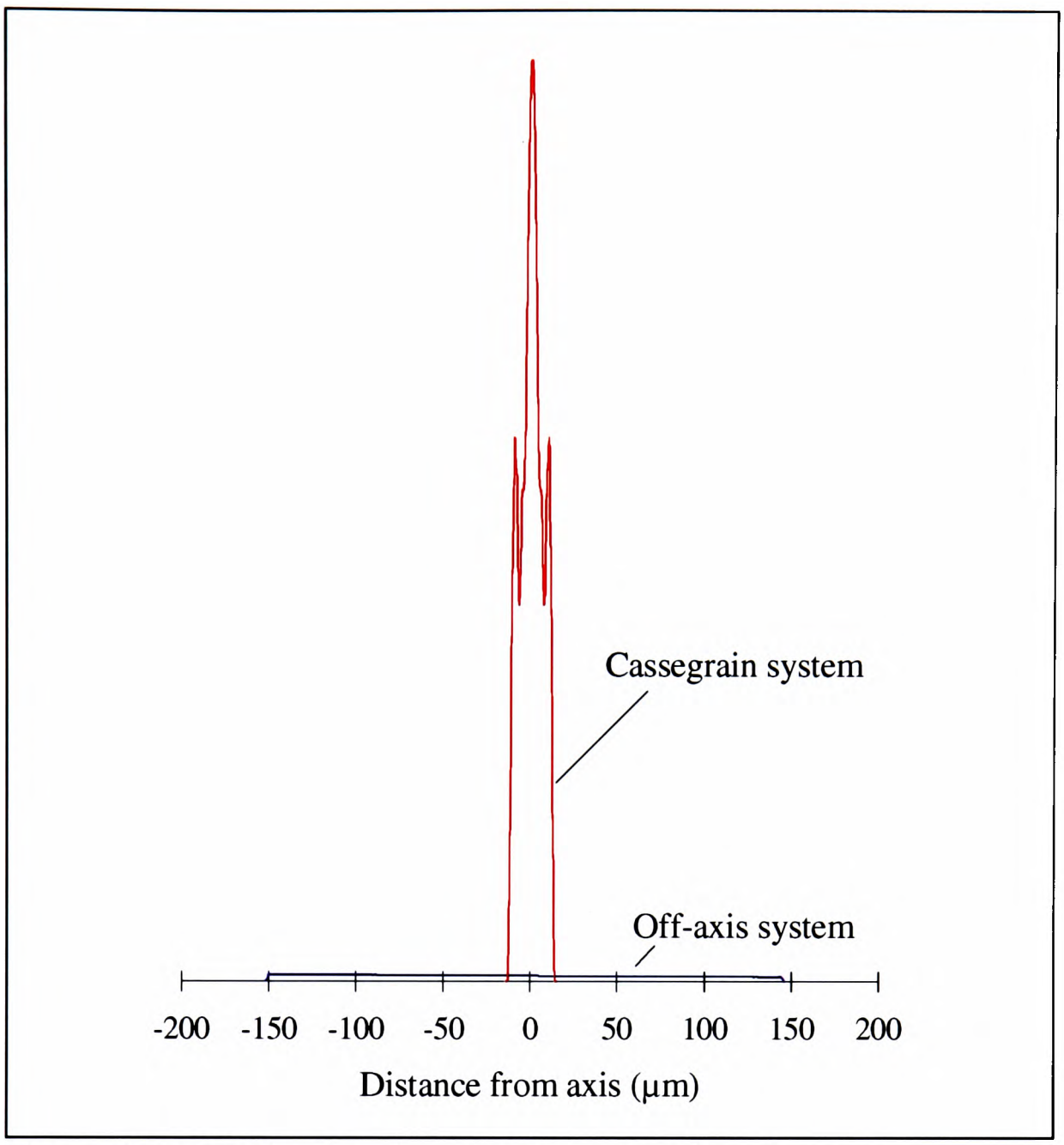

Figure 4.6 Relative Imaging of the Two Optical Systems

4.6 Experimental Method

In order to measure the surface temperature of a test specimen accurately it is important to focus the radiometer carefully on the area of interest on the specimen. It is also imperative that an accurate calibration is carried out.

4.6.1 Alignment

Coarse alignment of the optical system, with respect to the test specimen, was obtained using a fine metal pointer, temporarily mounted on the optics, representing the focal point of the imager. The optical system was then positioned so that the pointer was just touching the

specimen surface, at the area which is to be observed.

Improved alignment was achieved using a dummy test specimen positioned in precisely the same place as the real specimen. The dummy specimen had a hole (0.5mm diameter) drilled through the surface which was back-lit with a small light bulb, shown in Figure 4.6. A frame supporting a translucent screen was mounted on the back of the optical system, perpendicular to the axis, and in the focal plane of the optics. A small target dot was made on the screen at the position of the focal point. An image of the circular light source was created on the screen. By making fine adjustments to the position of the optical system, the image was brought into focus on the target.

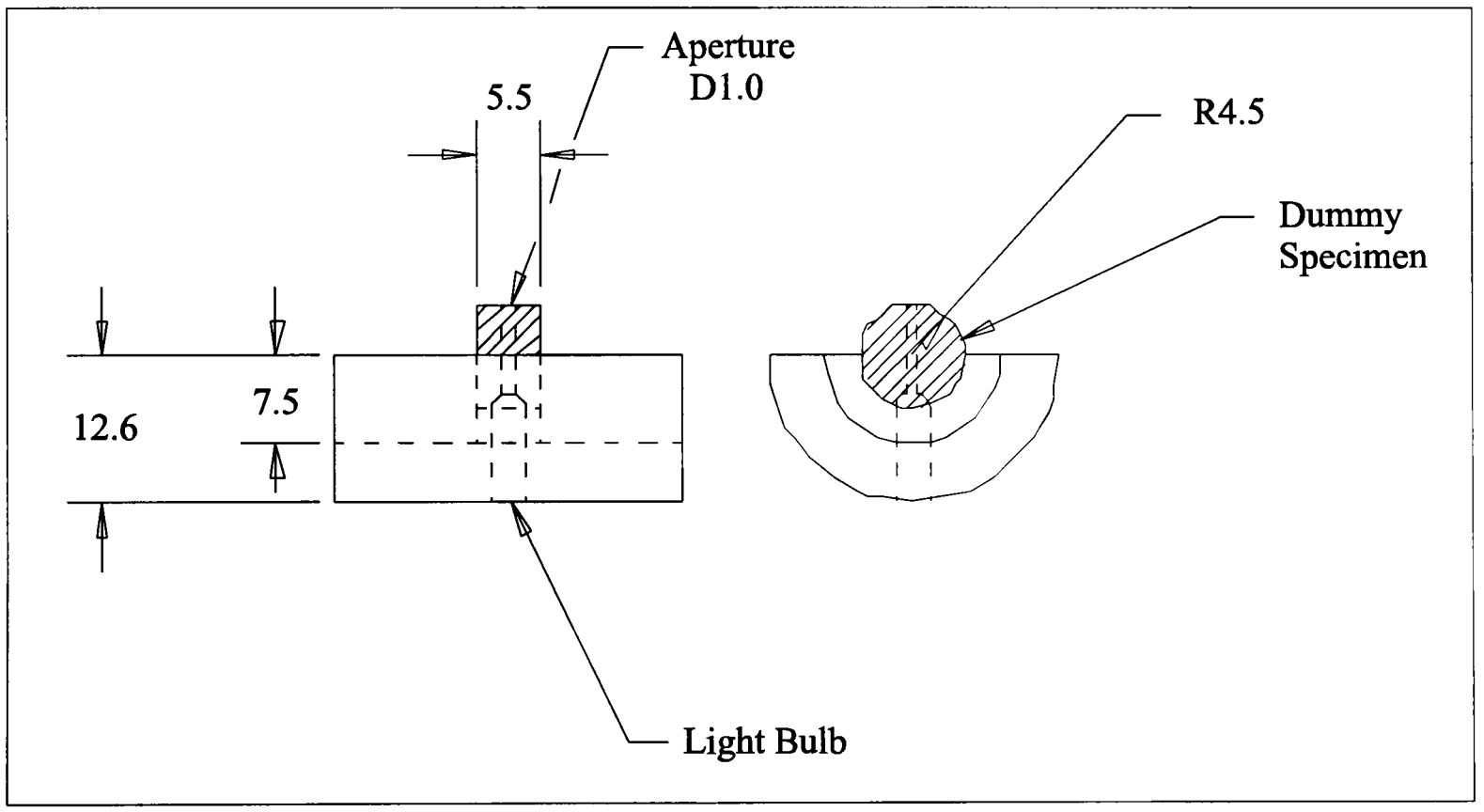

Figure 4.6 Secondary Alignment Using a Dummy Specimen

The final stage of alignment was to position the detector in front of the optical system. A specimen is heated in situ, as in calibration (see Section 4.6.2) and its temperature maintained at a constant value. Fine adjustment to the position of the radiometer and detector with respect to each other was carried out in the lateral and transverse directions to maximise the radiometer output signal. Vertical movement was not necessary since a custom made

location for the detector was used, thus making its height fixed.

Previous work carried by Craig, 1994, used an electrically heated black body source as a means of calibration. This posed a number of uncertainties. Firstly, the system was of a relatively crude design where the positioning of the heated black body source was essentially random and the position of the source in relation to the specimen position was inaccurate. Secondly, the emissivity of the specimen would not be the same as that for the black body source, even after sooting, so in effect the calibration was invalid.

4.6.2 Calibration Methods

By calibrating with a specimen in situ, one eliminates positional errors. The principal aim of the calibration is to heat a specimen whilst it is located in its test position and then to measure the radiated energy, by means of the radiometer, at various temperatures. Two distinctly different methods of calibration were employed. The first method used a copper block arrangement and a subsequent modification to it. Secondly, a hot air gun was used to heat the specimen. These methods are described below.

4.6.2.1 Copper Block #1

An implement was designed which would encapsulate a specimen in its test position (on the SHPB loading bars) and heat it to a particular temperature and maintain it. This was made from copper for its good heat transfer properties. Figure 4.7a shows a simple drawing of the copper block and Figure 4.7b shows a photograph of the copper heat source clamped onto the SHPB bars.

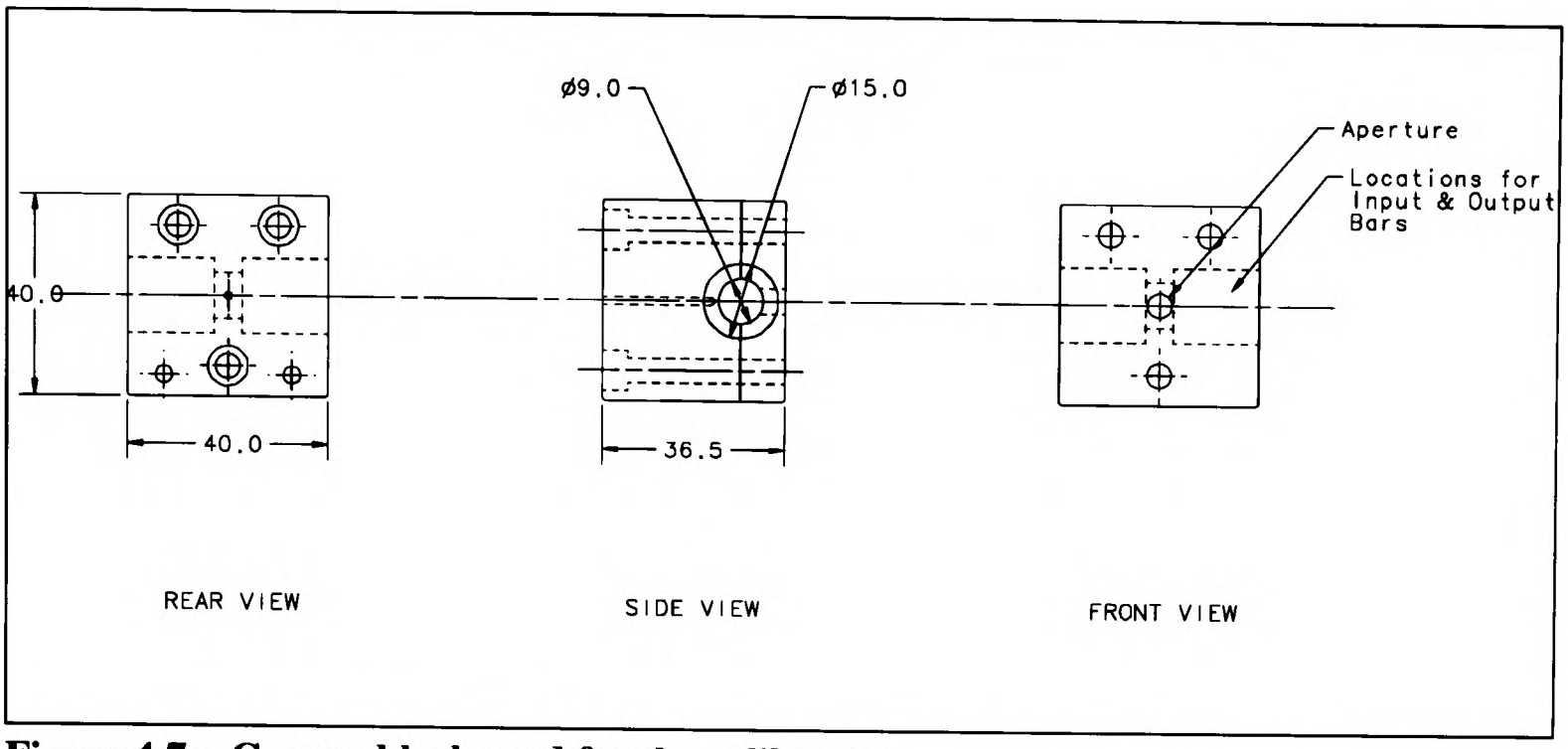

Figure 4.7a Copper block used for the calibration

The block and specimen were heated to a specific temperature by two 16W Watlow heater elements powered by a conventional d.c. bench power supply. The temperature of the block was monitored by a thermocouple, with an estimated accuracy of ±0.5°C, positioned

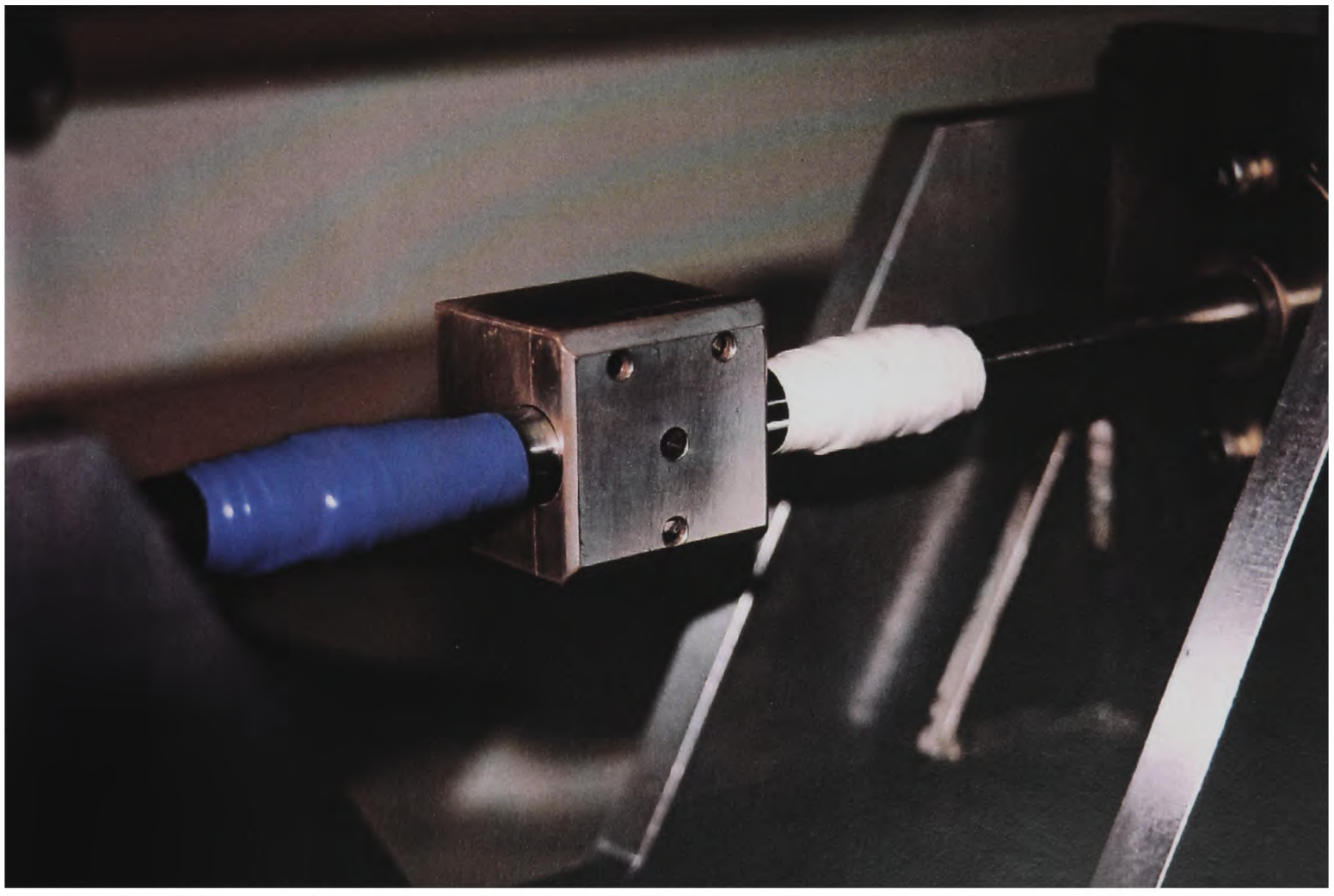

Figure 4.7b Copper block clamped onto SHPB bars

approximately 0.5mm from the back surface of the specimen. An aperture at the front of the copper block allowed the detector, by way of the imager, to be focussed onto the specimen. The front surface was coated with aluminium approximately 10μm thick with a 'sputterer', ensuring the radiation emitted from the surface facing the radiometer would be as small as possible. A rear view of the copper block is shown in Figure 4.7c, showing the heaters and thermocouple in place.

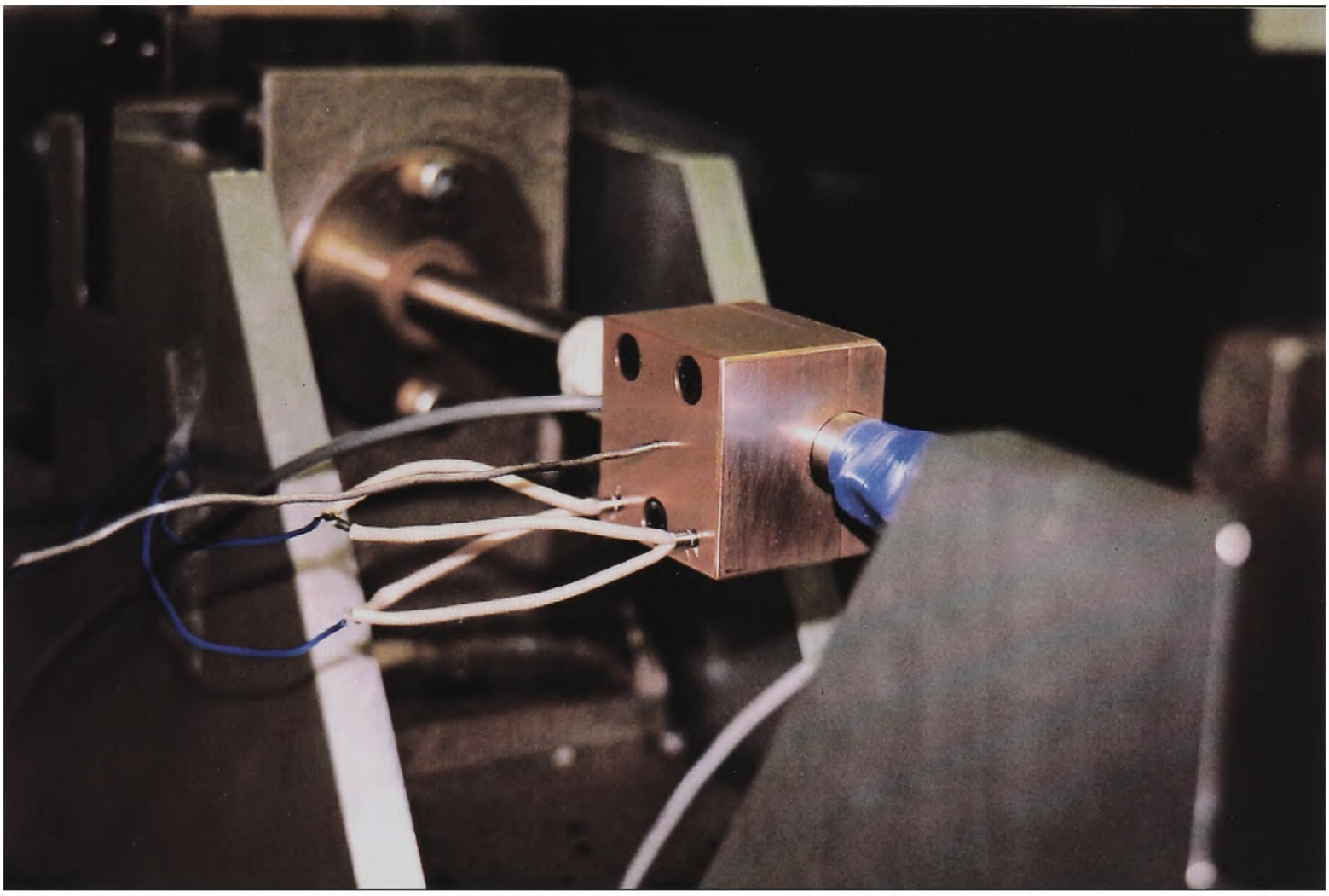

Figure 4.7c Rear View of Copper Block Showing Heaters and Thermocouple in Place

The specimen used in the calibration was a test specimen, and being made of epoxy resin, has relatively poor heat conduction properties. Thus it was necessary to ensure that the temperature of the block and the specimen (for both calibration methods) had reached equilibrium before any readings could take place. An equilibrium temperature was held until two minutes had elapsed before a reading was taken.

4.6.2.2 Copper Block #2

A modification was made to the copper block heat source which has been described in Section 4.6.2.1. It was considered that the aperture of Copper Block #1 was small in relation to the depth of the hole. In practice, the nearest one can get to black body radiation (which itself is an imaginary concept) is to produce a small hole in the wall of an enclosure at uniform temperature. Whilst the aperture in Copper Block #1 was not quite so extreme, it would still tend to produce radiation of a different distribution than what the specimen is really emitting. Therefore, version #2, seen in Figure 4.7d, was made with 0.5mm of copper between the specimen surface and the front face (Version #1 was 5mm thick).

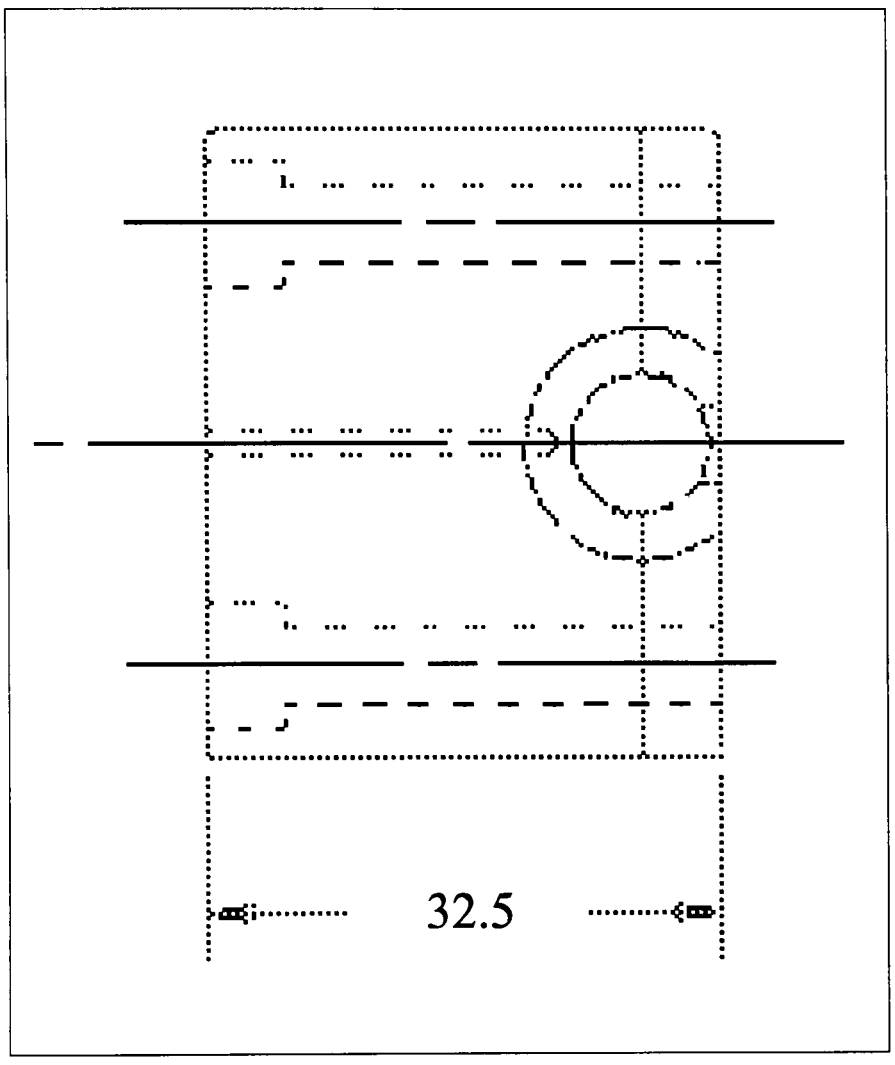

Figure 4.7d Copper Block #2

4.6.2.3 Free Air Calibration

An alternative method was used for calibration, called 'free air calibration'. The specimen was heated *in situ* using a hot air gun, then allowed to cool slowly. A thermocouple was placed in contact with the specimen to record the temperature, then measurements of the detector output were made every 5°C. The radiation was chopped using a d.c. motor and chopping disc to create an a.c. signal which the optics can 'see'.

The calibration was conducted with the specimen axially displaced with respect to the

imager and detector, i.e. aligned off-centre towards the 'output bar end' of the specimen. This is not detrimental to the calibration process, but ensures that more information is gathered during the compression of the specimen in a test than if it were aligned dead centre (since, as the specimen is compressed, both the input and output bars move; the input bar moving at a greater velocity than the output bar). An experimental calibration carried out before the test gave an accurate function between radiometer output and specimen temperature. However, this assumes that the specimen's surface characteristics remain constant during the test. For certain testing techniques the surface condition and geometry of the specimen can change during the test. For this reason it was often necessary to re-calibrate the specimen after the test. In instances where the specimen shattered, this was obviously not possible. So if complete failure had not occurred after the test had finished, a re-calibration would be performed. This was either used as validation of the original calibration, or if the change in calibration was considerable, the re-calibration could be used to modify the analysis and provide an assumed changing calibration function during the test.

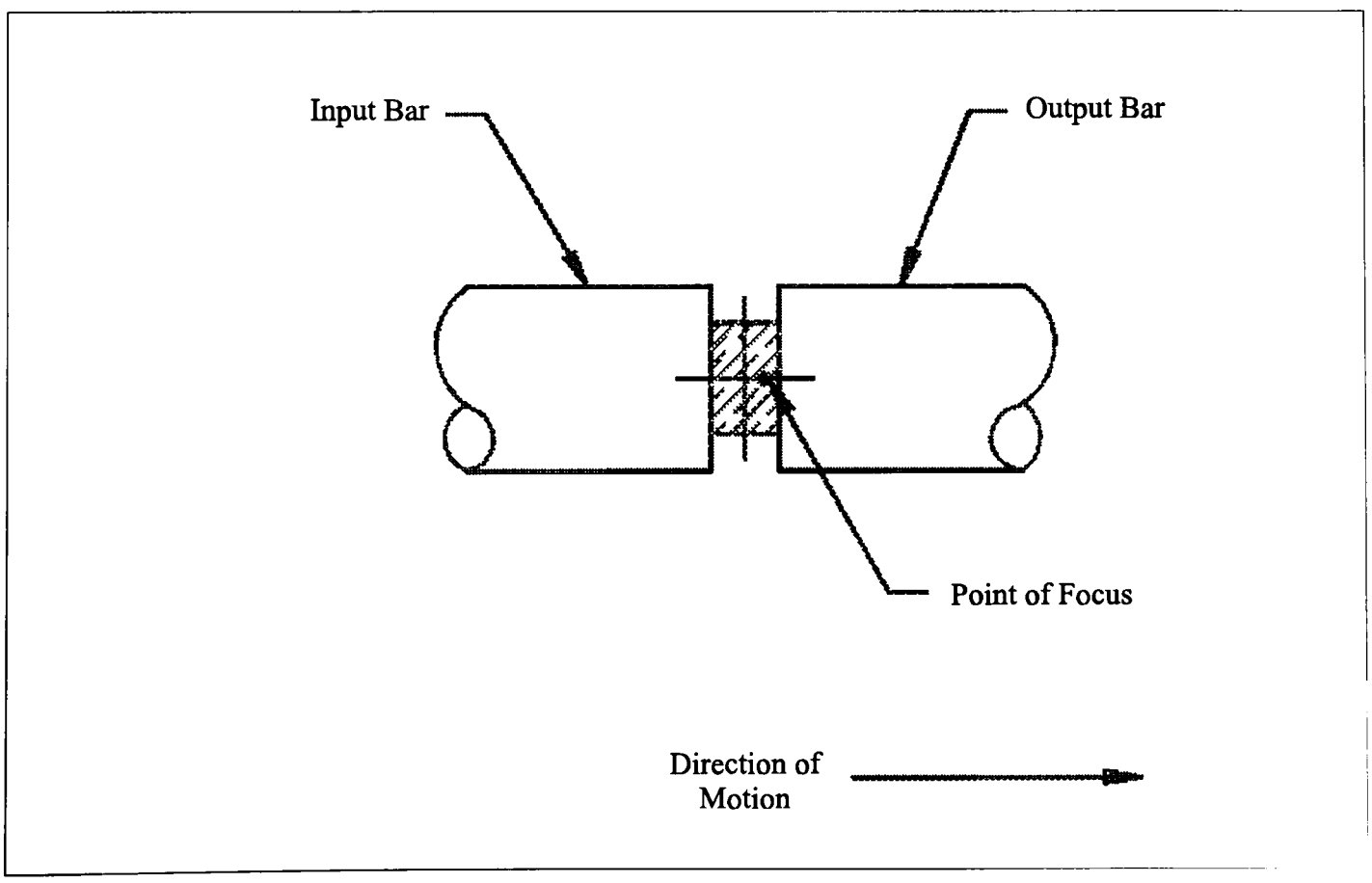

Figure 4.8 Alignment of Radiometer Off-Centre

4.6.3 Cooling Shield

A number of measures were taken to prevent any radiated energy from the copper block reaching the detector and giving an incorrect reading, so that only the specimen's radiation is 'viewed' by the detector. The front surface of the block was polished and coated with aluminium, ensuring that the emissivity was as low as possible. Another measure was to 'stop down' the imager's aperture, Figure.4.9, which again allowed only the required solid angle of energy to be 'seen' by the detector. This can reduce unwanted background radiation from 'hot' objects nearby which may be picked up by the detector. The shield was water cooled down to a temperature of approximately 10°C. Even though every material above absolute zero radiates infra-red energy, at this temperature it would appear invisible, since the detector is only capable of measuring within the range of 2μm-14μm. Separate calibrations were conducted with different surface finishes to the specimen. After casting, the polymer is transparent, but after machining the surface finish has a clouded/matt appearance due to roughening by the machine tool. The surface emissivity of the specimen was changed by applying soot, and for comparison a silver coated specimen was also used.

For each surface finish, the temperature of the block was increased from 20°C to 100°C in 5°C intervals. The signal amplitude from the detector at each temperature was measured and the process repeated three times and mean values were recorded. The surface conditions were 'as-machined', sooted and silvered.

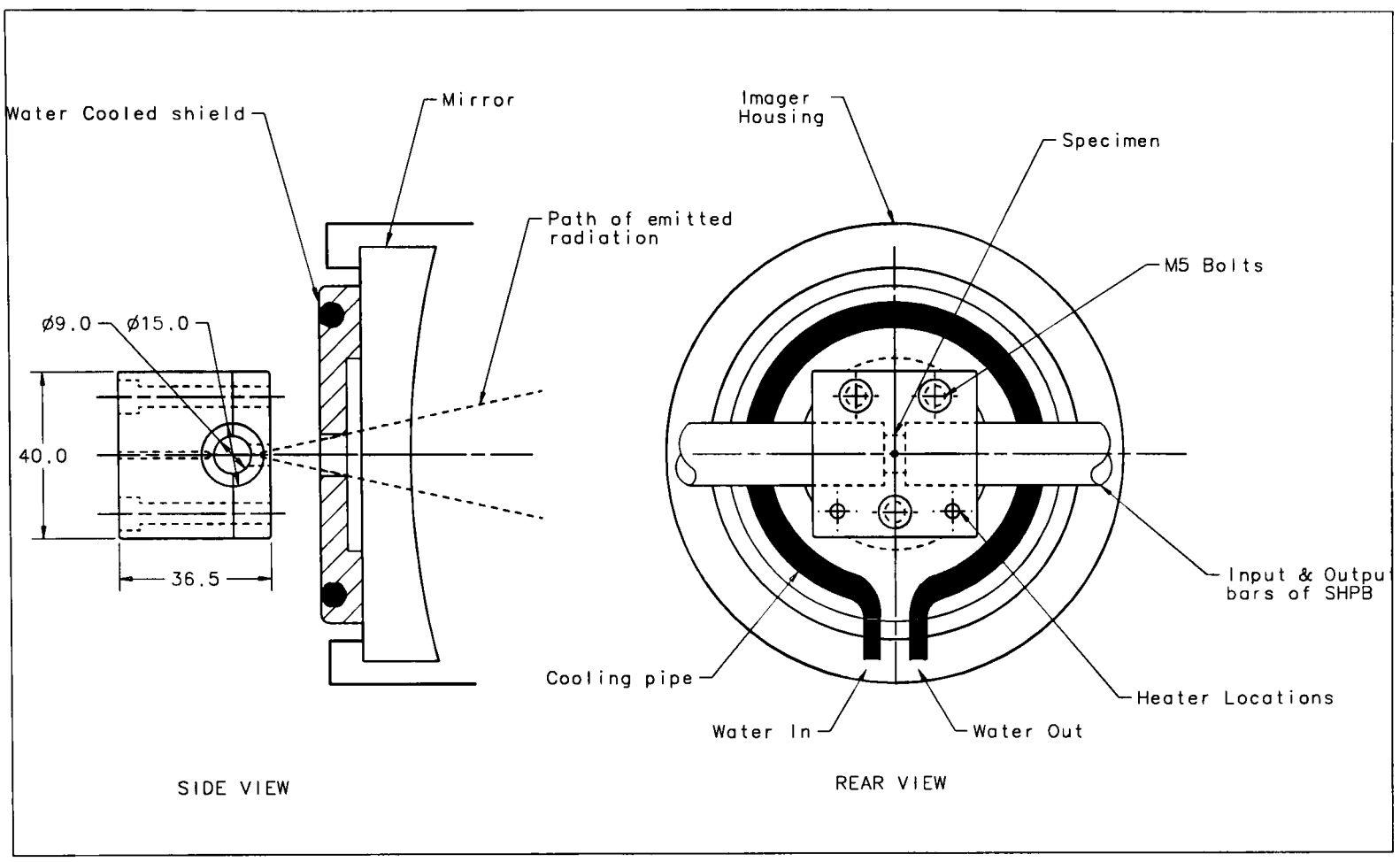

Figure 4.9 Cooling Shield Located on Imager

4.7 Analysis of Temperature Data

The surface temperature of polymeric test specimens was measured using a single element liquid nitrogen cooled infrared detector, as detailed earlier in this chapter. The apparatus used for loading the polymeric material was a split Hopkinson bar in compression, explained in Chapter 3. The specimen geometry used was a cylindrical billet of 9.0mm diameter and 5.5mm in length and with suitable lubrication, it is assumed that the visco-elastic and subsequent visco-plastic deformation is uniform. There is unlikely to be any localisation, so a uniform temperature distribution across the surface of the specimen can be assumed. Shear bands could be present, but the size of the detector makes these impossible to detect. Shear bands are of the size of 10μm and even though the localised temperature may be very high, the average temperature over a square millimetre would be much lower.

The data recorded throughout an experiment was as follows: i) strain gauge data from three strain gauge stations G_I, G_{II} and G_{III}, ii) radiometer output and iii) calibration of the

specimen surface prior to the test being carried out. The stress wave passing G_I triggers the transient recorders which begin recording. The radiometer output however must be synchronised to the point in time when the specimen starts being loaded. Thus the start of the record must be shifted by the length of time it takes for the stress wave to propagate from G_I to the specimen/bar interface. The distance being 320mm, and the loading bar wave speed being 4830m.s^{-1}, giving a delay of 66.2μs. Typical time synchronised traces of G_I, G_{II} and radiometer output signals are shown in Figure 4.10.

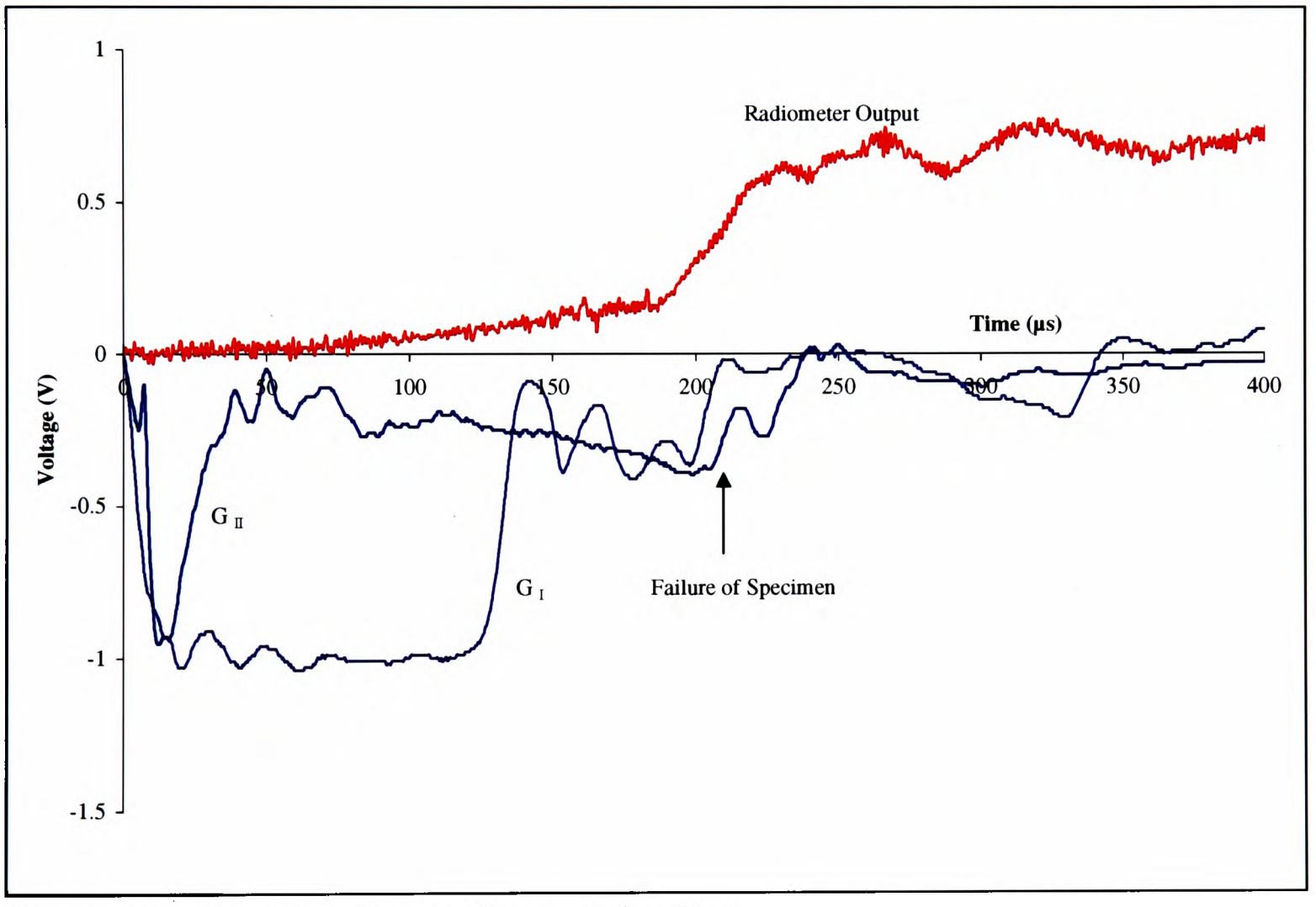

Figure 4.10 Raw Data from a Compression Test

Conversion of the radiometer output voltage into temperature data is done using the calibration carried out before the test, detailed in the previous sections. The calibrations showed an increasing radiometer output voltage with increasing temperature. To facilitate post-test analysis a cubic polynomial of best fit was obtained from the calibration data which

produced a relationship between specimen temperature and radiometer output

$$T = A.V^3 + B.V^2 + C.V + D \qquad \textbf{(4.5)}$$

A typical calibration is shown in Figure 4.11. The emissivity of the specimen surface has been maximised by using a layer of soot. A comparison of sooted and silvered surfaces was done, and as expected, the changes in surface emissivity are clear to see and are shown in Figure 4.12.

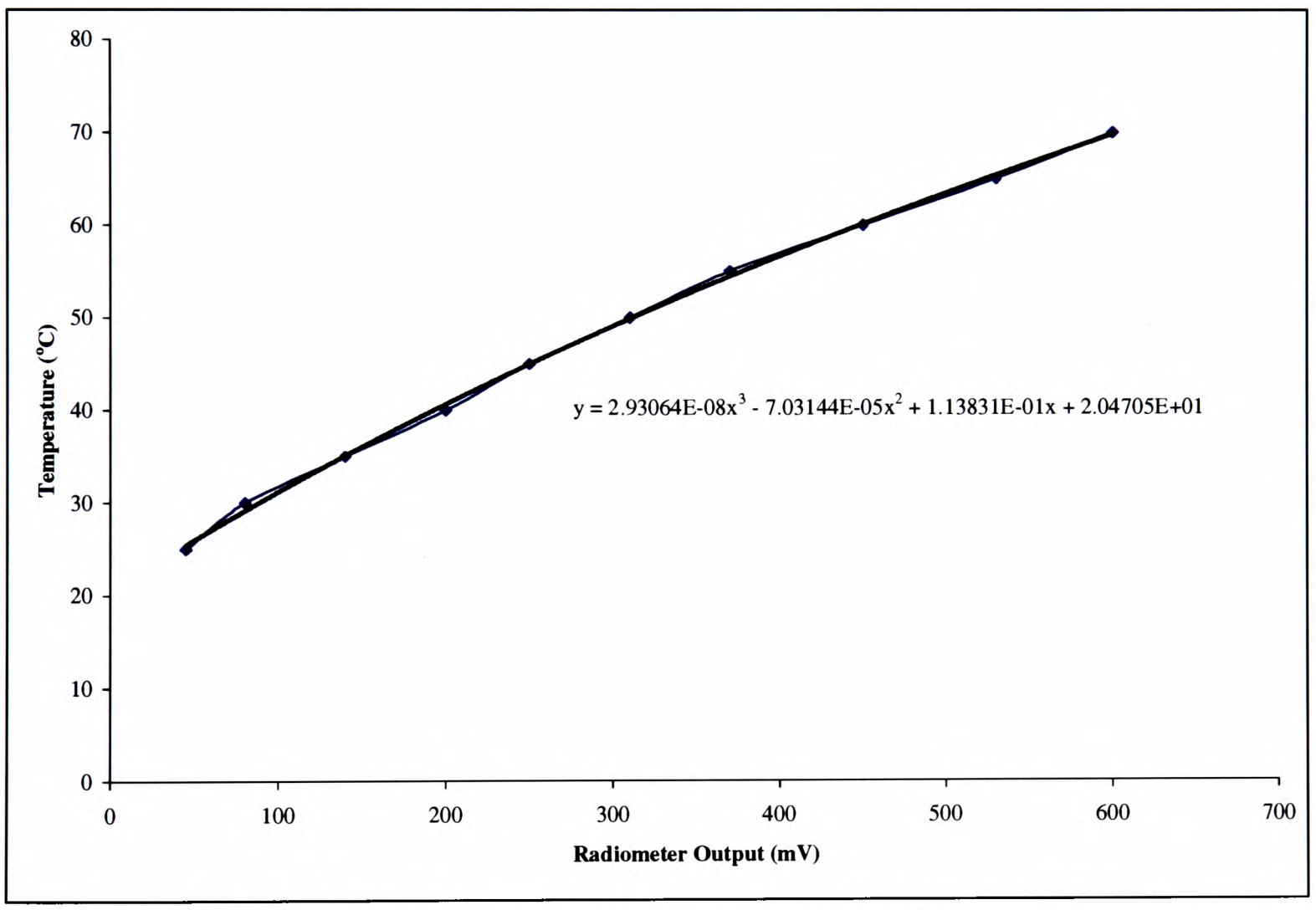

Figure 4.11 A Typical Calibration Curve with Fitted Cubic Polynomial

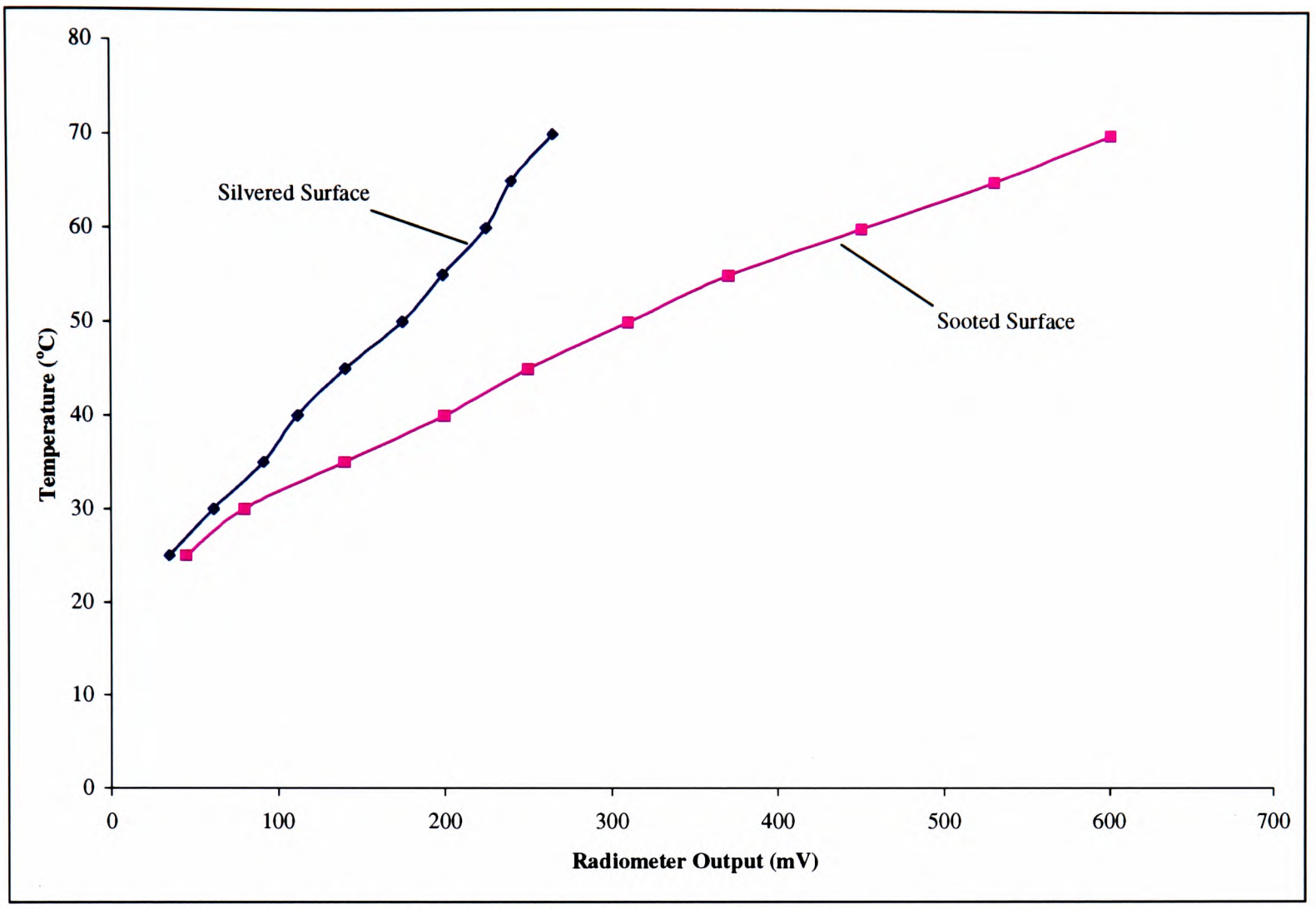

Figure 4.12 Comparison of Silvered and Sooted Specimen Calibrations

4.8 Errors

There are a number of uncertainties and assumptions in the data obtained from the radiometer during a high rate impact test. Firstly, the effect of other radiative sources surrounding the specimen during calibration; 'hot' objects near the specimen whose thermal radiation could be reflected from the specimen, although, these have been minimised by using the 'cooling shield'.

Secondly, whilst the specimen is expanding during its deformation, the layer of soot on the surface can be distorted or altered in a way which will change the emissivity of the specimen. This will have the effect of making the specimen appear to be cooler than it really is.

During deformation, the specimen is expanding in a radial direction. The original point of focus is now below the surface of the specimen and so the detector is effectively out of focus

and not operating at optimum conditions.

To combat the first error, it is necessary to exclude as far as possible any external sources of radiation other than the specimen. The 'shield' used to 'stop down' the imager described in section 4.6.2.2 demonstrated that the effect of external sources of radiation was small. The imager was designed to be immune to off-axis interference and this was shown to be the case. The shield is water cooled to approximately 10°C which makes it invisible to the detector. Calibrations of specimen surface was done with and without the shield in place, and the effect was shown to be negligible, a maximum variation of 1.5%, see Figure 4.13. Therefore, the shield was used in all tests as it also served as a form of protection to the imager against the shattering specimen and flying petroleum jelly!

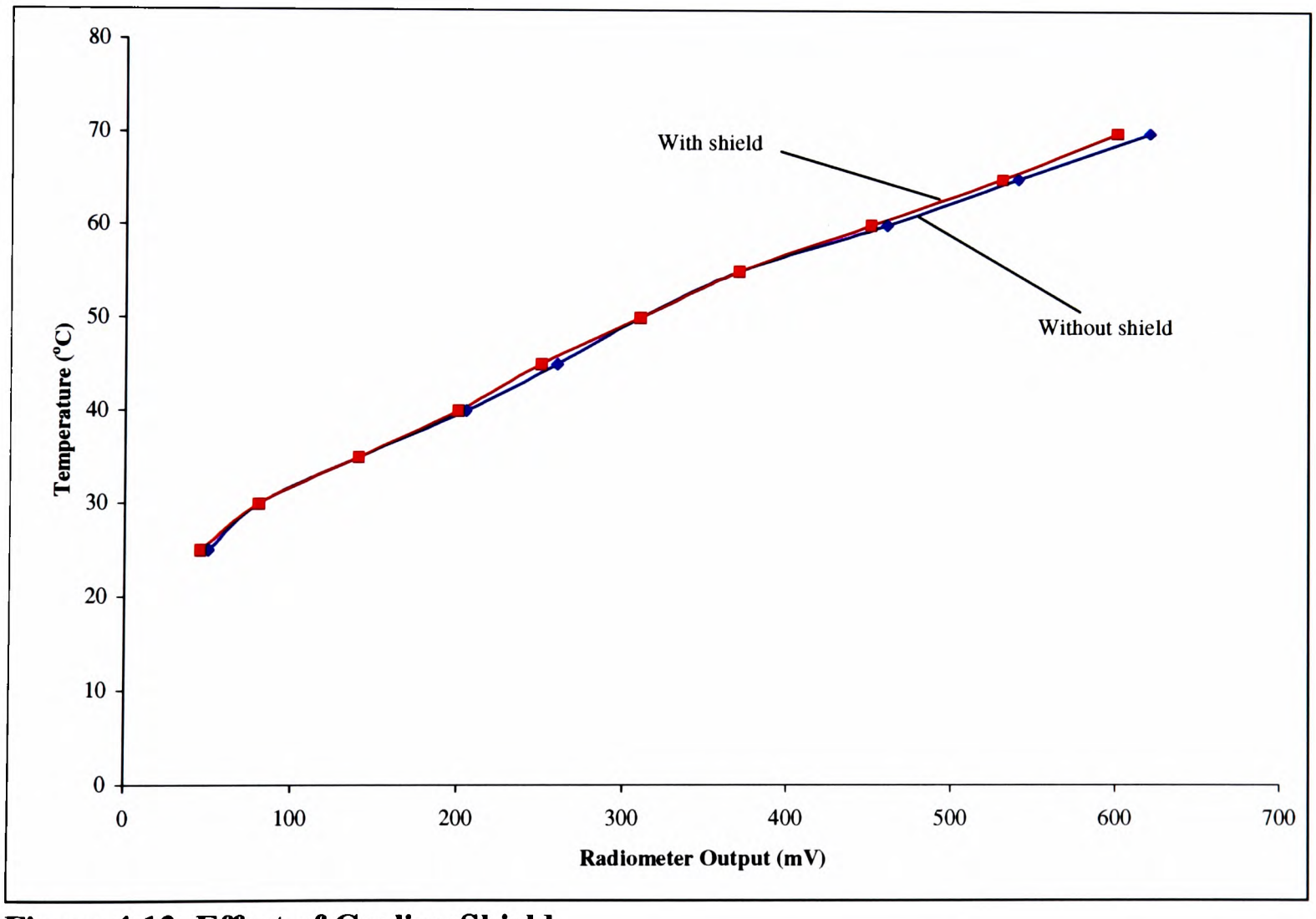

Figure 4.13 Effect of Cooling Shield

4.8.1 Correction for Changing Emissivity

Temperature data has been adjusted for the changing surface emissivity. The sooted surface showed a decrease in calibration, hence emissivity - varying between 12% and 17%. This is due to the changing diameter of the specimen which will cause a thinning or complete disintegration of the soot layer.

The temperature data obtained from tests has had an adjustment factor introduced, which takes into account the change in emissivity throughout a test. The first step was to perform a post-test calibration of a deformed specimen. A comparison between an initial calibration and a post-test calibration is shown in Figure 4.14. It shows that for an equilibrium temperature, the radiometer output is lower for the post-test calibration, which indicates the emissivity is lower. The difference between these two conditions is that the post-test specimen has experienced a strain of up to 70%. So, it is assumed that at a particular radiometer output, V_r, the temperature calculated using the fitted cubic polynomials from the pre-test calibration yields a value of T_{c1}. Using the post-test calibration polynomial yields a temperature of T_{c2}. The difference between these values is assumed to have occurred over 70% strain. Hence, this difference is divided by 70 and multiplied by the true strain at any point in a test. This is then added to the original pre-test calibration value for the particular temperature in order to obtain the emissivity adjusted temperature of the specimen surface. The equation used is shown in Equation 4.6.

$$T_t = T_{c1} + \left(\frac{T_{c1} - T_{c2}}{70} \right) . \varepsilon_{true} \qquad \textbf{(4.6)}$$

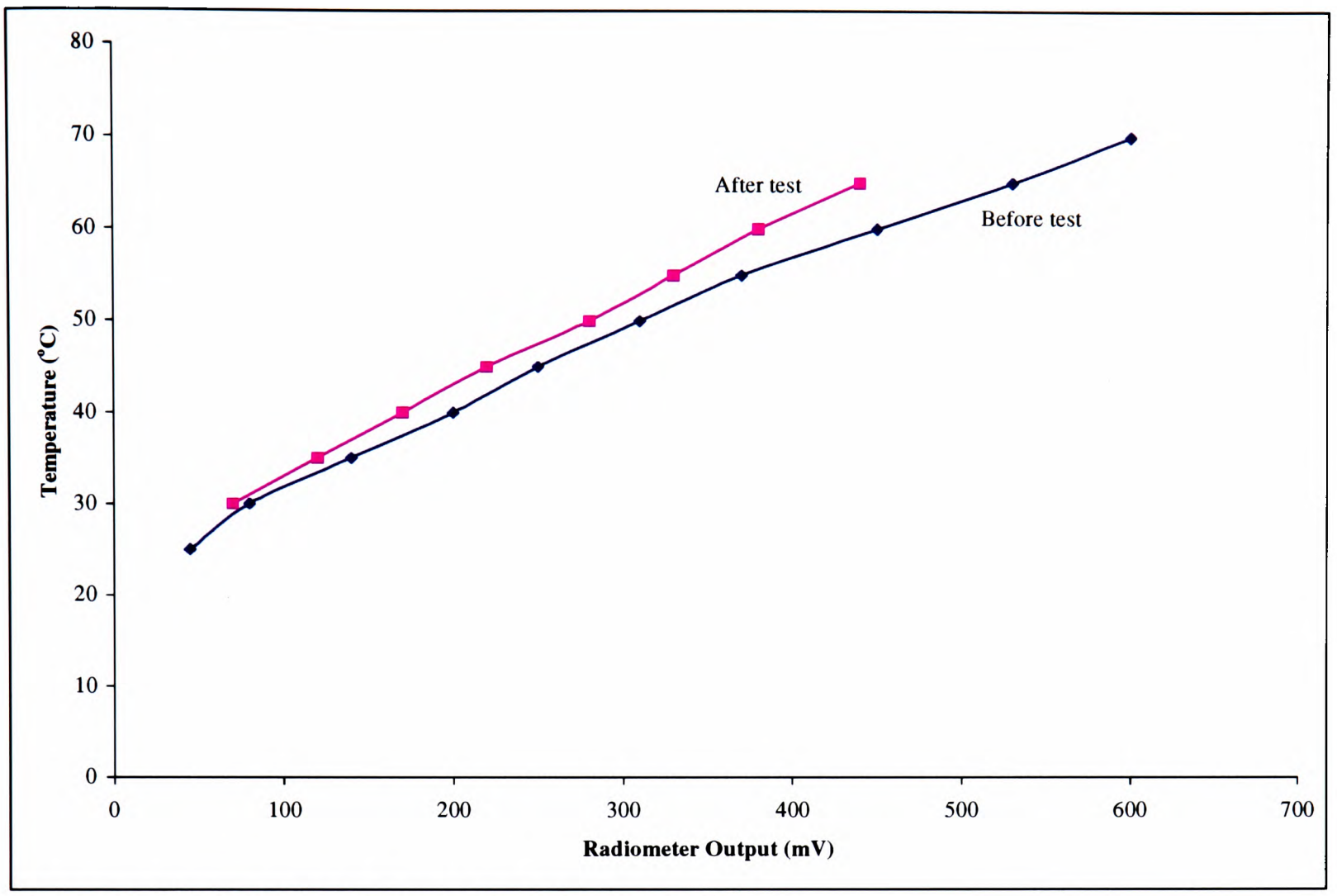

Figure 4.14 Initial and Post-Test Calibration Curves

4.9 References

Craig, S.J., Gaskell, D.R., Rockett, P. & Ruiz, C., An Experimental Technique for Measuring the Temperature Rise During Impact Testing, Journal de Physique III, 4, C8 pp.41-46, 1993.

Macdougall, D.A.S. & Harding, J., High Strain-Rate Behaviour of Ti-6Al-4V, Explomet '95, International Conference on Metallurgical Applications of Shock-Wave and HighStrain-Rate Phenomena, 1995.

Mason, J.J., Rosakis, A.J. & Ravichandran, G., On the Strain and Strain-Rate Dependance of the Fraction of Plastic Work Converted to Heat: An Experimental Study Using High Speed Infrared Detectors and the Kolsky Bar, Mech. Of Matls., 16, pp.135-145, 1994.

Trojanowski, A.S., Macdougall, D.A.S., Harding, J. & Ruiz, C., An Improved Technique for the Experimental Measurement of Surface Temperature During Hopkinson-bar Tests, Meas.Sci.Tech., 9, 1, pp.12-19, 1998.

Chapter 5

Experimental Results

5.1 Specimen Selection

Experimental work has been undertaken whose sequence followed a testing matrix shown below in Table 5.1. The ratio in specimen dimensions is $\sqrt{2}$ between each length and each diameter. Tests on these specimens were performed using a Split Hopkinson Pressure Bar and data from the gauges was recorded using a bank of Datalab DL912 Transient Recorders. A computer program, HOPBAR, was used to analyse the strain gauge data and a spreadsheet was used to create graphs of true stress vs true strain. From the literature, lubrication has been found to be important (Briscoe & Nosker, 1984), and for this reason, the tests in this programme were conducted both with and without lubricant for comparison. Previous workers have found petroleum jelly to be the best lubricant in high rate testing and so this type has been selected for use to reduce any end constraint. Each segment of the matrix was tested at two different strain-rates. This was achieved by varying the impact velocity of the projectile.

This series of tests is intended to form the basis for a fundamental understanding of the material behaviour under conditions of lubrication and varying strain-rate. To simplify the

identification of the tests, a coding system is employed which has a horizontal and vertical component plus a number. For example, AX5 denotes a specimen of length 8mm (A), diameter 12.7mm (X) and '5' means test number 5. The strain-rates quoted are average values, since it is not totally constant throughout the duration of the test. Table 5.1 gives the general specimen dimensions of the specimens. Specimens whose dimensions were such that their lengths approached or exceeded their diameters could be prone to buckling effects and so were ignored.

Table 5.1 Specimen Dimensions
√2 ratio (Aspect Ratio - L/D)

Diameter / Length		**X** - 12.7mm	Diameters (mm) **Y** - 9mm	**Z** - 6.4mm
8	**A**	✓ (0.63)	✓ (0.89)	———
5.5	**B**	✓ (0.43)	✓ (0.61)	———
4	**C**	✓ (0.31)	✓ (0.44)	✓ (0.63)
2.8	**D**	✓ (0.22)	✓ (0.31)	✓ (0.44)

5.1.1 Material Used in Testing Programme

The polymeric material used in this project contains two components for the resin (LY-564) and one component for the hardener (HY-2954). The chemical structures of all the components are shown overleaf, which also shows the reaction that occurs between the active groups during polymerisation. The final diagram is of the chain arrangement that will arise by the materials undergoing polymerisation, although this is only a fragment of a much larger molecule. In theory a reaction of this type mixed exactly stoichimetrically so that there are two epoxy groups for every primary amine would go to completion as the hardened resin would become a single macro molecule. In practice, this linking stops well short of the single molecule due to the inability of active groups to come into contact.

5.2 General Experimental Programme

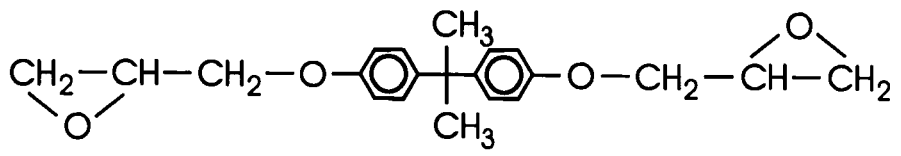

Bis-A epoxy resin

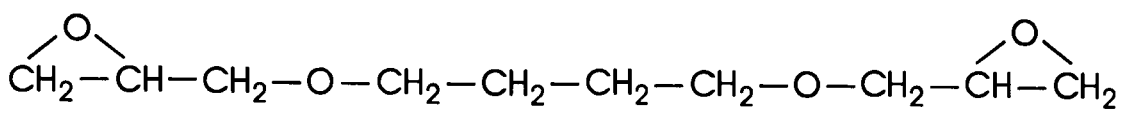

1,4 Butanediol diglycidyl ether

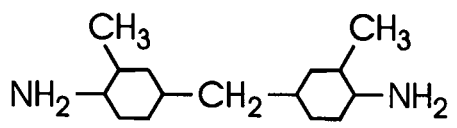

2,2' Dimethyl-4,4' methylene bis(cyclohexylamine)

The reaction that occurs between two epoxy groups and a primary amine group is:

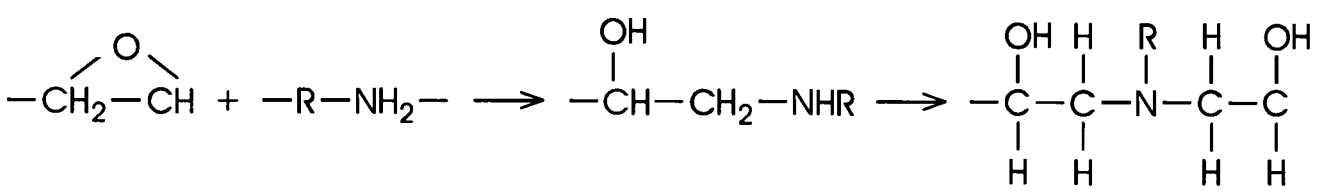

Reaction between 2 epoxy groups and a 1' amine

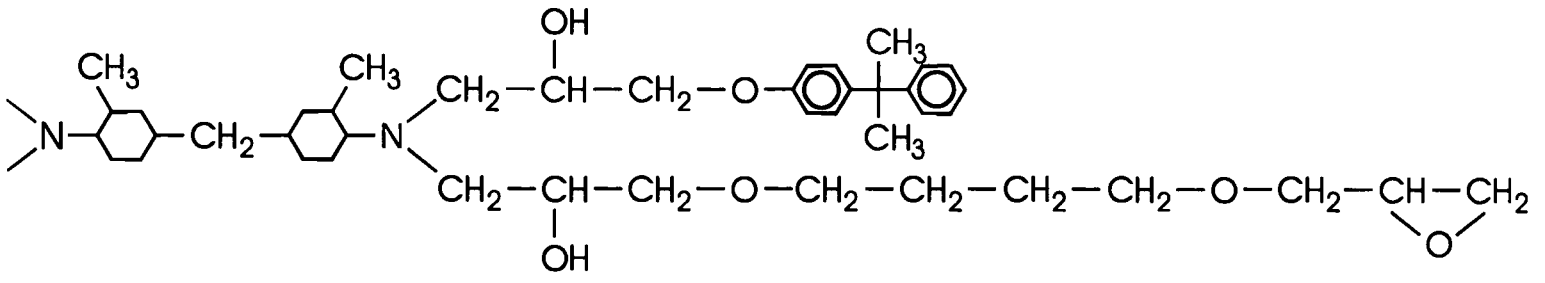

This eventually leads to a polymer structure as shown

A total of 68 preliminary tests were conducted to provide the information relating the effect of specimen dimension and of lubrication. These are listed in Table 5.2. In this table, 'E' denotes elastic deformation, ie. complete recovery of the specimen to its original dimensions and resulting in no permanent strain; 'L' indicates a lubricated test and 'S' indicates that the specimen shattered. A blank section means that the specimen deformed to give a permanent deformation, but did not shatter and was not lubricated.

Table 5.2 Preliminary Tests

Test #	Impact Velocity ($m.s^{-1}$)	Av.Strain-Rate (s^{-1})	Comments
AX1	18.17	2000	
AX2	18.28	1500	
AX3	9.94	600	E
AX4	12.58	1000	E
AX5	14.81	1200	
AX6	14.67	1200	
AX7	18.24	2000	L
AX8	18.13	1750	L
BX1	14.67	1500	
BX2	14.65	1500	
BX3	18.24	2250	
BX4	18.25	2250	
BX5	14.72	1750	L
BX6	18.27	2250	L
CX1	14.54	2000	
CX2	14.62	2000	
CX3	14.57	2000	L
CX4	19.71	3000	
DX1	12.50	2000	
DX2	12.52	2000	
DX3	12.47	2000	L
DX4	12.48	2000	L
DX5	18.13	3500	S
DX6	18.16	3500	S

DX7	18.06	3750	L,S
DX8	18.00	4000	L,S
AY1	12.35	1400	
AY2	12.21	1300	
AY3	12.49	1400	L
AY4	18.09	2000	S
AY6	18.10	2000	L,S
BY1	14.68	2250	
BY2	14.71	2250	
BY3	9.94	1500	
BY4	9.96	1400	
BY5	14.67	2500	L
BY6	9.94	1500	L
BY7	9.81	1500	L
CY1	12.62	2500	S
CY2	12.62	2500	S
CY3	12.58	2500	L
CY4	18.27	4000	S
DY4	14.65	4000	S
DY5	14.62	4000	S
DY6	14.67	4000	L,S
DY7	14.52	4000	L,S
CZ1	14.77	3500	S
CZ2	14.73	3500	S
CZ5	18.28	4500	S
CZ6	12.55	3000	S
CZ7	12.54	3000	S

CZ8	12.53	3000	L,S
DZ1	12.53	3750	S
DZ2	12.57	3750	S
DZ3	12.51	3750	L,S
DZ4	14.73	4750	S
DZ5	14.75	4750	S
DZ6	14.74	4750	L,S
DZ7	14.61	4750	L,S
DZ8	14.50	5000	L,S
DZ9	14.46	4750	L,S

E=Elastic, L=Lubricated, S=Shattered

After the preliminary tests, all further tests used specimens type BY (diameter 9mm and length 5.5mm) since it gave the most consistent results. The following tests were conducted:-

- Quasistatic tests (3)
- Intermediate strain-rate tests (3)
- High strain-rate tests with temperature measurement (24)
- Interrupted tests (15)

These tests are described in following sections.

5.3 Preliminary Tests

These tests were conducted at strain-rates between $600s^{-1}$ and $5000s^{-1}$. Their purpose was:

- to examine the reproducibility of the experimental data.
- to study the effect of lubrication.
- to select specimen dimensions as a standard.
- to find stress-strain curves at the appropriate strain-rates.

5.3.1 Reproducibility of Experimental Data

In Figures 5.1 to 5.9 we see a good illustration of reproducibility of results. There are only a few cases where there is any difference between the stress-strain curves, usually at the point of unloading. This difference was approximately 5%. The maximum difference in stress is also 5%.

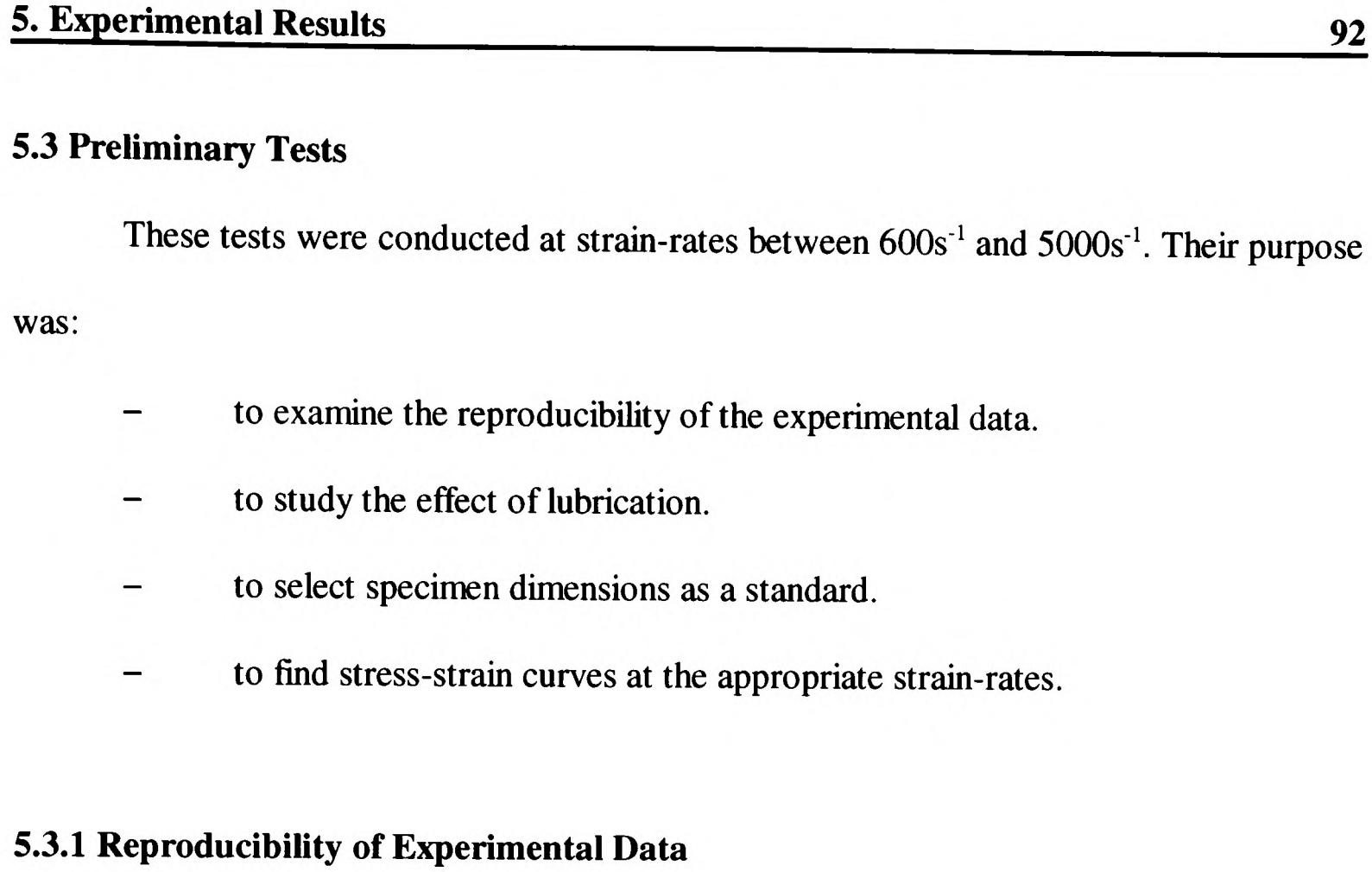

Figure 5.1 Comparing Nominally Identical Tests - AX5,6 Strain-Rate ≈1250s^{-1}

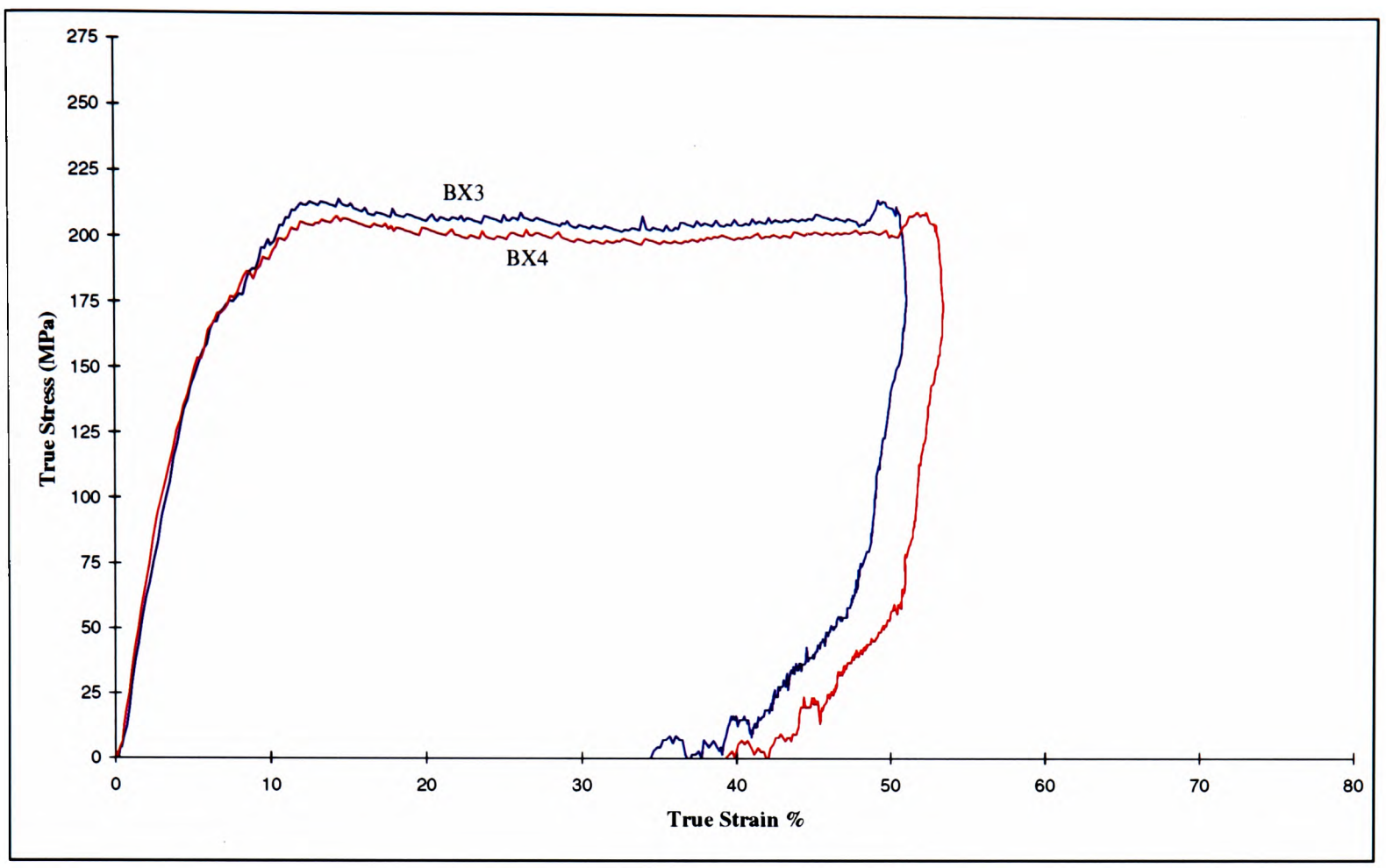

Figure 5.2 Comparing Nominally Identical Tests - BX3,4 Strain-Rate ≈2250s^{-1}

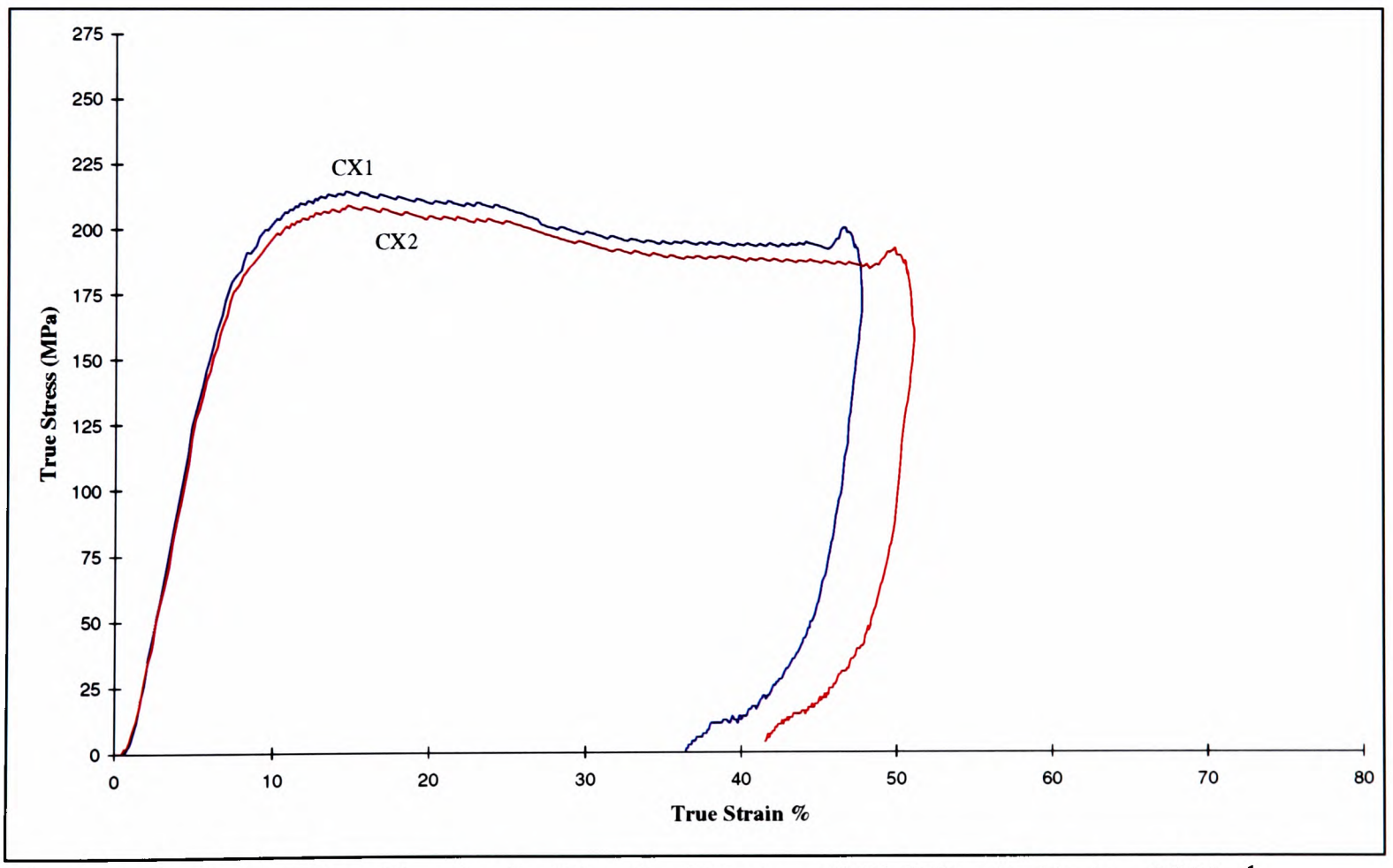

Figure 5.3 Comparing Nominally Identical Tests - CX1,2 Strain-Rate ≈2000s^{-1}

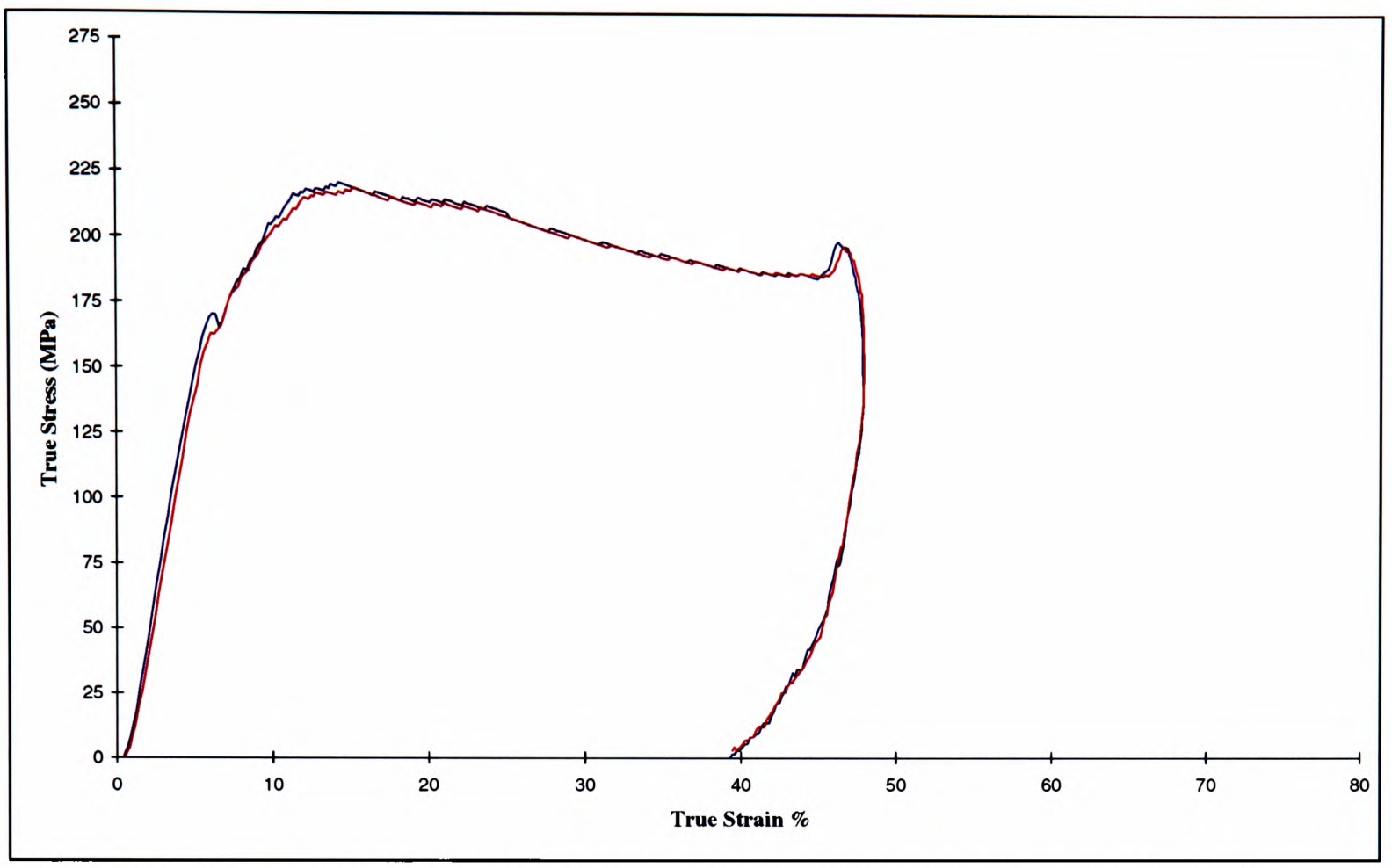

Figure 5.4 Comparing Nominally Identical Tests - DX1,2 Strain-Rate ≈2000s^{-1}

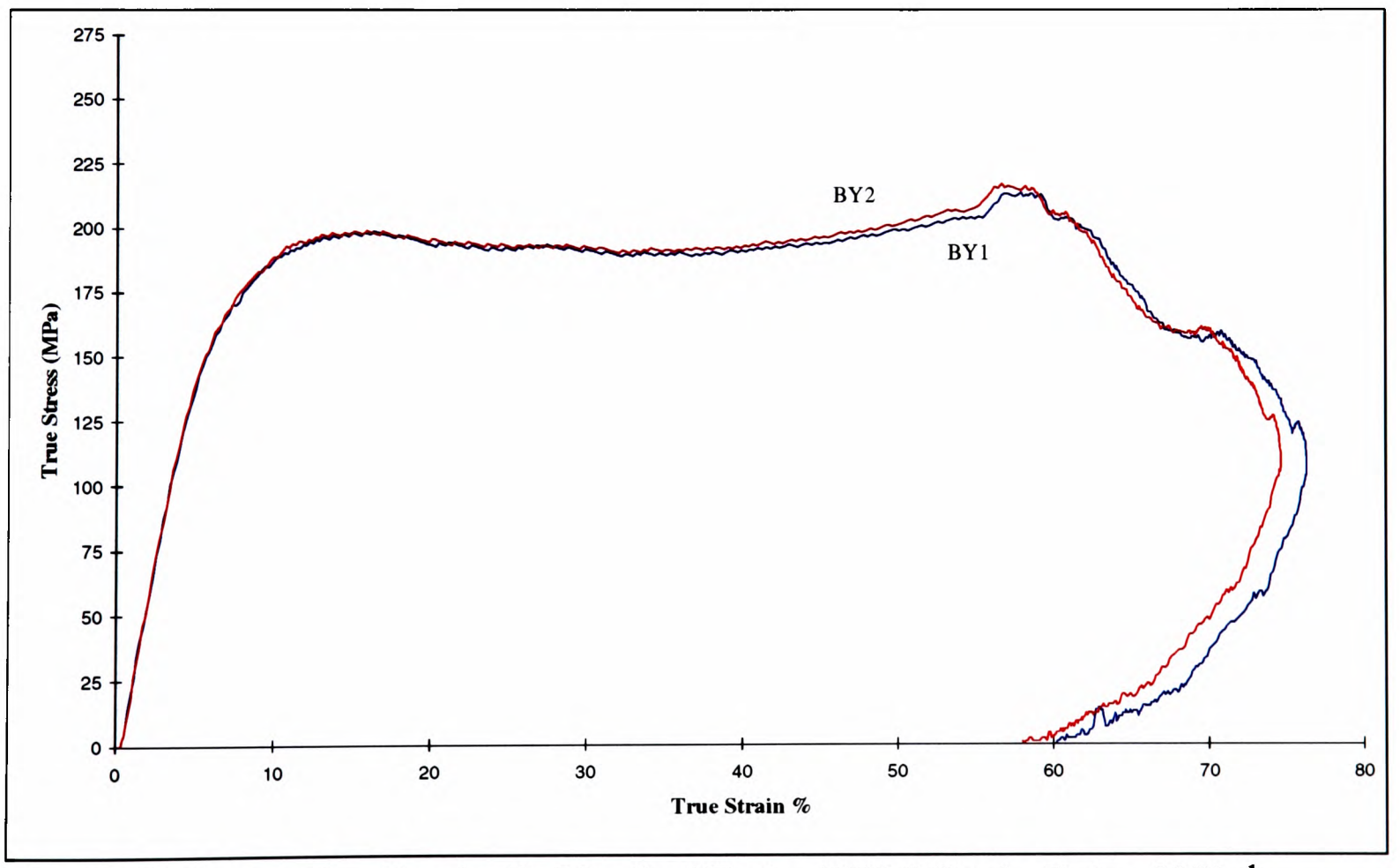

Figure 5.5 Comparing Nominally Identical Tests - BY1,2 Strain-Rate ≈2250s^{-1}

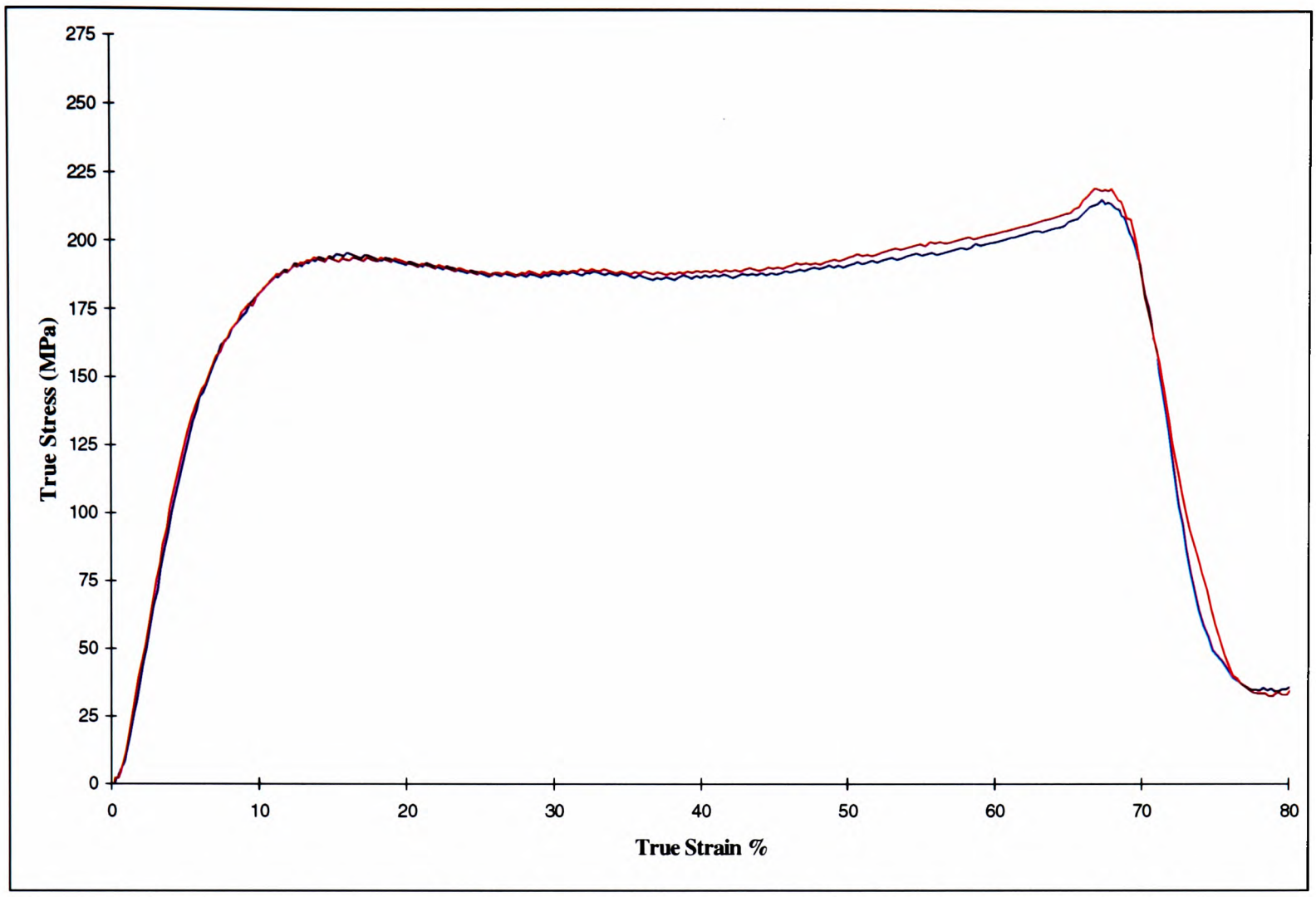

Figure 5.6 Comparing Nominally Identical Tests - CY1,2 Strain-Rate ≈2500s^{-1}

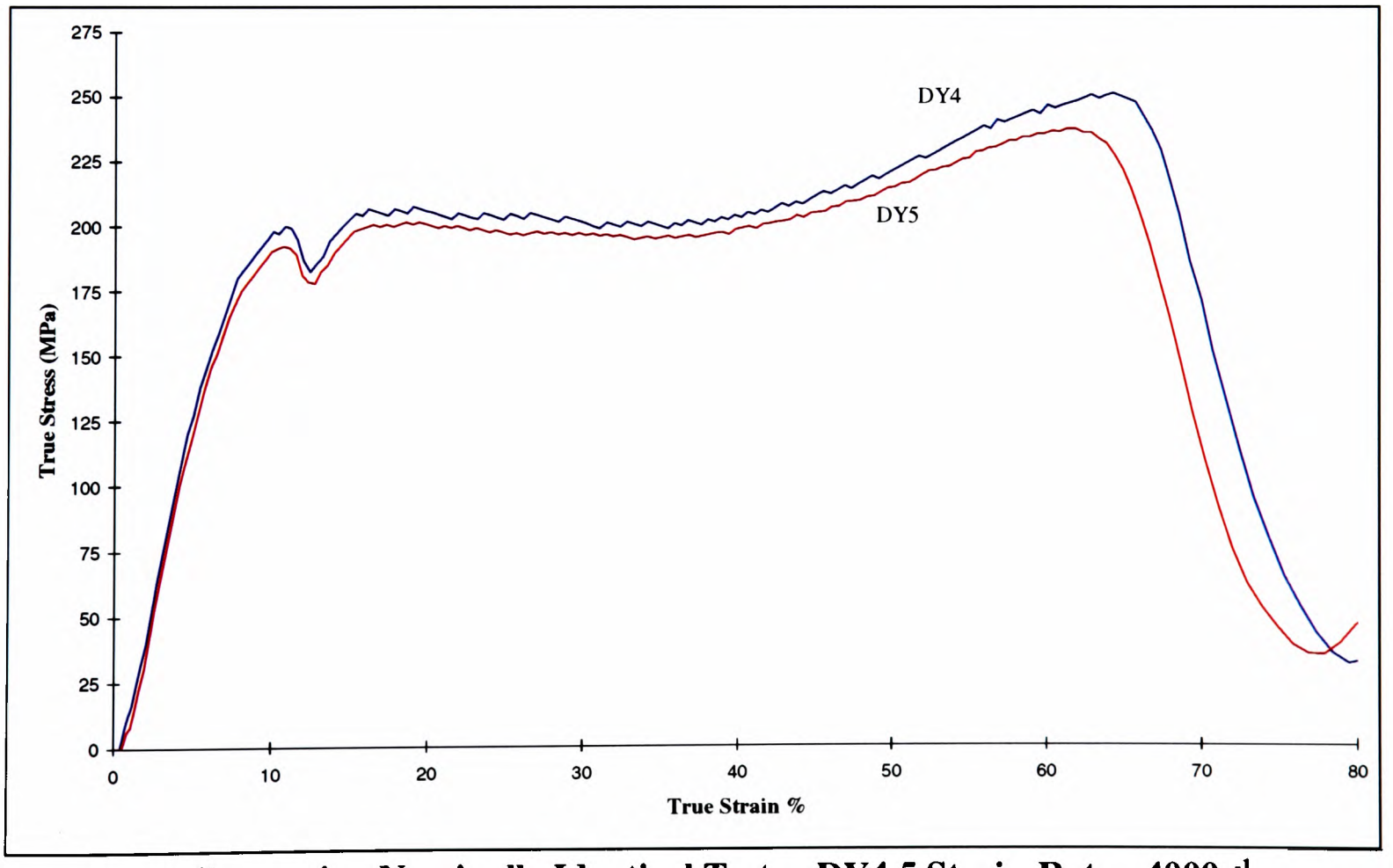

Figure 5.7 Comparing Nominally Identical Tests - DY4,5 Strain-Rate ≈4000s^{-1}

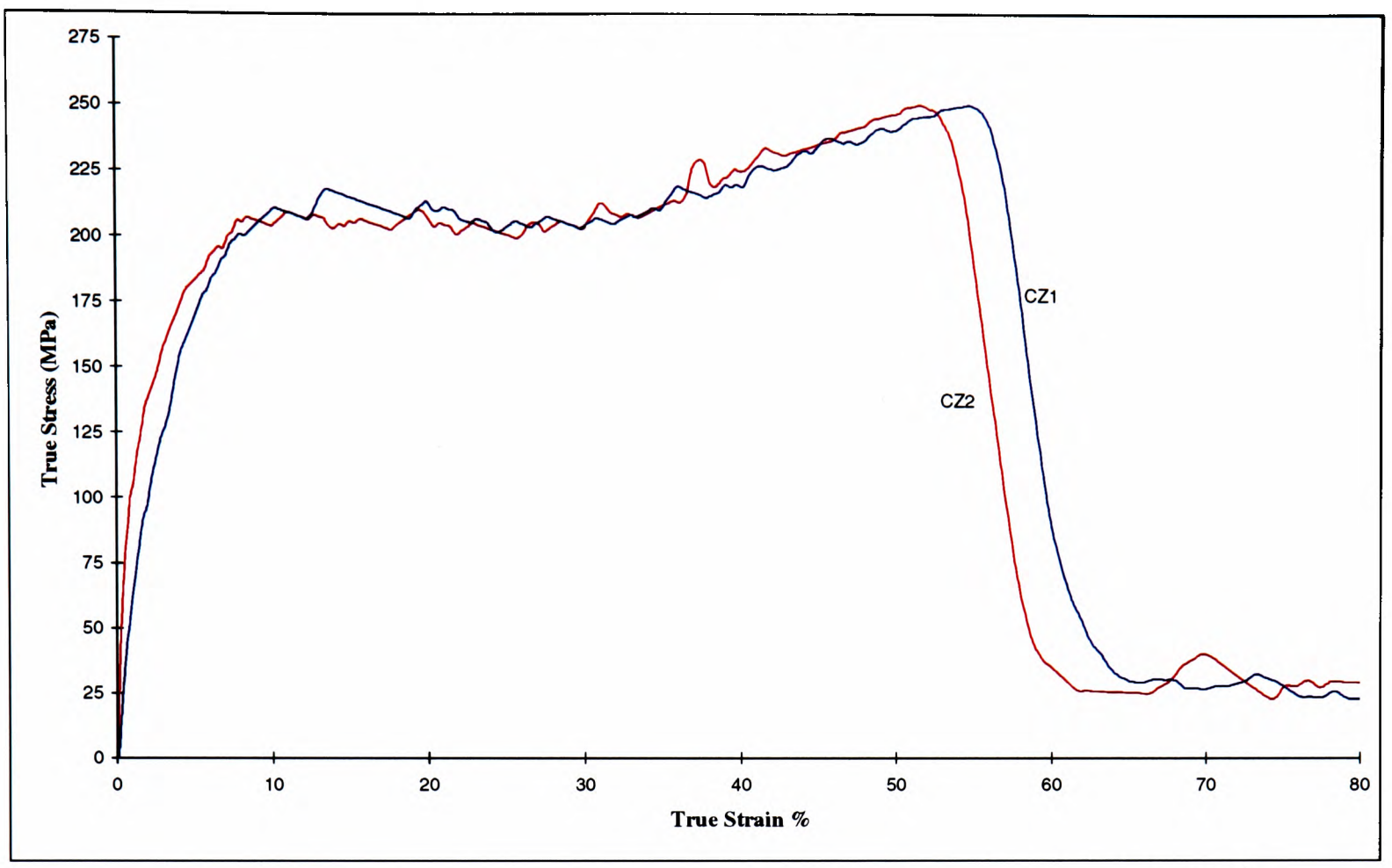

Figure 5.8 Comparing Nominally Identical Tests - CZ1,2 Strain-Rate ≈3500s^{-1}

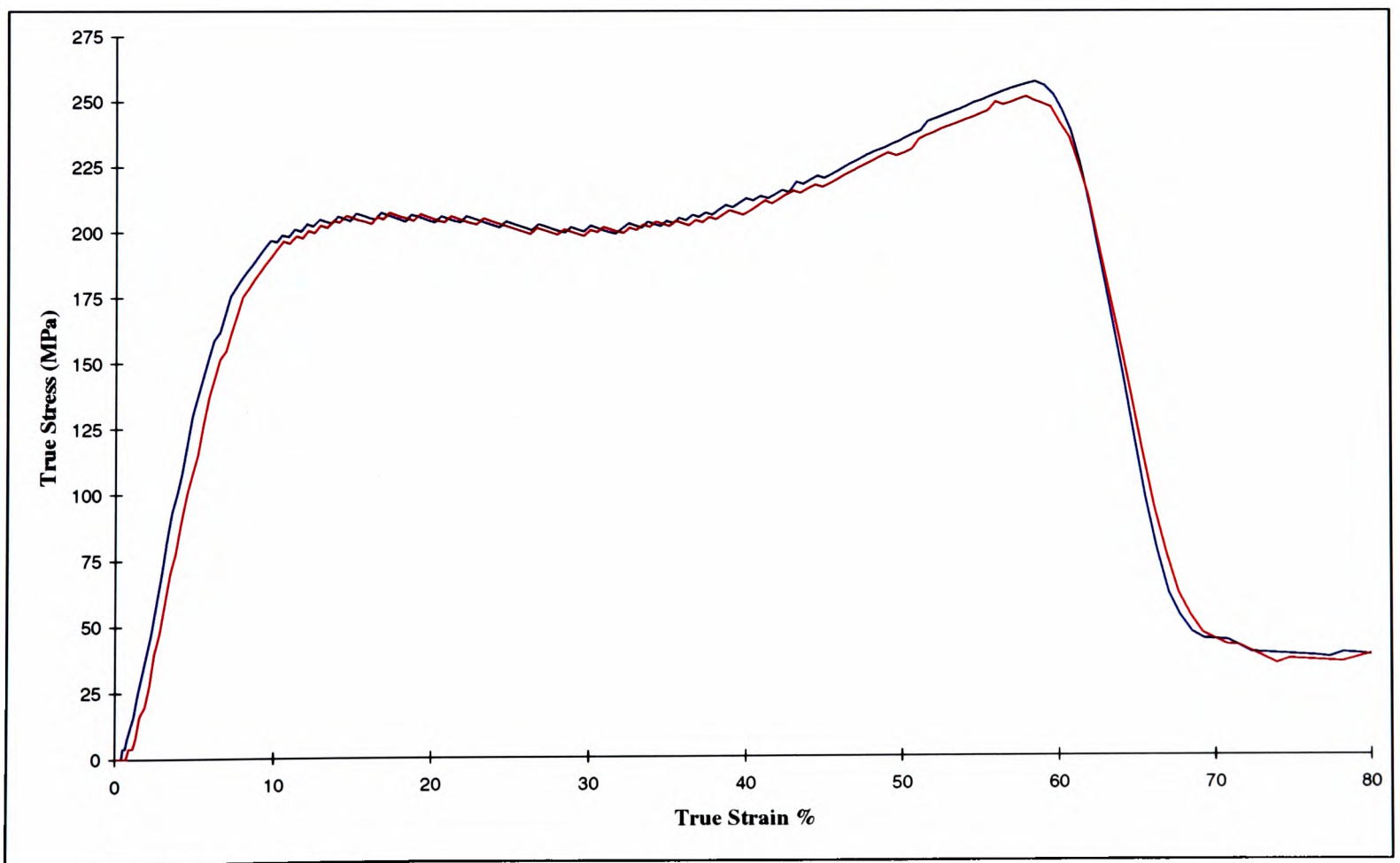

Figure 5.9 Comparing Nominally Identical Tests - DZ1,2 Strain-Rate ≈3750s^{-1}

5.3.2 Comparison of Tests With and Without Lubrication

As discussed in the literature review in Chapter 2, lubrication is essential to minimise the end constraint between the specimen and bar interface. A hydrocarbon based lubricant was used to eliminate frictional stresses between the specimens and the anvils at high strain-rates. Walley *et al*, 1994, found that petroleum jelly gave the best lubrication for strains up to 40%. In this preliminary study, high strain-rate compression was performed with and without lubrication to the specimen/anvil faces. As mentioned in the literature review, failure to attend to such sources of error will show an apparent increase in flow stress and this was found to be the case. A number of tests performed with and without lubrication are shown below in Figures 5.10 to 5.21. A discussion of this lubrication problem is included in Chapter 6, 'Interpretation of Results'. An immediate conclusion from these figures is that lubrication does affect the stress-strain curves for the long specimens and larger diameter specimens - this effect becoming less pronounced as diameter and length decrease.

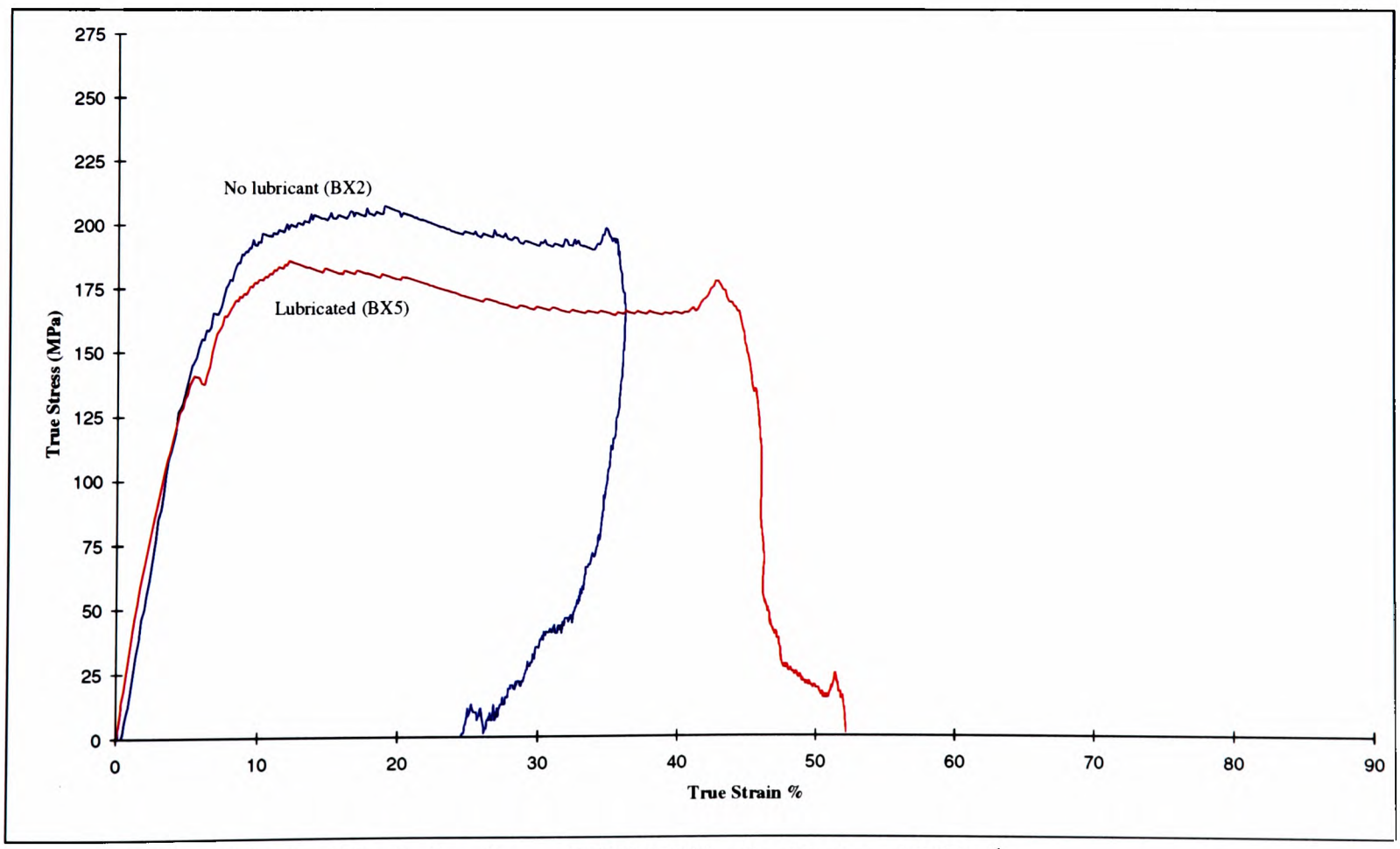

Figure 5.10 Effect of Lubrication - BX2/5 Strain-Rate ≈1500s^{-1}

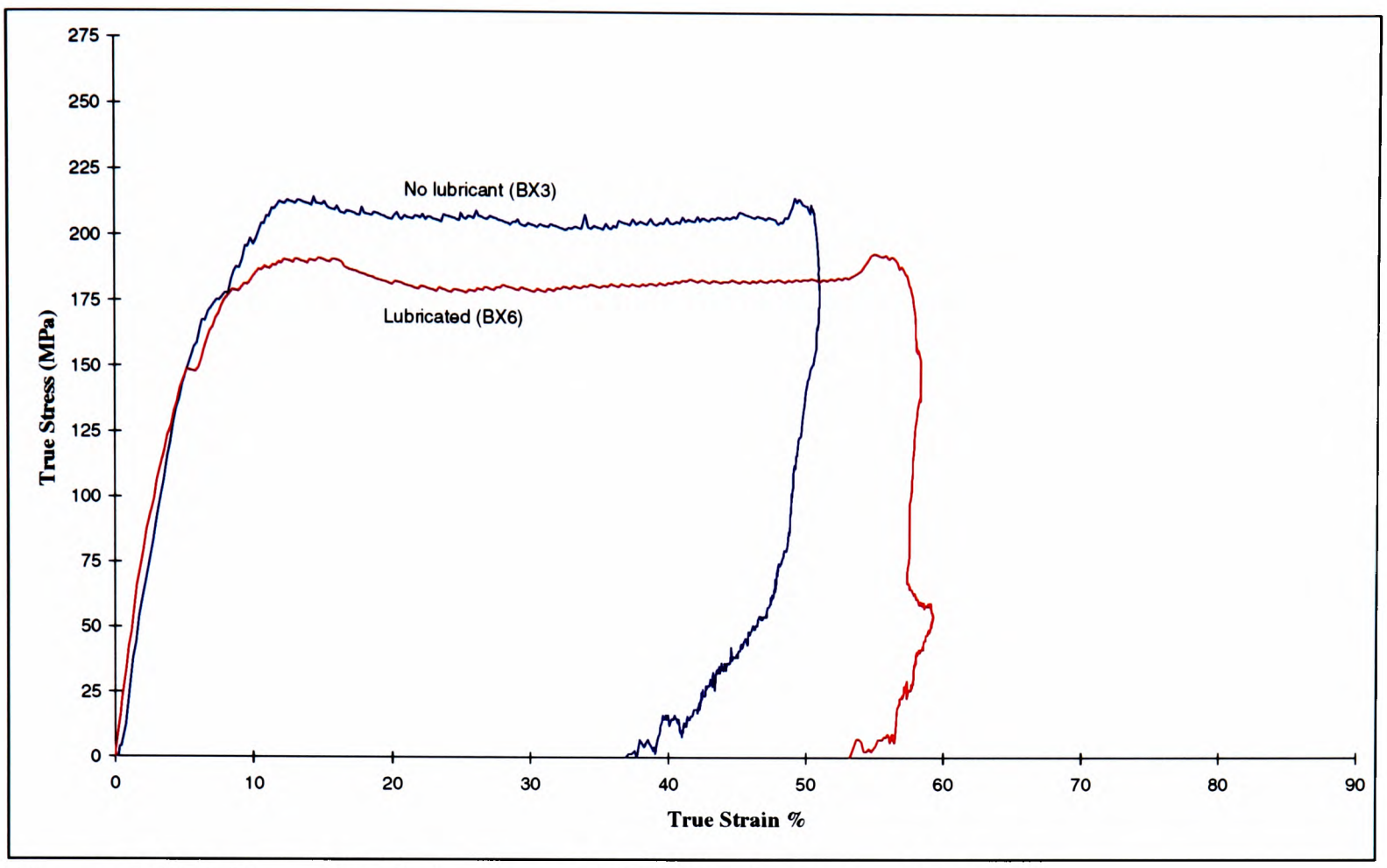

Figure 5.11 Effect of Lubrication - BX3/6 Strain-Rate ≈2250s^{-1}

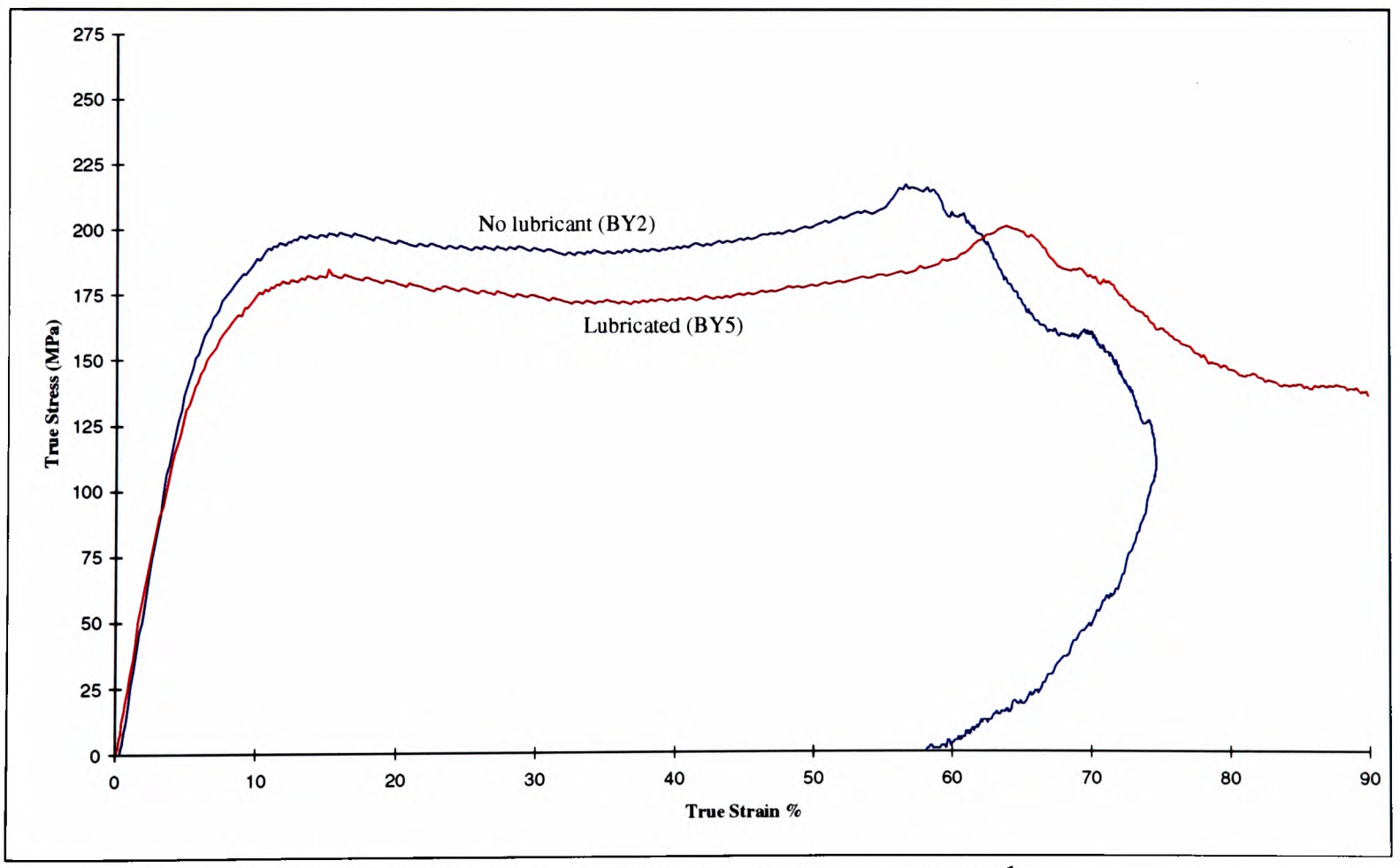

Figure 5.12 Effect of Lubrication - BY2/5 Strain-Rate ≈2500s^{-1}

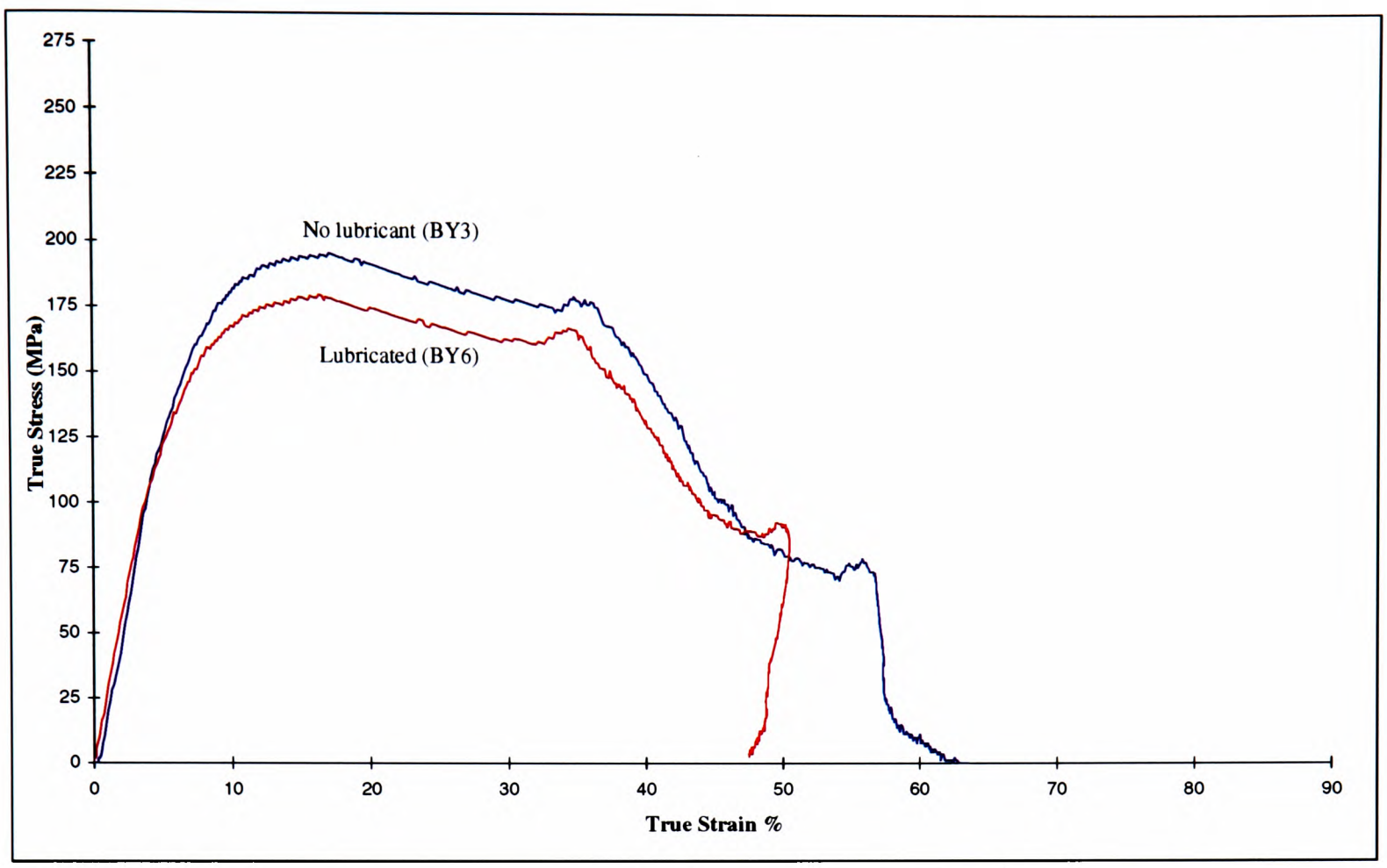

Figure 5.13 Effect of Lubrication - BY3/6 Strain-Rate ≈1500s^{-1}

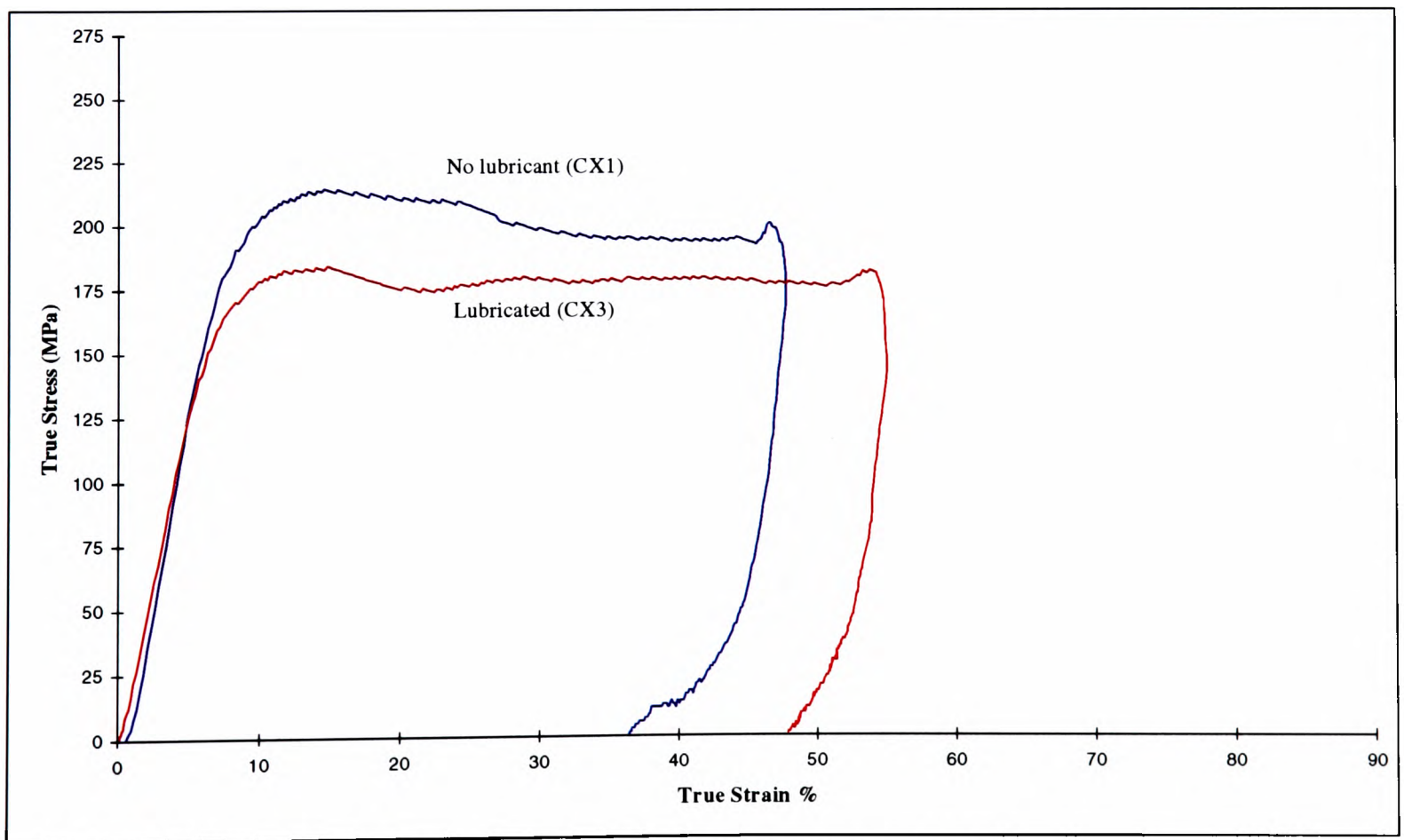

Figure 5.14 Effect of Lubrication - CX1/3 Strain-Rate ≈2000s^{-1}

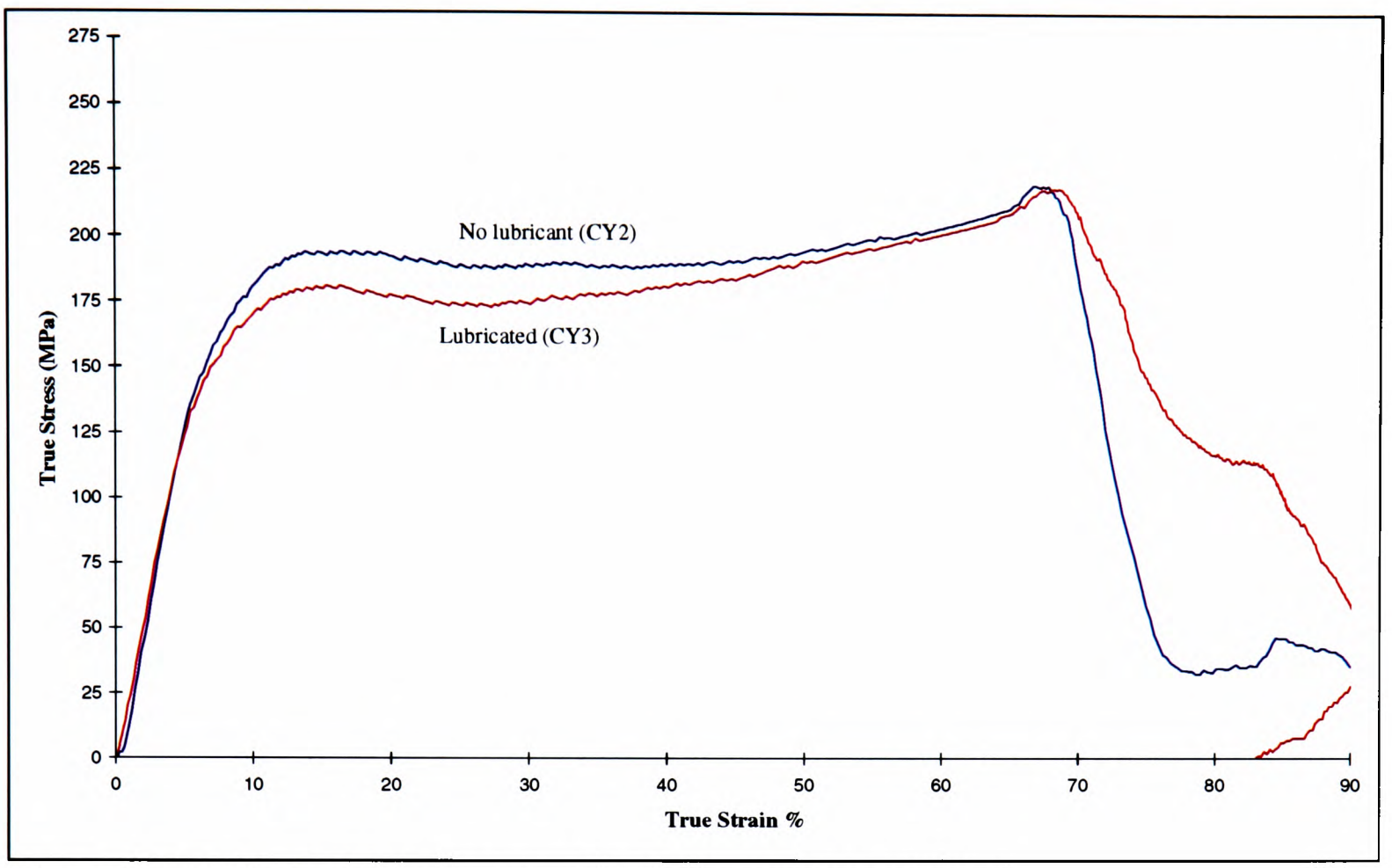

Figure 5.15 Effect of Lubrication - CY2/3 Strain-Rate ≈2500s^{-1}

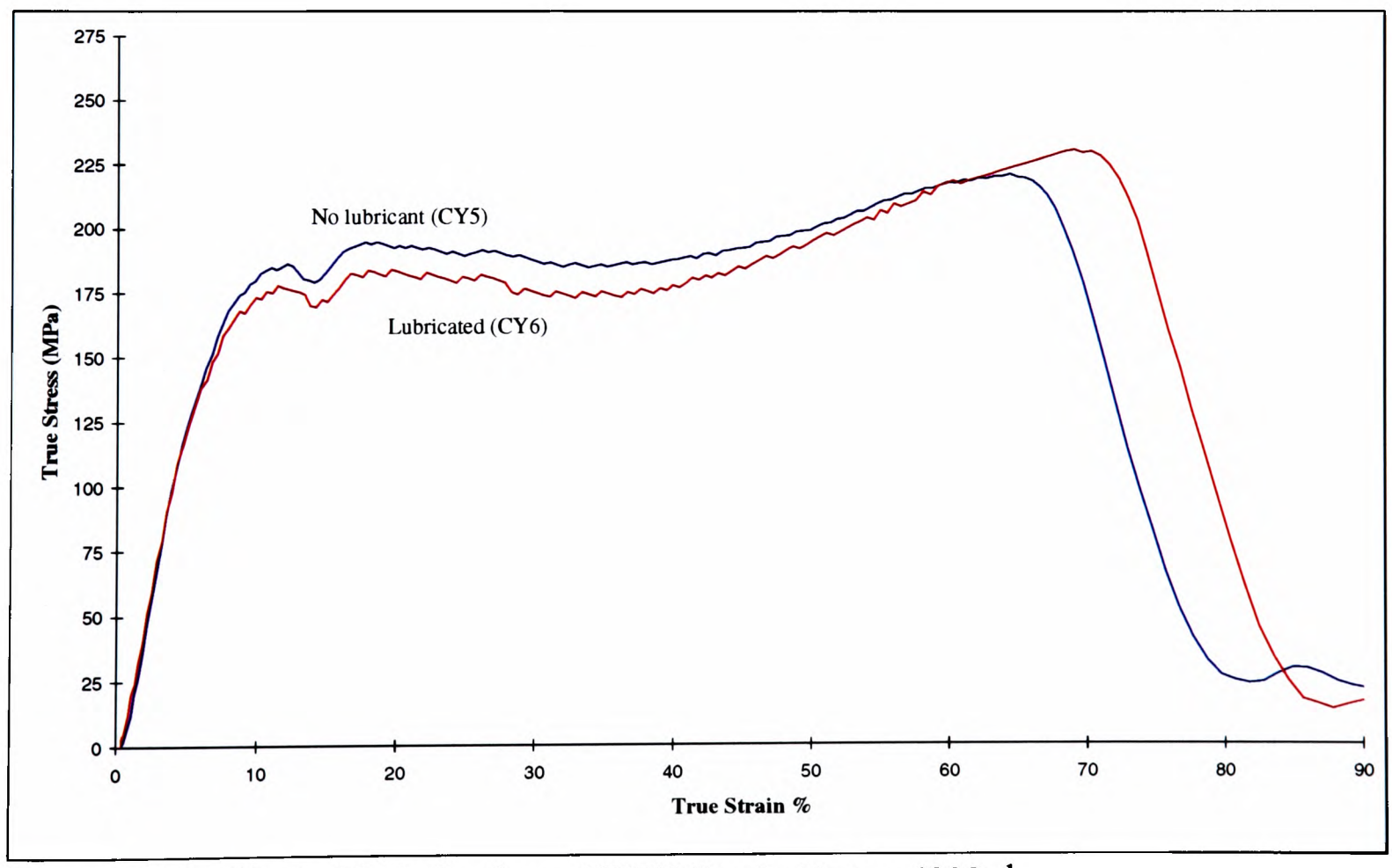

Figure 5.16 Effect of Lubrication - CY5/6 Strain-Rate ≈4000s^{-1}

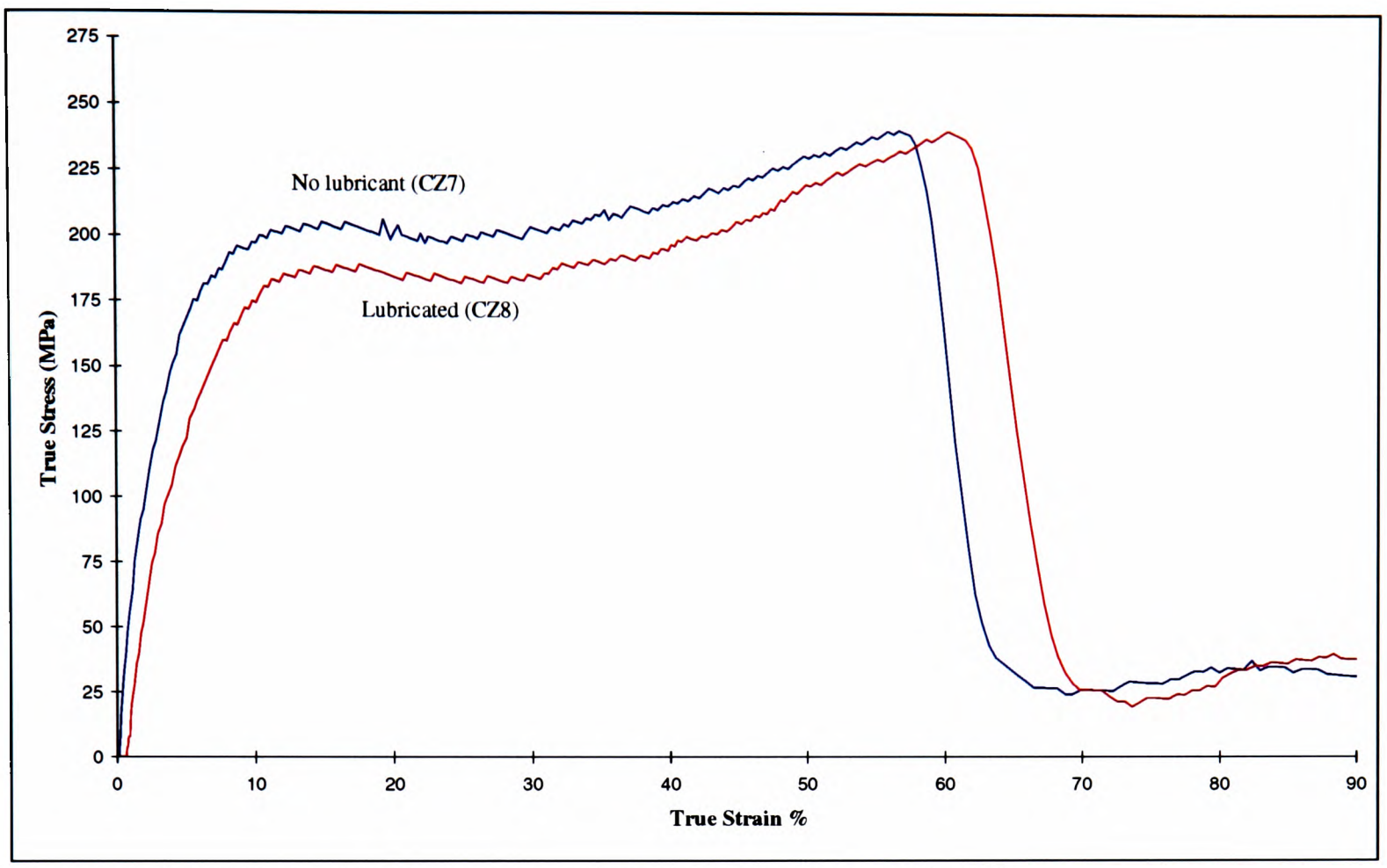

Figure 5.17 Effect of Lubrication - CZ7/8 Strain-Rate ≈3000s^{-1}

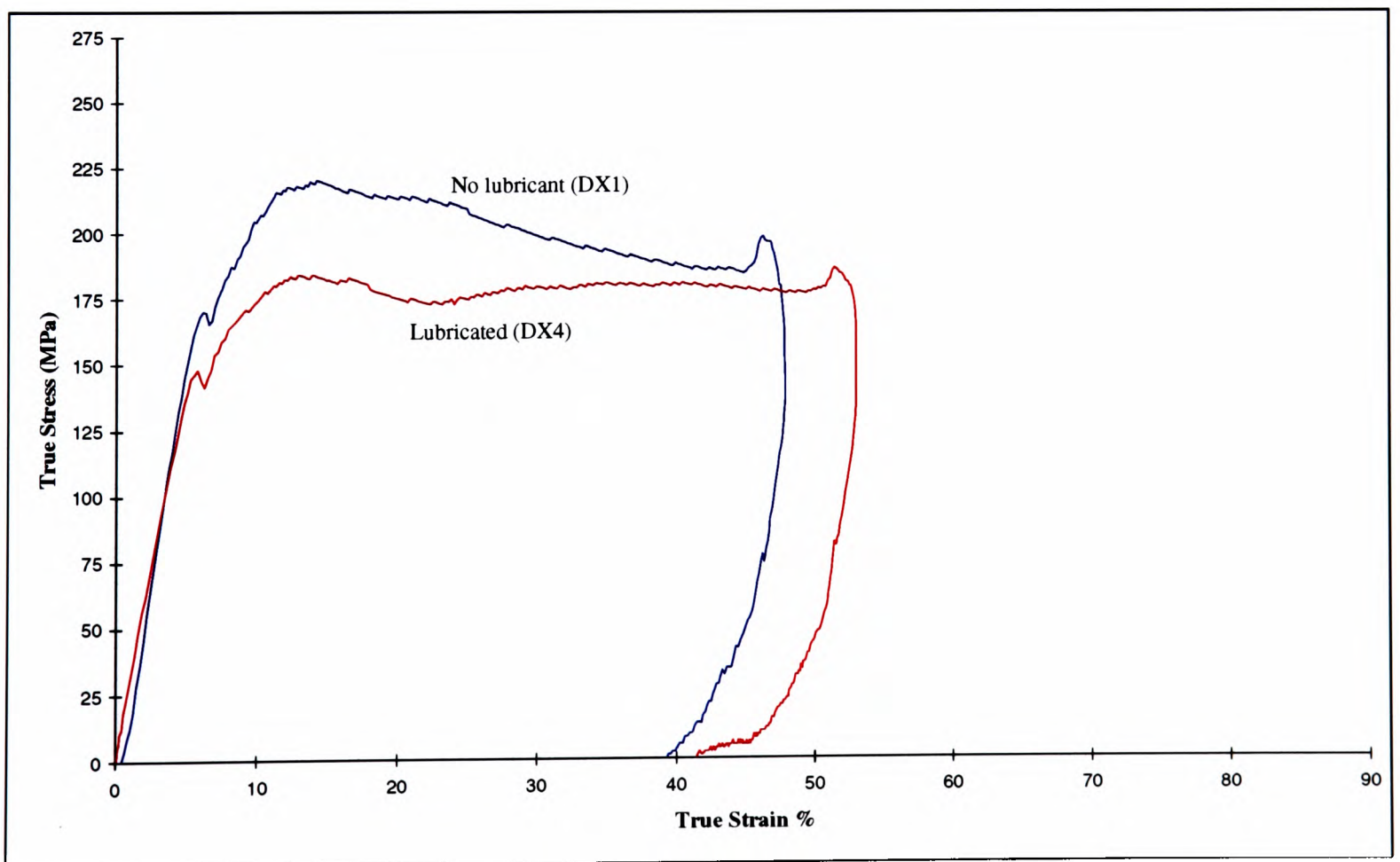

Figure 5.18 Effect of Lubrication - DX1/4 Strain-Rate ≈2000s^{-1}

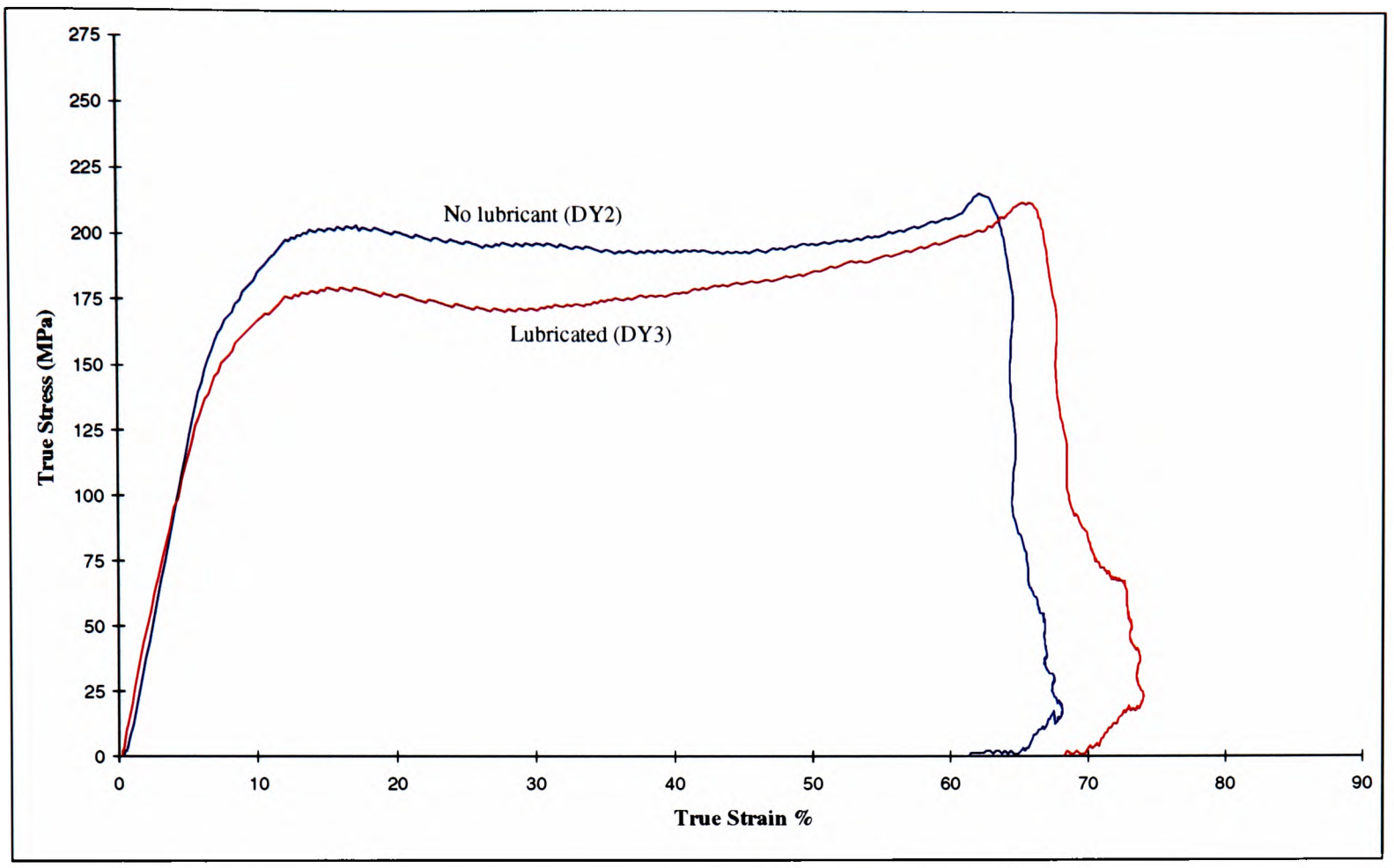

Figure 5.19 Effect of Lubrication - DY2/3 Strain-Rate ≈2500s^{-1}

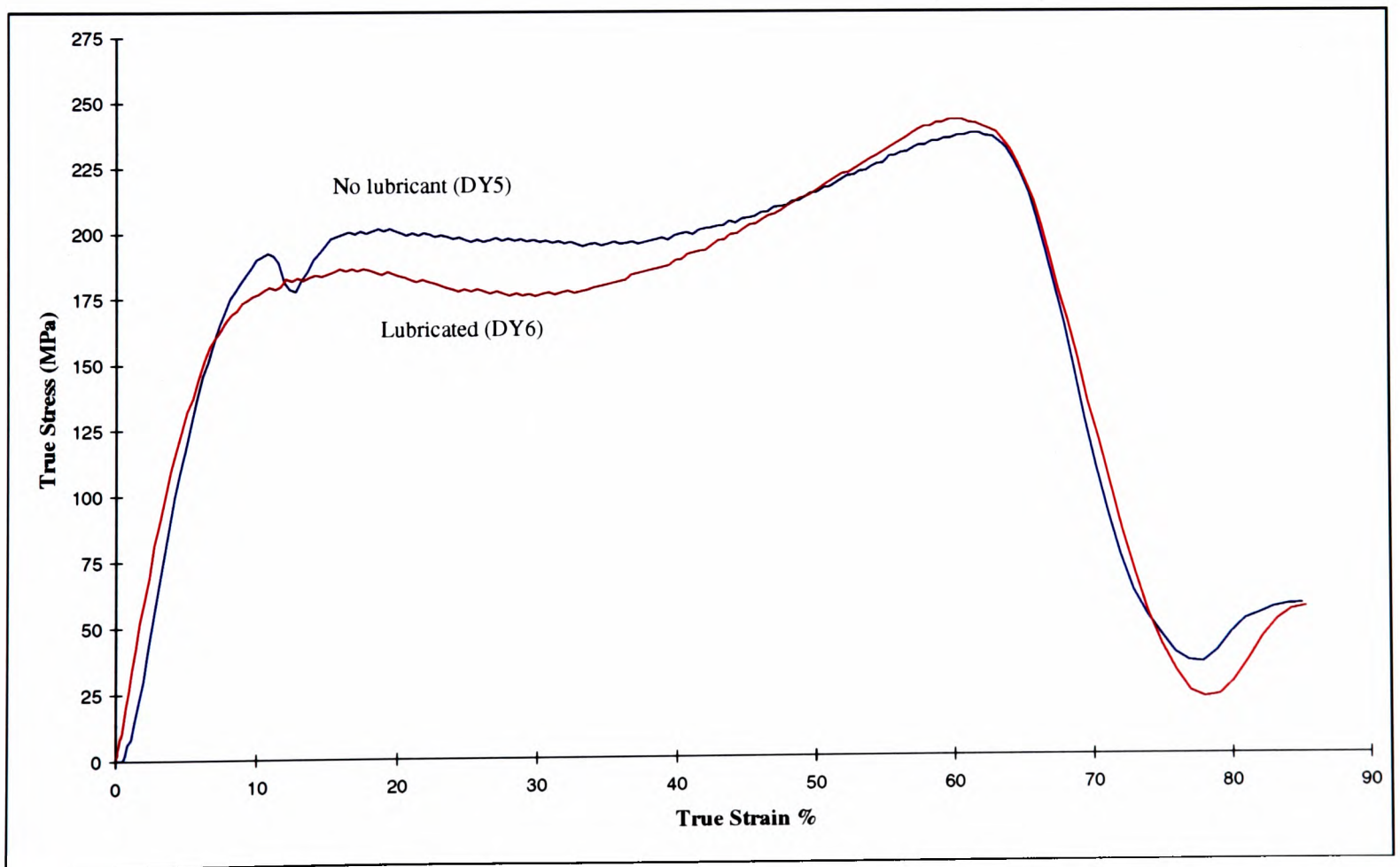

Figure 5.20 Effect of Lubrication - DY5/6 Strain-Rate ≈4000s^{-1}

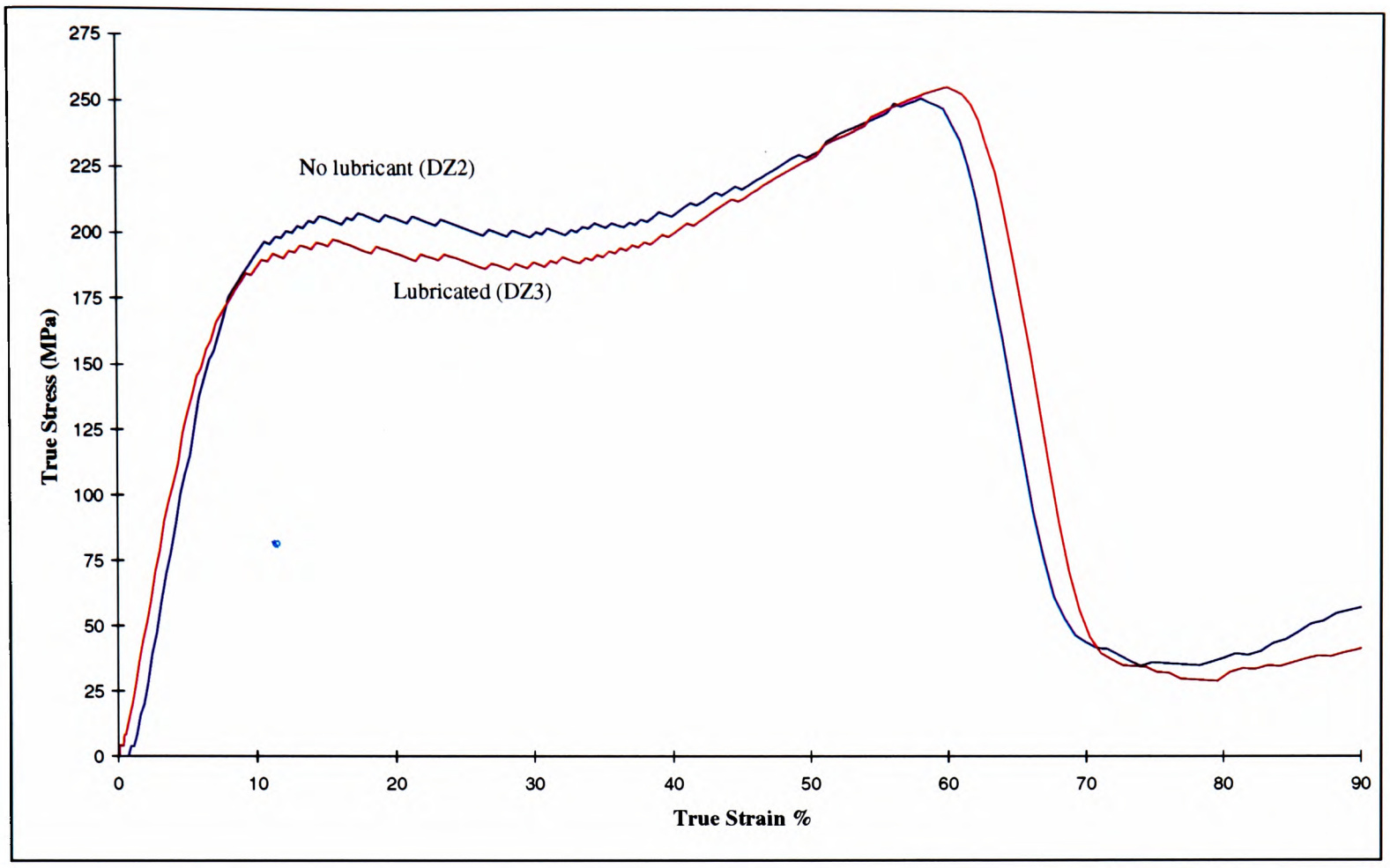

Figure 5.21 Effect of Lubrication - DZ2/3 Strain-Rate ≈3750s^{-1}

5.3.3 Quasistatic Testing

Specimen BY (diameter 9mm, length 5.5mm) gave good and consistent results, as discussed in Chapter 6, and so was selected for use in the testing programme.

The quasistatic testing method is detailed in Chapter 3. Lubrication of the platen-specimen interface was in the form of thin PTFE sheet which, at low strain-rates, ensures homogeneous deformation. A typical test is shown below in Figure 5.22, where the strain-rate was approximately constant at $6x10^{-3}s^{-1}$.

5.3.4 Intermediate Strain-Rate Testing

Intermediate rates of strain of approximately $100s^{-1}$ were achieved with the use of a hydraulic machine, detailed in Section 3.2. Lubrication of the specimen ends and platens was done with petroleum jelly and repeated with PTFE sheet. The largest strains were obtained with petroleum jelly, as shown in Figure 5.23.

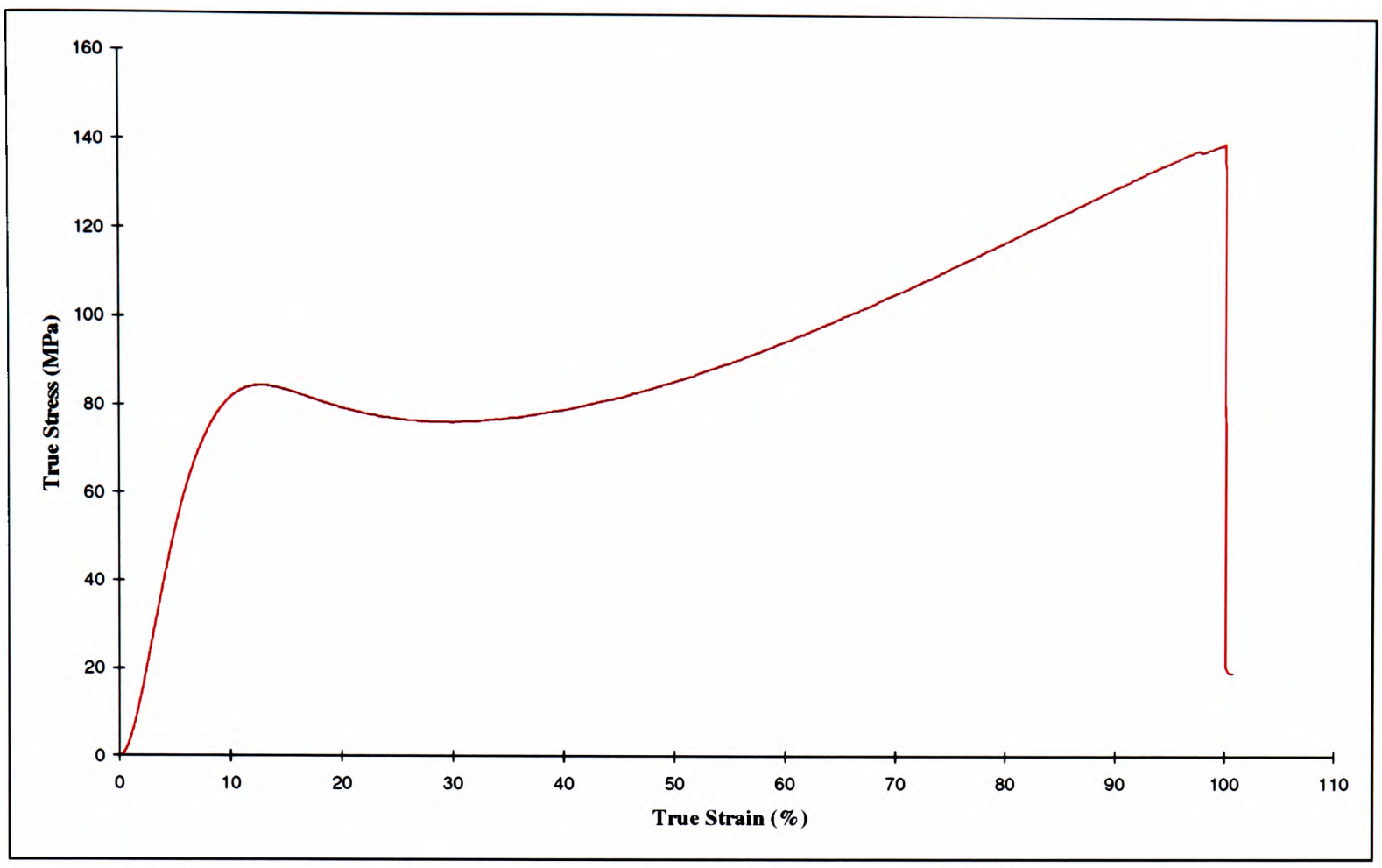

Figure 5.22 Lubricated Quasistatic Test - Strain-Rate ≈$6x10^{-3}s^{-1}$

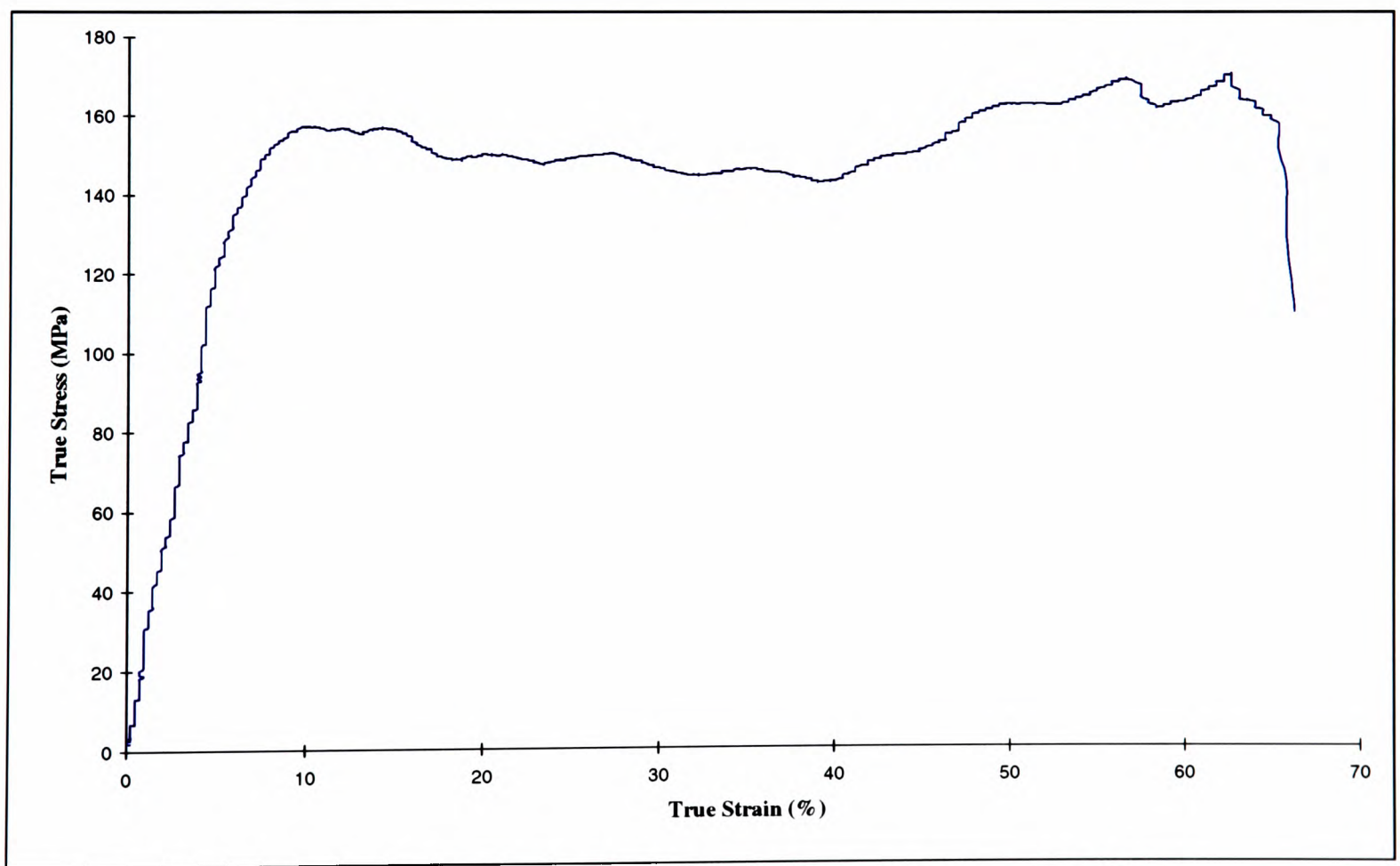

Figure 5.23 Lubricated Intermediate Rate Test - Strain-Rate ≈$100s^{-1}$

5.4 High Rate Testing with Temperature Measurement

A number of different types of test have been performed on the selected specimen aspect ratio. The first type was termed 'Continuous Tests' which involved scrutinising the material behaviour under high strain-rate compression. The bulk temperature rise of the specimen was also investigated by means of the fast response infra-red radiometer, described in Chapter 4.

The second set of tests were termed '*Single Specimen Interrupted Tests*' which involved the use of one specimen, repeatedly deformed to increasing strain increments. By advancing the state of deformation by small increments, this would, in theory, mean that isothermal conditions would prevail.

Finally, the third type of test were simply termed '*Multi Specimen Interrupted Tests*'. For each increment of strain, a fresh specimen was used. The collars used for the interrupted tests, seen in Figure 5.35a & 5.35b, were modified to allow for temperature measurement.

5.4.1 Continuous Tests

A summary of the results obtained from continuous tests is shown in Table 5.3. The strain-rates quoted are calculated mean values from data for the duration of the test. Other values such as stress at fracture, strain at fracture and temperature data are obtained directly from graphs. Figures 5.24 to 5.30 show the stress-strain plots together with the temperature rise measured during the test.

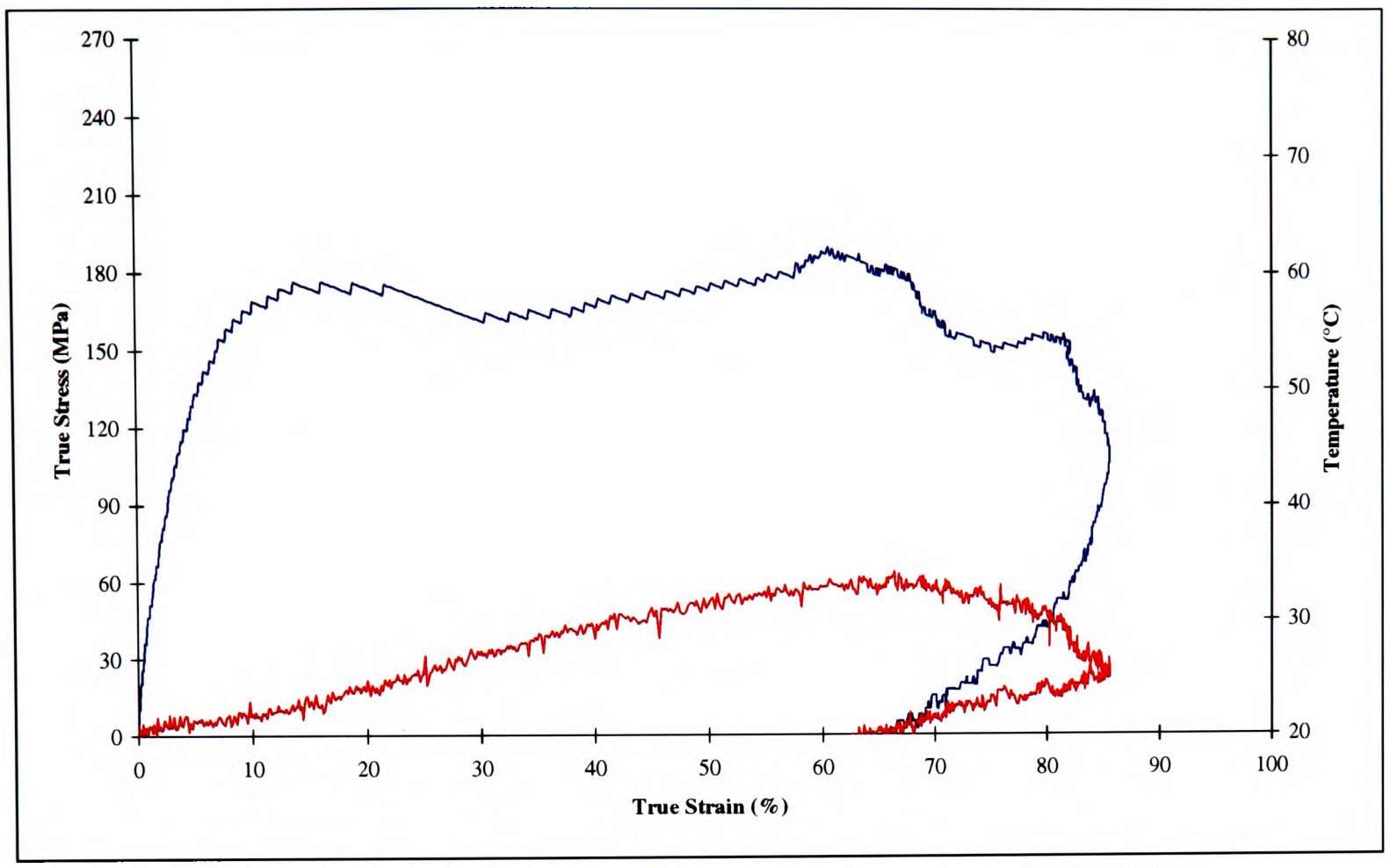

Figure 5.24 True Stress and Temperature vs True Strain for Test: TEMP4

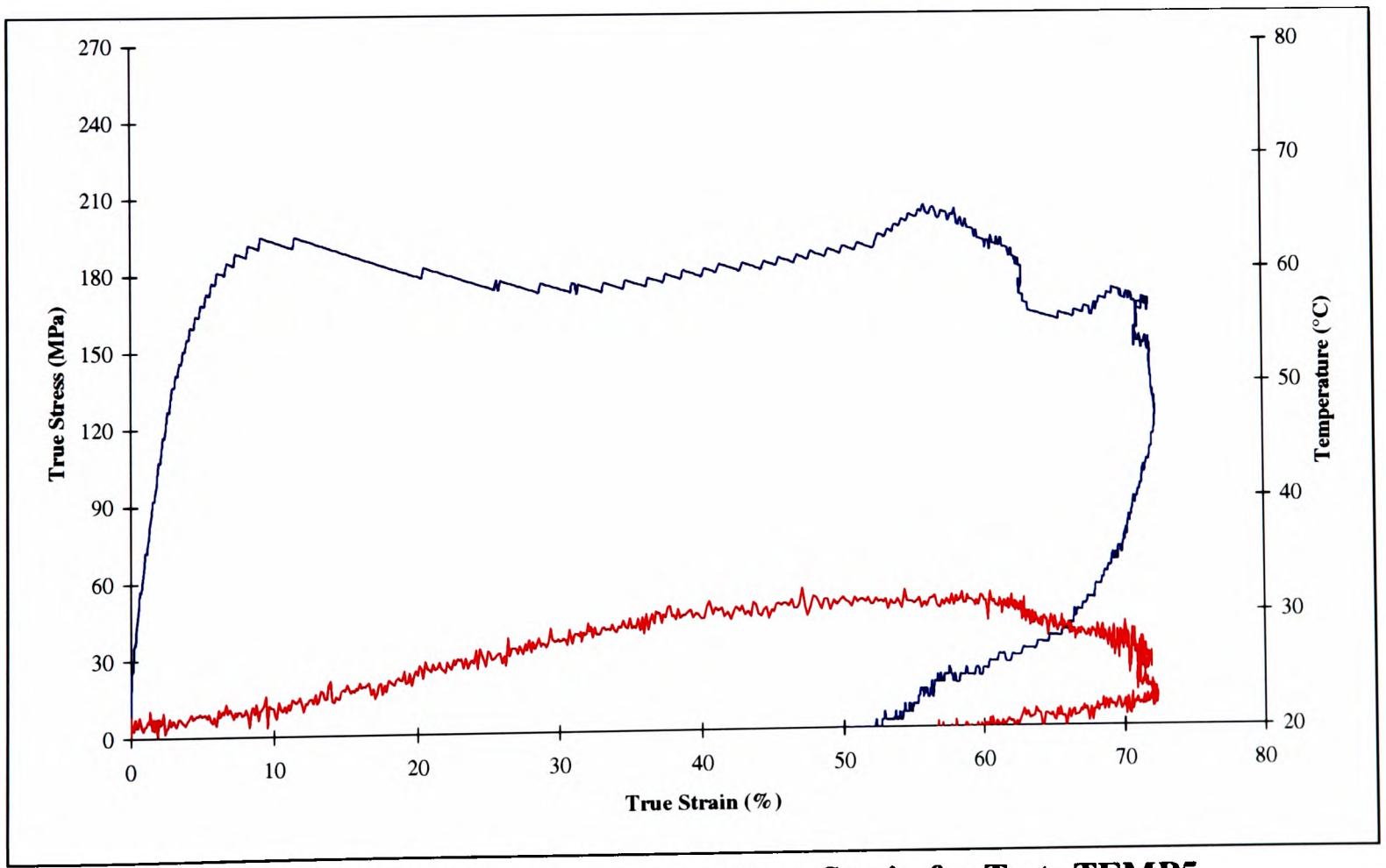

Figure 5.25 True Stress and Temperature vs True Strain for Test: TEMP5

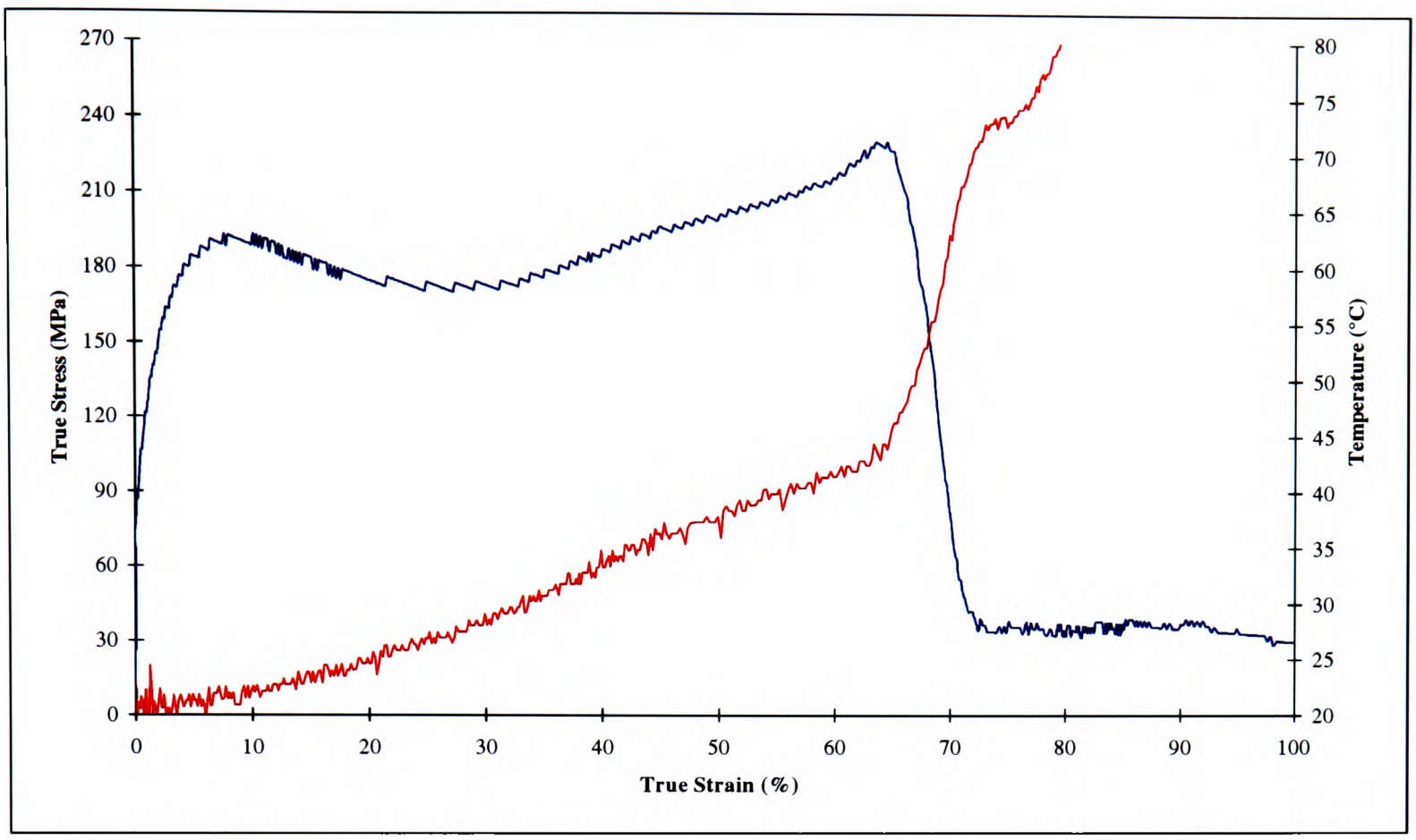

Figure 5.26 True Stress and Temperature vs True Strain for Test: TEMP6

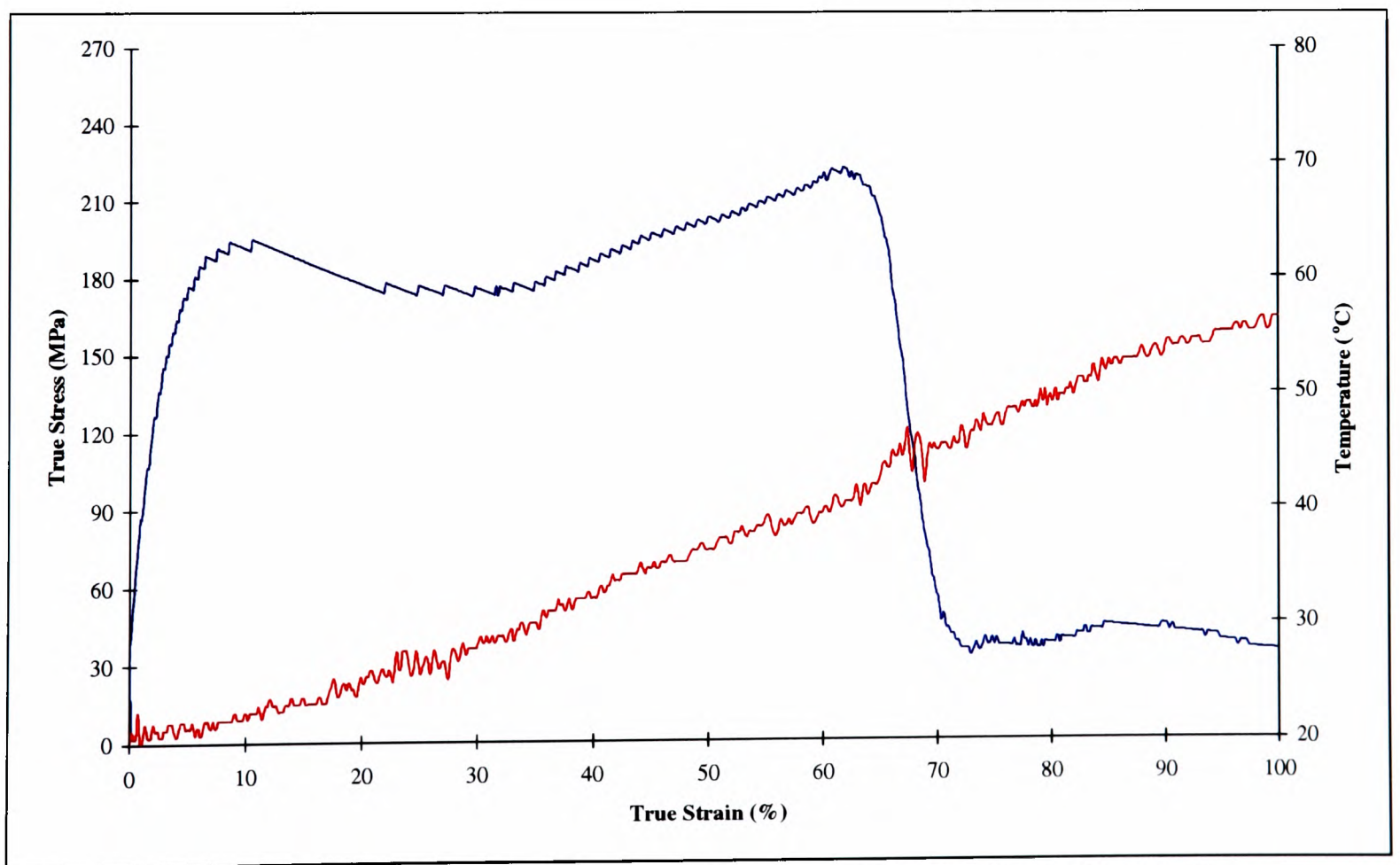

Figure 5.27 True Stress and Temperature vs True Strain for Test: TEMP7

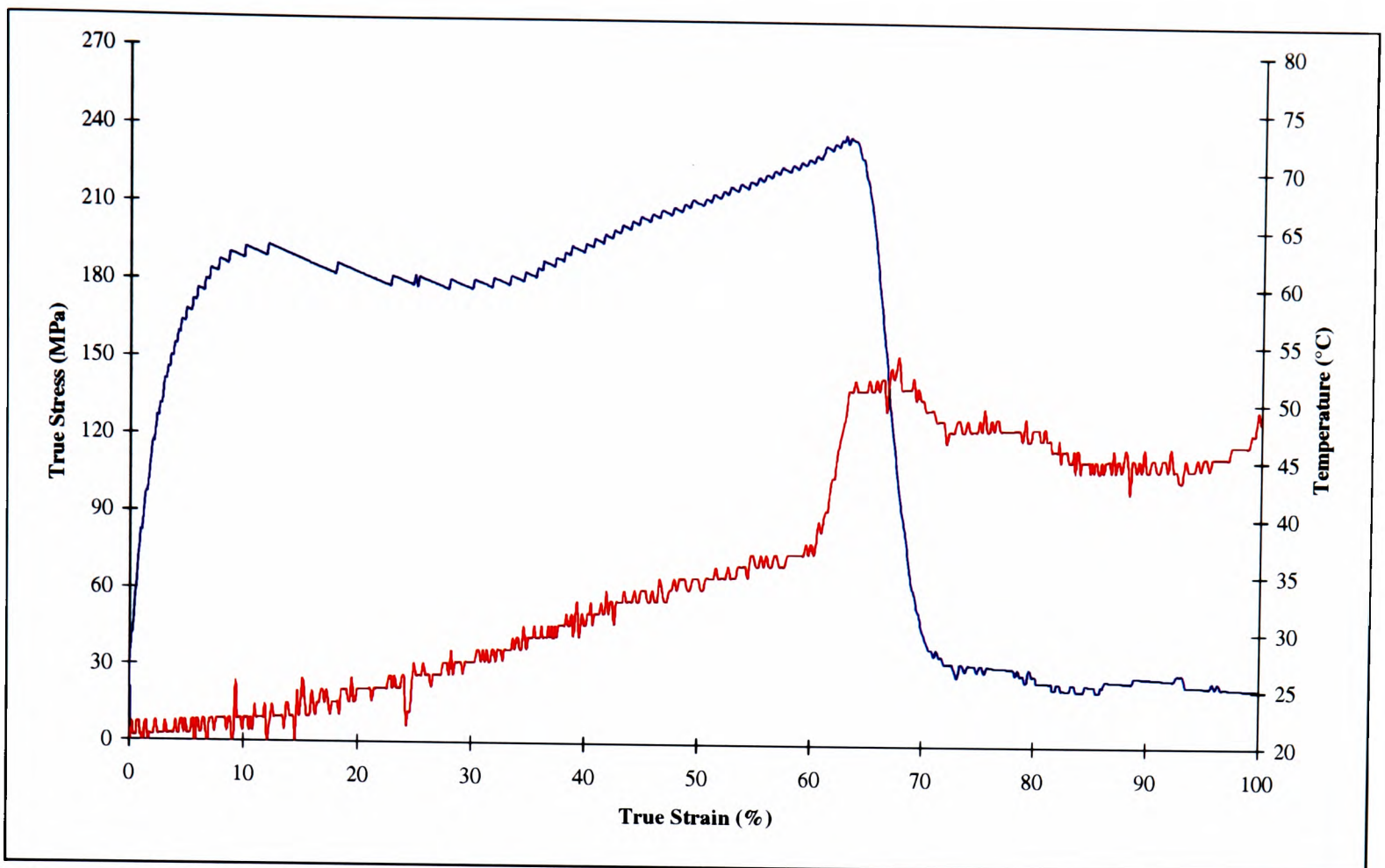

Figure 5.28 True Stress and Temperature vs True Strain for Test: TEMP8

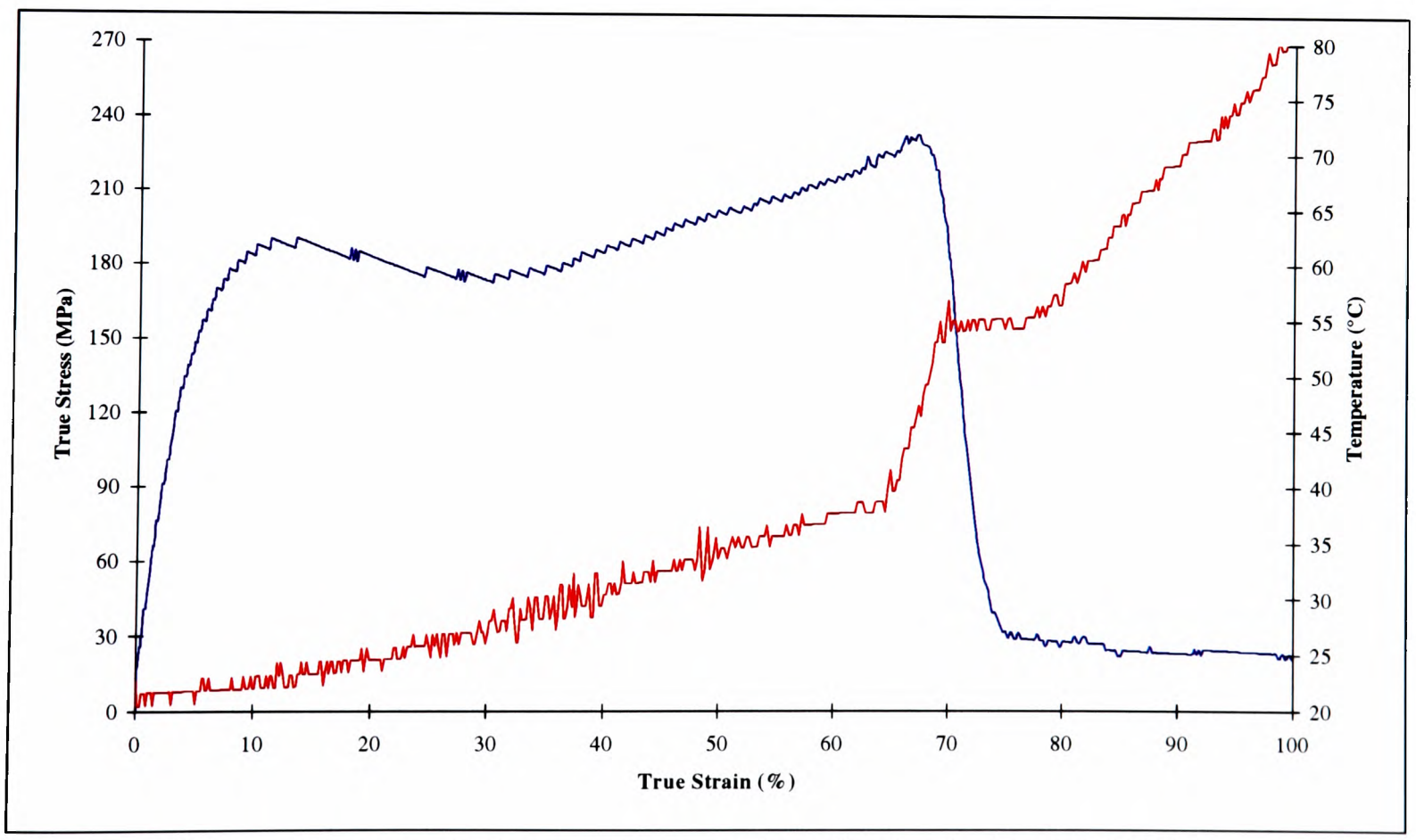

Figure 5.29 True Stress and Temperature vs True Strain for Test: TEMP9

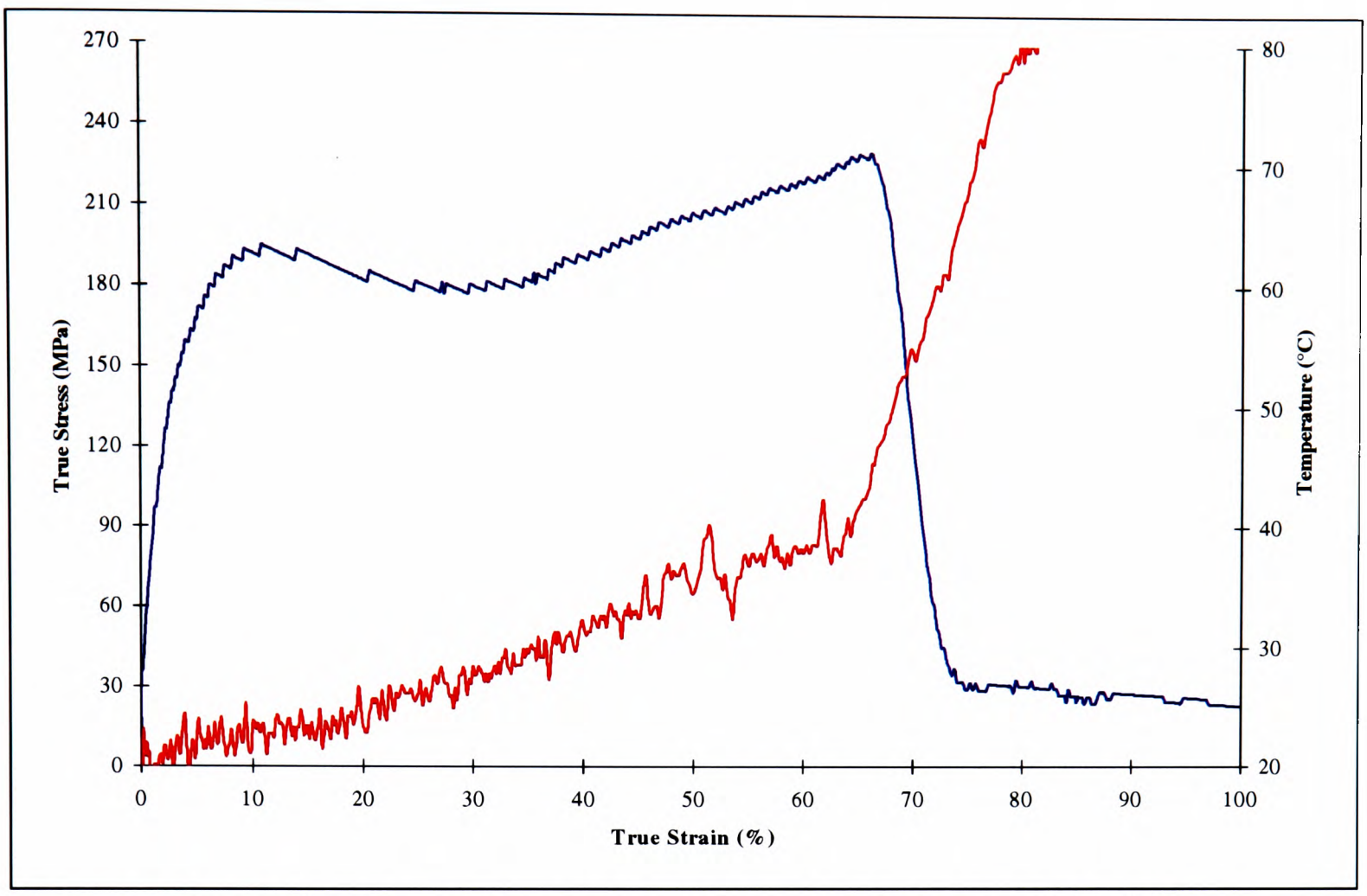

Figure 5.30 True Stress and Temperature vs True Strain for Test: TEMP10

Table 5.3 Summary of Continuous Tests with Temperature Measurement (with repeats)

	Impact Velocity (m/s)	Strain-Rate (s^{-1})	Stress@ Fracture (MPa)	Strain@ Fracture (%)	Temp@ Fracture (°C)	Max. Temp (°C)	Time for max. Temp(μs)
TEMP4	14.75	2275	(*1)	(*1)	(*1)	28.3	225
TEMP5	14.74	2175	(*1)	(*1)	(*1)	26.5	183
TEMP6	16.60	2500	231	65	42	(*2)	(*2)
TEMP7	16.65	2480	225	63	34	54	450
TEMP8	16.56	2460	235	63	42	92	490
TEMP9	16.61	2520	234	67	39	79	530
TEMP10	16.60	2532	231	65	38	71	500

(*1)No specimen failure.
(*2)Signal topped out.

Two impact velocities were used to obtain a variation in strain-rate and tests were repeated to ensure accuracy. Tests TEMP 4 & 5 were conducted at an impact velocity of 14.75m/s - there is some variation in the resulting stress-strain curves, 10% variation in 'yield stress'. Tests TEMP 6-10 were conducted at a higher impact velocity, 16.6m/s, which was sufficient to cause failure in the specimen. True stress-true strain curves of each set of nominally identical tests lay within 5% of each other, which is within the acceptable limits of experimental error.

The data from the nominally identical tests, TEMP 4 & 5 and TEMP 6 to 10, shown in Figures 5.24 to 5.30, have been combined into mean stress-strain curves together with temperature and shown in Figures 5.31 & 5.32. The temperature measurements show some scatter, but this is due to small variations in experimental conditions. Also mean temperature-time curves have been constructed to clarify the data and are also shown in these figures. A discussion of the temperature data can be found in Chapter 6.

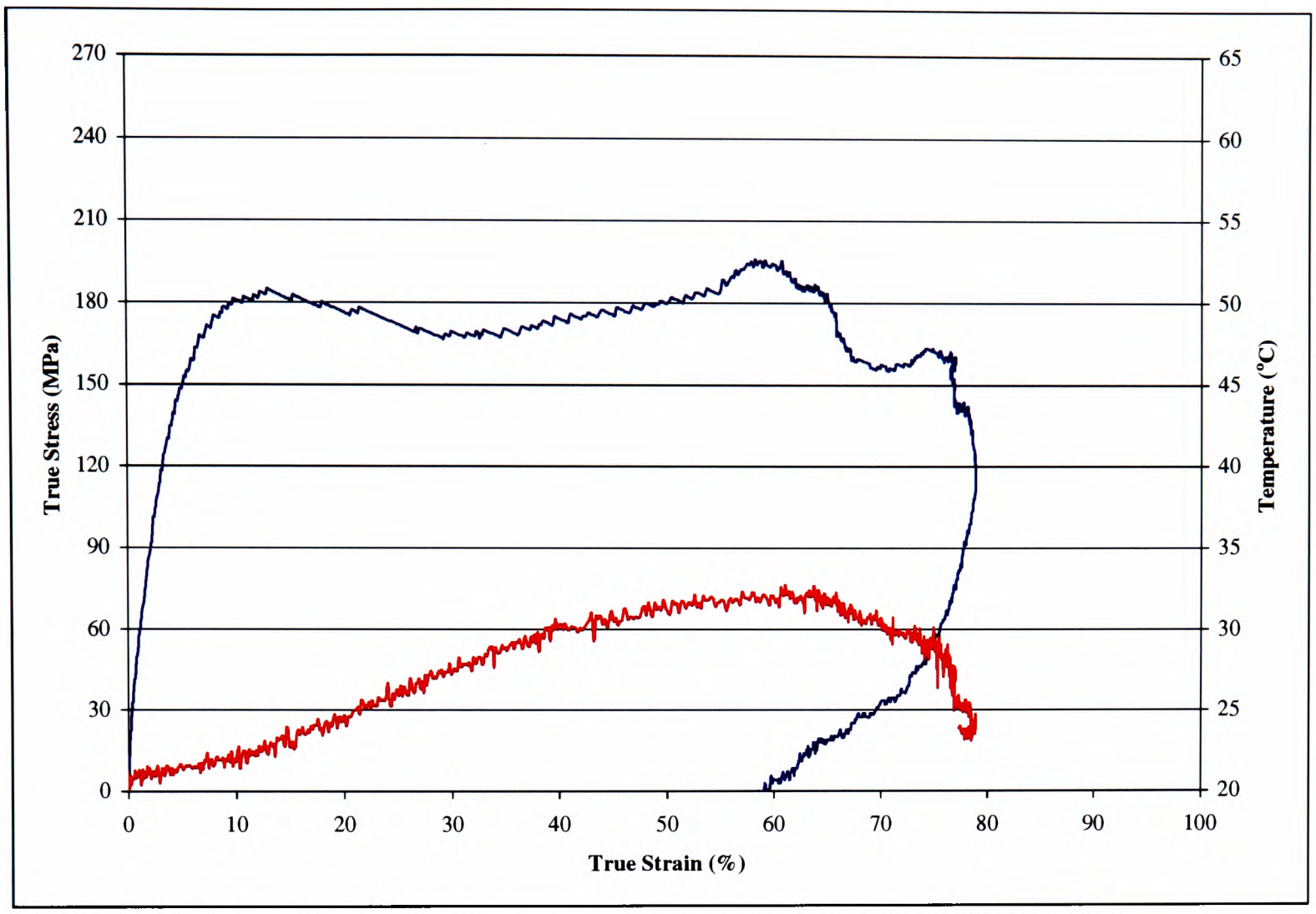

Figure 5.31 Mean Stress/Strain Temperature Curves for Test: TEMP4&5

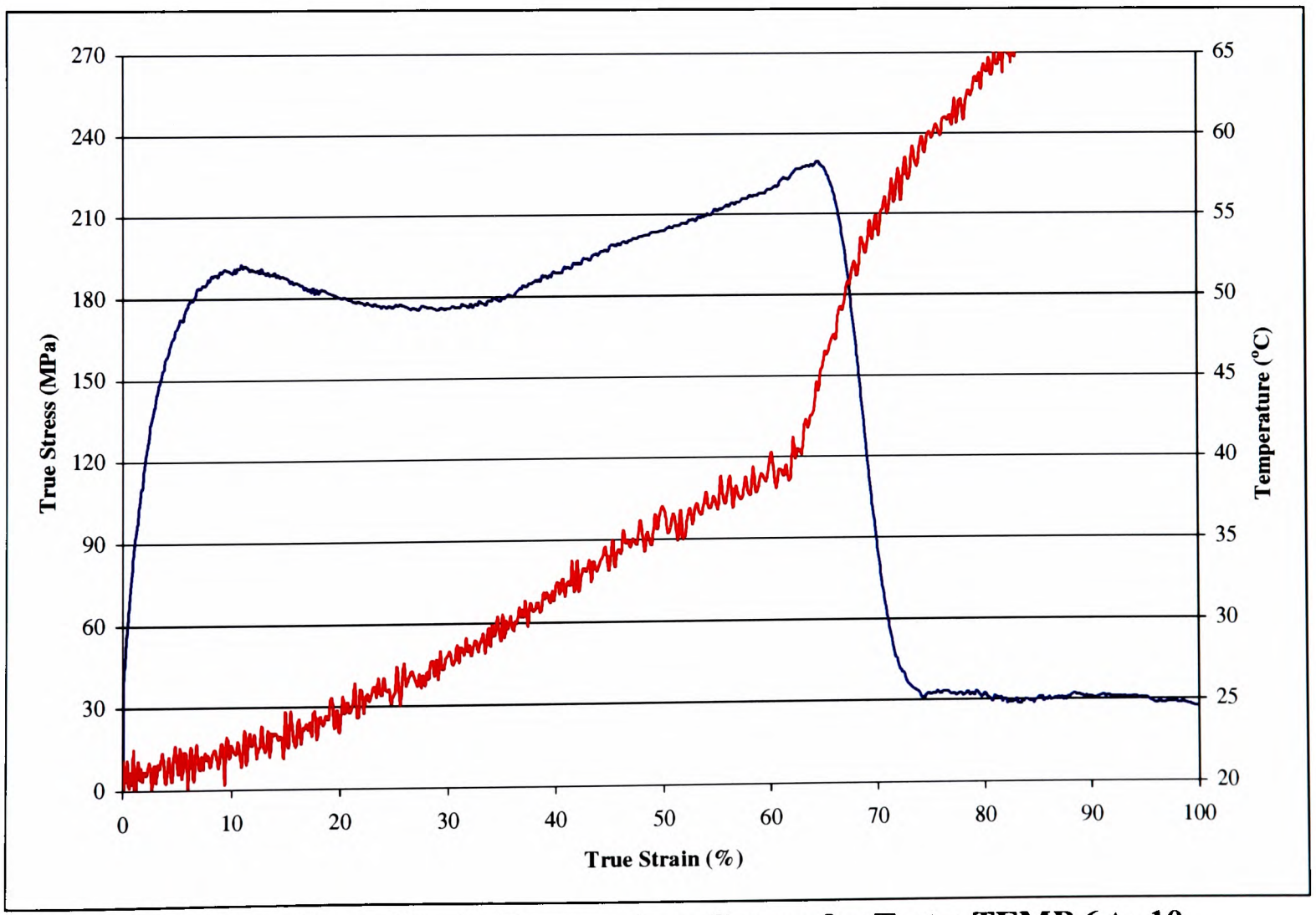

Figure 5.32 Mean Stress/Strain Temperature Curves for Tests: TEMP 6 to 10

5.4.2 High Speed Photography

High-speed photography was used to look at the behaviour of the specimen during a compression test. High-speed photography and temperature measurement cannot be performed simultaneously due to limited access around the specimen and to the interference that the flash guns would cause to the sensitive temperature apparatus. A set of photographs, seen in Figures 5.33a & 5.33b, from a previous test (PHOTO4), have been synchronised to correspond with the mean Temperature vs Time graph (from tests TEMP6 to TEMP10) which can be seen in Figure 5.34.

During the early part of the compression of the specimen, there is a constant temperature rise of approximately 36.7×10^3 °C.s^{-1}. After ~60μs, the rate of temperature rise starts to increase to a rate of ~141×10^3 °C.s^{-1} after 110μs. This rate is maintained up until approximately 190μs when failure of the specimen is imminent (at approximately 200μs). The final and repeatable rise is 975×10^3 °C.s^{-1}. At 300μs, pieces of specimen are seen to move in all directions and it is considered that the calibration before the test is no longer valid and any temperature measurement after failure should be used only as an indicator as to what is occurring and not a definitive measure.

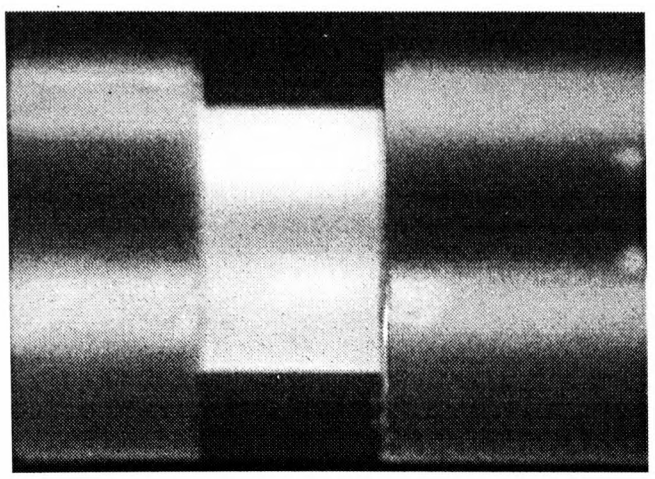

-20μs

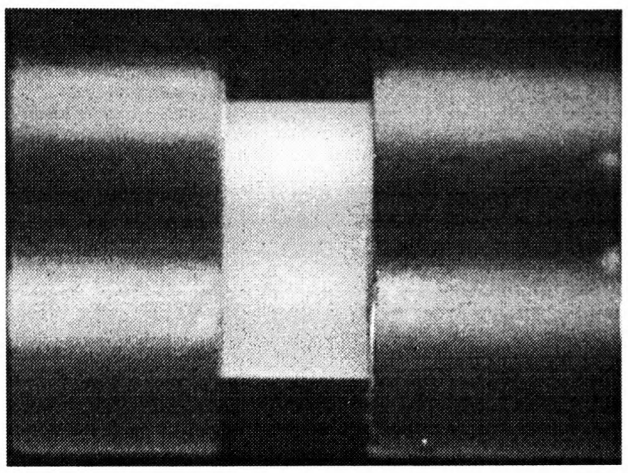

60μs

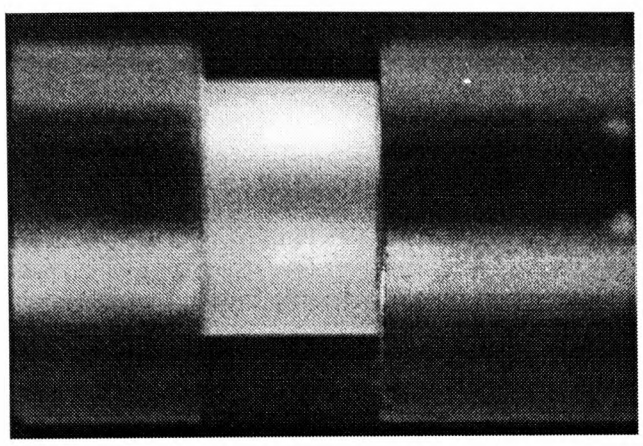

0μs

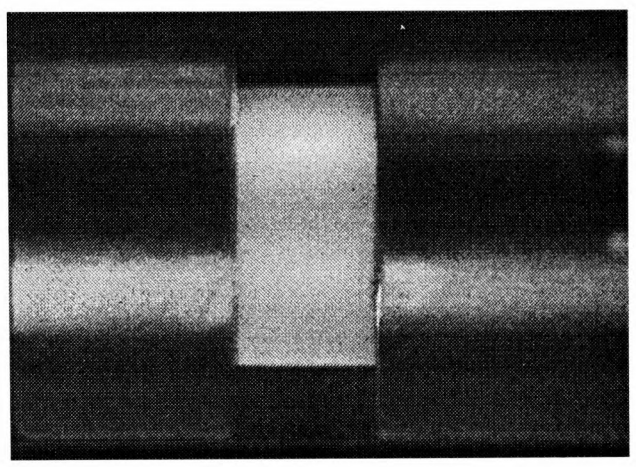

80μs

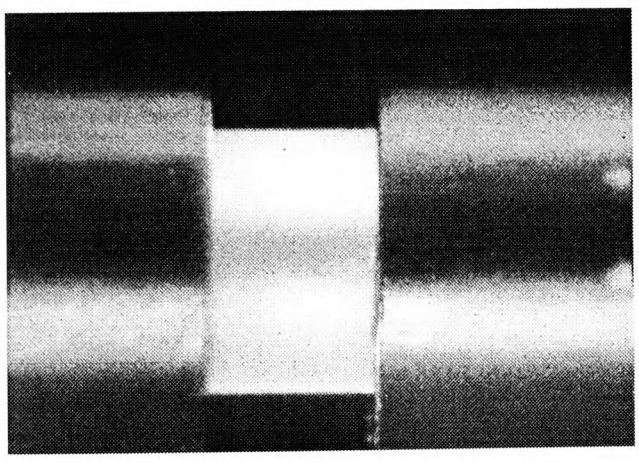

20μs

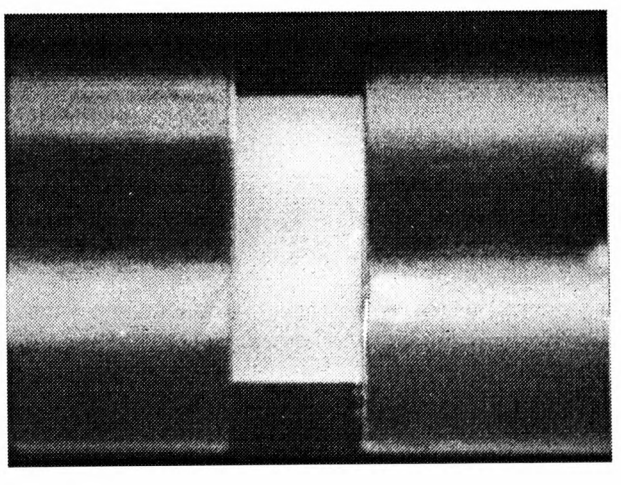

100μs

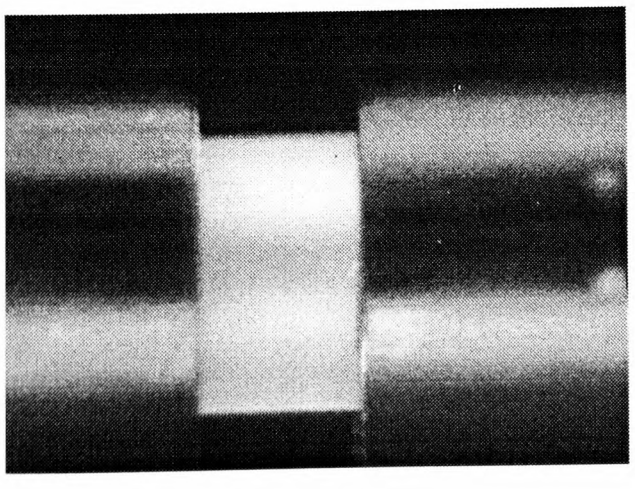

40μs

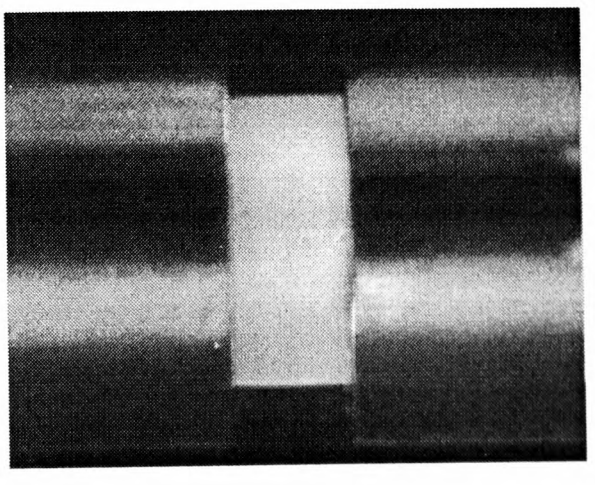

120μs

Figure 5.33a High Speed Photographs From Test: PHOTO4

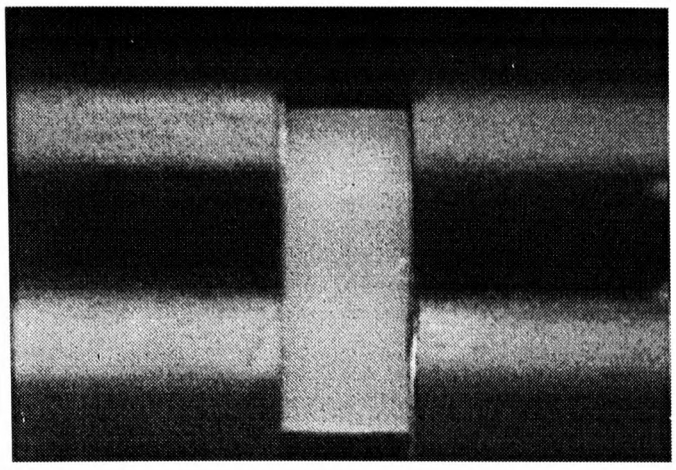

140μs

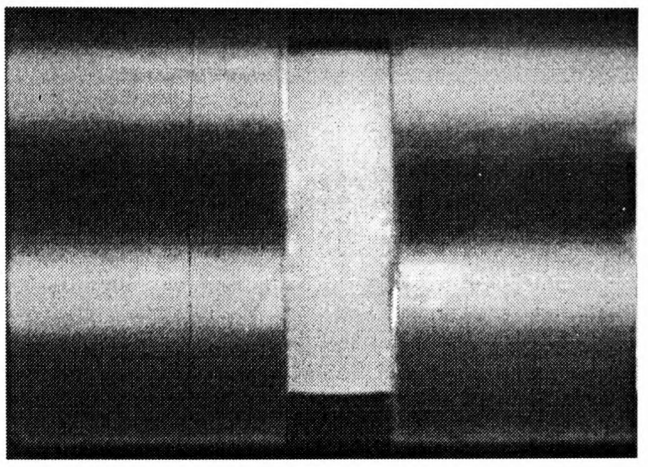

190μs

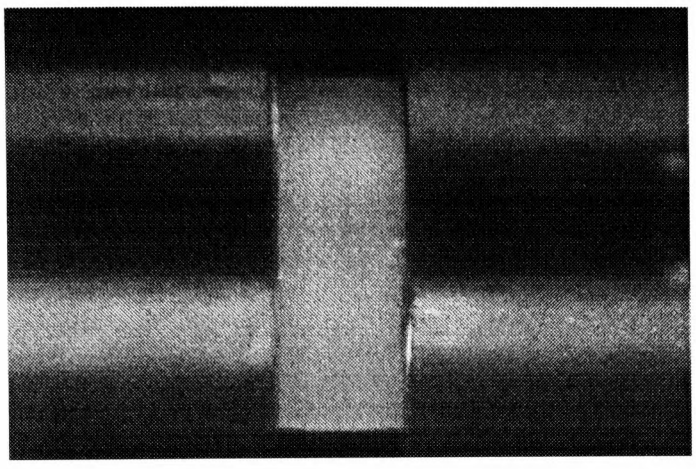

160μs

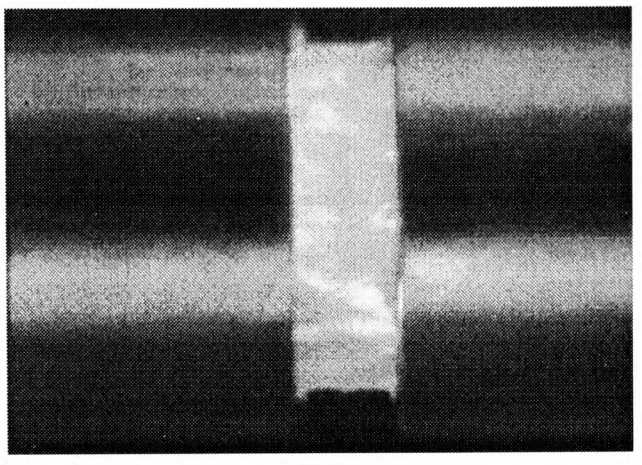

200μs

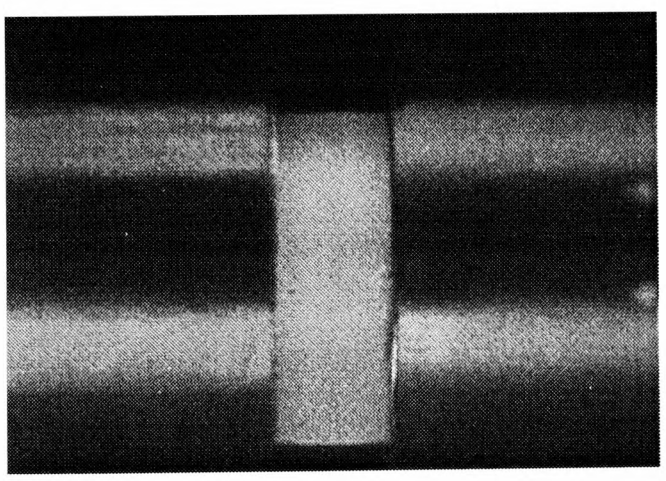

170μs

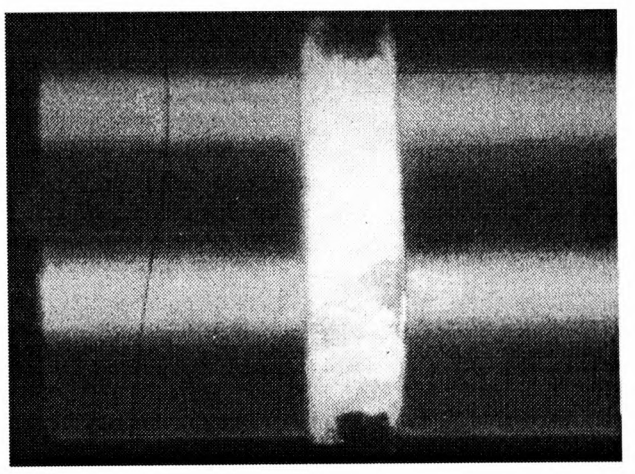

210μs

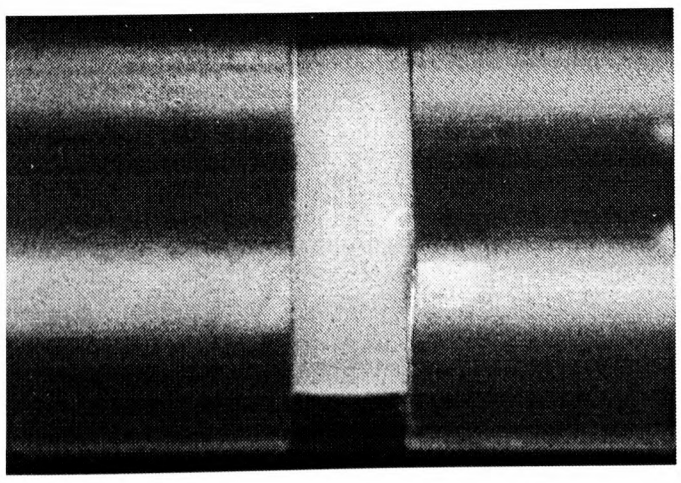

180μs

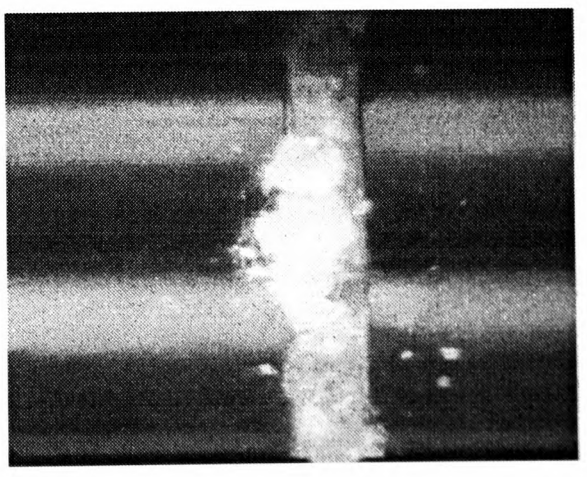

300μs

Figure 5.33b High Speed Photographs From Test: PHOTO4

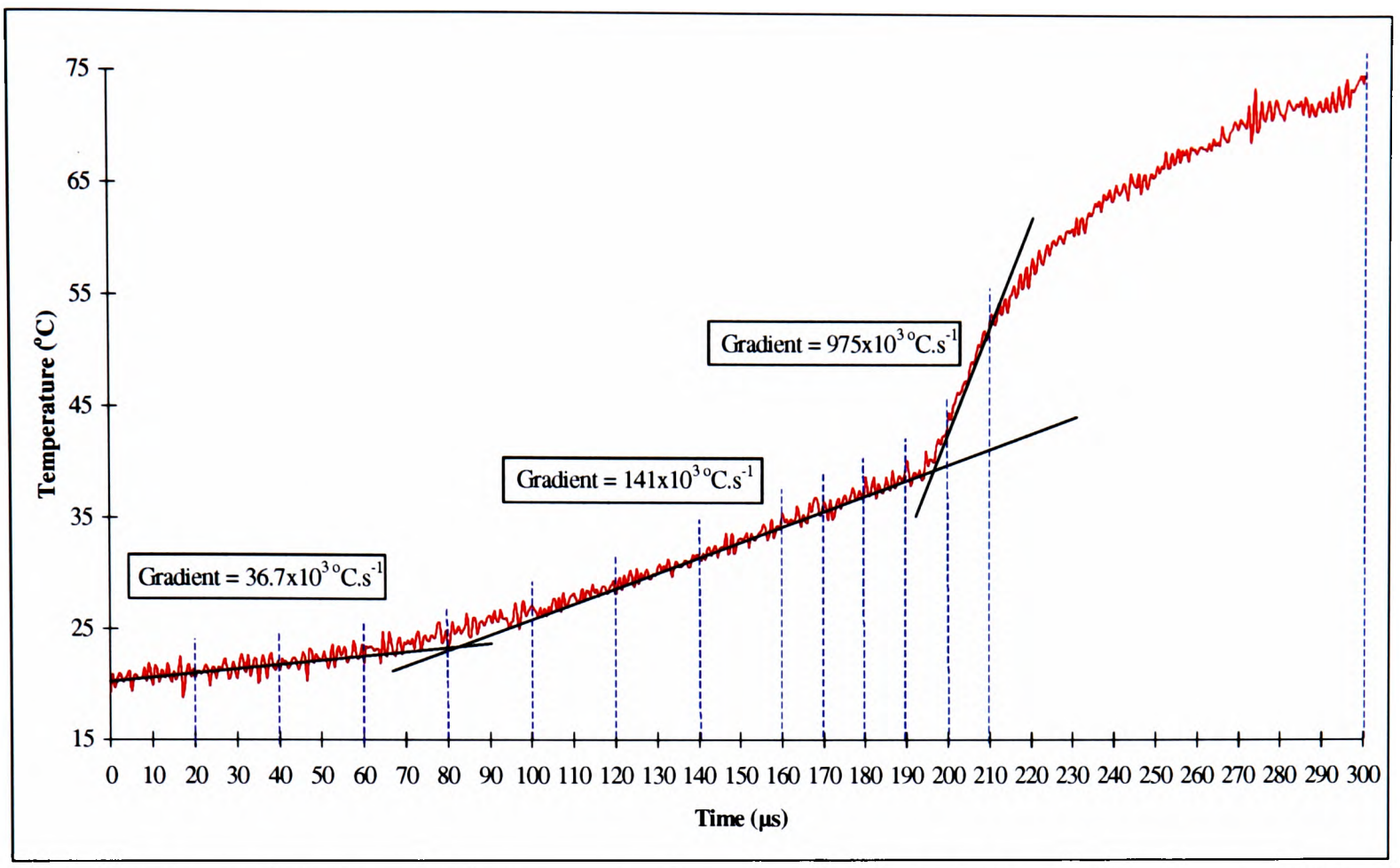

Figure 5.34 High Speed Photographs Synchronised with Mean Temperature/Time Curve for Tests: TEMP 6 to 10

5.4.3 Interrupted Tests

The purpose of these tests was to achieve an isothermal condition or, at least, to limit the amount of heat generated during the test and hence to minimise the thermal effect on the properties of the material. Two ways to achieve this aim were chosen:

- a single specimen was impacted at a velocity of 16.5m.s^{-1} to a strain of 9.5%. The deformation was limited by means of the collar shown in Figure 5.35a, and shown located on the testing apparatus in Figure 5.35b. The same specimen was then re-tested to an increased strain of 20%, using a second collar and, in subsequent stages, the strain was raised to 32%, 45% and finally 60%. These are denoted as *Single Specimen Interrupted Tests*.
- a number of specimens were tested under the same conditions as before, to a strain limited by similar collars in one single loading, i.e. one specimen was

loaded to a strain of 4.5%, a second specimen was loaded to 9%, a third to 14%, etc. up to a maximum strain of 60% for the tenth specimen. These are denoted as *Multi Specimen Interrupted Tests.*

The results of the single specimen interrupted tests are summarised in Table 5.4 and shown in Figure 5.36. The results of a single multi specimen interrupted test is shown in Figure 5.37 and summarised in Table 5.5 and Figure 5.38. In this case, the collars had windows machined in them to permit the measurement of the temperature.

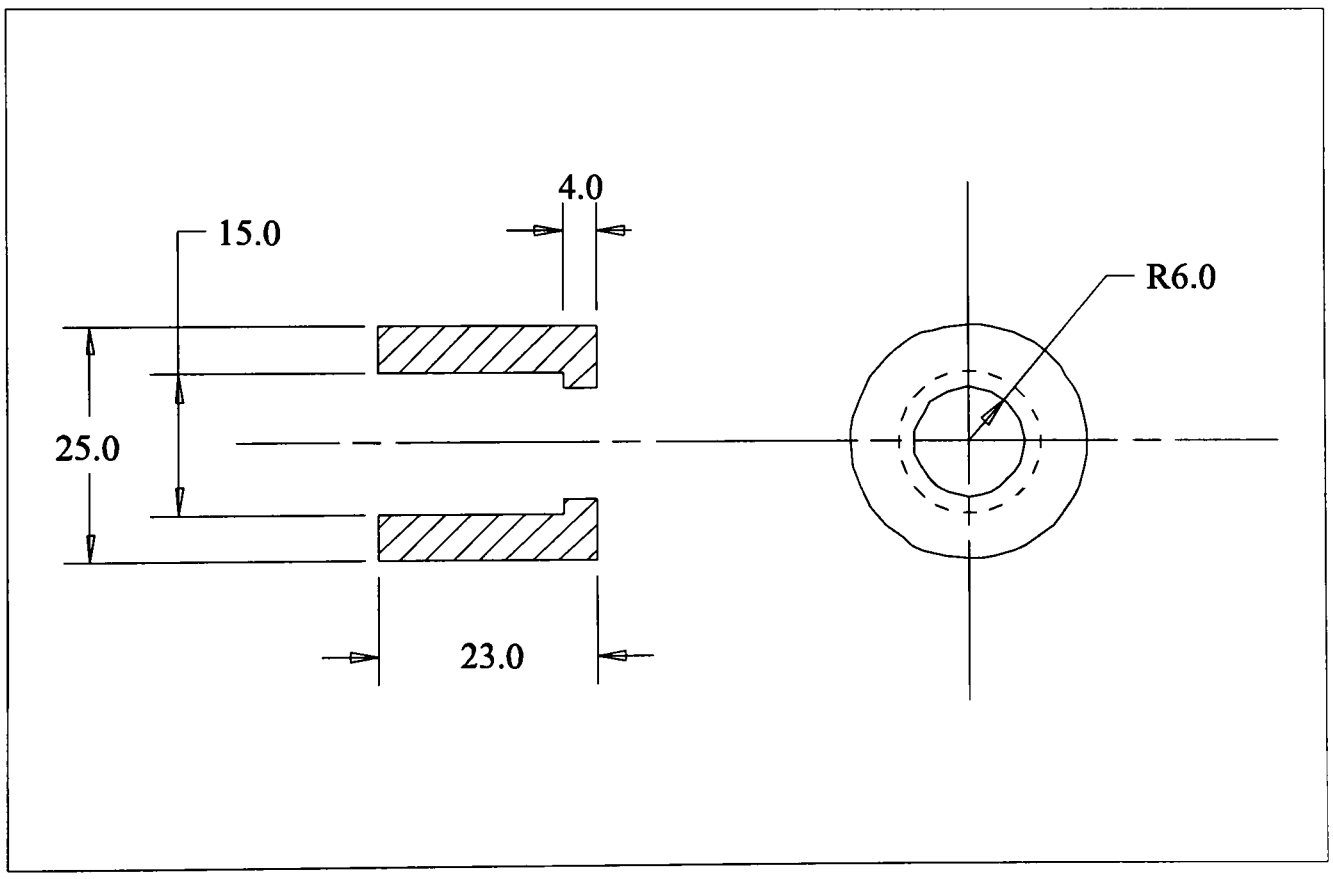

Figure 5.35a Collar Used in an Interrupted Tests

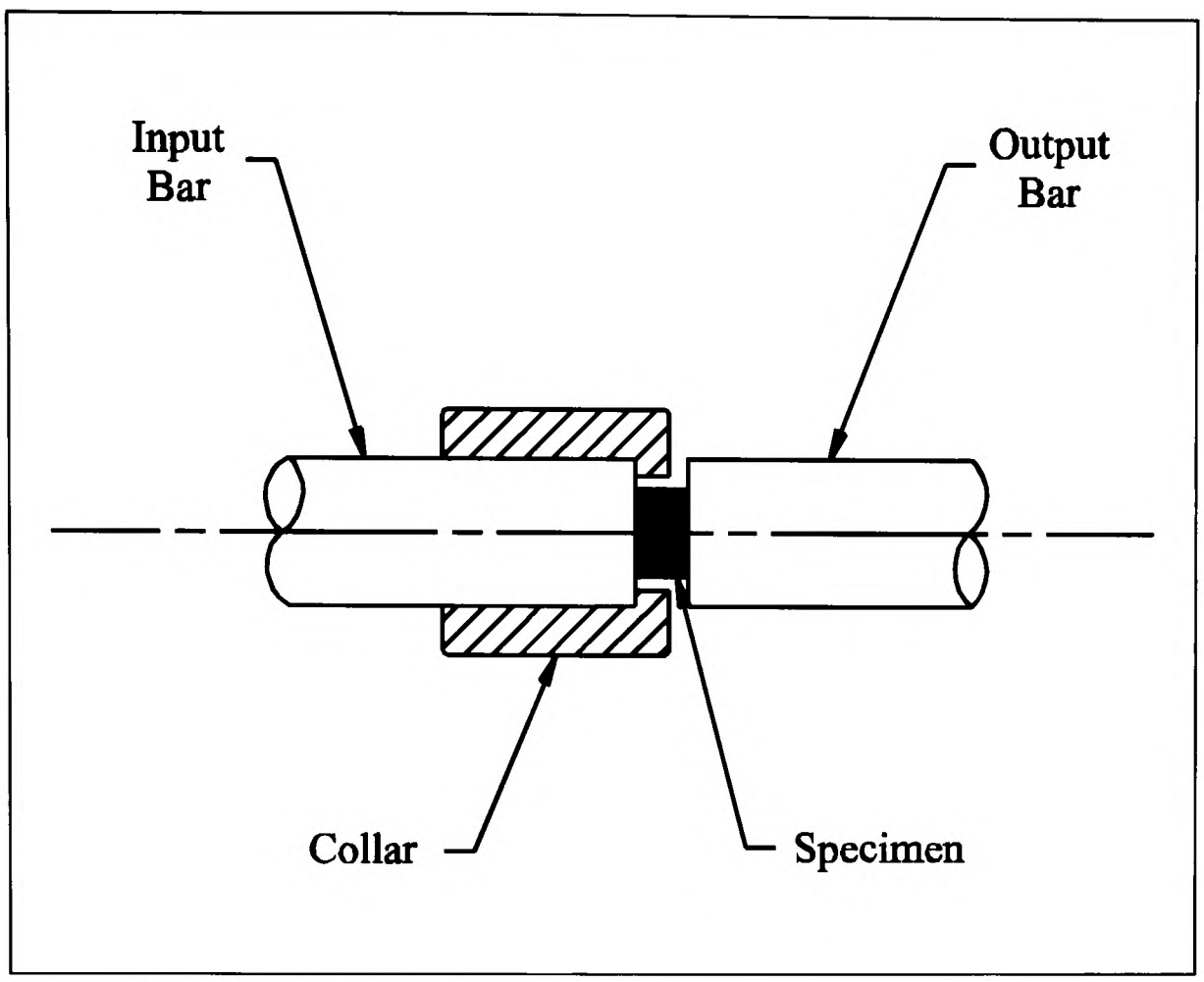

Figure 5.35b Collar Located on the split-Hopkinson Bar Apparatus

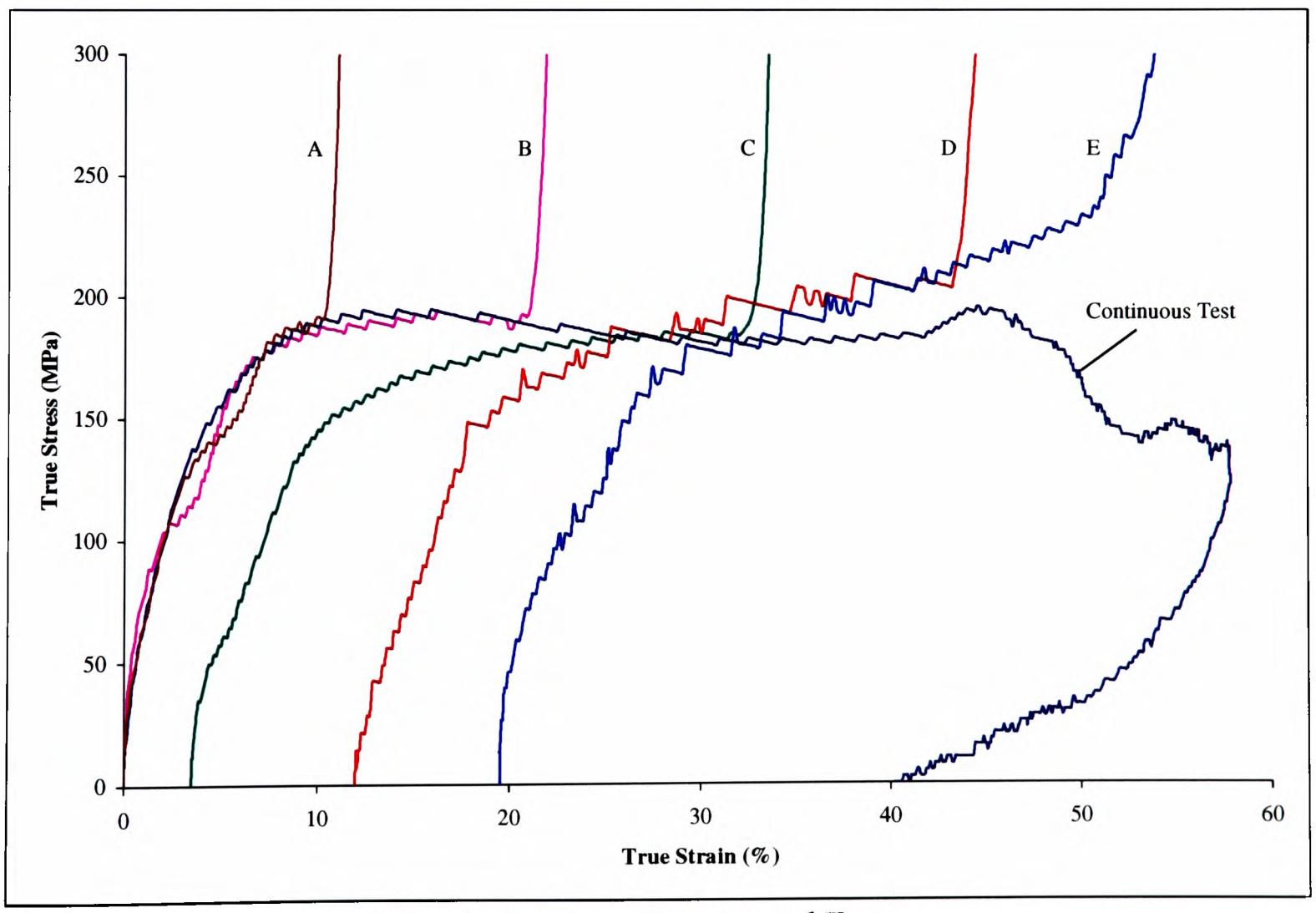

Figure 5.36 Summary of *Single Specimen Interrupted Tests*

Table 5.4 Data from Single Specimen Interrupted Tests

Test No.	Strain Increment (%)	Residual Strain (%)
A	9	0
B	20	3.5
C	32	11.9
D	45	19.5
E	60	Shattered

The results from tests TINT1 to TINT10 are brought together in Figures 5.38 and 5.39. The former shows the true stress vs true strain curves for all ten tests. The point at which the test is terminated is when the collar (located on the input bar) comes into contact with the output bar and the stress increases.

The associated temperature curves for the tests have been overlayed and presented in two ways. Firstly, Temperature vs True Strain in Figure 5.39a. Here, the temperature data is displayed only until the point of interruption in loading in which each test follows a common path until the point of interruption. Figure 5.39b shows the temperature profiles with respect to time. As seen in Figure 5.37, the rise in temperature continues to rise after loading stops, this being reflected in all tests. Markers indicating the time at interruption for each test have been omitted, since the graph becomes extremely cluttered; times are shown in Table 5.5. As expected, tests with small amounts of deformation exhibited small temperature rises. In a few tests, some electrical spikes affected parts of the data. These were occasional and random events and should be ignored.

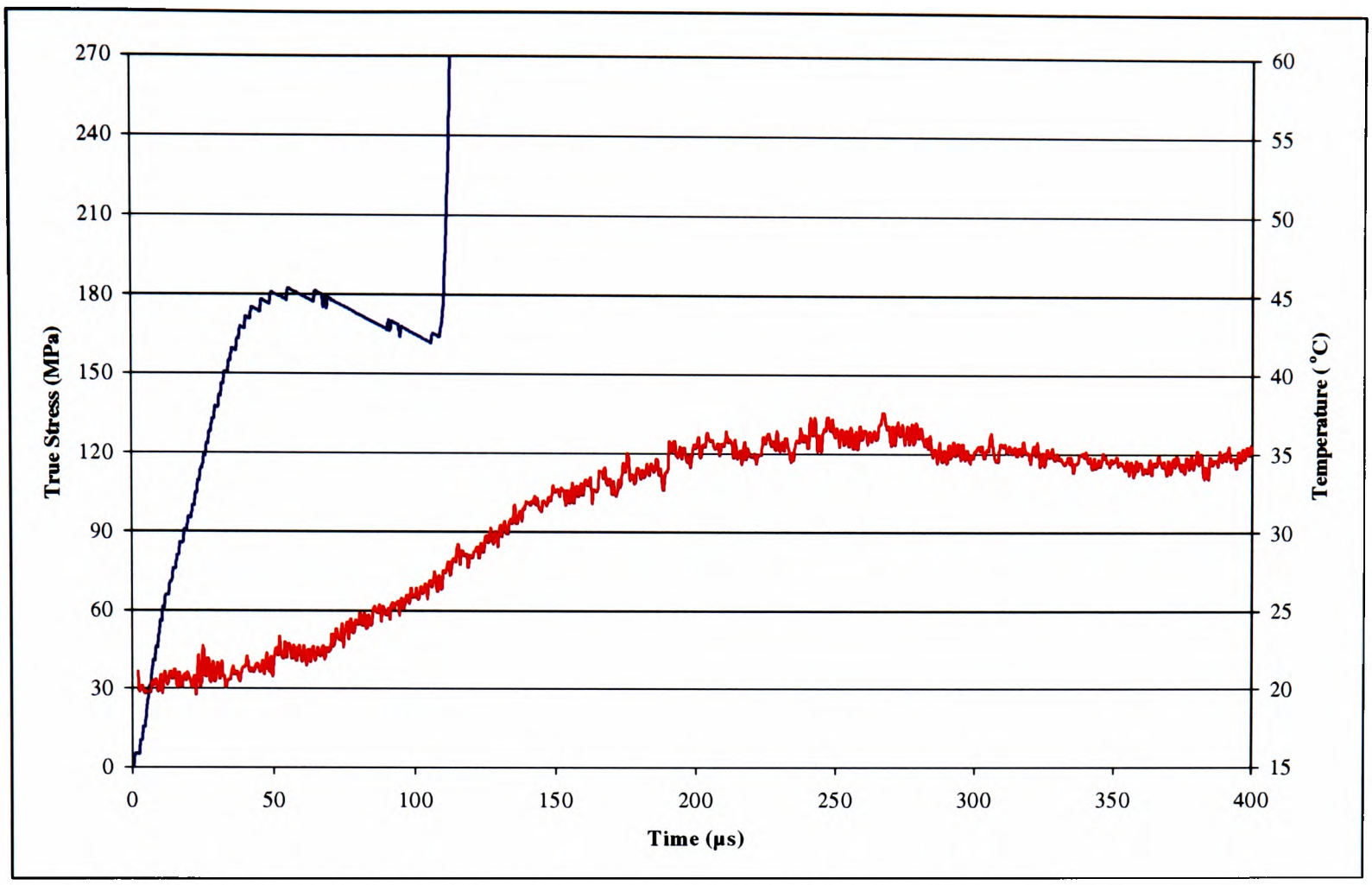

Figure 5.37 A Sample *Multi-Specimen Interrupted Test*: TINT1

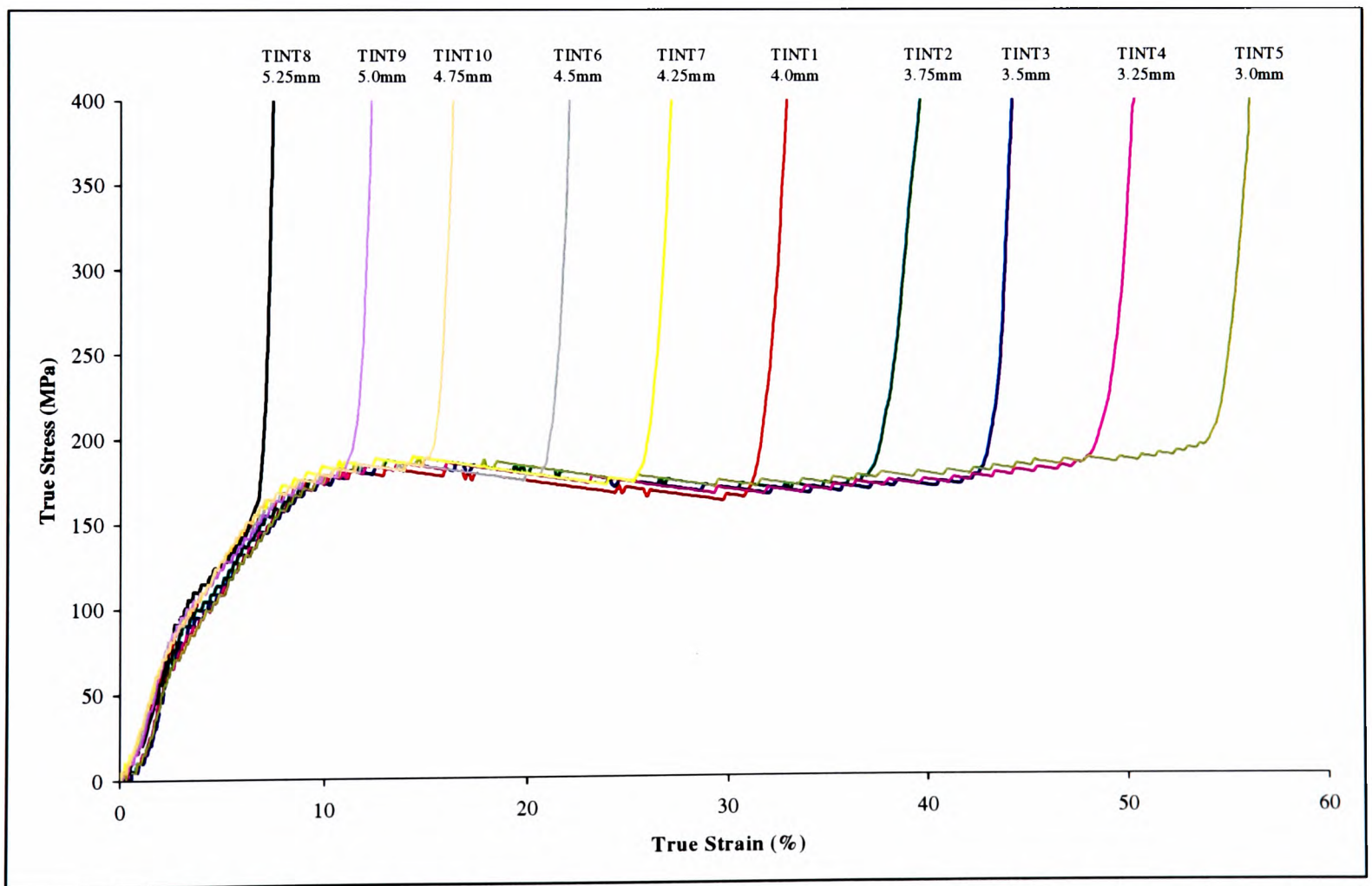

Figure 5.38 Combined True Stress vs True Strain Curves for *Multi Specimen Interrupted Tests*: TINT1-10

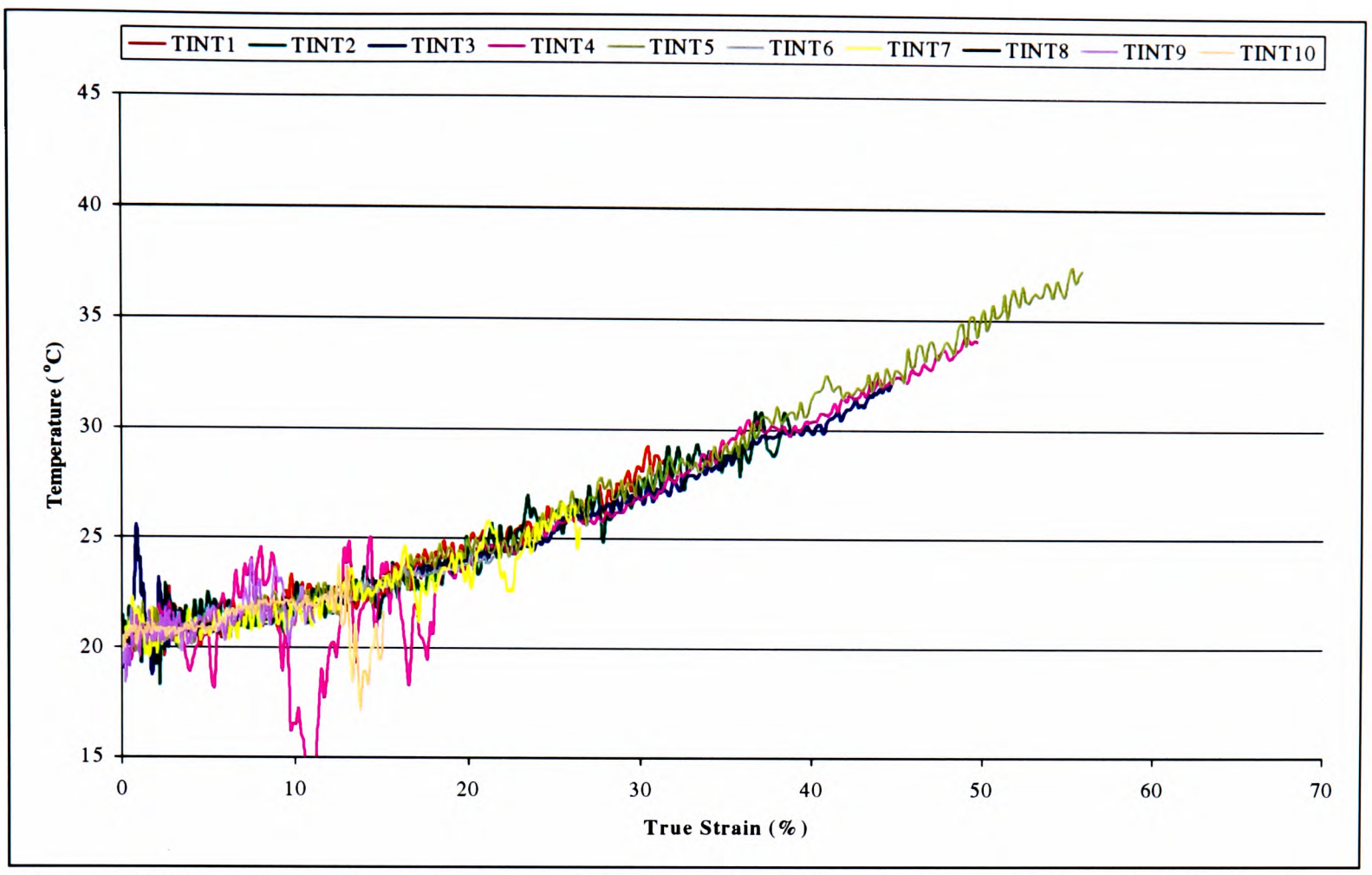

Figure 5.39a Combined Temperature vs True Strain Curves for *Multi Specimen Interrupted Tests:* TINT1 to TINT10

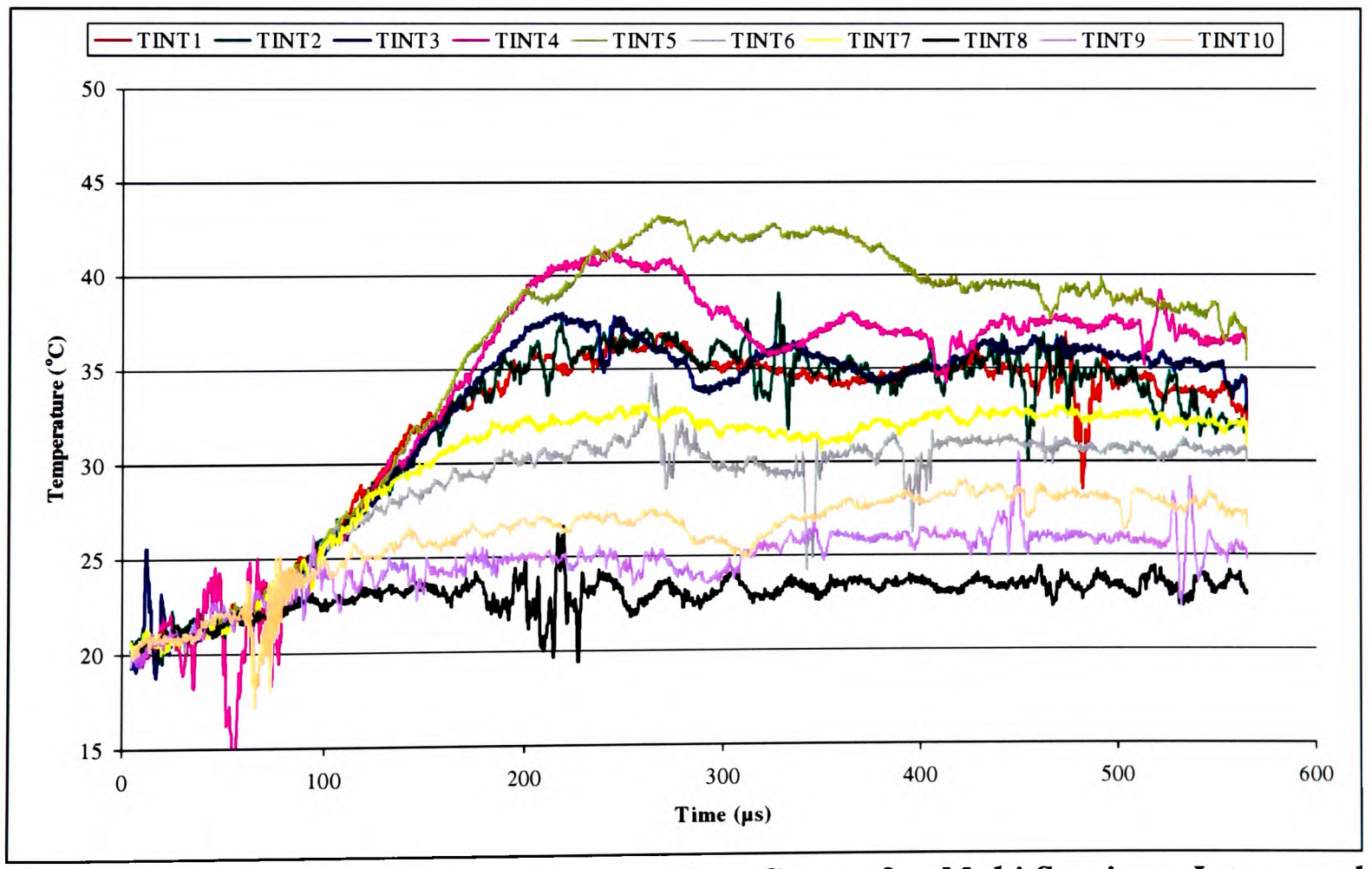

Figure 5.39b Combined Temperature vs Time Curves for *Multi Specimen Interrupted Tests:* TINT1 to TINT10

Table 5.5 Summary of Continuous Interrupted Tests with Temperature Measurement

					At Yield[1]		At Interrupt				Max Temp.	
Test #	Collar Size	AvStrain-Rate	Impact Vel.	Res. Strain(%)	T.Stress (MPa)	T.Strain (%)	T.Stress (MPa)	T.Strain (%)	Time (µs)	Temp (°C)	Time (µs)	Temp (°C)
TINT1	4.0	2410	16.6	14.3	180	13.0	164	31.0	120	27.5	240	36.25
TINT2	3.75	2380	16.5	18.8	188	14.0	180	39.0	137	29.75	245	36.5
TINT3	3.5	2440	16.6	22.5	184	12.5	180	44.5	150	31.25	215	38.0
TINT4	3.25	2390	16.6	24.2	184	13.75	184	49.5	165	34.0	230	41.0
TINT5	3.0	2390	16.6	24.4	186	14.5	190	55.5	177	37.0	265	43.0
TINT6	4.5	2310	16.6	2.2	186	12.5	182	21.0	90	23.5	225	31.0
TINT7	4.25	2360	16.6	8.8	186	12.5	172	26.5	105	26.0	245	32.75
TINT8	5.25	1810[2]	16.6	0	n/a	n/a	171[3]	5.0[3]	40	21.0	120	23.5
TINT9	5.0	2100[2]	16.6	0	n/a	n/a	180	11.0	58	21.0	170	24.25
TINT10	4.75	2210[2]	16.6	0	186	12.5	186	15.0	70	22.5	70	28.5

[1] The term 'yield' is used somewhat loosely, since this is an undefined area in the deformation of visco-elastic materials.
[2] The duration of the test was so short that the strain-rate had not yet stabilised.
[3] Difficult to resolve where the sharp increase in stress begins as loading is still in early stages.

5.5 References

Briscoe, B.J. & Nosker, R.W., The Influence of Interfacial Friction on the Deformation of HDPE in an SHPB, Wear, 95, pp.241-262, 1984.

McCrum, N.G., Buckley, C.P., Bucknall, C.B., Principles of Polymer Engineering, Oxford University Press, 1988.

Pogany, G.A., "The Elastic and Viscoelastic Properties of Epoxy Resins", D.Phil. Thesis, University of Oxford, 1967.

Walley, S.M. & Field, J.E., Strain-Rate Sensitivity of Polymers in Compression from Low to High Rates, DYMAT, 1, No.3, pp.211-227, 1994.

Chapter 6

Interpretation of Results

6.1 Preliminary Tests

It has been shown that a large number of tests have been performed in order to determine a suitable specimen geometry for the advanced testing programme. The test results varied considerably with geometry and strain-rate and it may be possible to place such variations into trends, possibly three dimensional trends.

Data from the preliminary tests was examined by plotting characteristic points, such as the 'yield stress' (taken to be the peak stress) and failure stress for tests where the length was varied but diameter was kept constant, and vice versa. The testing matrix, in Table 5.1, enabled such comparisons to be made as there is sufficient scope in specimen aspect ratio. In this way, geometrical effects could be isolated and a proper judgement made on a particular suitability.

6.1.1 Effect of Lubrication

The lubricant used in this investigation was petroleum jelly. Immediate observations of lubricated/unlubricated results show an overall tendency for graphs to show similar

characteristics. That is to say that the lubricated test follows a similar path to the unlubricated stress-strain graph albeit at a lower flow stress. Indeed, lubrication is seen to decrease the flow stress for some aspect ratios by between 5% to 15%. A comparison can be seen in Figure 6.1.

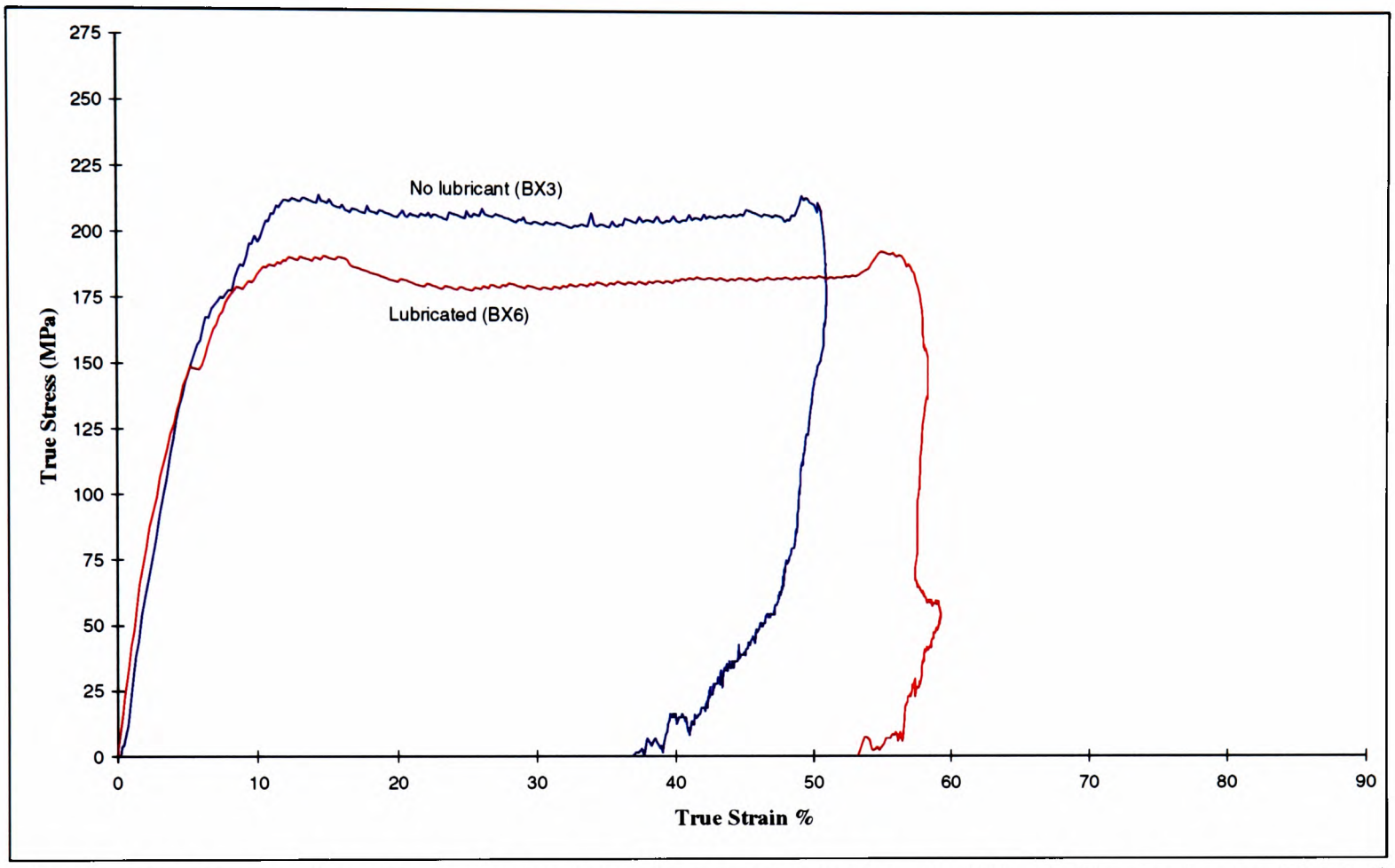

Figure 6.1 Comparison Between Lubricated and Unlubricated Test, Strain-Rate ~2250s^{-1}

In most cases, lubricated and unlubricated curves follow identical elastic paths, but then tend to diverge upon approaching the 'yield stress'. It is observed that the unlubricated specimen then shows an enhancement in flow stress over the lubricated case, this being equal to the constraining end effect which hinders the uniform flow and deformation within the specimen. These differences tend to decrease and sometimes disappear at higher strain-rates, as seen in Figure 6.2, resulting in a 'yield stress' which has increased for the lubricated case and lowered in the unlubricated case, as compared to a test at lower strain-rate. This could however simply be a strain-rate effect for the lubricated case, while for the yield stress to be lower for the unlubricated condition may be attributed to experimental error. The diminishing

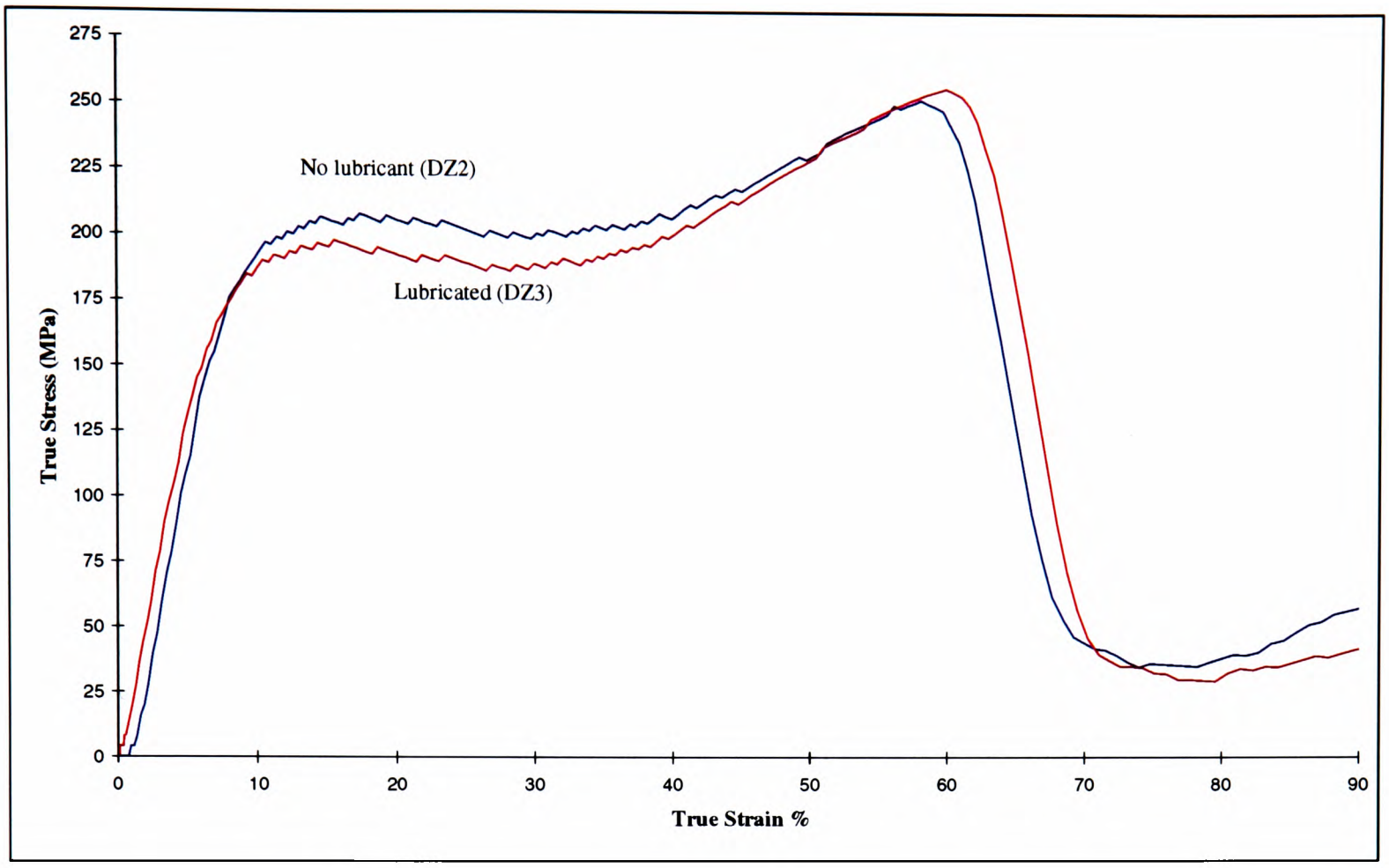

Figure 6.2 Difference Between Lubricated and Unlubricated Tests, Strain-Rate~ 3750s^{-1}

difference could possibly indicate that the lubricant is becoming ineffective at the higher strain-rates. The value of strain observed at failure, or unloading depending on strain-rate and size of specimen, is also seen to be sensitive to lubrication in the aforementioned manner. The main effect of lubricating the specimen/bar interface was to increase the value of strain at which the specimen fails. Lubrication allows the specimen to deform freely and with minimum constraint. At the highest strain-rates, this difference is almost reduced to zero. Additional examples of the effect of lubrication are shown in Section 6.1.2 below.

In general, it was found that for strain-rates of up to 3000s^{-1}, lubrication of the specimen ends caused an increase in the strain at which failure occurred. In all cases the strain measured at failure, or in cases where failure did not occur, the strain measured at the point when deformation ceased, was greater for lubricated specimens than for the unlubricated ones. It is noted that as the specimen size decreases and the strain-rate increases, the differences between

the lubricated and unlubricated graphs tends to reduce. The smaller specimens, which were able to be tested at higher strain-rates, show what appears to be a strain hardening effect. The stress at failure at these conditions for both lubricated and unlubricated tests are comparable. As specimen size is decreased and with increasing strain-rate, it was seen that the influence of lubrication became less. This could be simply due to the high rate of compression when the lubricating properties of the petroleum jelly become redundant.

6.1.2 Effect of Changing Dimensions

For very large specimens such as AX & AY with a common length of 8mm and diameters of 12.7mm and 9mm respectively, there was no appreciable difference in flow stress, shown in Figure 6.3. When working with such large specimens, the strain-rate is kept very low ($\sim 1000 s^{-1}$). Some tests were performed at impact velocities of about $18 m.s^{-1}$ but these velocities are bordering on the upper limit of the gun's capabilities and strain gauge failure is a likely consequence. However, impact velocities of approximately $18 m.s^{-1}$ were performed on AX specimens but repeatability was severely impaired.

Tests with specimen dimensions BX & BY (at an average strain-rate of $\sim 2000 s^{-1}$) exhibited a marked difference in yield stress when specimen ends were lubricated, approximately 25MPa, seen in Figure 6.4. The difference in the flow stress when moving from BY to BX, with the respective diameters increasing from 9mm to 12.7mm, was less than 5MPa for the lubricated case and approximately 10MPa for the dry (unlubricated) condition. If we compare tests of shorter length again, in this case CX to CZ in Figure 6.5, we see that as the diameter of the specimen decreases from12.7mm to 9mm (CX to CY) at an average strain-rate of $\sim 2250 s^{-1}$, the lubricated case remains at a constant stress, whilst the unlubricated case

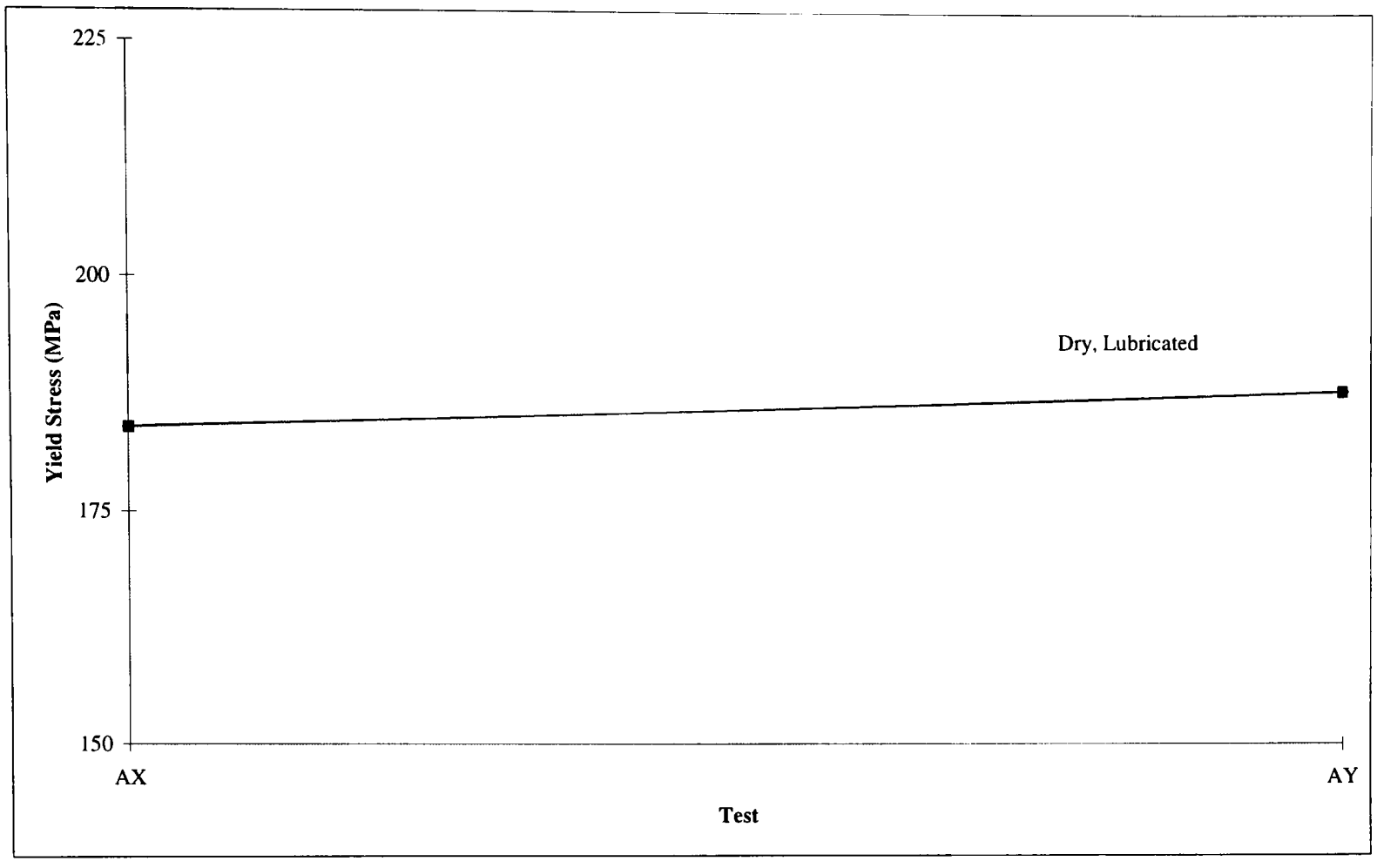

Figure 6.3 Differences in Yield Stress for AX & AY Specimens

shows a marked decrease. This is despite a small increase in strain-rate of ~500s^{-1} for CY, but this is a relatively small change as far as strain-rate effects are concerned. It is known that the hydrostatic component of the applied stress is largest in the case of thin discs, i.e. specimens with a small aspect ratio, L/D. The lubricated condition of CX to CY experience a drop in stress of about 2MPa, so it would appear that the significance of σ_h is negligible and that the decrease in stress can be wholly attributed to the change in end conditions, i.e. lack of lubrication. Moving from CY to CZ gives an increased stress, even for the lubricated case. This is assumed to be a small strain-rate effect, since CZ specimens were very small and resulted in an average strain-rate of about 3000s^{-1} being achieved. The fact that both conditions experienced similar increases would lead to this conclusion.

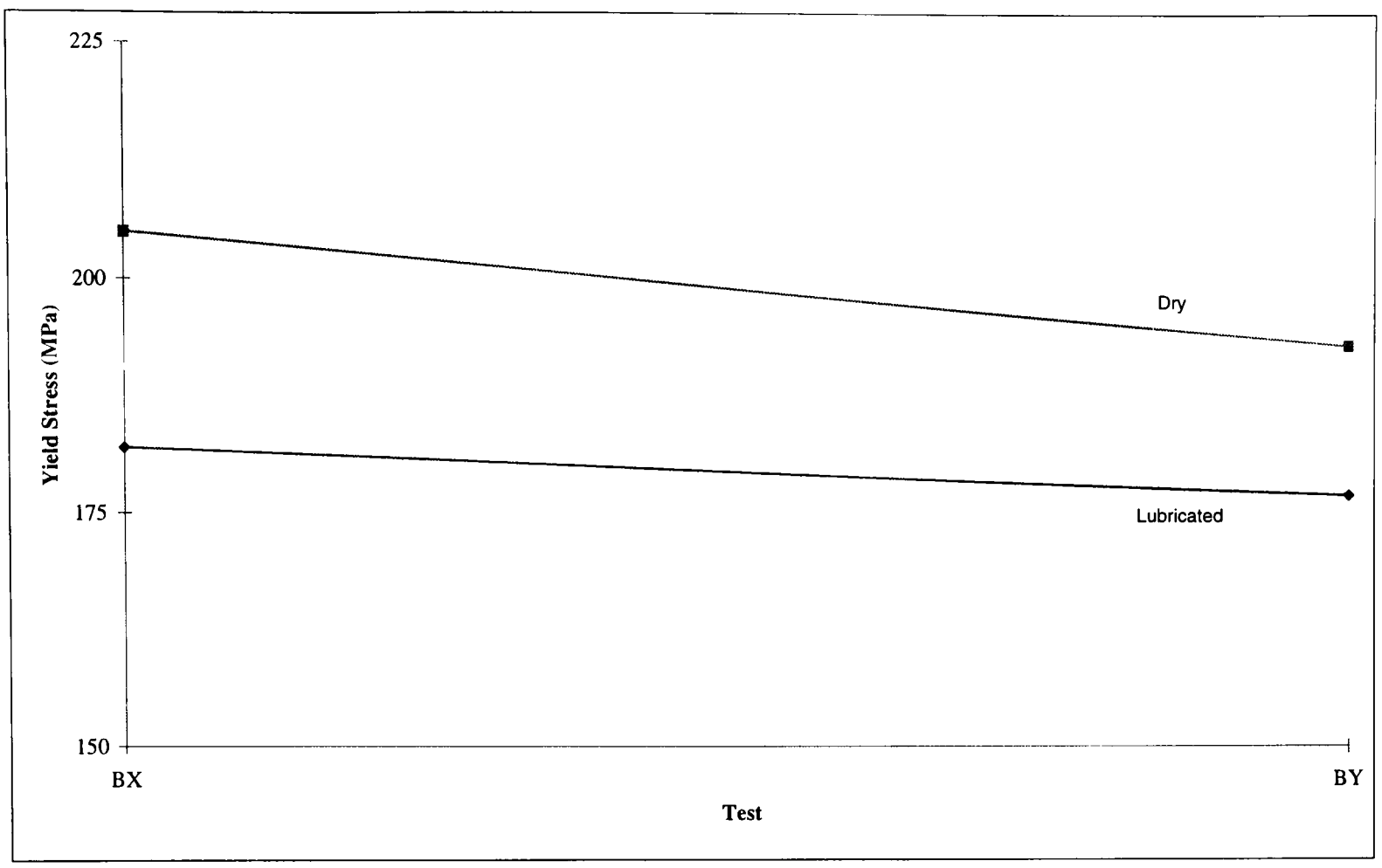

Figure 6.4 Variations in Yield Stress for BX & BY Specimens

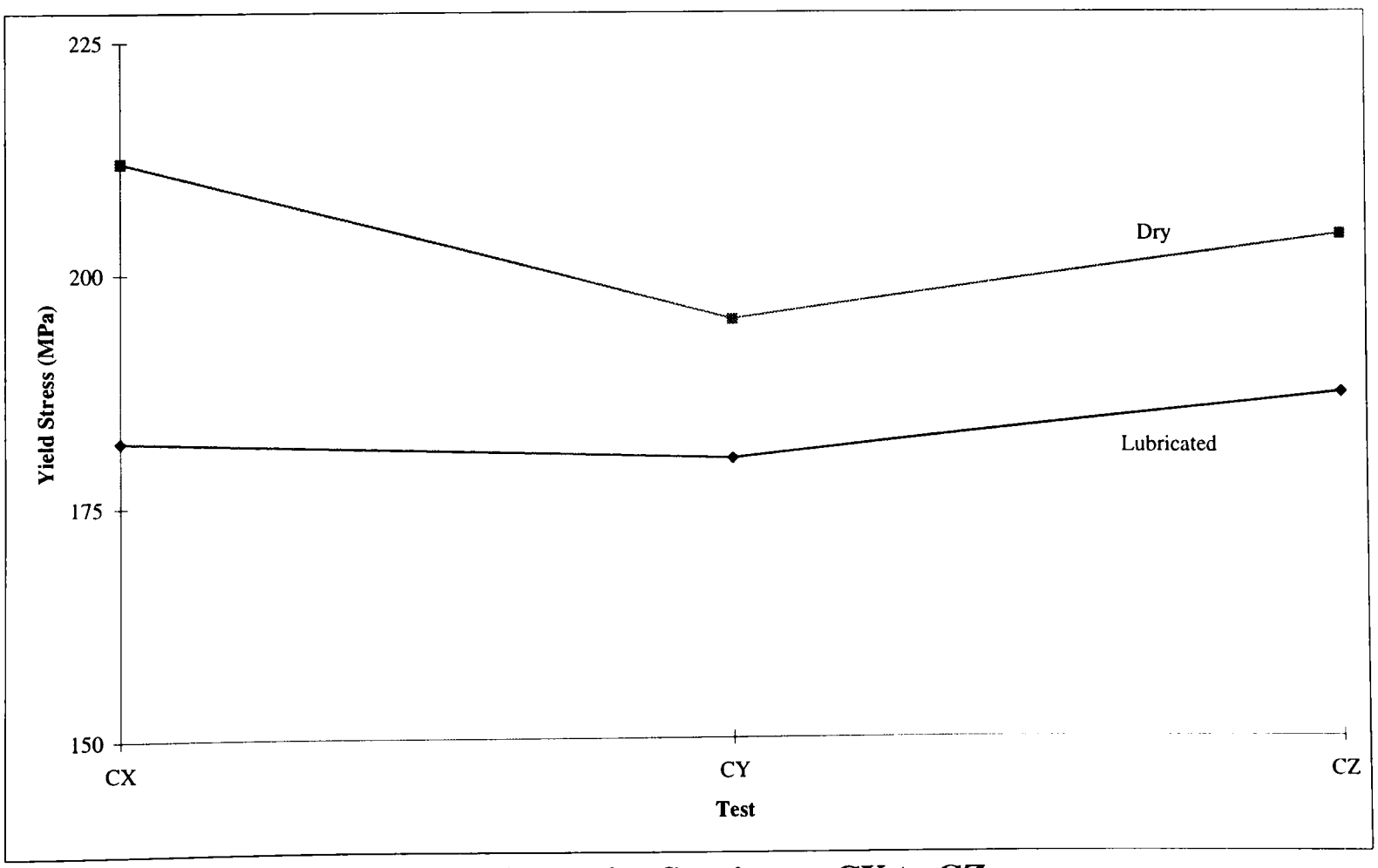

Figure 6.5 Variations in Yield Stress for Specimens CX to CZ

Figure 6.6 shows the variations in stress for specimens DX, DY and DZ, which have a constant length of 2.8mm and a changing diameter from 12.7mm through to 6.4mm respectively. The observation for the previous set of results (CX to CZ) apply to this case also, in which the DX specimen has a greatly enhanced yield stress with respect to its lubricated counterpart. This type of specimen is the thinnest disc of greatest diameter. Hence, any hydrostatic effects would be at their most prominent. Clearly, these effects are very small, approximately ~2MPa from DX to DY, and ~15MPa for dry specimens. Again a strain-rate effect is assumed to be responsible for the upturn in stress for DZ. Here, very short specimens are used and a combination of effects could influence the overall behaviour, such as interaction between ends, barrelling and a complex state of stress.

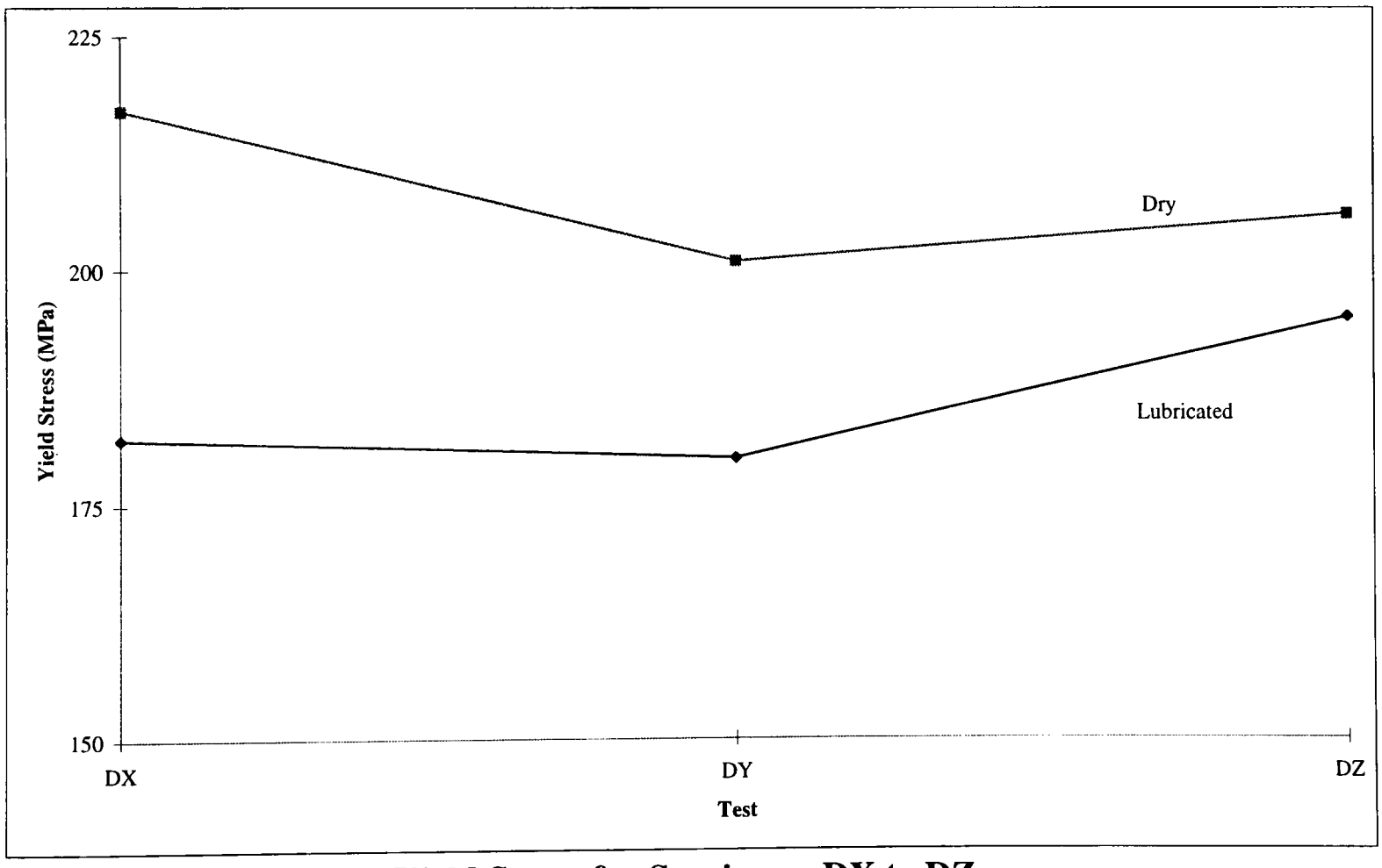

Figure 6.6 Variation in Yield Stress for Specimens DX to DZ

Similar graphs have been constructed for specimens whose diameter varies with constant length. Figure 6.7 shows specimen AX to DX, of constant diameter 12.7mm (X), and

lengths varying from 8mm (A) through to 2.8mm (D). For the dry specimens, the graph shows that the yield stress increases as length decreases. With friction present at the specimen/bar interfaces, σ_h increases significantly with reducing L/D. The absence of friction in lubricated tests (for decreasing length) shows that the yield stress is maintained at a near constant value, showing there is no effect from σ_h. Figure 6.7 is perhaps the clearest picture of a clouded situation. The data is complicated by the fact that as the length of specimens decreases the strain-rate increases and maintaining a constant strain-rate for all aspect ratios is difficult to achieve.

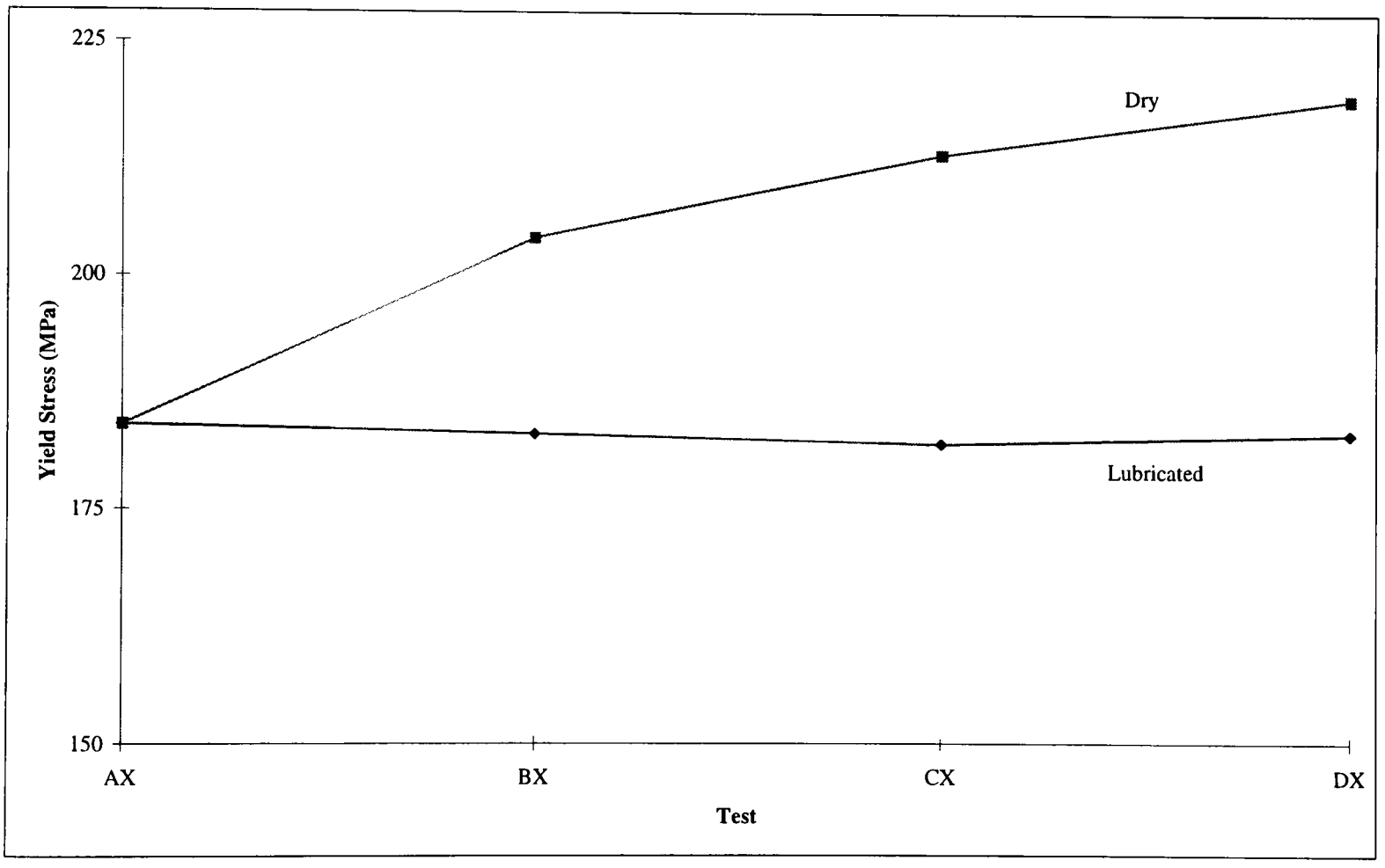

Figure 6.7 Variation of Yield Stress for Specimens AX to DX

Similar results were obtained for AY to DY tests, shown in Figure 6.8, as were shown in Figure 6.7. As before, after no difference in stress for end conditions of dry and lubricated tests, the yield stresses tend to diverge. CY experiences an unexpected dip, but is most likely to be a rogue result. Again it is observed that the lubricated series of data shows none of the

traits of increasing hydrostatic pressure. In fact, the stress decreases at a faster rate than previously, indicating that the lubrication is becoming more effective.

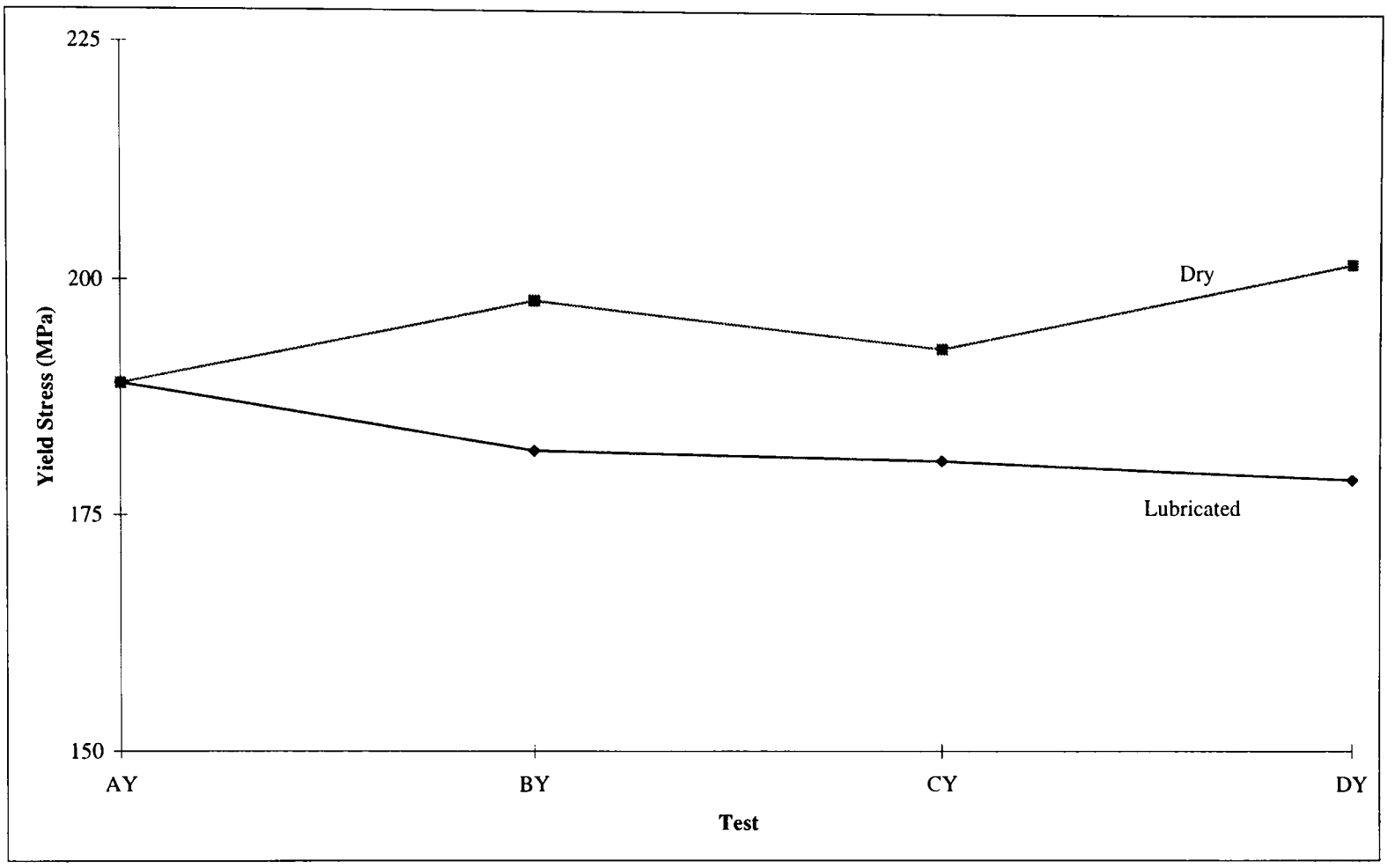

Figure 6.8 Variations in Yield Stress for Specimens AY to DY

The final graph of this series, Figure 6.9, compares specimens CZ and DZ. There are only two specimen geometries to compare, but it shows an increase in yield stress with decreasing length. The strain-rate is slightly higher for DZ, by approximately $750s^{-1}$, which could be effecting the flow stress.

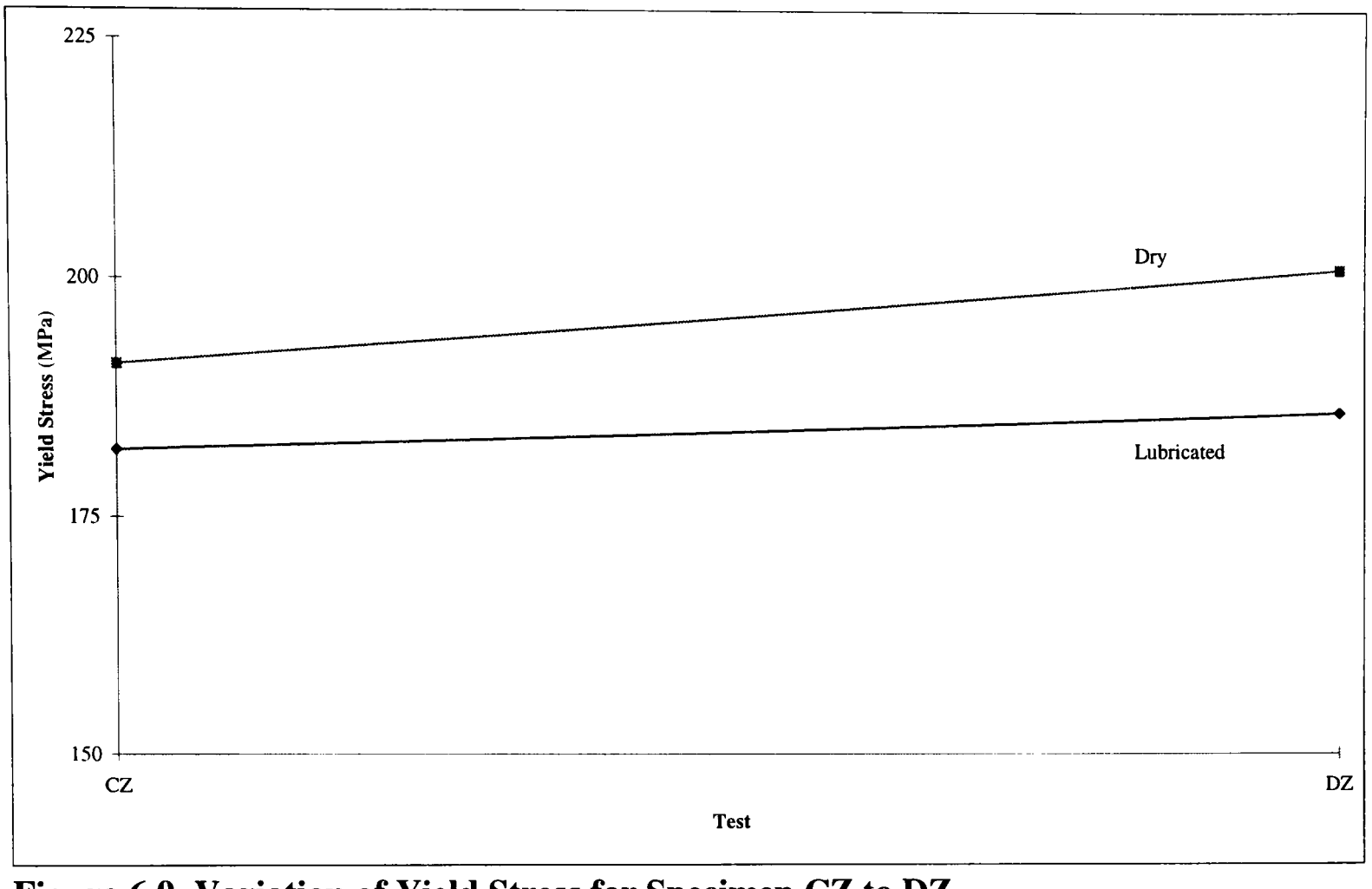

Figure 6.9 Variation of Yield Stress for Specimen CZ to DZ

The large quantity of information is shown in graphs which are at more or less constant strain-rate. However to show the strain-rate effect, three quantities, i.e. strain-rate, aspect ratio and yield stress have been shown as three dimensional surface plots. Each quantity affects the other and so it is important to show such information which will usually expose trends not seen in two dimensional plots. Figure 6.10 shows how the yield stress varies with strain-rate and aspect ratio for lubricated tests only. The trend shows a small strain-rate dependance for most aspect ratios. For strain-rates of approximately $3000s^{-1}$ a marked drop in yield stress is observed..

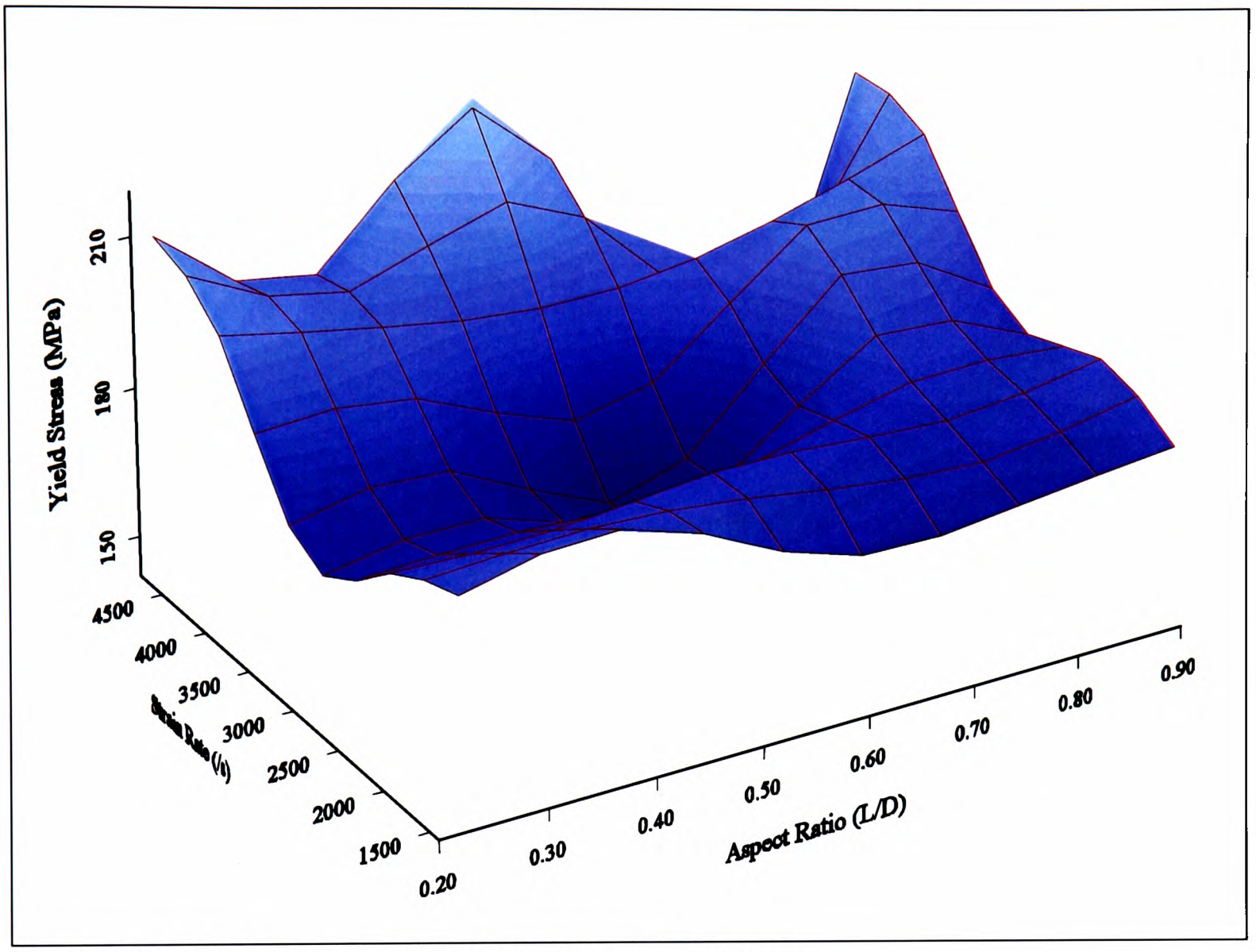

Figure 6.10 Yield Stress vs Strain-Rate vs Aspect Ratio

A similar graph has been constructed showing the stress at failure with respect to strain-rate and aspect ratio. Here a fairly clear rate dependance is shown, be it a rather bumpy surface plot, but the general trend is upwards, seen in Figure 6.11. The large increase in failure stress at around the aspect ratio value of 0.9 and strain-rate of approximately $3200s^{-1}$ should be ignored as this is a result of the computer program used to fit a surface to the points, which has extrapolated points at large L/D and low strain-rate, and also at constant strain-rate of approximately $3000s^{-1}$.

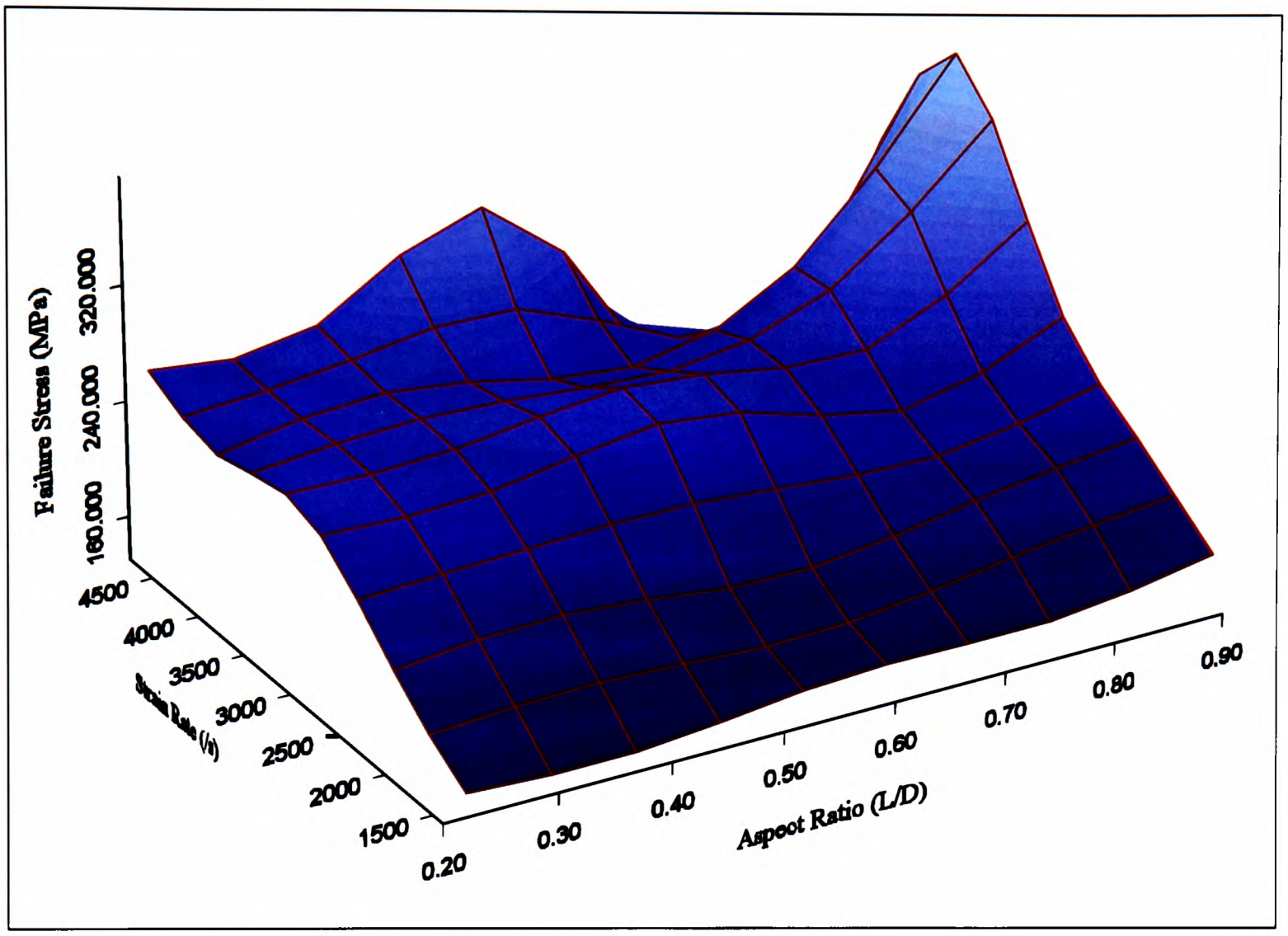

Figure 6.11 Failure Stress vs Strain-Rate vs Aspect Ratio

Considering the observations made of test data for a variety of specimen sizes, strain-rates and specimen lubrication conditions, it was necessary to choose a size of specimen for use in the second stage of the testing programme. The conditions which needed to be met when choosing the optimum sized specimen would be:

- Consistent and repeatable results
- Minimum contribution of end constraint to results
- Minimum contribution of σ_H to results
- Optimum L/D ratio (dependant on all of the above)

Results of all tests have been shown to be very repeatable when compared with other tests of identical aspect ratios. Some anomalies do exist though. In very short and thin specimens, such as CY, there is a consistent dip in stress on approaching yield, a reproducible result, but one which is out of character with the rest of the data. This fairly isolated feature occurred occasionally in DY as well. Therefore, thin short specimens will not be considered.

Lubrication was shown to be very important and this was illustrated best by Figure 6.7 where a large difference in yield stress was observed between lubricated and unlubricated conditions. The magnitude of this effect varied with specimen size, but generally, once a specimen was lubricated, there was little difference in yield stress. This excludes the highest strain-rate tests (DY & DZ for example) which have been discarded, due to unexpected dips in stress before yield.

The hydrostatic component has a negligible effect on results up to 20% strain, in the order of 2MPa, so this was not a deciding factor in which specimen size to choose.

Specimens of short gauge length have been discarded due to possible end interactions/effects. This excludes specimens of very short lengths, i.e. D. Large specimen sizes (AX & AY) will also be avoided, since the range of strain-rates is limited and failure cannot be achieved, even when operating the gun at its maximum capacity. The remaining specimen lengths were 5.5mm and 4.0mm. Both BX and CX have a reproducibility band which is bettered only by BY and CY. With CZ, it is difficult to achieve consistency. In view of the next phase of testing, it was decided to adopt the BY specimen (diameter 9.0mm and length 5.5mm) for use in further tests since this has shown to give very consistent and repeatable results for a range of strain-rates, and having a longer gauge length that CY would in turn enable the radiometer to view the specimen for longer.

6.2 Continuous Tests

Quasistatic, intermediate and high strain-rate tests were done to show the effect of strain-rate on the polymers mechanical behaviour. The stress/strain curves from three tests have been plotted on one graph to demonstrate this effect, seen in Figure 6.12.

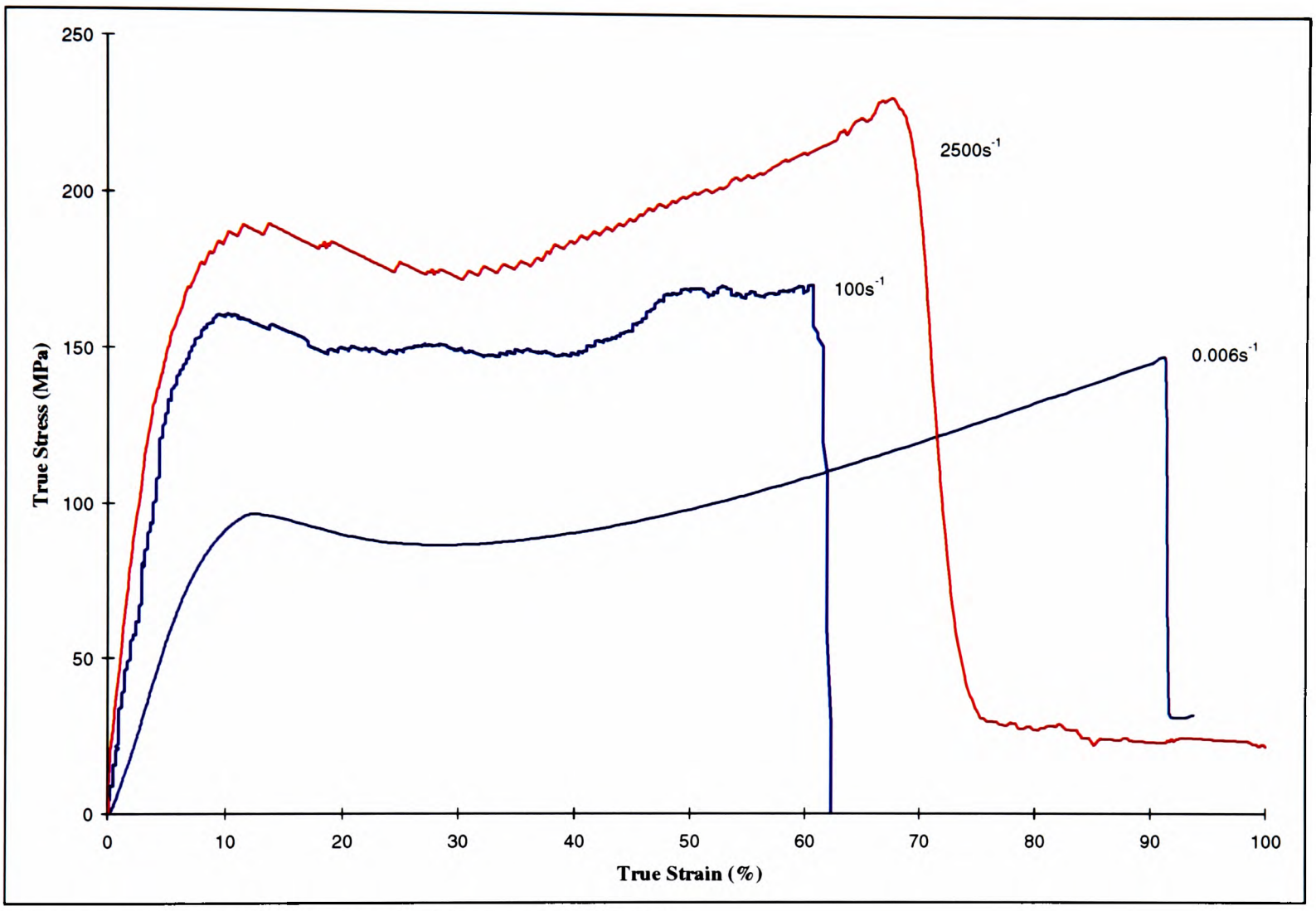

Figure 6.12 Effect of Strain-Rate on LY-564

In all three cases, the specimen was tested to failure at the strain-rates marked on the graph. Clearly, the yield stress is rate sensitive and shows an increase by a factor of almost 2. The stiffness of the material is also rate dependant, shown by the increase in slope. The failure strain decreases with increasing strain-rate, with the exception being the test of intermediate strain-rate. It would be this test rather than the high rate one which is likely to be suffering from inadequate lubrication. Both PTFE film and petroleum jelly were tried and PTFE gave best results. The point of transition from PTFE to petroleum jelly to provide best lubrication is

unknown precisely, but is between $10^2.s^{-1}$ and $2x10^3.s^{-1}$.

In high rate tests a drop in the flow stress of between 11.1 and 13.4MPa is observed at approximately 30% true strain, which is due to the evolution of the orientation process of the polymer chain network. Weak secondary bonds are broken and bond rotation begins and individual chains are able to move small distances. At the local minima of this curve (at the point of maximum drop in flow stress), strain stiffening begins to manifest itself. At this point, the chain network is now becoming oriented and primary bonds or cross-links become the main inhibitors to further deformation. The strain stiffening continues until primary bonds break and the network begins to disintegrate. Orientation has been shown to exist by observing thin slices of partially deformed material, transverse to the loading direction, through a polariscope - see Section 6.6.

The temperature measurement data shows an insignificant quantity of heat evolving during the initial parts of the test (Figure 5.34). This is most likely because the majority of the input energy is stored as elastic recoverable energy and used to break secondary bonds, and only a little being dissipated in the form of heat. The onset of inelastic deformation in glassy polymers is believed to occur once individual polymer chain segments overcome local resistance to motion. This initial yield depends strongly on temperature and strain-rate. The continuing plastic flow is characterised by strain softening followed by strain stiffening. Strain softening can be described as a de-aging process related to an evolution in structure. The evolution of structure that occurs during strain softening erases the initial ageing histories of the material. Following initial yield, most materials are expected to strain soften under axial compression and subsequently to strain harden. The additional 'paths' for chain orientation in polymers under uniaxial compression permit larger strains, thus 'delaying' the orientation-

dependant strain stiffening and extending the 'locking' or 'limiting strain' achieved in uniaxial compression, beyond that achieved in plane strain compression. Strain stiffening can be considered to be the result of an evolving resistance to chain alignment and that it is also a result of decreasing entropy of a network of oriented chains. The strain-induced orientation acts to preferentially strengthen the polymer, producing an anisotropic material.

As the now highly oriented chain network approaches the point at which primary bonds begin to break, energy is no longer absorbed for various deformation processes and all evolves as heat. At this point, failure occurs which is likely to be assisted by the high temperature rises immediately preceding failure. The rate of temperature rise at this point is approximately $0.975\,°C.\mu s^{-1}$, approaching a million degrees per second. The duration of such high rates however is very short lived, of the order of ~28μs.

6.2.1 Proportion of Work Converted to Heat

A measure of the quantity of work converted to heat during a deformation process is denoted as β. The method used to calculate β in this investigation was similar to that used by Mason *et al* (1994). The work rate per unit volume on the specimen was compared to the rate of thermal energy per unit volume which evolved, using the equations below:

$$\textit{Work rate on specimen per unit volume},\qquad \dot{W} = \dot{\varepsilon}\sigma \tag{6.1}$$

$$\textit{Rate of thermal energy increase per unit volume},\qquad \dot{E}_{th} = c\rho\dot{T} \tag{6.2}$$

$$\textit{Proportion of work converted to heat},\qquad \beta = \frac{\dot{E}_{th}}{\dot{W}} \tag{6.3}$$

The work performed on unit volume of a test specimen is equal to the area under the true stress-true strain curve. The instantaneous rate of work on the specimen can be calculated

by multiplying the stress and strain-rate at a particular moment in time.

These two curves are shown in Figure 6.13. The rate of increase in thermal energy is calculated from the temperature-time graph. The temperature data contains noise, which, upon differentiating, gives a very messy result since the slope changes with the noise and becomes very erratic. By fitting a polynomial trend line through the data shown in Figure 6.14, it is possible to eliminate the effect of the noise and determine the rate of temperature increase more accurately.

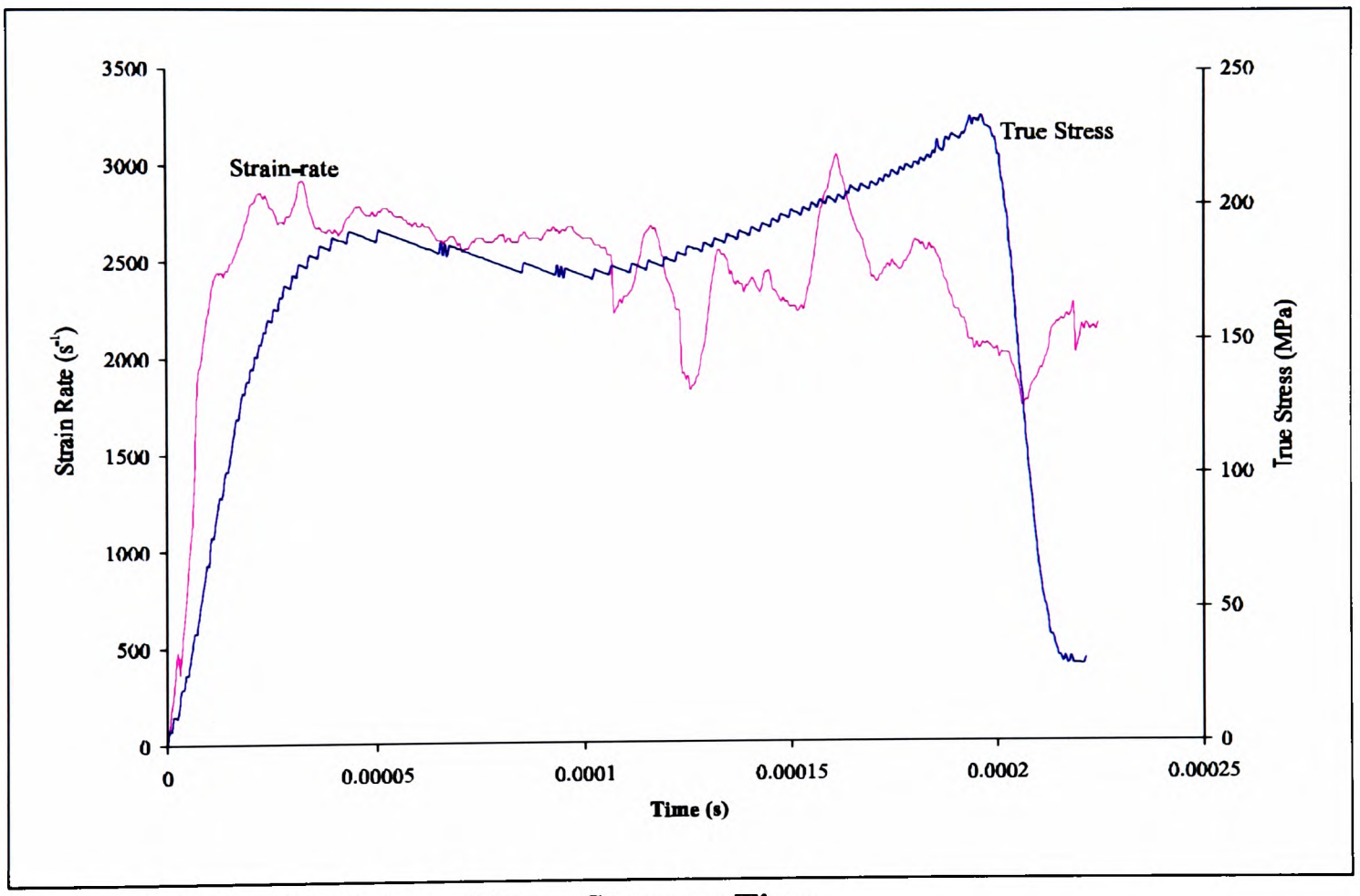

Figure 6.13 Strain-Rate and True Stress vs Time

Figures 6.15 & 6.16 show the results of calculations for β data from test TEMP9. This test has an average strain-rate of approximately $2500s^{-1}$. Figure 6.15 shows the work rate and the rate of thermal energy produced. As seen in Figure 6.13, the strain-rate fluctuates somewhat and this is reflected in the work rate; this same fluctuation is seen in the β calculation, although the general trend is that of an increasing value of β with increasing strain.

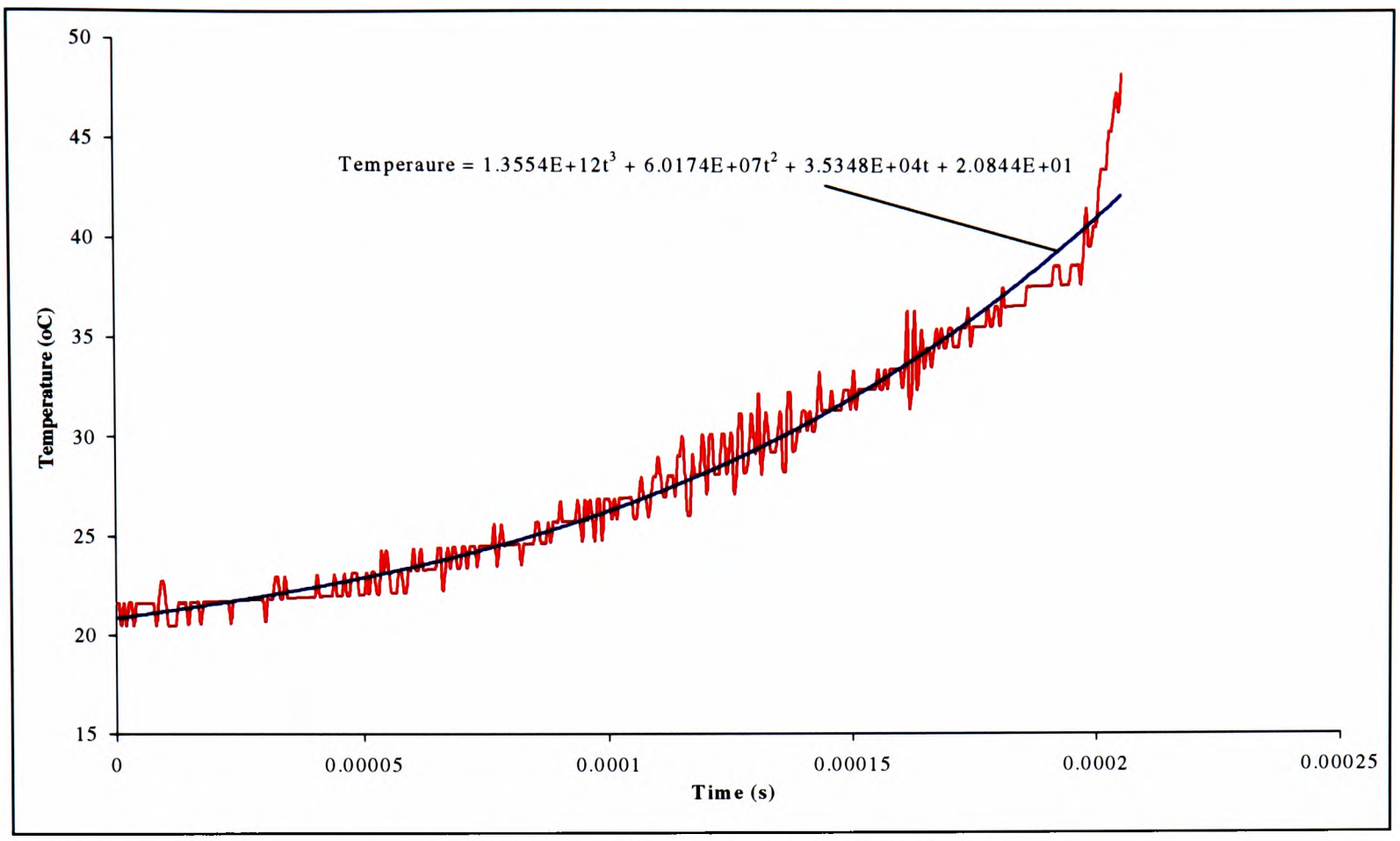

Figure 6.14 Temperature Data With Fitted Cubic Polynomial

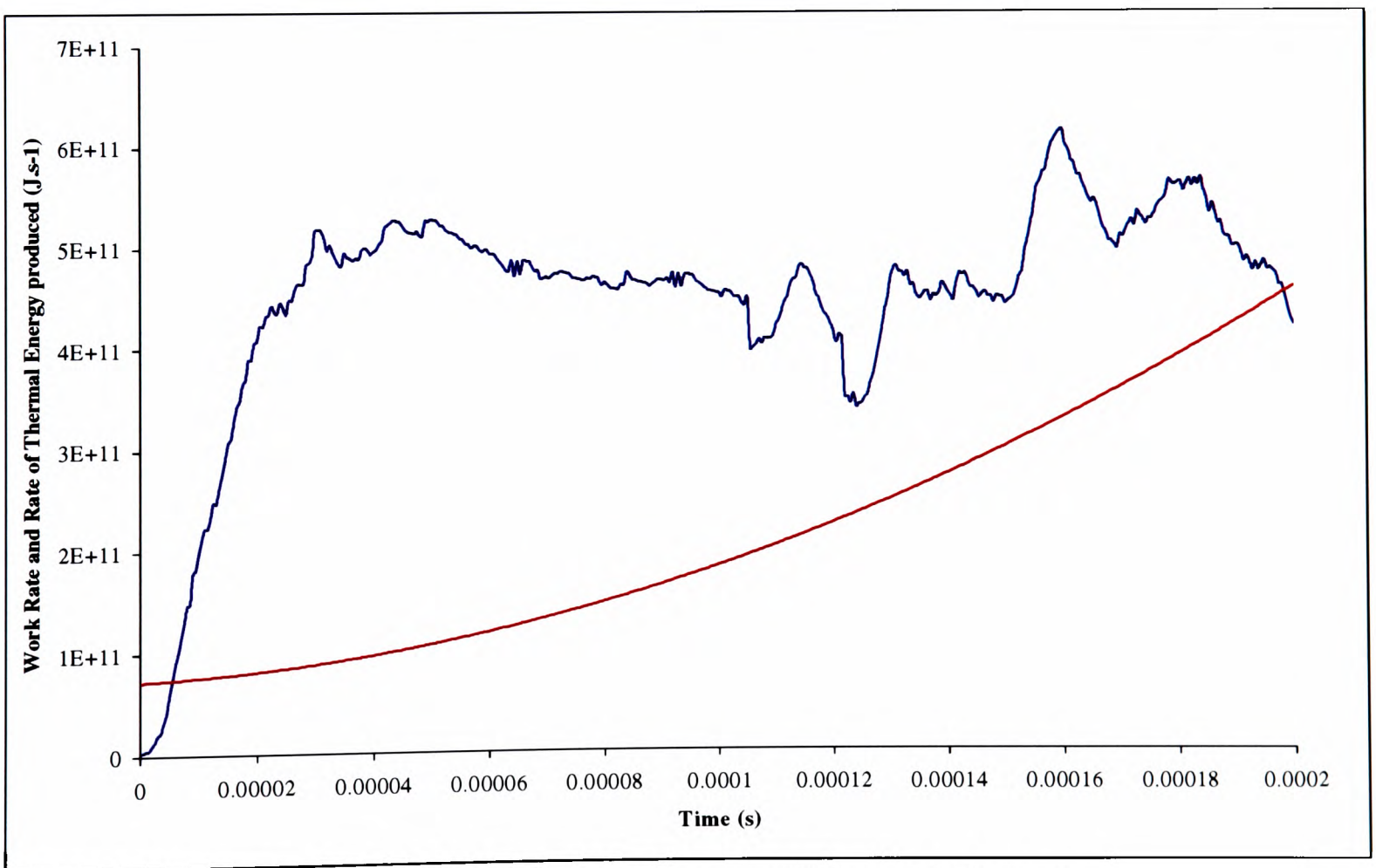

Figure 6.15 Work Rate and Rate of Production of Thermal Energy

The calculations assume that the tests were purely adiabatic and that thermal diffusion is not significant. This will reduce the measured temperature slightly, thereby reducing the calculated values of β.

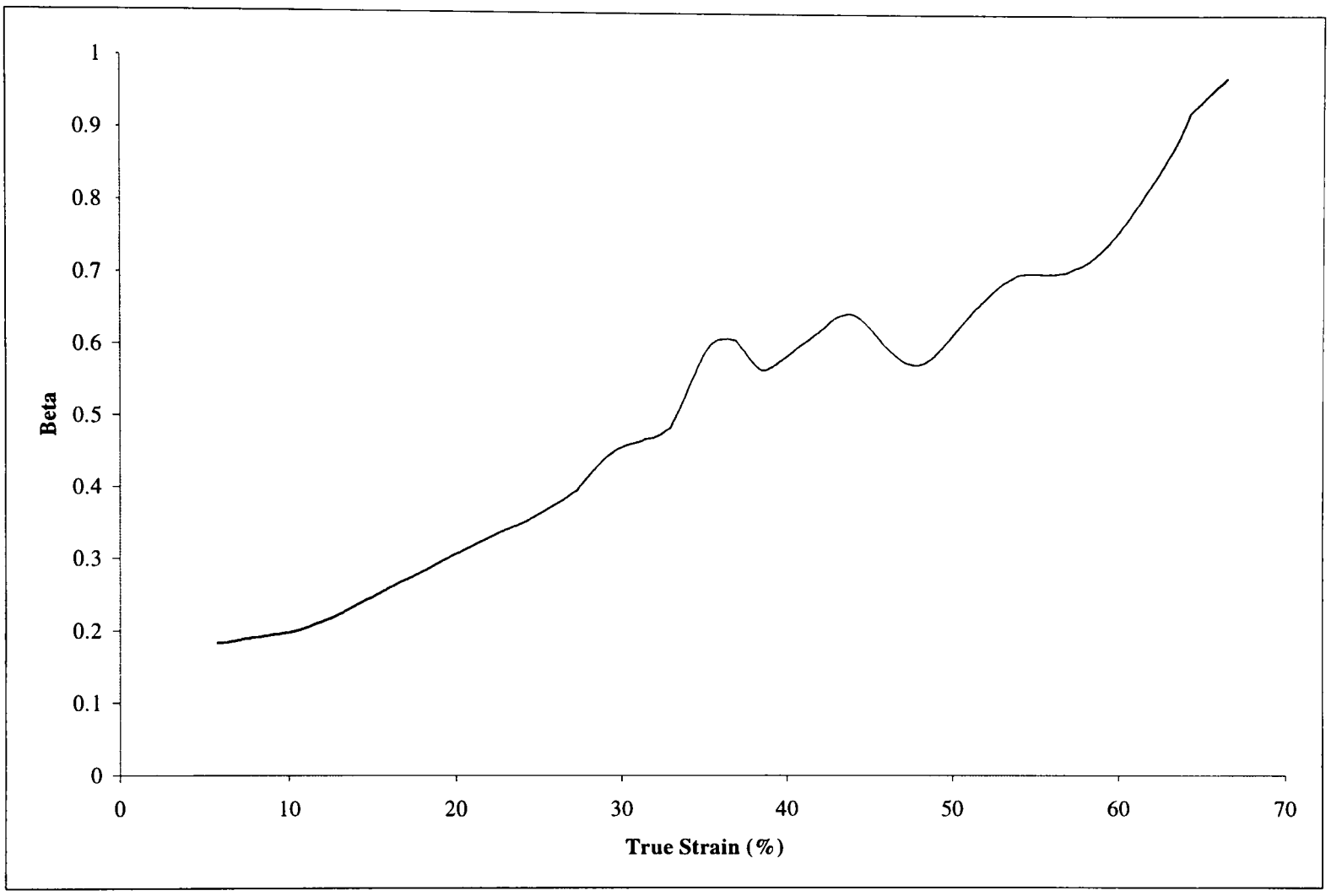

Figure 6.16 Variation of Beta with Strain

6.3 Single Specimen Repeated Tests

With repeated application of load to a specimen, crazing effects incurred during each impact leading to the observed damage. Once the polymer chain network approaches a state of partial orientation after, say, impact 'C', then there is little scope for further molecular alignment. This sequence of tests showed that this epoxy resin was sensitive to repeated impacts. It will be noted that the isothermal tests lie within the continuous test data.

6.4 Multi Specimen Interrupted Tests

It is evident that the temperature of the specimen continues to rise after interruption of the loading. The times and temperatures achieved are represented in Figures 6.17 and 6.18. The S-N ratio at low temperatures is about 1 and therefore it is difficult to measure temperatures with great accuracy. This is the probable cause of the drop in 'Time for Maximum Temperature' in Figure 6.18 for increment 0.75mm. The deformation is slight and temperature rise small. Assuming the system is entropic, the initial orientation of the polymer chains results in a decrease in entropy. This is not to say that there is a temperature drop, but a small net temperature increase. Once the bars have met the arresting collars, unloading occurs, and as the polymer recovers, i.e. the system attempts to return to a less ordered state with an entropy increase.

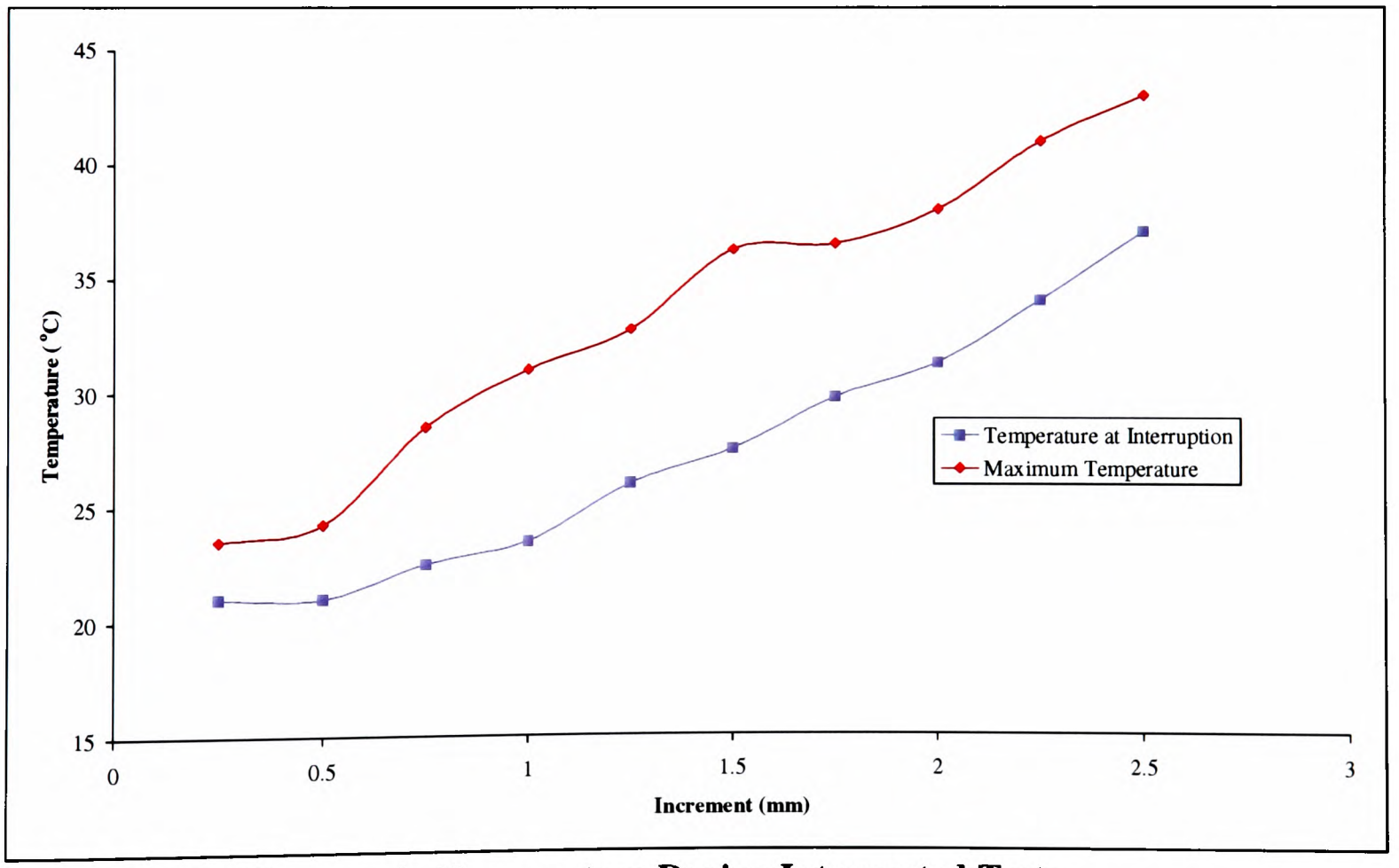

Figure 6.17 Differences in Temperature During Interrupted Tests

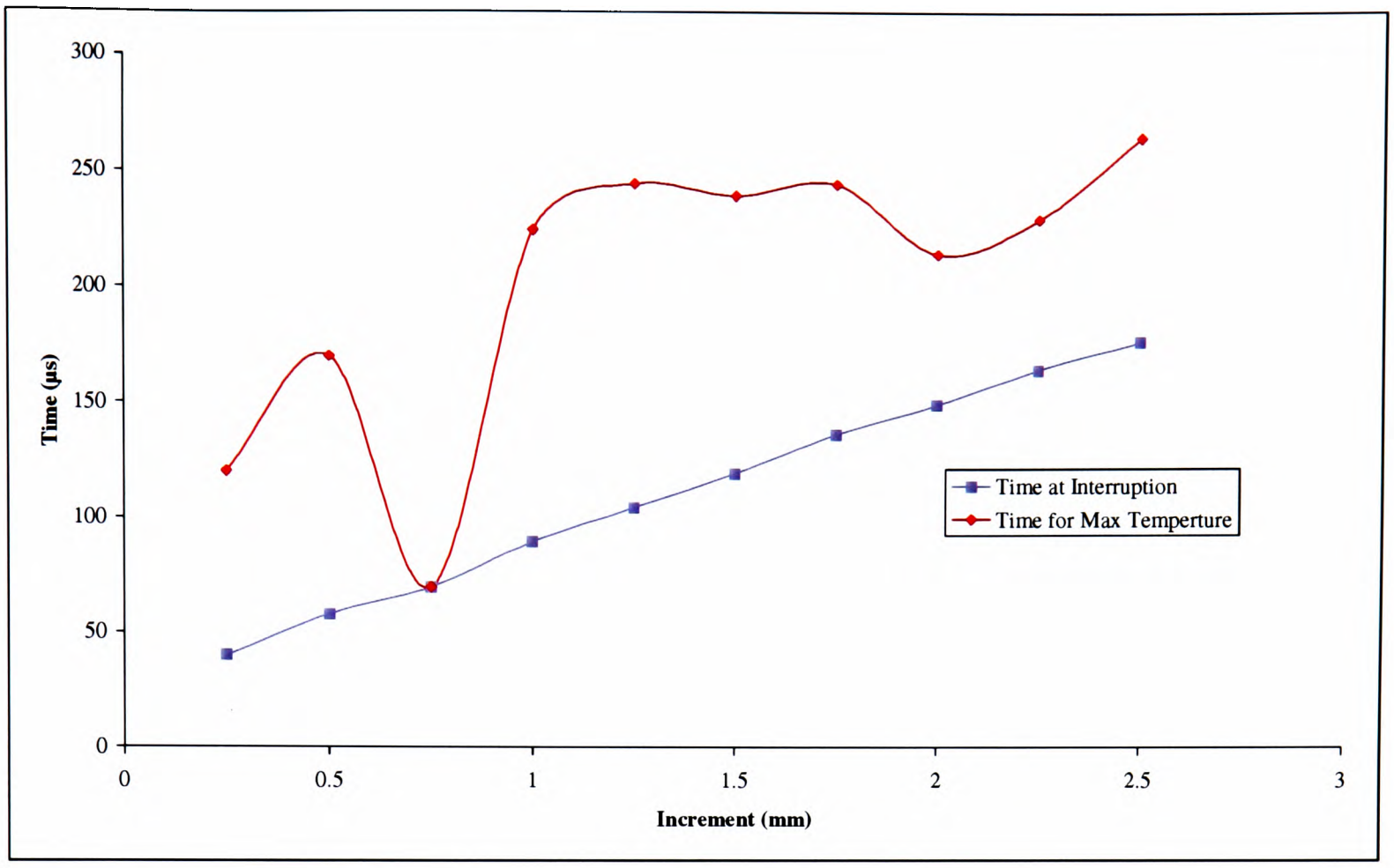

Figure 6.18 Times When Temperatures Achieved

A possible failure mechanism during large deformations is that of *crazing*. This is the formation of thin sheets perpendicular to the stress direction which contain fibrils and voids. The fibrils and the molecular chains in them are aligned parallel to the stress direction. Crazing is often enhanced by rubber inclusions which impart increased toughness to the polymer and reduce brittle fracture by initiating or terminating crazes at the rubber particle surface.

Crazing is the first stage of fracture in many glassy polymers - it is a localised process that produces thin sheets of deformed, 'crazed', material with the sheets perpendicular to the principal stress axis. Craze material may have an average density of only 20% of that of the bulk polymer (ie. if 80% of the craze is void) but the craze can still support a significant load because of the oriented fibrils.

Eventually, crazes break down to form cracks, and when the cracks grow to critical size the specimen fails. Although crazes lead to failure in this way they can be useful, since if many

crazes are produced before failure occurs, energy is absorbed by the material as the local yielding takes place.

When a small strain is applied to a polymer, there is a molecular rearrangement in the solid induced by the stress. On release of the stress, the molecules slowly recover their former spatial arrangement and the strain returns to zero. Polymers are viscoelastic at all temperatures and have properties which are highly temperature dependant, so that in considering the strains induced during service for example, it is always required to take into account not only the stress, but the temperature at which the polymeric material will operate. Also, the dissipation of mechanical energy can raise the temperature within a polymer, causing significant softening - an effect which increases with strain-rate.

The mechanical behaviour of polymers subjected to large strain deformations is primarily governed by the evolution of the polymer chain network with deformation state and temperature from that of an initially random configuration to a highly oriented state.

6.5 The Eyring Equation

Eyring's flow model provides a basis for analysis and contains the necessary elements for further development and refinement. Its aim is to correlate the effects of strain-rate and temperature on flow stress, and it seeks to do this from a molecular model of the flow mechanism, which is related to the Arrhenius equation. The fundamental idea is that a segment of a macromolecule in moving from one position to another in the solid, must pass over an energy barrier. In the absence of stress, the segments of the polymer jump over the barrier very infrequently and they do so in random directions - the mean time-of-stay, between segment jumps in the solid may be measured in years.

The final form of the Eyring equation is of the form:

$$\dot{\varepsilon}_y = \dot{\varepsilon}_0 \exp\left[-\left(\frac{\Delta H}{kT}\right)\right] \exp\left(\frac{V\tau}{2kT}\right) \qquad \textbf{(6.4)}$$

and can be rearranged to:

$$\left(\frac{\sigma_y}{T}\right) = \left(\frac{2}{V}\right)\left[\left(\frac{\Delta H}{T}\right) + 2.303.k.\log\left(\frac{\dot{\varepsilon}_y}{\dot{\varepsilon}_0}\right)\right] \qquad \textbf{(6.5)}$$

Below is a first approximation for the activation volume.

The Eyring plot can show, with a series of lines at constant temperature, that σ_y /T increases linearly with $\log_{10}\dot{\varepsilon}$, shown schematically in Figure 6.19, ie. the yield stress is rate dependant, and that at constant $\log_{10}\dot{\varepsilon}$, the yield stress is temperature dependant (assuming V, ΔH and $\dot{\varepsilon}_0$ are constant). Data from tests previously done at Oxford on Ciba LY-564, was added to existing data to obtain Figure 6.20 although there was not enough variation in strain-rate to construct additional lines. However, the slopes should in theory be identical, so parallel lines to the 20°C (the ambient temperature during the tests) slope were added to enable an estimate of the activation enthalpy, shown in Figure 6.20.

Data from tests at three different strain-rates has been used to construct an Eyring plot, assuming that there are no temperature effects. From this plot, one can obtain an estimate for the activation volume V (from the slope of a graph of σ_y /T vs $\log_{10}\dot{\varepsilon}$)

$$\frac{d(\sigma_y/T)}{d(\log\dot{\varepsilon}_y)} = \frac{2\,.\,2.303\,.\,k}{V} \qquad \textbf{(6.6)}$$

From the graph, the slope is calculated to be 62.5kPa.K^{-1}, and V to be 0.613x10^{-3} m^3.mol^{-1}. To obtain the size of V per segment, the value is divided by Avogadro's number, thus V = 1.02nm^3.

In order to obtain an idea of the scale of this activation volume, an approximation can be made on the volume between cross links. From the manufacturers data sheet (Ciba, 1994), "the Bisphenol epoxy resin has a molecular weight of less than 700". By using Avogadro's number and the density, a volume between cross links can be calculated thus:

$$\frac{MW\,(g.mol^{-1})}{Avogadro\,(mol^{-1})\,.\,\rho\,(gm^{-3})} = \frac{700}{6.022x10^{23}\,.\,1200x10^{3}} = 0.97nm^{3}$$

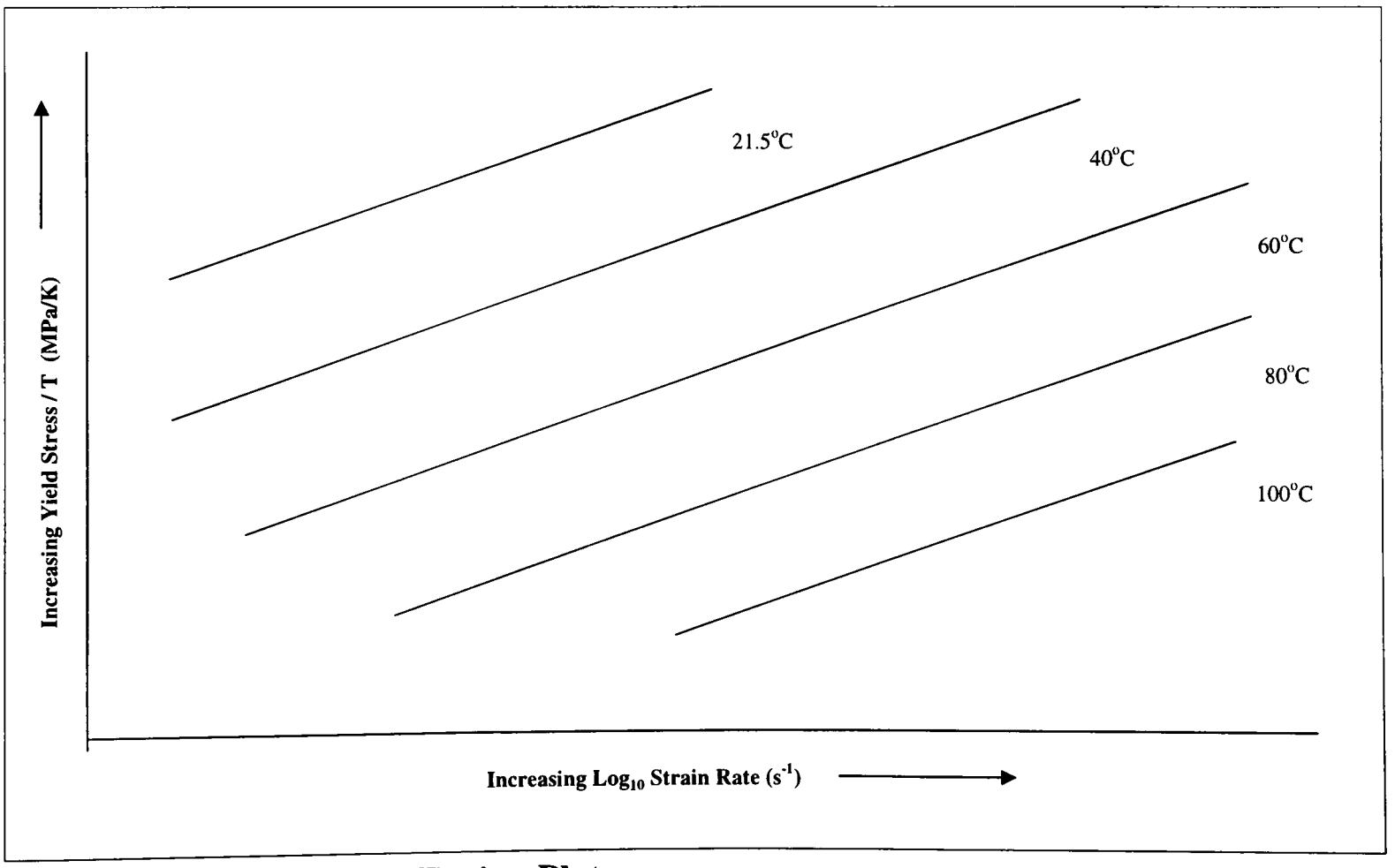

Figure 6.19 A Schematic Eyring Plot

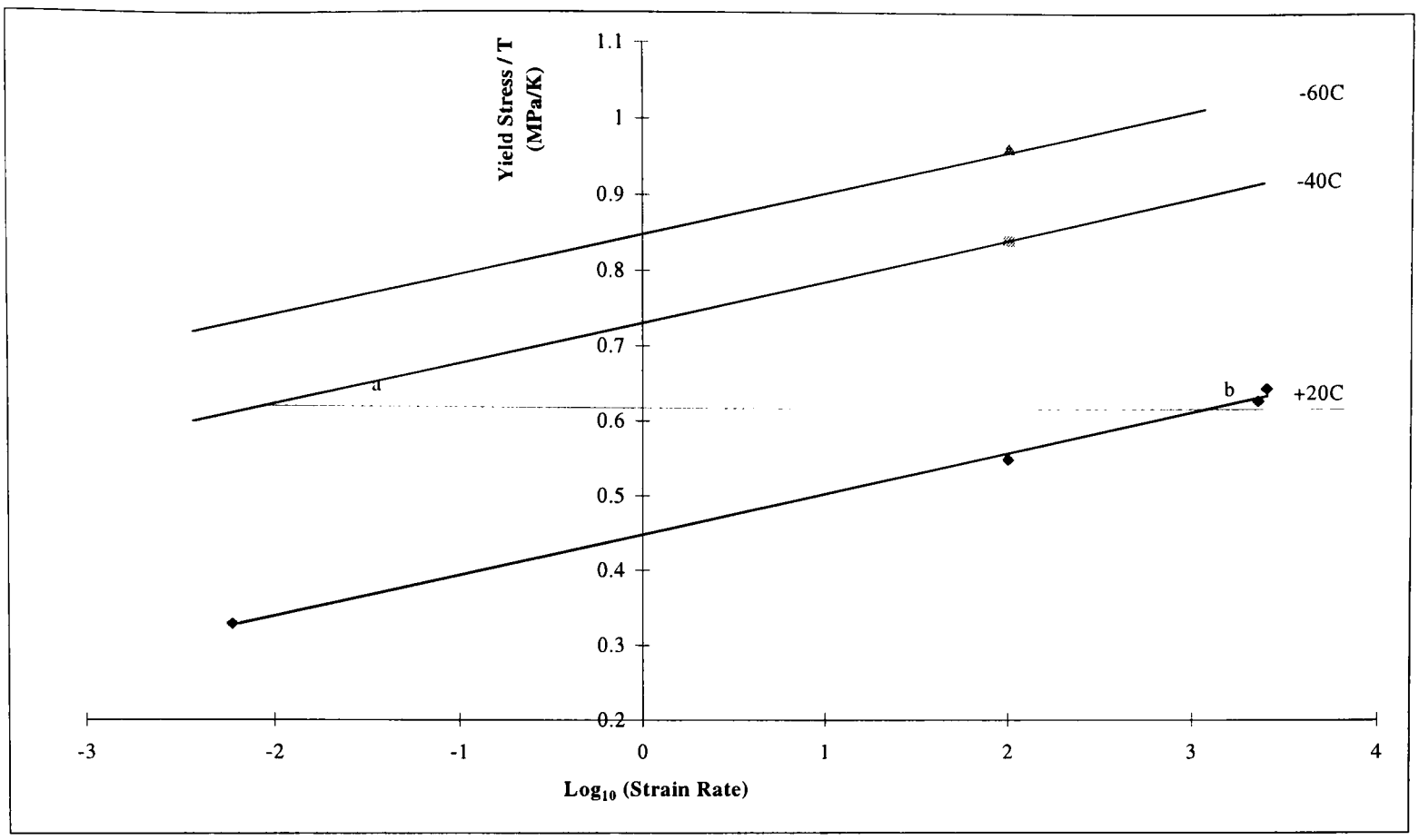

Figure 6.20 Eyring Plot

The chain segment between cross links is the most flexible part of the polymer, ie. requires the least amount of energy to change its position. From the calculations above, it has been shown that the activation volume, V is of the same order as the volume between cross links. Once activation volumes increase to more than one segment volume, the energy required to initiate yield increases considerably due to the constraints from the rigid covalent bonds, preventing segment motion.

Taking the separation *ab* in Figure 6.20 (constant σ_y/T) and from Equation 6.5 we get:

$$\left(\frac{\Delta H}{T_1}\right) + 2.303k\log\dot{\varepsilon}_y^{T_1} = \left(\frac{\Delta H}{T_2}\right) + 2.303k\log\dot{\varepsilon}_y^{T_2} \qquad \textbf{(6.7)}$$

It follows that:

$$\Delta H = \frac{2.303\,k\,(\log \dot{\varepsilon}_y^{\,T_2} - \log \dot{\varepsilon}_y^{\,T_1})}{\left(\frac{1}{T_1} - \frac{1}{T_2}\right)}$$

Measuring the lines at $T_1 = -40°C$ and $T_2 = +20°C$ gives a separation of 4.7 decades. And so:

$$\Delta H = \frac{2.303\,x\,8.314\,x\,4.7}{233^{-1} - 293^{-1}} = 102\,kJ/mol.$$

The activation energy obtained in this calculation is typical of deformation processes in plastics.

A small number of quasistatic tests have been performed and these showed the expected trends, such as reduced flow stress, simply due to strain-rate sensitivity, Figure 6.12. One can use the analogy of the simple spring-dashpot model; when the loading becomes faster the whole system becomes stiffer, because of the dashpot, representing the viscoelastic element. There are a number of features which are common to all strain-rates - an initial 'yield' point and a subsequent drop in flow stress. For the quasistatic test, the true stress at 'yield' was 85MPa and drops by approximately 11.1MPa before the strain stiffening mechanism becomes prominent. The higher rate tests are similar during the early parts of the stress-strain curve since despite the impact velocities being different, the strain-rates are comparable ($2500s^{-1}$ and $2250s^{-1}$). Yield was 190MPa and 180MPa respectively with drops in flow stress of approximately 13.4MPa and 12.6MPa. This could indicate that the rate of straining has an effect on the amount of strain softening in the material. At present, it is uncertain whether any

thermal softening is present, due to the modest temperature measurements observed.

6.6 Specimen Analysis Using the Polariscope

Plastic deformation in a material is a consequence of material flow. Since the material flow during plastic deformation results in some kind of ordering in molecular structure, one could use the results of this phenomenon to obtain information regarding the plastic flow. The molecular orientation in many transparent materials which display birefringency, can be obtained using an optical instrument, called a *polariscope*. Birefringency, or double-refraction, is an optical anisotropy, where the refractive index of the material varies with direction and is observed in many transparent non-crystalline materials under certain conditions. Molecular orientation, frozen-in or imposed strains are known to cause the birefringency in these materials.

The objective of this brief part of the study was to determine whether one could detect molecular ordering within a specimen and to what degree this was apparent. A quantitative analysis was not attempted. Details of the method used are given in Appendix C. It was found that the specimens exhibit a noticeable birefringence after loading, which indicates a certain degree of orientation of the molecules.

6.7 References

Ciba Polymers Matrix Systems, Material Data Sheet ARALDITE LY-564, March 1994.

Dally, J.W. & Riley, W.F., Experimental Stress Analysis, 3rd Ed., McGraw Hill, 1991.

Mason, J.J., Rosakis, A.J. & Ravichandran, G., On the Strain and Strain-Rate Dependance of the Fraction of Plastic Work Converted to Heat: An Experimental Study Using High

Speed Infra-red Detectors and the Kolsky Bar, Mech. Of Matls., 17, pp.135-145, 1994.

Chapter 7

Conclusions

7.1 Summary

A high strain-rate material testing programme was carried out on an epoxy resin, Ciba LY-564, using the split Hopkinson pressure bar. A small number of tests were carried out on the material using an Instron machine for quasistatic rates, and a hydraulic machine for intermediate rates of strain. A preliminary testing programme was carried out to establish a suitable specimen aspect ratio. High speed photography was used to validate the computer programs used in calculating the specimen stress and strain from strain gauge stations on the loading bars of the split Hopkinson pressure bar. A radiometric testing technique was established which enabled the measurement of the specimen surface temperature during impact tests. A newly designed radiometer, comprising of a liquid nitrogen cooled detector and an imager were used for this process.

7.2 Conclusions

The preliminary testing programme was carried out to determine a suitable specimen geometry for further testing with the radiometer. The range of specimen aspect ratios was fairly extensive, but the results produced an overall rather confusing picture. Some anomalies in trends for the high rate tests were shown to exist. A contributing factor in this was the difficulty in maintaining a uniform strain-rate for series of tests where the length of the specimen was decreasing. For specimens of very short gauge length, the strain-rate was generally high, in the order of $4x10^3s^{-1}$, even when operating the gun at a low projectile impact velocity. The reproducibility of data was shown to be very good for the specimen size, BY (diameter 9.0mm by 5.5mm long). This aspect ratio (0.61) was selected, which was a compromise between a long cylindrical and a thin disk specimen. The lubrication of the specimen/loading bar interfaces was examined and it was shown that provided a suitable lubricant is used, the hydrostatic stress due to frictional constraints is minimised. Petroleum jelly was used in high rate tests ($2x10^3s^{-1}$) and this was found to be suitable. For quasistatic tests ($6x10^{-3}s^{-1}$), PTFE sheet was used and found to be satisfactory. Hydraulic tests ($1x10^2s^{-1}$) used petroleum jelly as the lubricant. A clear strain-rate dependance was observed for the material at the three strain-rates.

The measurement of bulk surface temperature was performed using a newly designed radiometer. Calibration of the specimen prior to the test was performed with the use of the revised copper block (#2). The surface of the specimen was coated with soot to maximise the emissivity. This method was found to be very satisfactory; once the radiometer position has been optimised, subsequent calibrations for further tests were identical. The temperature profile observed by the radiometer shows three distinct gradients during the deformation of the specimen. A small amount of heat is evolved in the early stages of the test; up until 60μs the

rate of temperature increase is $36.7x10^3$ °C.s^{-1}. The rate begins to increase until it stabilises at $141x10^3$ °C.s^{-1} at a time of 110μs. The final increase in rate comes at approximately 190μs when the rate reaches $975x10^3$ °C.s^{-1}. Shortly afterwards, the specimen shatters with a sudden release of energy. The temperature recorded at failure is approximately 45°C. Post-failure temperature data can only be used as a guide to events.

During the deformation of the specimen, several factors can affect the gathered radiation. Firstly, since the circumference of the specimen is increasing during deformation, the density of soot covering the surface may be reduced, so reducing the emissivity of the surface. Again, whilst the specimen is expanding radially, the surface on which the detector is focussed appears to move towards the detector. This has the effect of de-focussing the radiometer. These two conditions can lead to an underestimate of the surface temperature. A post test calibration to determine the change in emissivity was performed on a specimen whose deformation was halted just prior to failure. The change in calibration, approximately 15%, has been assumed to vary linearly with strain. The change in emissivity throughout the test has been calculated for all temperature data and adjusted accordingly. High speed photography shows the deformation of the specimen and its subsequent failure. It may be possible that the large increase in temperature in the final part of the test is due to friction between specimen fragments or even that the radiometer is viewing the 'hot' insides of the specimen.

The proportion of work converted to heat, known as β, has been calculated. The value of β has an initial value of ~0.2, which rises almost linearly with strain to a value of ~0.95 just prior to failure.

Interrupted tests proved difficult to carry out. In theory, small increments of strain would minimise any effect that temperature would have on the material property. However, the level of damage sustained by a single specimen on repeated loading resulted in it varying

considerably in physical appearance from a specimen which had been deformed to an equivalent strain in one loading. Therefore these results are considered unreliable.

Experimental values for the activation enthalpy, ΔH, was calculated to be 102 $kJ.mol^{-1}$, and V, the activation volume per jumping segment was 1.02nm^3. The value for the activation volume calculated from the manufacturers data sheet was 0.97nm^3. The Eyring equation only predicts yielding and so therefore a dynamic temperature is not required. What is really needed is a constitutive relation to follow the behaviour of the material to the point of failure. The techniques developed in this investigation are regarded as essential for the development of such constitutive equations, since it is shown that the temperature rise is particularly pronounced after yield. Therefore, the temperature has an important effect on the mechanical properties in the final stage of deformation.

Slices from deformed specimens were examined in a polariscope for evidence of molecular orientation. The intention was to observe the degree of molecular orientation and to relate this information to the temperature profile obtained from a continuous test. The deformed specimen shown in Appendix C had been deformed to 60% and it is clear from observing the isoclinics that molecular alignment is present. However, this effect becomes virtually insignificant in specimens which have been subjected to a strain of less than 60%.

7.3 Further Work

The scope for further work in this field is considerable. Four areas have been identified for future consideration.

a) The most obvious continuation would perhaps be the expansion of the bank of data to include data from high rate tension and torsion tests as well. Subsequently, stress and thermal analysis of specimen geometries; cylindrical specimens, single waisted tension

specimens and thin walled tubular specimens for torsion tests.

b) Different polymeric materials could be investigated, extending the work into toughened epoxies and thermoplastics, as many of these are of interest to aerospace companies.

c) A detailed investigation into the damage sustained by repeated impacts on a specimen can be performed, which can explore the failure mechanisms involved.

d) Perhaps the most important work that remains to be done is the development of constitutive equations that will extend the Eyring equation to model the large strain flow of polymers. This will require a more detailed thermal analysis of the specimen, which will combine the experimental observations with finite element thermomechanical analysis.

Appendix A

Equations for Manual Analysis of Split Hopkinson Bar Signals

A.1 Input Bar Analysis

A.1.1 Stress

$0 < t \le T_2\ \sigma_{(t)} = \sigma_{I\,(t)} - X_{(t+T1)}$

$T_2 < t \le T_1 + T_2\ \sigma_{(t)} = \sigma_{I\,(t)} - X_{(t+T1)} - X_{(t+T1-T2)}$

$T_1 + T_2 < t \le 2T_2\ \sigma_{(t)} = \sigma_{I\,(t)} - X_{(t+T1)} - X_{(t+T1-T2)} + X_{(t-T2)}$

$2T_2 < t \le 2T_2 + T_1\ \sigma_{(t)} = \sigma_{I\,(t)} - X_{(t+T1)} - X_{(t+T1-T2)} + X_{(t-T2)} - X_{(t+T1-2T2)}$

$2T_2 + T_1 < t \le 3T_2\ \sigma_{(t)} = \sigma_{I\,(t)} - X_{(t+T1)} - X_{(t+T1-T2)} + X_{(t-T2)} - X_{(t+T1-2T2)} + X_{(t-2T2)}$

$3T_2 < t \le 3T_2 + T_1\ \sigma_{(t)} = \sigma_{I\,(t)} - X_{(t+T1)} - X_{(t+T1-T2)} + X_{(t-T2)} - X_{(t+T1-2T2)} + X_{(t-2T2)} - X_{(t+T1-3T2)}$

$3T_2 + T_1 < t \le 4T_2\ \sigma_{(t)} = \sigma_{I\,(t)} - X_{(t+T1)} - X_{(t+T1-T2)} + X_{(t-T2)} - X_{(t+T1-2T2)} + X_{(t-2T2)} - X_{(t+T1-3T2)} + X_{(t-3T2)}$

$4T_2 < t \le 4T_2 + T_1\ \sigma_{(t)} = \sigma_{I\,(t)} - X_{(t+T1)} - X_{(t+T1-T2)} + X_{(t-T2)} - X_{(t+T1-2T2)} + X_{(t-2T2)} - X_{(t+T1-3T2)} + X_{(t-3T2)} - X_{(t+T1-4T2)}$

$4T_2 + T_1 < t \le 5T_2\ \sigma_{(t)} = \sigma_{I\,(t)} - X_{(t+T1)} - X_{(t+T1-T2)} + X_{(t-T2)} - X_{(t+T1-2T2)} + X_{(t-2T2)} - X_{(t+T1-3T2)} + X_{(t-3T2)} - X_{(t+T1-4T2)} + X_{(t-4T2)}$

$T_1 = 16.6\mu s$

$T_2 = 111.8\mu s$

$\sigma_{(0\to111.8)} = \sigma_{I\,(0\to111.8)} - X_{(16.6\to128.4)}$

$\sigma_{(111.8\to128.4)} = \sigma_{I\,(111.8\to128.4)} - X_{(128.4\to145)} - X_{(16.6\to33.2)}$

$\sigma_{(128.4\to223.6)} = \sigma_{I\,(128.4\to223.6)} - X_{(145\to240.2)} - X_{(33.2\to128.4)} + X_{(16.6\to111.8)}$

$\sigma_{(223.6\to240.2)} = \sigma_{I\,(223.6\to240.2)} - X_{(240.2\to256.8)} - X_{(128.4\to145)} + X_{(111.8\to128.4)} - X_{(16.6\to33.2)}$

$\sigma_{(240.2\to335.4)} = \sigma_{I\,(240.2\to335.4)} - X_{(256.8\to352)} - X_{(145\to240.2)} + X_{(128.4\to223.6)} - X_{(33.2\to128.4)} + X_{(16.6\to111.8)}$

$\sigma_{(335.4\to352)} = \sigma_{I\,(335.4\to352)} - X_{(352\to368.6)} - X_{(240.2\to256.8)} + X_{(223.6\to240.2)} - X_{(128.4\to145)} + X_{(111.8\to128.4)} - X_{(16.6\to33.2)}$

$\sigma_{(352\to447.2)} = \sigma_{I\,(352\to447.2)} - X_{(368.6\to463.8)} - X_{(256.8\to352)} + X_{(240.2\to335.4)} - X_{(145\to240.2)} + X_{(128.4\to223.6)} - X_{(33.2\to128.4)} + X_{(16.6\to111.8)}$

$\sigma_{(447.2\to463.8)} = \sigma_{I\,(447.2\to463.8)} - X_{(463.8\to480.4)} - X_{(352\to368.6)} + X_{(335.4\to352)} - X_{(240.2\to256.8)} + X_{(223.6\to240.2)} - X_{(128.4\to145)} + X_{(111.8\to28.4)} - X_{(16.6\to33.2)}$

$\sigma_{(463.8\to559)} = \sigma_{I\,(463.8\to559)} - X_{(480.4\to575.6)} - X_{(368.6\to463.8)} + X_{(352\to447.2)} - X_{(256.8\to352)} + X_{(240.2\to335.4)} - X_{(145\to240.2)} + X_{(128.4\to223.6)} - X_{(33.2\to128.4)} + X_{(16.6\to11.8)}$

where $X_t = (\sigma_I - \sigma_{II})_t$

A.1.2 Velocity

$0 < t \le T_2$ $\quad \sigma_{(t)} = \rho cv_{(t)} = \sigma_{I\,(t)} + X_{(t+T1)}$

$T_2 < t \le T_1 + T_2 \sigma$ $\quad {}_{(t)} = \rho cv_{(t)} = \sigma_{I\,(t)} + X_{(t+T1)} + X_{(t+T1-T2)}$

$T_1 + T_2 < t \le 2T_2$ $\quad \sigma_{(t)} = \rho cv_{(t)} = \sigma_{I\,(t)} + X_{(t+T1)} + X_{(t+T1-T2)} + X_{(t-T2)}$

$2T_2 < t \le 2T_2 + T_1$ $\quad \sigma_{(t)} = \rho cv_{(t)} = \sigma_{I\,(t)} + X_{(t+T1)} + X_{(t+T1-T2)} + X_{(t-T2)} + X_{(t+T1-2T2)}$

$2T_2 + T_1 < t \le 3T_2$ $\quad \sigma_{(t)} = \rho cv_{(t)} = \sigma_{I\,(t)} + X_{(t+T1)} + X_{(t+T1-T2)} + X_{(t-T2)} + X_{(t+T1-2T2)} + X_{(t-2T2)}$

$3T_2 < t \le 3T_2 + T_1$ $\quad \sigma_{(t)} = \rho cv_{(t)} = \sigma_{I\,(t)} + X_{(t+T1)} + X_{(t+T1-T2)} + X_{(t-T2)} + X_{(t+T1-2T2)} + X_{(t-2T2)} + X_{(t+T1-3T2)}$

$3T_2 + T_1 < t \le 4T_2$ $\quad \sigma_{(t)} = \rho cv_{(t)} = \sigma_{I\,(t)} + X_{(t+T1)} + X_{(t+T1-T2)} + X_{(t-T2)} + X_{(t+T1-2T2)} + X_{(t-2T2)} + X_{(t+T1-3T2)} + X_{(t-3T2)}$

$4T_2 < t \le 4T_2 + T_1$ $\quad \sigma_{(t)} = \rho cv_{(t)} = \sigma_{I\,(t)} + X_{(t+T1)} + X_{(t+T1-T2)} + X_{(t-T2)} + X_{(t+T1-2T2)} + X_{(t-2T2)} + X_{(t+T1-3T2)} + X_{(t-3T2)} + X_{(t+T1-4T2)}$

$4T_2 + T_1 < t \le 5T_2$ $\quad \sigma_{(t)} = \rho cv_{(t)} = \sigma_{I\,(t)} + X_{(t+T1)} + X_{(t+T1-T2)} + X_{(t-T2)} + X_{(t+T1-2T2)} + X_{(t-2T2)} + X_{(t+T1-3T2)} + X_{(t-3T2)} + X_{(t+T1-4T2)} + X_{(t-4T2)}$

$T_1 = 16.6\mu s$
$T_2 = 111.8\mu s$

$\sigma_{(0 \to 111.8)} = \rho cv_{(0 \to 111.8)} = \sigma_{I\,(0 \to 111.8)} + X_{(16.6 \to 128.4)}$

$\sigma_{(111.8 \to 128.4)} = \rho cv_{(111.8 \to 128.4)} = \sigma_{I\,(111.8 \to 128.4)} + X_{(128.4 \to 145)} + X_{(16.6 \to 33.2)}$

$\sigma_{(128.4 \to 223.6)} = \rho cv_{(128.4 \to 223.6)} = \sigma_{I\,(128.4 \to 223.6)} + X_{(145 \to 240.2)} + X_{(33.2 \to 128.4)} + X_{(16.6 \to 111.8)}$

$\sigma_{(223.6 \to 240.2)} = \rho cv_{(223.6 \to 240.2)} = \sigma_{I\,(223.6 \to 240.2)} + X_{(240.2 \to 256.8)} + X_{(128.4 \to 145)} + X_{(111.8 \to 128.4)} + X_{(16.6 \to 33.2)}$

$\sigma_{(240\,2 \to 335.4)} = \rho cv_{(240.2 \to 335.4)} = \sigma_{I\,(240.2 \to 335.4)} + X_{(256.8 \to 352)} + X_{(145 \to 240.2)} + X_{(128.4 \to 223.6)} + X_{(33.2 \to 128.4)} + X_{(16.6 \to 111.8)}$

$\sigma_{(335.4 \to 352)} = \rho cv_{(335.4 \to 352)} = \sigma_{I\,(335.4 \to 352)} + X_{(352 \to 368.6)} + X_{(240.2 \to 256.8)} + X_{(223.6 \to 240.2)} + X_{(128.4 \to 145)} + X_{(111.8 \to 128.4)} + X_{(16.6 \to 33.2)}$

$\sigma_{(352 \to 447.2)} = \rho cv_{(352 \to 447.2)} = \sigma_{I\,(352 \to 447.2)} + X_{(368.6 \to 463.8)} + X_{(256.8 \to 352)} + X_{(240.2 \to 335.4)} + X_{(145 \to 240.2)} + X_{(128.4 \to 223.6)} + X_{(33.2 \to 128.4)} + X_{(16.6 \to 111.8)}$

$\sigma_{(447.2 \to 463.8)} = \rho cv_{(447.2 \to 463.8)} = \sigma_{I\,(447.2 \to 463.8)} + X_{(463.8 \to 480.4)} + X_{(352 \to 368.6)} + X_{(335.4 \to 352)} + X_{(240.2 \to 256.8)} + X_{(223.6 \to 240.2)} + X_{(128.4 \to 145)} + X_{(111.8 \to 28.4)} + {}_{(16.6 \to 33.2)}$

$\sigma_{(463.8 \to 559)} = \rho cv_{(463.8 \to 559)} = \sigma_{I\,(463.8 \to 559)} + X_{(480.4 \to 575.6)} + X_{(368.6 \to 463.8)} + X_{(352 \to 447.2)} + X_{(256.8 \to 352)} + X_{(240.2 \to 335.4)} + X_{(145 \to 240.2)} + X_{(128.4 \to 223.6)} + X_{(33.2 \to 128.4)} + X_{(16.6 \to 11.8)}$

where $X_t = (\sigma_I - \sigma_{II})_t$

A.2 Output Bar Analysis

A.2.1 Stress

$0 < t \le T_1 \sigma_t = (\sigma_{III})_t$
$T_1 < t \le T_1 + T_2\ \sigma_t = (\sigma_{III})_t + (\sigma_{III})_{(t - T1)}$
$T_1 + T_2 < t \le 2T_1\ \sigma_t = (\sigma_{III})_t + (\sigma_{III})_{(t - T1)} - (\sigma_{III})_{(t - T1 - T2)}$
$2T_1 < t \le 2T_1 + T_2\ \sigma_t = (\sigma_{III})_t + (\sigma_{III})_{(t - T1)} - (\sigma_{III})_{(t - T1 - T2)} + (\sigma_{III})_{(t - 2T1)}$
$2T_1 + T_2 < t \le 3T_1\ \sigma_t = (\sigma_{III})_t + (\sigma_{III})_{(t - T1)} - (\sigma_{III})_{(t - T1 - T2)} + (\sigma_{III})_{(t - 2T1)} - (\sigma_{III})_{(t - 2T1 - T2)}$

$\sigma_{(0 \to 190)} = (\sigma_{III})_{(0 \to 190)}$
$\sigma_{(190 \to 206.6)} = (\sigma_{III})_{(190 \to 206.6)} + (\sigma_{III})_{(0 \to 16.6)}$
$\sigma_{(206.6 \to 380)} = (\sigma_{III})_{(206.6 \to 380)} + (\sigma_{III})_{(16.6 \to 190)} - (\sigma_{III})_{(0 \to 173.4)}$
$\sigma_{(380 \to 396.6)} = (\sigma_{III})_{(380\text{-}396.6)} + (\sigma_{III})_{(190 \to 206.6)} - (\sigma_{III})_{(173.4 \to 190)} + (\sigma_{III})_{(0 \to 16.6)}$
$\sigma_{(396.6 \to 570)} = (\sigma_{III})_{(396.6 \to 570)} + (\sigma_{III})_{(206.6 \to 380)} - (\sigma_{III})_{(190 \to 363.4)} + (\sigma_{III})_{(16.6 \to 190)} - (\sigma_{III})_{(0 \to 173.4)}$

A.2.2 Velocity

$0 < t \le T_1$	$\sigma_t = \rho c v_t = (\sigma_{III})_t$
$T_1 < t \le T_1 + T_2$	$\sigma_t = \rho c v_t = (\sigma_{III})_t + (\sigma_{III})_{(t - T1)}$
$T_1 + T_2 < t \le 2T_1$	$\sigma_t = \rho c v_t = (\sigma_{III})_t + (\sigma_{III})_{(t - T1)} + (\sigma_{III})_{(t - T1 - T2)}$
$2T_1 < t \le 2T_1 + T_2$	$\sigma_t = \rho c v_t = (\sigma_{III})_t + (\sigma_{III})_{(t - T1)} + (\sigma_{III})_{(t - T1 - T2)} + (\sigma_{III})_{(t - 2T1)}$
$2T_1 + T_2 < t \le 3T_1$	$\sigma_t = \rho c v_t = (\sigma_{III})_t + (\sigma_{III})_{(t - T1)} + (\sigma_{III})_{(t - T1 - T2)} + (\sigma_{III})_{(t - 2T1)} + (\sigma_{III})_{(t - 2T1 - T2)}$

$\sigma_{(0 \to 190)} = \rho c v_{(0 \to 190)} = (\sigma_{III})_{(0 \to 190)}$
$\sigma_{(190 \to 206.6)} = \rho c v_{(190 \to 206.6)} = (\sigma_{III})_{(190 \to 206.6)} + (\sigma_{III})_{(0 \to 16.6)}$
$\sigma_{(206.6 \to 380)} = \rho c v_{(206.6 \to 380)} = (\sigma_{III})_{(206.6 \to 380)} + (\sigma_{III})_{(16.6 \to 190)} - (\sigma_{III})_{(0 \to 173.4)}$
$\sigma_{(380 \to 396.6)} = \rho c v_{(380 \to 396.6)} = (\sigma_{III})_{(380\text{-}396.6)} + (\sigma_{III})_{(190 \to 206.6)} - (\sigma_{III})_{(173.4 \to 190)} + (\sigma_{III})_{(0 \to 16.6)}$
$\sigma_{(396.6 \to 570)} = \rho c v_{(396.6 \to 570)} = (\sigma_{III})_{(396.6 \to 570)} + (\sigma_{III})_{(206.6 \to 380)} - (\sigma_{III})_{(190 \to 363.4)} + (\sigma_{III})_{(16.6 \to 190)} - (\sigma_{III})_{(0 \to 173.4)}$
$T_1 = 190\mu s$, $T_2 = 16.6\mu s$

Appendix B

Circuit Diagram for Detector Electronics

The electronic circuitry for the liquid nitrogen cooled infra-red detector is shown in Figure B.1. The electronics amplified the signal 725 times and acted as a band-pass filter in the range 10Hz - 145kHz.

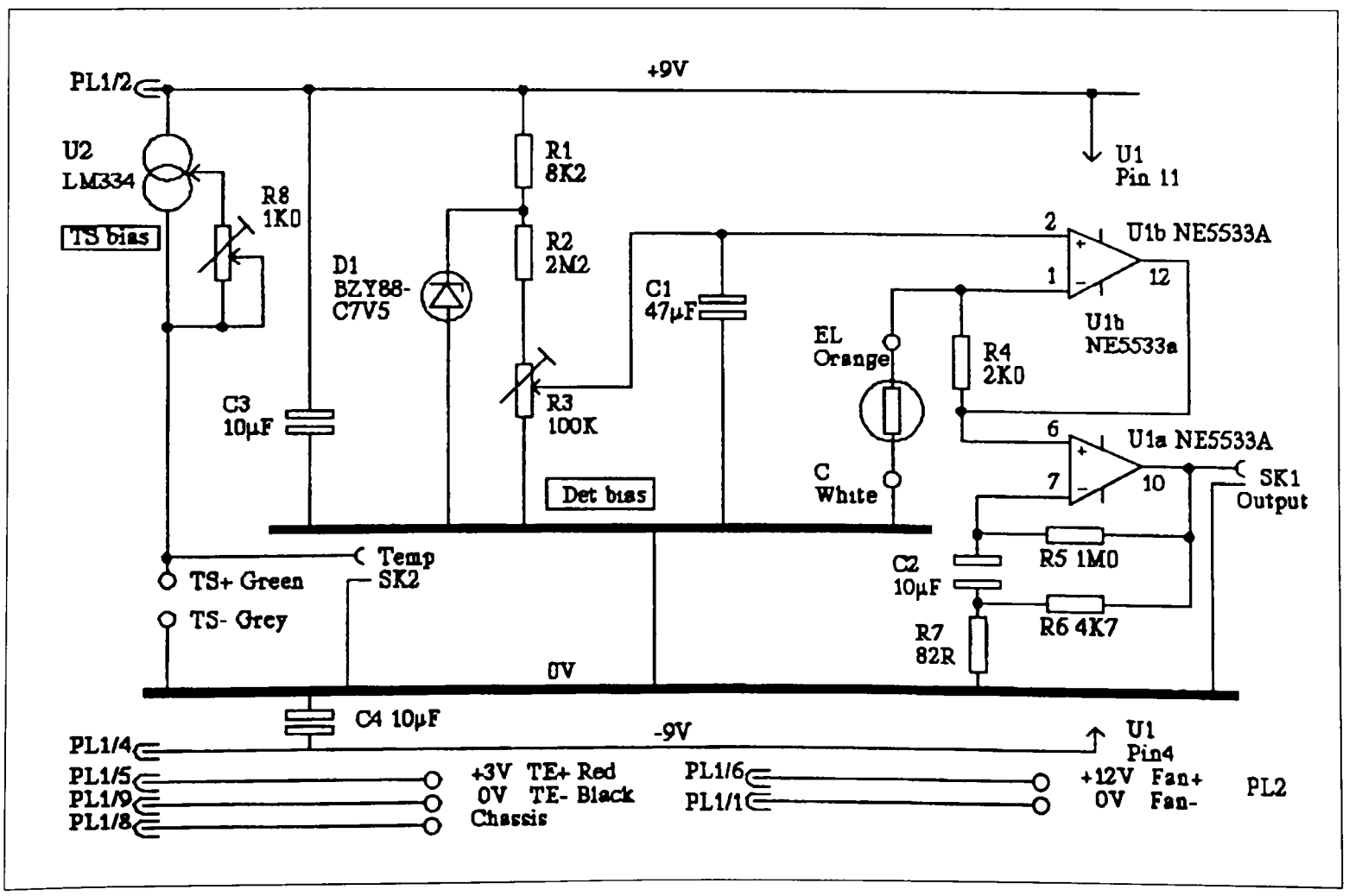

Figure B.1 Detector Electronics

Appendix C

Specimen Analysis Using the Polariscope

C.1 The Polariscope

The polariscope is an optical instrument that utilises the properties of polarised light to measure birefringency, most commonly used in stress analysis. It incorporates polarisers which filter the light by using strained and oriented molecules. For experimental stress-analysis work, two types of polarised light are frequently used: plane polarised and circularly polarised light. When a light wave strikes a plane polariser, this optical element resolves the wave into two mutually perpendicular components. The component parallel to the axis of polarisation is transmitted while the component perpendicular to the axis of polarisation is absorbed, shown in Figure C.1. The plane polariscope is the simplest optical system used in photoelasticity and it consists of two linear polarisers and a light source arrangement as illustrated in Figure C.2. The linear polariser nearest the light source is called the *polariser*, while the second linear polariser is known as the *analyser*. In a plane polariscope the two axes of polarisation are always crossed, no light is transmitted through the analyser, and this optical system produces a dark field. In operation a photoelastic model is inserted between the two crossed elements and

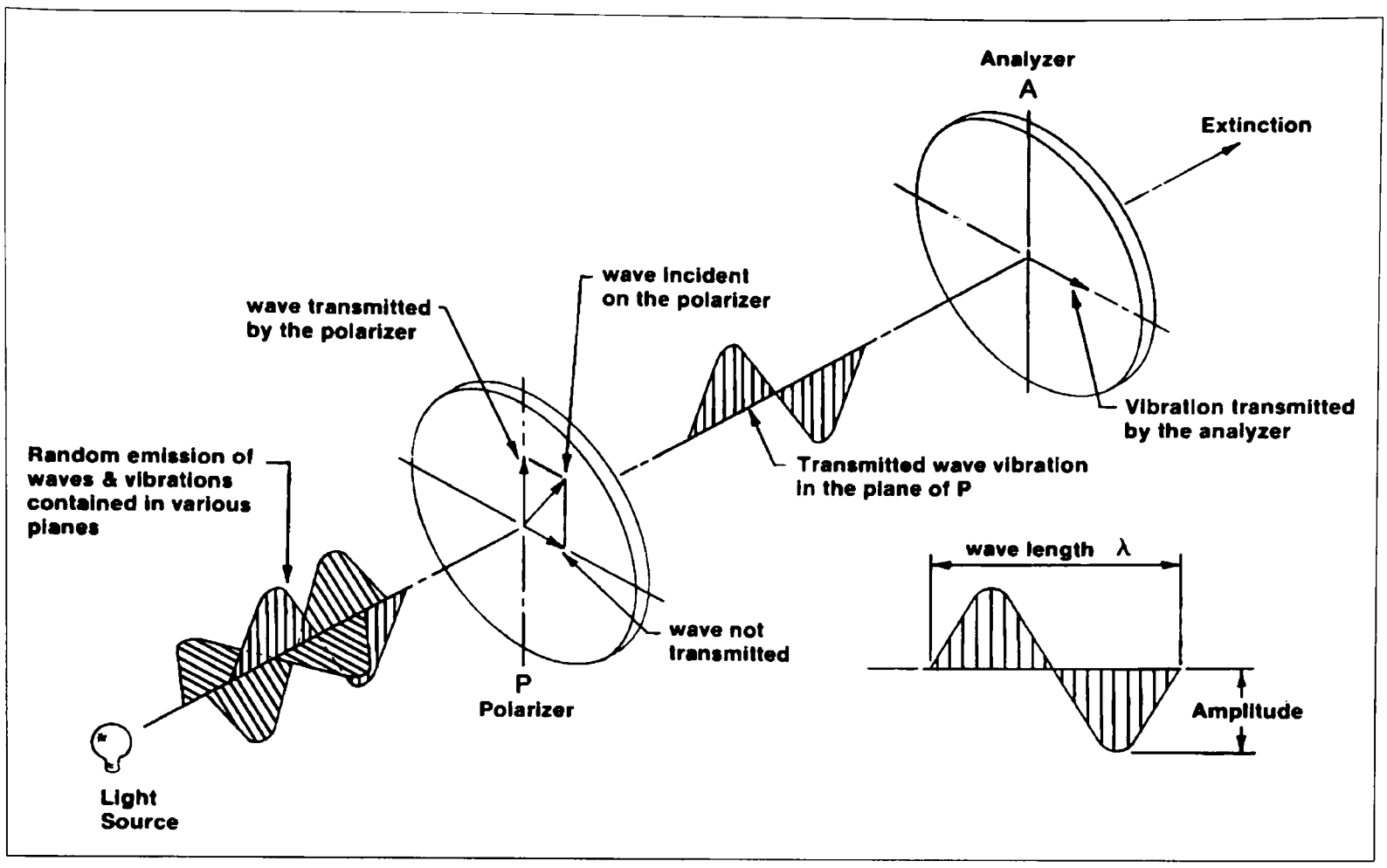

Figure C.1 Polarisation of Light

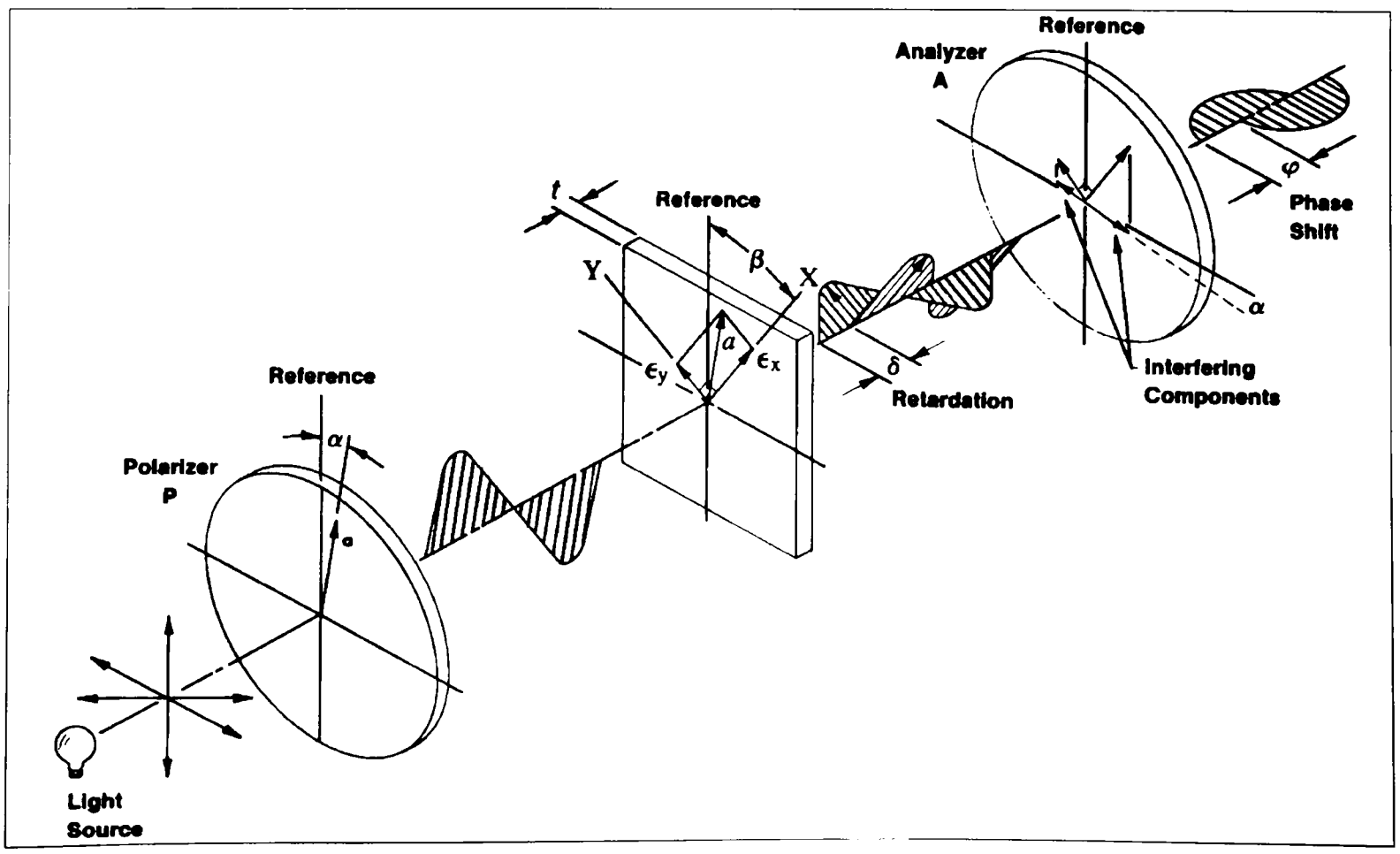

Figure C.2 Plane Polariscope

viewed through the analyser.

In the manufacture of polariser films, a thin sheet of polyvinyl alcohol is heated, stretched and immediately bonded to a supporting sheet of cellulose acetate butyrate. The polyvinyl face of the assembly is then stained by a liquid rich in iodine, where the amount of iodine diffused into the sheet determines its quality.

When a specimen is placed between the polariser and analyser, the birefrengent material results in the polarised light wave to resolve a light vector into two orthogonal components and to transmit the components with different velocities. The transmission of light along axis 1 proceeds at velocity c_1 and along axis 2 at velocity c_2. The light components travel at different velocities and so emerge from the specimen at different times. Therefore one component is retarded in time relative to the other. This retardation produces a relative phase shift, Δ, between the two components, which is dependant on the thickness of the sample. Upon passing through the analyser, the two waves are projected onto the axis of polarisation. The velocity of each wave is proportional to the relative retardation at that point and is proportional to the principal stress difference.

The deformed polymeric specimen produces fringe patterns due to the aforementioned optical interference effect. Two types of data can be obtained by photoelastic analysis; *isoclinics* and *isochromatics*. Since the intensity of light is proportional to the square of the amplitude of the light wave, the intensity of the light emerging from the analyser of a plane polariscope is given by Equation C.1 (Dally *et al*, 1991).

$$I = K.\sin^2 2\alpha.\sin^2\frac{\Delta}{2} \qquad \textbf{(C.1)}$$

where

$$\Delta = \Delta_2 - \Delta_1 = \frac{2\pi h}{\lambda}(n_2 - n_1) = \frac{2\pi hc}{\lambda}(\sigma_1 - \sigma_2)$$

Equation C.1 indicates that extinction (I=0) occurs either when $\sin^2 2\alpha = 0$ or when $\sin^2 (\Delta/2) = 0$, the former being related to the direction of the principal refractive indicies and to the principal-stress directions and the latter to the principal-stress difference.

When $2\alpha = n\pi$, where $n = 0, 1, 2,...$, $\sin^2\alpha = 0$ and extinction occurs. This indicates that, when one of the principal-stress directions coincides with the axis of the polariser ($\alpha = 0, \pi/2,$ or any exact multiple of $\pi/2$) the intensity of the light is zero and this is valid for all points in the specimen. The fringe patterns produced are loci of points where the principal-stress directions (either σ_1 or σ_2) coincide with the axis of the polariser. This is the isoclinic fringe pattern.

When $\Delta/2 = n\pi$, where $n = 0, 1, 2, ...$, $\sin^2(\Delta/2) = 0$ and extinction occurs. When the principal-stress difference is either zero ($n = 0$) or sufficient to produce an integral number of wavelengths of retardation ($n = 1, 2, ...$), the intensity of the emerging light from the analyser is zero. When a specimen is viewed through the polariscope, this condition for extinction yields a second fringe pattern where the fringes are loci of points exhibiting the same order of extinction ($n = 0, 1, 2, ...$). The fringe pattern produced by the $\sin^2(\Delta/2)$ term in Equation C.1 is the isochromatic fringe pattern The magnitude of the principal stress difference is determined by the following relationship in Equation C.2.

$$\sigma_1 - \sigma_2 = \frac{Nf_\sigma}{t} \qquad \textbf{(C.2)}$$

where σ_1 and σ_2 = Principal stresses ($N.m^{-2}$)

N = Fringe order

f_σ = Material fringe constant ($N.m^{-2}.m^{-1}.fringe^{-1}$)

t = Specimen thickness

When a stressed model is observed through a polariscope the fringe pattern consists of both isoclinics and isochromatics. The distinction between the two can be made by choosing the appropriate light source. In monochromatic light, both isoclinics and isochromatics appear as black fringes, whereas with a white light source the colour of the isochomatics is in the white light spectrum, while isoclinics remain black.

Circular slices of tested specimens were taken perpendicular to the loading direction, since it was considered that the material flow is most apparent in this direction. A sample was cut from the central portion of a specimen which had previously been deformed at a strain-rate of approximately $2000s^{-1}$ to 60% true strain. The cutting process was performed using a diamond impregnated eroding wire and a specialised cutting machine seen in Figure C.3. Care was taken for the specimen slice to be parallel to the specimen faces. An initial thickness of approximately 1mm was cut and then both surfaces were polished using fine 1200-grade Emery paper. The resulting polished surface was wetted with light paraffin oil to reduce the interference of slight surface imperfections. Light paraffin oil is used since its refractive index is identical to that of epoxy.

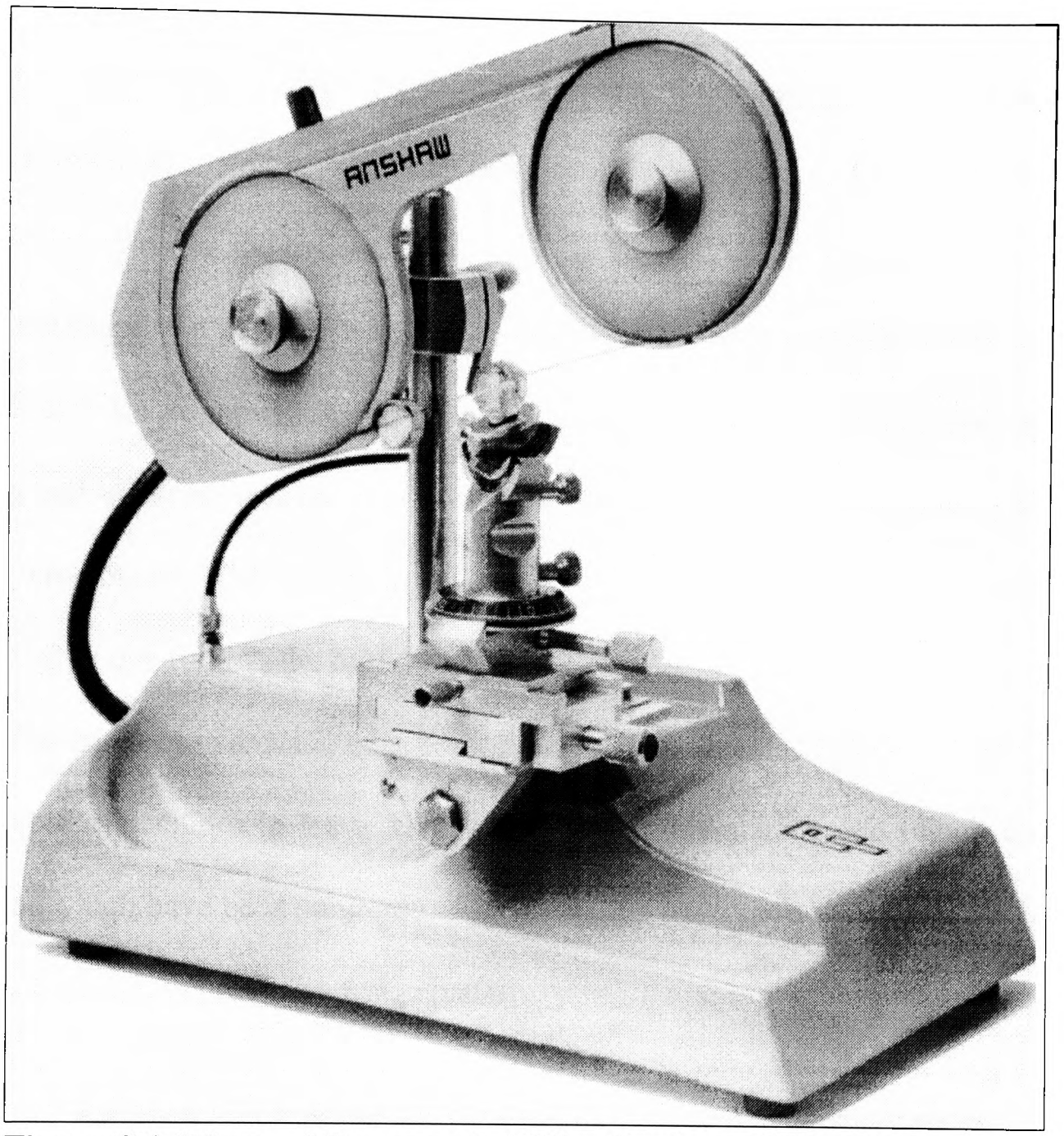

Figure C.3 Diamond Impregnated Wire Eroder and Machine

To provide a comparison between deformed and undeformed states, a slice of material was also produced from an undeformed specimen. This was part of the same batch of specimens manufactured for testing and an identical procedure was employed for slicing and polishing as for the deformed specimen. Both samples were placed in the polariscope with the polariser and analyser set to 0° and 90° for complete extinction of light. Figure C.4 represents the image observed for an undeformed specimen, whilst Figures C.5a & C.5b show the effect that deformation has on a deformed specimen. Both images were taken at 0°.

The undeformed specimen in Figure C.4 is grey in appearance, representing uniform retardation, and shows no fringe patterns. The absence of fringe patterns indicates that the material is optically isotropic, where the molecular chains have a random orientation.

At the centre of the deformed specimen, in Figure C.5a, is a pattern which is tending towards the shape of a 'cross'. This image is taken in plane polarised light and both isoclinics and isochromatics are shown. Isoclinics, as explained previously, represent the principal-stress direction and hence molecular alignment. The 'cross' is seen to rotate as the polariser and analyser are rotated. The radial extinction, hence the ordering, is seen to becomes less pronounced as one follows the cross from the centre to the circumference. Isochromatics are observed as fringes towards the outside of the specimen. Circularly polarised light was used to remove the isoclinics to leave an image of just isochromatics, see Figure C.5b. Other specimens which have been subjected to lower strains have been sliced, but the flow is not significant enough to produce a fringe pattern.

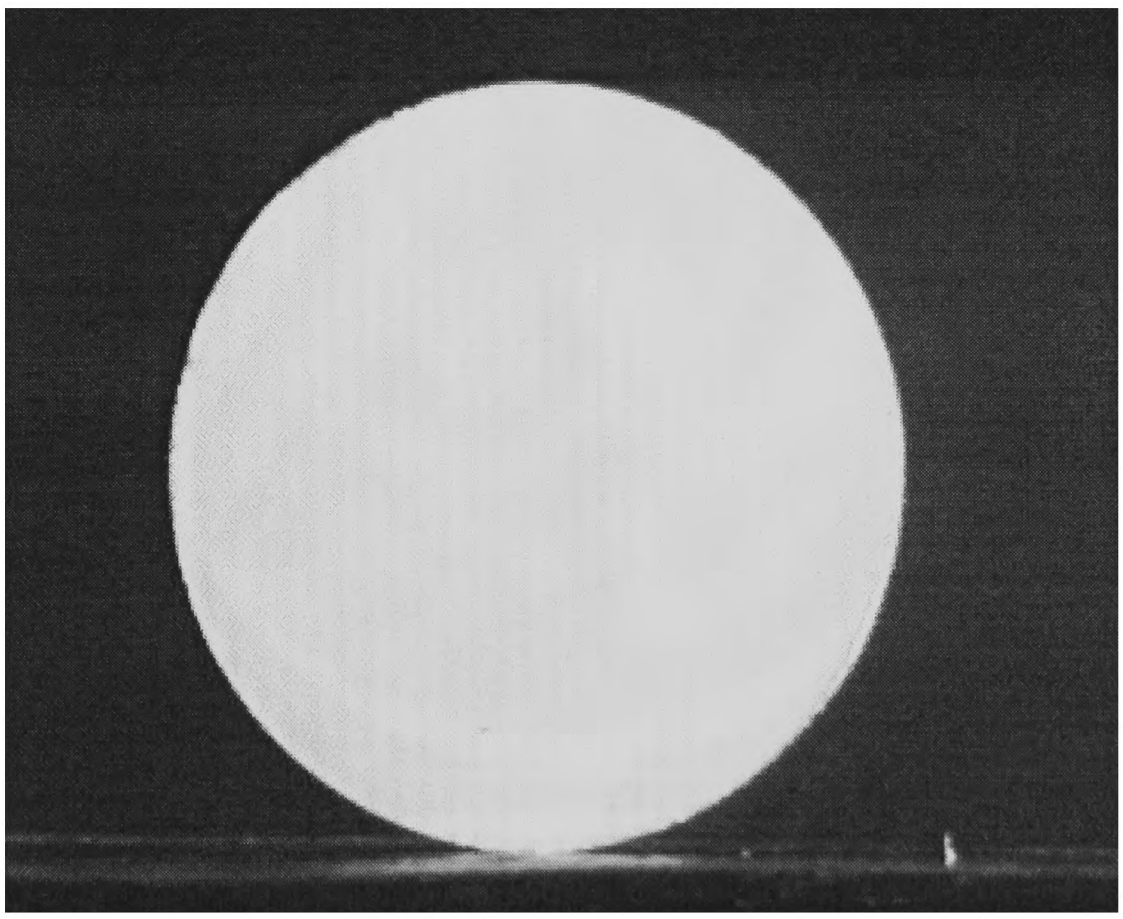

Figure C.4 Undeformed Specimen in Polarised Light

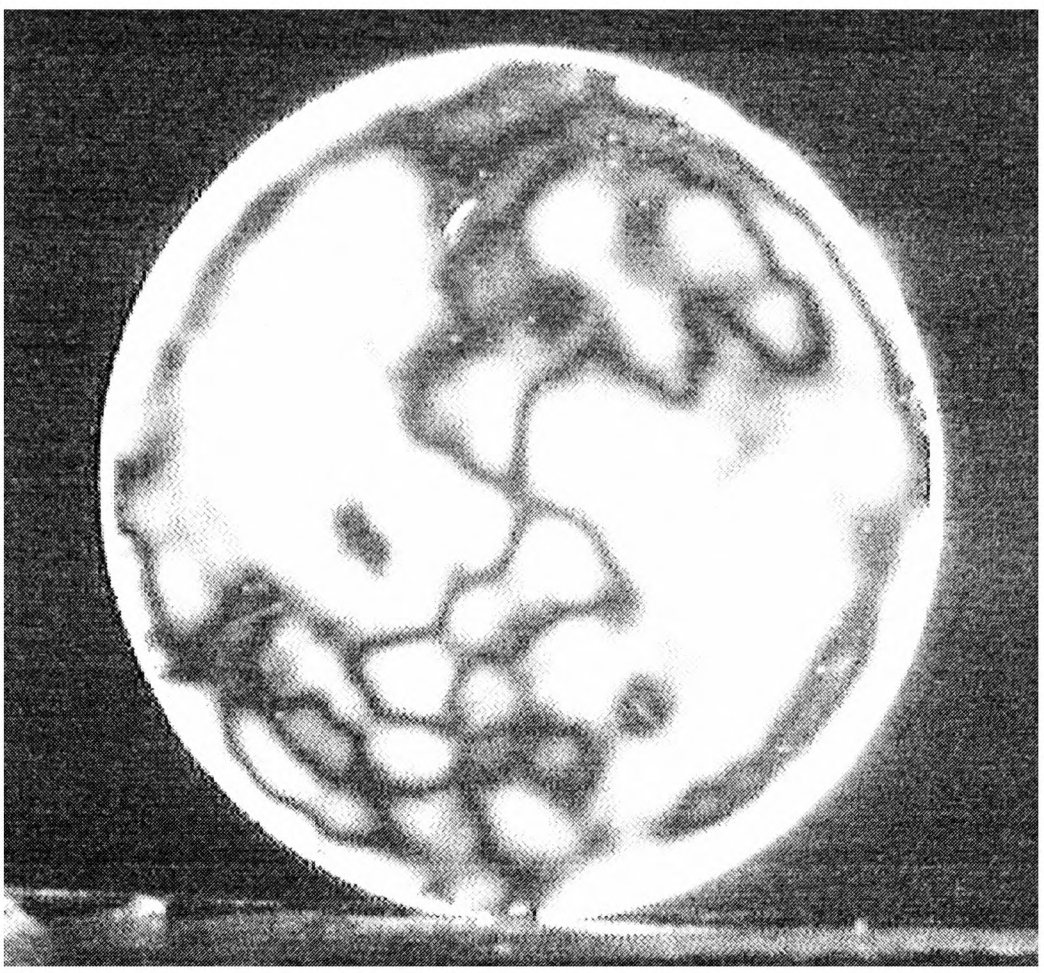

Figure C.5a Deformed Specimen Showing both Isoclinics and Isochromatics

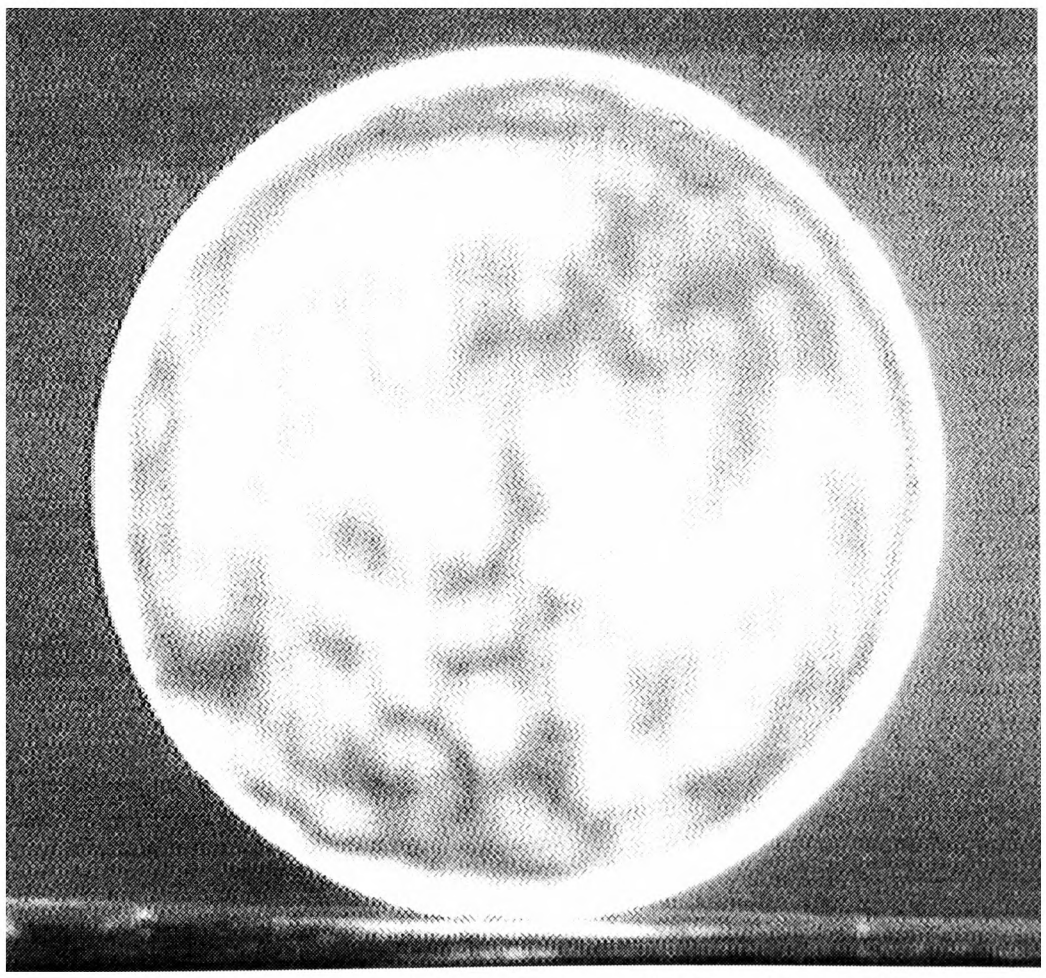

Figure C.5b Deformed Specimen with Isoclinics Removed

C.2 References

Dally, J.W. & Riley, W.F., Experimental Stress Analysis, 3rd Ed., McGraw Hill, 1991.